UNIVERSITY OF PADOVA

PADOVA NEUROSCIENCE CENTER

PhD Course in Neuroscience - Cycle: XXXV

Investigating the brain's 'dark energy' through the complex coupling of [^{18}F]FDG PET and resting-state functional MRI

Candidate:

Tommaso Volpi

Headmaster of the School:

Prof. Antonino Vallesi

Supervisor:

Prof. Maurizio Corbetta

Co-Supervisor:

Prof. Alessandra Bertoldo

Contents

Abstract

The human brain has a remarkable metabolic budget, and most of its glucose and oxygen consumption happen during rest. However, the precise factors that control resting-state metabolism across different brain regions are still unknown. Two functional imaging tools that can provide a window into the complex mechanisms of brain metabolism and spontaneous activity are positron emission tomography (PET) and functional MRI (fMRI). In particular, the PET radiotracer [^{18}F]fluorodeoxyglucose ([^{18}F]FDG) allows to track the first steps of glucose metabolism in the brain *in vivo*; resting-state fMRI (rs-fMRI), on the other hand, has a offered a powerful non-invasive tool for assessing proxies of spontaneous brain activity through blood oxygenation, as well describing a large-scale brain organization into 'functional connectivity' (FC) networks, composed of brain regions whose rs-fMRI signals fluctuate in synchrony. Trying to disentangle both the redundancy and the complementarity in the information coming from these two imaging modalities is extremely relevant for both neuroscientific and technical questions, e.g., 1) to characterize the functional drivers of local glucose consumption, 2) to better understand the somewhat unclear physiological and metabolic bases of the rs-fMRI signal, 3) to describe the large-scale functional network architecture of the resting brain both in hemodynamic and in metabolic terms, 4) to provide reliable fMRI-based proxies of glucose metabolic consumption to use as biomarkers of disease etc.

In this thesis work, organized into three main parts, we have broadened the horizon of [^{18}F]FDG PET vs. rs-fMRI integration on multiple levels.

First, we assess the relationship between [^{18}F]FDG standard uptake value ratio ($SUVR$), a relative and semiquantitative proxy of glucose metabolism, and a large range of fMRI-derived variables (= 50) to understand if the metabolic information probed by [^{18}F]FDG was more related to the fMRI signal local activity and coherence, or large-scale static and time-varying FC, expanding on previous assessments based only on a handful of fMRI features. Also, we develop a new methodological framework (including multiple regression and multilevel hierarchical modelling) to explore whether a *combination* of rs-fMRI variables could meaningfully explain more of the regional metabolic variability than simple pairwise associations.

Then, we expand our assessment by exploring the details of metabolic physiology thanks to full kinetic modelling of [^{18}F]FDG dynamic PET data: in particular, we move away from $SUVR$ by estimating parametric maps of the [^{18}F]FDG delivery (K_1 [ml/cm^3/min]) and phosphorylation (k_3 [min^{-1}]), and evaluate their peculiar regional distribution, never previously described at this level of spatial resolution. We proceed by assessing how these parameters, including the tracer uptake rate (K_i [ml/cm^3/min]), interact not only with rs-fMRI features, but also with regional cerebral blood flow (CBF) and metabolic rate of oxygen ($CMRO_2$), to have the most complete vision possible of these complex metabolic and hemodynamic relationships.

Finally, we try to understand if a closer match between [^{18}F]FDG and rs-fMRI information can be attained at the large-scale network level by obtaining a single-subject 'metabolic connectivity'(MC) estimate, i.e., a PET counterpart to fMRI FC. To do so, we provide a completely new methodological framework for single-subject MC estimation, by employing a distance-based (and not a correlation-based) metric, and using kinetic modelling to differentiate MC matrices based on tracer inflow vs. metabolic events. These individual MC estimates are then compared to traditional across-subject covariation matrices of [^{18}F]FDG parameters, and both are related to fMRI FC to understand which approach has a higher level of similarity.

Sommario

Il cervello umano ha un notevole budget metabolico, e la gran parte del suo consumo di glucosio e ossigeno avviene a riposo. Tuttavia, i precisi fattori che controllano il metabolismo delle diverse regioni cerebrali nello stato di riposo (resting state) sono ancora sconosciuti.
Due strumenti di imaging funzionale che possono fornire una finestra di osservazione sui complessi meccanismi del metabolismo e dell'attività spontanea cerebrale sono la tomografia a emissione di positroni (PET) e la risonanza magnetica funzionale (fMRI). In particolare, il tracciante PET [^{18}F]Fluorodeossiglucosio ([^{18}F]FDG) consente di seguire i primi step del metabolismo del glucosio nel cervello *in vivo*; la fMRI in resting state (rs-fMRI), dall'altro lato, ha fornito un potente strumento non invasivo per misurare dei succedanei dell'attività spontanea cerebrale basati sull'ossigenazione ematica, e per descrivere un'organizzazione su larga scala del cervello in reti di 'connettività funzionale' (FC), costituite da regioni cerebrali i cui segnali rs-fMRI fluttuano in sincronia. Cercare di dipanare gli elementi ridondanti e quelli complementari nelle informazioni provenienti da queste due modalità di imaging è estremamente rilevante per domande sia neuroscientifiche che tecniche, ad esempio, 1) per caratterizzare i substrati funzionali del consumo locale del glucosio, 2) per comprendere meglio le basi fisiologiche e metaboliche, ancora parzialmente non chiare, del segnale rs-fMRI, 3) per descrivere l'architettura di reti funzionali su larga scala del cervello a riposo sia in termini emodinamici che funzionali, 4) per fornire succedanei affidabili basati su fMRI del consumo metabolico di glucosio, da usare come biomarcatori di malattia, ecc.
In questo lavoro di tesi, organizzato in tre parti principali, abbiamo ampliato l'orizzonte dell'integrazione tra [^{18}F]FDG PET e rs-fMRI su multipli livelli.
In primo luogo, abbiamo valutato la relazione tra lo standard uptake value ratio ($SUVR$) di [^{18}F]FDG, un succedaneo relativo e semi-quantitativo del metabolismo del glucosio, e un ampio range di variabili derivate da fMRI (= 50) per com-

prendere se l'informazione metabolica valutata da [^{18}F]FDG fosse maggiormente legata all'attività e alla coerenza locale del segnale fMRI, o alla FC statica e dinamica su larga scala, ampliando la visione rispetto ai risultati precedenti basati solo su poche variabili fMRI. Inoltre, abbiamo sviluppato una nuova impalcatura metodologica (che include regressione multipla e modellistica gerarchica multilivello) al fine di esplorare se una *combinazione* di variabili rs-fMRI potesse spiegare in modo significativo una maggior percentuale di variabilità metabolica regionale rispetto a semplici associazioni bivariate.
Successivamente, abbiamo espanso la nostra valutazione esplorando i dettagli della fisiologia metabolica grazie a modelli cinetici dei dati [^{18}F]FDG PET dinamici: in particolare, ci siamo lasciati alle spalle il $SUVR$ andando a stimare mappe parametriche di ingresso (K_1 [ml/cm^3/min]) e fosforilazione (k_3 [min^{-1}]) del [^{18}F]FDG, e studiando la loro peculiare distribuzione regionale, mai descritta prima a questo livello di risoluzione spaziale. Inoltre, abbiamo valutato come questi parametri, compresa la velocità di accumulo del tracciante (K_i [ml/cm^3/min]), interagiscono non solo con le variabili rs-fMRI, ma anche con il flusso ematico cerebrale (CBF) e il tasso metabolico dell'ossigeno ($CMRO_2$) regionale, per avere una visione il più completa possibile di queste complesse relazioni metaboliche ed emodinamiche.
Infine, abbiamo cercato di comprendere se fosse possibile raggiungere una più stretta corrispondenza tra informazioni [^{18}F]FDG e rs-fMRI a livello di reti di larga scala ottenendo una stima a singolo soggetto di 'connettività metabolica' (MC), cioè una controparte PET alla FC di fMRI. Per fare questo, abbiamo fornito una impalcatura metodologica completamente nuova per la stima della MC a singolo soggetto, utilizzando una metrica basata sulla distanza (e non sulla correlazione) e usando i modelli cinetici per differenziare tra matrici MC basate sull'ingresso del tracciante da quelle basate sugli eventi metabolici. Queste stime di MC individuali sono poi state confrontate alle tradizionali matrici di covariazione attraverso i soggetti dei parametri [^{18}F]FDG, ed entrambe sono state messe in relazione alla FC di fMRI per comprendere quale approccio avesse il maggior livello di similarità.

List of Figures

List of Tables

Acronyms

$[^{18}F]FDG$ = $[^{18}F]$fluorodeoxyglucose

$[^{15}O]H_2O$ = $[^{15}O]$water

$[^{15}O]O_2$ = $[^{15}O]$oxygen

AIF = arterial input function

$ALFF$ = amplitude of low-frequency fluctuations

$ApEn$ = approximate entropy BBB = blood-brain barrier

BC = betweenness centrality

BOLD = blood oxygen level-dependent

BNV = between-network variability

BSV = between-subject variability

CBF = cerebral blood flow

CBV = cerebral blood volume

CC = clustering coefficient

$CMRglc$ = cerebral metabolic rate of glucose

$CMRO_2$ = cerebral metabolic rate of oxygen

CSF = cerebro-spinal fluid

CV% = percentualized coefficient of variation

DAN = dorsal attention network

DEG = degree

DMN = default mode network

dMRI = diffusion magnetic resonance imaging

DSC = Dice similarity coefficient

EC = eigenvector centrality

EF = extraction fraction

EPI = echo-planar imaging

ES = Euclidean similarity

$fALFF$ = fractional amplitude of low-frequency fluctuations

FC = functional connectivity

FDR = false discovery rate

FOV = field of view

fPET = 'functional' positron emission tomography

FWHM = full-width-at-half-maximum GE = global efficiency

GETS = general-to-specific modelling

GM = grey matter

HRF = hemodynamic response function

ICA = independent component analysis

IDIF = image-derived input function

K_1 = influx/delivery rate

k_2 = efflux rate

k_3 = phosphorylation rate

K_i = fractional uptake rate, net trapping rate

LC = lumped constant

LE = local efficiency

LME = linear mixed-effects modelling

MAD = median absolute deviation

MC = metabolic connectivity

MLM = multilevel modelling

NAD = naïve average data

NNLS = non-negative least squares

NPD = naïve pooled data

OLS = ordinary least squares

PCA = principal component analysis

PET = positron emission tomography

PVE = partial volume effect

$ReHo$ = regional homogeneity

ROI = region of interest

rs-fMRI = resting-state functional magnetic resonance imaging

RSN = resting-state network

RSS = residual sum of squares

SAL = salience network

$SampEn$ = sample entropy

SC = structural connectivity

SD = standard deviation

SE = standard error

sFC = static functional connectivity

SMN = sensorimotor network

SNR = signal-to-noise ratio

ss-MC = *subject series* metabolic connectivity

STR = strength

SUB = subcortical

$SUVR$ = standardized uptake value ratio

TAC = time-activity curve

ts-MC = *time series* metabolic connectivity

tvFC = time-varying functional connectivity

VAN = ventral attention network

V_b = blood volume fraction

VB = Variational Bayes

VIS = visual network

WM = white matter

WNLLS = weighted nonlinear least squares

WRES = weighted residuals

Chapter 1

Introduction and Motivation

> ≪*The mammalian brain is a complex heterogeneous organ comprising many components with different [. . .] levels of functional activity and energy metabolism.*≫ (L. Sokoloff et al. 1977)

> ≪*The brain apparently uses most of its energy for functions unaccounted for – dark energy, in astronomical terms. What do we know about this dark energy?"*≫ (Marcus E. Raichle 2006)

The human brain is responsible for at least 20-25% of the body's glucose metabolic consumption, while accounting for only 2% of the body's weight, and in physiological conditions glucose represents its only source of energy (Kety 1957; Clarke and Louis Sokoloff 1999).

The cerebral metabolic rate of glucose ($CMRglc$) is known to be coupled to the cerebral metabolic rate of oxygen ($CMRO_2$), as most of glucose consumption happens through oxidative phosphorylation (Magistretti and Pellerin 1999), and the cerebral blood flow (CBF), responsible for carrying the nutrients necessary to the brain. Importantly, glucose expense displays significant *regional variability* in the healthy brain, but the reasons governing this heterogeneity remain largely unexplained.

The majority of energy expenditure in terms of glucose ($CMRglc$) and oxygen consumption ($CMRO_2$) seems to happen while the brain is idle at rest (Louis Sokoloff et al. 1955): this remarkable metabolic budget, which was famously called '*the brain's dark energy*' (Marcus E. Raichle 2006), is expected to be mainly employed for maintaining resting potentials and subthreshold synaptic transmission (Marcus E. Raichle 2006), since most of the energy budget of a neuron is utilized at the level of the *synapses*, rather than in the neuron's body (Louis

Sokoloff 1999). This putative importance of spontaneous activity is a key reason for trying to integrate resting-state measurements of glucose metabolism with complementary imaging techniques attempting to capture the patterns of brain intrinsic activity.
Traditionally, $CMRglc$ is calculated using positron emission tomography (PET) and the [^{18}F]fluorodeoxyglucose ([^{18}F]FDG) radiotracer (L. Sokoloff et al. 1977; Phelps et al. 1979). While full kinetic modelling is known to provide more accurate and precise information (Lammertsma 2017), a simplified proxy of glucose metabolism requiring only a short, static [^{18}F]FDG PET scan has been devised, i.e., standardized uptake value ratio ($SUVR$), now used in most clinical and research studies (Hamberg et al. 1994).
On the other hand, one of the most frequently employed tools to study intrinsic activity in the brain is resting-state functional magnetic resonance imaging (rs-fMRI), which is based on the so-called blood oxygen level-dependent (BOLD) contrast resulting from changes in hemoglobin oxygenation in response to brain activity (S. Ogawa, T. M. Lee, et al. 1990). BOLD rs-fMRI has allowed to map many properties of the brain's intrinsic functional architecture, in particular its 'functional connectivity' (FC), i.e., the statistical association between low-frequency fluctuations of BOLD time series of different areas, which allows to describe an organization into resting-state networks (RSNs) (M. D. Fox and Marcus E. Raichle 2007). However, the physiological interpretation of the BOLD signal is still difficult. Physiological models of BOLD have shown how local neural activity can give rise to BOLD signal fluctuations once convolved with the hemodynamic response function (HRF), which involves changes in blood volume (CBV), CBF, and $CMRO_2$ (Buxton, Uludağ, et al. 2004; Kim and Seiji Ogawa 2012), but many interpretation problems are left open.
Building upon the previous considerations, the relationship between the spatial information provided by [^{18}F]FDG PET and by rs-fMRI needs to be thoroughly investigated with two main aims:

1) first, the sources of *regional variability* in glucose expense need to be better understood, and rs-fMRI features should provide relevant insights; in particular, we might wonder how much of the brain's energy consumption is related to a) *local activity* and *synchronization* of spontaneous activity patterns; b) local information on the HRF; c) inter-regional *static* synchrony (FC); d) *dynamic*, time-varying interactions between regions (Allen et al. 2014)?

2) second, from the opposite perspective, the physiological basis of BOLD-

derived properties needs to be further characterized, and [^{18}F]FDG PET can help in this by elucidating the underlying metabolic processes. In the growing literature on [^{18}F]FDG vs. fMRI comparisons, the main findings are an overall good spatial match between [^{18}F]FDG parameters (usually $SUVR$, rarely $CMRglc$) and rs-fMRI regional homogeneity ($ReHo$), i.e., the *local* coherence of the BOLD signal (D. Tomasi, G. J. Wang, and Volkow 2013; Marco Aiello et al. 2015; Bernier et al. 2017; J. Wang et al. 2021). Less stable/weaker associations are found for *large-scale* FC (D. Tomasi, G. J. Wang, and Volkow 2013; Marco Aiello et al. 2015; Palombit et al. 2022). Notably, only bivariate associations have been tested in the majority of these works.
Another possible approach to look for a match between [^{18}F]FDG and rs-fMRI properties is to bring them both to a 'connectivity' framework, which means comparing FC to its PET counterpart, i.e., 'metabolic connectivity' (MC), describing the relationships between metabolic rates of different brain regions. Most of the MC literature, however, resorts to measures of across-subject covariation of $SUVR$ (Horwitz, Duara, and Rapoport 1984; Yakushev, Drzezga, and Habeck 2017; Di, Gohel, et al. 2017) instead of deriving single-subject estimates that could directly match individual-level FC. A few studies have attempted to use dynamic PET to obtain subject-level MC estimates (Wehrl et al. 2013; Ionescu et al. 2021; Jamadar et al. 2021), but these methodologies, though promising, are still in their infancy.

1.1 Aim

The aim of this thesis was to explore the coupled and complementary information that [^{18}F]FDG PET and rs-fMRI can provide on metabolism and spontaneous activity across the whole brain.
To this end, we first evaluated the association of [^{18}F]FDG $SUVR$ to a large battery of features obtained from rs-fMRI using a new multivariable modelling framework (chapter 4).
Then, we expanded our assessment to [^{18}F]FDG kinetic model parameters (K_i, K_1, k_3) for the first time, to evaluate how their regional variability could relate to rs-fMRI, as well as to other metabolic properties such as CBF and $CMRO_2$, using the aforementioned statistical framework (chapter 5).
Finally, we moved from a local, *region*-based [^{18}F]FDG analysis to a large-scale, *network*-based approach, assessing different ways to compute single-subject and

across-subject MC though the lens of PET kinetic modelling, with the hypothesis that applying a ‘connectivity’ approach also to PET would improve the similarity with rs-fMRI FC (chapter 6).
Several methodological challenges were addressed during this research work, related in particular to appropriate estimation of rs-fMRI features, tuning of multiple regression and feature selection strategies, voxel-wise estimation of [^{18}F]FDG kinetic model parameters and CBF using an image-derived input function (IDIF) (see Chapter 8), selection of the most appropriate estimation approaches for single-subject MC.

1.2 Thesis Contributions and Outline

Here is a list which briefly describes the topics covered in each chapter of this dissertation and the contributions made to them.

Chapter 1: Introduction and Motivation
The current chapter provides an introductory overview and motivation for the research presented in this dissertation.

Chapter 2: [^{18}F]FDG Positron Emission Tomography
This chapter introduces the principles of PET, in particular with reference to the [^{18}F]FDG tracer. A description is given of static vs. dynamic PET experiments, and of kinetic modelling as a means of deriving specific physiological information about the tracer delivery and binding. A brief comment on the role of the input function (also discussed in Chapter 8) is provided. Moreover, we give an overview of the approaches employed for across-subject and within-subject MC calculation.

Chapter 3: Resting-state Functional Magnetic Resonance Imaging
This chapter introduces the basic principles of rs-fMRI. A brief description of the main features that can be derived from rs-fMRI, i.e., those related to the 1) signal and its local properties, 2) HRF, 3) static FC, 4) time-varying FC, is given.

Chapter 4: Modelling the complex spatial relationship between [^{18}F]FDG SUVR and resting-state fMRI features
In this chapter we study the spatial coupling between [^{18}F]FDG $SUVR$, a static semi-quantitative index of glucose metabolism, and 50 different rs-fMRI features,

representative of all the main types of information that can be obtained from the BOLD signal, in a group of healthy individuals.

One main contribution of this study is to extend the assessment of the [^{18}F]FDG-fMRI coupling to a large range of rs-fMRI features (including, for the first time, HRF-related and tvFC-based features). Moreover, for the first time, we assess the *multivariable* information provided by rs-fMRI predictors of $SUVR$ regional variability to see how much explanatory power we can reach, both at group and single-subject level.

Overall, we find that $SUVR$ still contains a large portion of spatial information which is not explained by the available rs-fMRI features, and that only *local* rs-fMRI information is promising for explaining [^{18}F]FDG metabolism.

Chapter 5: The spatial distribution of [^{18}F]FDG delivery and phosphorylation, and their coupling with fMRI

This chapter builds upon the limitations of the previous analysis, which was restricted to a static [^{18}F]FDG approach and a limited number of subjects. Here, we expand our assessment to around 50 individuals with dynamic [^{18}F]FDG PET acquisitions, which allow us to estimate the kinetic parameters of interest (K_i, K_1, k_3) using an IDIF approach (see Chapter 8).

The main contribution of this study pertains to how the [^{18}F]FDG kinetic parameters, which have a clear physiological interpretation (as seen above, related to glucose uptake, delivery and phosphorylation), have been obtained at a high level of resolution, allowing us to study their peculiar spatial distribution for the first time. Moreover, the availability of CBF and $CMRO_2$ estimates from ^{15}O PET data has allowed us to try and understand which combination of rs-fMRI and ^{15}O PET information could best explain the observed [^{18}F]FDG PET spatial patterns.

Again, even when [^{18}F]FDG kinetic parameters are considered, we find that *local* rs-fMRI variables are still the most predictive of the regional variability of glucose metabolism.

Chapter 6: Bringing [^{18}F]FDG PET to the 'brain connectivity' framework to explore its match with functional connectivity

In this chapter, we move away from the *region*-level approach, to extend it to a *network*-level, brain connectivity framework. Our main aims are: 1) to develop an approach for estimating single-subject PET connectivity using dynamic PET time-activity curves (TACs), 2) to assess the relationships between our single-subject approach and the traditional across-subject metabolic connectivity (MC), 3) to verify if a single-subject approach improves the match with rs-fMRI FC. The main contributions of this study are the use of a new, distance-based metric for single-subject MC calculation, the use of concepts from PET kinetic modelling for both across-subject and within-subject MC (i.e., kinetic parameters, compartment time courses, as in Chapter 5), and the demonstration of a good match with fMRI FC, potentially implying that *network*-level information becomes relevant when both PET and fMRI are brought to a connectivity framework.

Chapter 7: Conclusions
The final chapter summarizes the dissertation's contributions and discusses some perspectives for the topics under study.

Chapter 2

Positron Emission Tomography

In the field of functional brain imaging, PET is among the most well-known techniques. Pioneered by Dr. Louis Sokoloff in the 1970s (L. Sokoloff et al. 1977), it allows for in vivo quantification of the kinetics of enzymes and receptors by means of injectable radiotracers such as the aforementioned [^{18}F]FDG, which images tissue glucose consumption and has such widespread use in the fields of oncology, neurology and cardiology to have been called the “molecule of the millennium” (Britz-Cunningham and Adelstein 2003).

Two experimental frameworks are typically employed in PET imaging, i.e., *static* acquisitions, the most frequent in the clinical setting, where a single image is reconstructed from the acquired radioactive counts in a given window of time, and *dynamic* acquisitions, usually reserved to the research environment, where a multi-frame reconstruction of the tracer kinetics over time is obtained (Figure 2.1) (Alessandra Bertoldo, Rizzo, and Veronese 2014).

PET is known to be highly sensitive and biochemically specific, with the ability to detect concentrations of enzymes and receptors ranging up to 10^{-11} mol/L and 10^{-12} mol/L, and, differently from MRI in general, it can provide quantitative estimates (Catana 2017; Meikle et al. 2021). On the other hand, PET conventionally suffers from limited spatial resolution, which is in the order of 5-6 mm for standard PET cameras, making it susceptible to partial volume effects (PVEs) (Rousset et al. 2007). Moreover, its temporal resolution is traditionally in the order of minutes, making it difficult to follow fast processes, and it also carries (minor) radioactivity-related risk for the subjects undergoing the study. These are among the reasons why over time it has become less popular, even leading to some researchers calling it as a ‘dying white elephant’ (Cumming 2014).

However, in addition to its continued clinical utility, new developments in both hardware and software are pushing these boundaries and opening up new and exciting scenarios for PET imaging, both in the brain and in the rest of the body (Meikle et al. 2021; T. Feng et al. 2021).

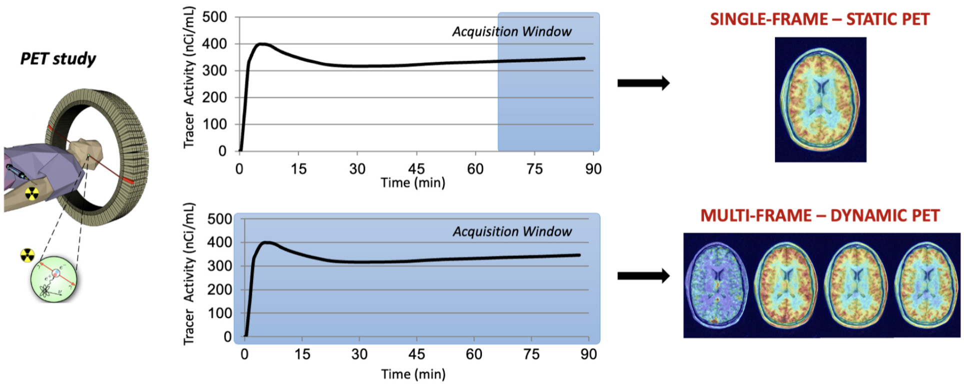

Figure 2.1: *Static* vs. *dynamic* brain PET imaging. In *static* scans, the activity of the tracer is counted over a given time window and reconstructed into a single image. In *dynamic* studies, the activity of the tracer is measured at multiple time points, resulting in four-dimensional data. Adapted from (Alessandra Bertoldo, Rizzo, and Veronese 2014).

2.1 $[^{18}F]$FDG PET quantification: from compartmental modelling to $SUVR$

To quantify $CMRglc$ and other physiological parameters related to glucose metabolism, $[^{18}F]$FDG is the tracer of choice, a glucose analogue with favorable pharmacokinetic properties, which make it more tractable than the ideal tracer $[^{11}C]$glucose (Blomqvist et al. 1990).

Assuming glucose metabolism to be in steady state, according to tracer-tracee theory, $[^{18}F]$FDG kinetics can be described by linear time-invariant differential equations based on considerations of *mass* conservation, then translated into *concentration* changes by assuming a given dilution volume (Alessandra Bertoldo, Rizzo, and Veronese 2014). $[^{18}F]$FDG kinetics is traditionally described by a two-tissue three-rate-constant (3K) compartmental model, which was developed by Dr. Louis Sokoloff (L. Sokoloff et al. 1977; Phelps et al. 1979), and still represents the gold-standard approach to $[^{18}F]$FDG quantification (Figure 2.2). For parameter identification, a noise-free input is typically derived by arterial sampling of the $[^{18}F]$FDG plasma concentration $C_p(t)$, i.e., the so-called arterial input function (AIF). Then, the PET measurement equation,

$$C_{measured}(t) = (1 - V_b)(C_1(t) + C_2(t)) + V_b C_b \tag{2.1}$$

can be used to describe the total concentration of radioactivity over time, $C_{measured}(t)$, measured by the PET scanner, as the sum of the concentration of unmetabolized [^{18}F]FDG, $C_1(t)$, and metabolized (phosphorylated) [^{18}F]FDG, $C_2(t)$, while also accounting for the vascular volume fraction in the tissue, V_b ([%]), and the arterial blood tracer concentration $C_b(t)$,

$$C_b(t) = C_p(t)(1 - 0.3H) \tag{2.2}$$

obtained from $C_p(t)$ and the subject's hematocrit H. The differential equations describing the rates of concentration changes for $C_1(t)$ and $C_2(t)$ are:

$$\dot{C}_1(t) = K_1 C_p(t) - (k_2 + k_3)C_1(t) \qquad C_1(0) = 0 \tag{2.3}$$

$$\dot{C}_2(t) = k_3 C_1(t) \qquad C_2(0) = 0 \tag{2.4}$$

All the model parameters, i.e., K_1, k_2, k_3, V_b, are a priori uniquely identifiable (E. Carson 2013; Cobelli and E. R. Carson 2008). Other than V_b, three single rate constants, or microparameters, can be estimated:

- K_1 ([ml/cm^3/min]), which quantifies the arterial influx of [^{18}F]FDG across the blood-brain barrier (BBB) through glucose transporters (GLUT (Pessin and Bell 1992; Barrio et al. 2020)) with a saturable Michaelis-Menten kinetics;
- k_2 ([min^{-1}]), which quantifies the venous efflux of [^{18}F]FDG across the BBB;
- k_3 ([min^{-1}]), which quantifies the phosphorylation rate of [^{18}F]FDG into [^{18}F]FDG-6-P by the hexokinase enzyme in neurons and glia.

In Sokoloff's model, the dephosphorylation rate of [^{18}F]FDG-6-P to [^{18}F]FDG (k_4[min^{-1}]) is considered negligible during standard 60-minute acquisitions, which makes [^{18}F]FDG a tracer with irreversible kinetics. In longer experiments (> 120 min), k_4 can in fact be observed, requiring an adjustment to a four-rate-constant reversible model (4K); if observed in experiments shorter than 2 hours, however, k_4 was demonstrated to be an artifact of tissue heterogeneity (K. Schmidt et al. 1992). The K_1, k_2, k_3 rate constants are usually combined into a macroparameter called net trapping rate, K_i, ([ml/cm^3/min]),

$$K_i = \frac{K_1 k_3}{k_2 + k_3} \tag{2.5}$$

which is converted to

$$CMRglc = \frac{\hat{C}_p^{glc}}{LC} K_i \tag{2.6}$$

by a simple scaling factor, comprising blood glucose ($\hat{C}_p^{glc}$) and the *lumped constant* (LC), necessary to adjust for the different enzyme affinities between glucose and the [^{18}F]FDG tracer analogue (Reivich et al. 1985). Notably, even though this is usually not considered, the LC displays significant regional heterogeneity, with lower values for the cerebellum and infratentorial structures (Graham et al. 2002).

Importantly, [^{18}F]FDG PET quantification does not limit itself to the full kinetic description offered by compartmental modeling: less comprehensive approaches based on linearization of compartmental model equations have been developed, such as *input-output* methods and *graphical* methods.
Amongst the first, spectral analysis (A. Bertoldo, Vicini, et al. 1998; Cunningham and Jones 1993) is one of the most useful, as it can provide estimates not only of K_i, but also of other parameters (K_1 and V_b). Amongst graphical methods, Patlak's approach for irreversible tracers can provide a robust estimate of K_i (Patlak, Blasberg, and Fenstermacher 1983).
These approaches, however, still require an estimate of the $C_p(t)$, which is highly impractical to obtain, especially in a clinical context (see below).
A higher simplification is reached with semi-quantitative approaches, like the standardized uptake value (SUV),

$$SUV = \frac{[^{18}\text{F]FDG concentration [kBq/ml]}}{\frac{\text{injected dose [MBq]}}{\text{body weight [kg]}}} \tag{2.7}$$

which usually involves normalizing a static PET image by the injected dose and body weight (S.-C. Huang 2000). If each voxel's SUV (SUV_{target}) is normalized to the tracer uptake in a reference region ($SUV_{reference}$), or its whole-brain average (Byrnes et al. 2014), SUV becomes its relative counterpart, the SUV ratio ($SUVR$):

$$SUVR = \frac{SUV_{target}}{SUV_{reference}} \tag{2.8}$$

While these semi-quantitative indices have been validated in healthy subjects and

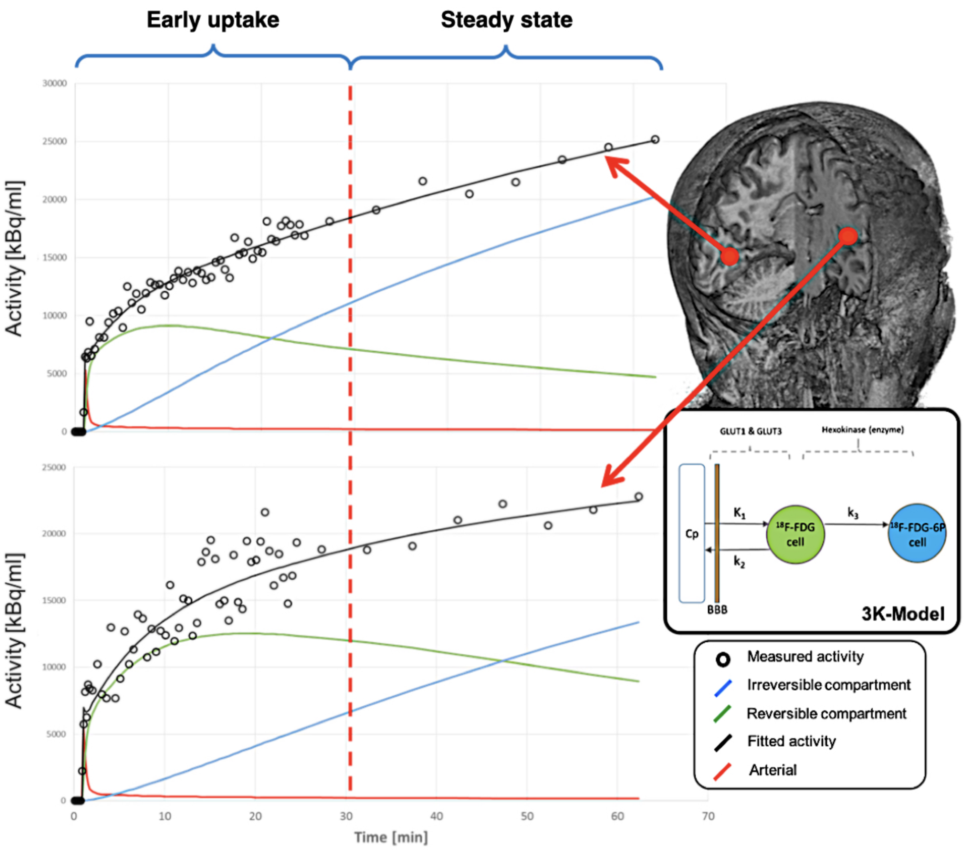

Figure 2.2: Schematics of [18F]FDG PET compartmental analysis in two brain areas with different kinetic properties. The dynamic PET data $C_{measured}(t)$ (*black circles*) measured in the two regions can be quantified using compartmental modeling: this produces a prediction (*black line*) which is given by the contribution of activity in both the first, reversible compartment $C_1(t)$ (*green line*) and second, irreversible compartment $C_2(t)$ (*blue line*), plus arterial blood activity $V_bC_b(t)$ (*red line*). The two represented brain areas display examples of different contributions of the first compartment (predominant in the *bottom* region) and second compartment (predominant in the *top* region). In the inset, Sokoloff's two-tissue compartmental model (3K) for [18F]FDG is shown (*circles* represent homogenous tissue compartments, while *arrows* indicate material fluxes between compartments due to transport, chemical transformations or both). Credits for this image go to Dr. Erica Silvestri.

proved to be extremely useful, their careful interpretation is necessary, as they may give a biologically confounded view of glucose metabolism (Hamberg et al. 1994; Keyes 1995; Yamaji et al. 2000; Boellaard 2009; Lammertsma 2017).
Only a handful of studies, mainly from the early decades of PET, have tried to disentangle the contributions of the different physiological processes involved in the whole PET signal (represented by K_1, k_2 and k_3) (Table 2.1). Some examples exist for healthy subjects (Heiss 1984), but also for pathological conditions such as Alzheimer's disease (Piert et al. 1996), epilepsy (Cornford et al. 1998), traumatic brain injury (Hattori et al. 2003), stroke and brain tumors (Wienhard et al. 1991). The main obstacle to a higher translational power, aside from the aforementioned

References	K_1	k_2	k_3	V_b	Input
Bowen et al. 2013	0.068 ± 0.023	0.18 ± 0.06	0.09 ± 0.025	–	AIF
Hattori et al. 2004	0.010 ± 0.014	0.23 ± 0.08	0.175 ± 0.04	0.04 ± 0.02	AIF
Huisman et al. 2012	0.062 ± 0.008	0.071 ± 0.04	0.067 ± 0.03	–	AIF
Heiss et al .1984	0.07 ± 0.1	0.13 ± 0.15	0.06 ± 0.082	–	AIF
Kawai et al. 2005	0.082 ± 0.012	–	0.064 ± 0.014	–	AIF
Lucignani et al. 1993	0.11 ± 0.02	0.07 ± 0.02	0.04 ± 0.01	–	AIF
Mosconi et al. 2007	0.11 ± 0.03	0.3 ± 0.08	0.11 ± 0.02	–	AIF
O' Sullivan et al. 2010	0.13 ± 0.05	0.15 ± 0.1	0.1 ± 0.1	0.085 ± 0.05	AIF
Reicich et al. 1985	0.105 ± 0.006	0.148 ± 0.008	0.074 ± 0.005	–	AIF
Sari et al. 2017	0.43 ± 0.1	0.22 ± 0.06	0.046 ± 0.007	0.076 ± 0.02	IDIF
Overall	0.12 ± 0.098	0.18 ± 0.065	0.08 ± 0.036	0.06 ± 0.024	

Table 2.1: Summary of literature results of [^{18}F]FDG compartmental modelling applied to the time-activity curves of healthy grey matter. For each study, the estimates of the model parameters (i.e., K_1, k_2, k_3, V_b), as well as the type of input function (AIF, IDIF) are reported. In the last row, the mean and standard deviation across studies are reported for each parameter. Reproduced from (Silvestri E., PhD Thesis, 2018, http://hdl.handle.net/11577/3426715).

issues (i.e., long scans, necessity to obtain an AIF), has surely been related to the low spatial resolution of older scanners, and the limited number of subjects.

2.1.1 The input function problem: noninvasive alternatives to arterial sampling

The $C_p(t)$ is needed as the forcing function for quantification of PET data, but due to the difficulties associated with arterial sampling, other noninvasive options are actively being investigated.
An attractive alternative is the image-derived input function (IDIF), which is extracted from the radioactivity of a blood pool identified within the PET images: for brain [^{18}F]FDG studies, this is typically represented by the internal carotid arteries. This site, however, is difficult to segment and prone to PVEs and spillover effects from the high-activity tissue in the background in the late phase (Zanotti-Fregonara, K. Chen, et al. 2011). In addition, IDIFs usually still require calibration with venous blood samples, which can be employed thanks to the fact that [^{18}F]FDG reaches arteriovenous equilibration after 15-20 minutes (K. Chen et al. 1998), but these are not always available in clinical settings. When directly compared with the gold-standard AIF, IDIFs are frequently found to underestimate the peak and overestimate the tail of the curve, due to spill-out and spill-in of radioactivity, respectively. Also, at least in older studies, the IDIF approach is found to lead to biased estimates (Zanotti-Fregonara, K. Chen, et al.

2011).
Despite these drawbacks, thanks to more refined algorithms and modern PET/CT and PET/MR scanners with higher spatiotemporal resolution, new reports of successful IDIF applications, especially for [^{18}F]FDG, are emerging (Sundar et al. 2019; Meikle et al. 2021). Our work on IDIF extraction and calibration for [^{18}F]FDG quantification is briefly reported in Chapter 8.

2.1.2 Voxel-wise parametric imaging for complex compartmental models

Depending on the aim of the study, PET quantification can be performed at either region of interest (ROI) or voxel level, both of which have pros and cons. ROI-level analysis benefits of a higher signal-to-noise ratio (SNR), allowing for more accurate identification of the parameters, but at the expense of the spatial resolution and the possibility to evaluate within-region TAC variability. On the other hand, voxel-level analysis maintains the spatial resolution of the images, but is hampered by the typically low SNR of voxel TACs, and is computationally intensive (due to the number of voxels to estimate) (Alessandra Bertoldo, Rizzo, and Veronese 2014).
The gold-standard method for region-level quantification of [^{18}F]FDG PET compartmental models is the weighted nonlinear least squares (WNLLS) estimator, due to its accurate (unbiased) and precise (low-variance) estimates. In the context of noisy voxel-wise estimation, however, this estimator incurs into significant issues, such as 1) lack of convergence, 2) very high computational time, 3) unacceptable precision (high variance) or 4) inaccuracy (non-physiological values) of the estimates (Castellaro et al. 2017).
If one aims only to obtain an estimate of the K_i, Patlak's graphical method (Patlak, Blasberg, and Fenstermacher 1983) can be easily used to generate parametric maps, as it is both fast and robust. Patlak's K_i estimates usually agree well with WNLLS estimates. However, Patlak's approach does *not* solve the underlying compartmental model and does not return any information on the microparameters, nor on the V_b (Patlak, Blasberg, and Fenstermacher 1983).
Our group has thus developed a reliable, general-purpose parametric imaging method, based on Variational Bayesian (VB) inference (Castellaro et al. 2017), which can obtain parametric maps of microparameters even for the most complex model structures, like the three-tissue-compartment model of [^{18}F]FDG in the skeletal muscle (A. Bertoldo, Peltoniemi, et al. 2001). Notably, the *a priori*

information employed in the VB approach is data-driven, thanks to a hierarchical scheme: regions are first defined using an atlas parcellation or data-driven clustering, then region-level estimates are obtained with gold-standard WNLLS, and finally transferred to the voxels within each region as prior information. Variations in the parameter estimates at voxel level are still permitted: a low variance of the prior will anchor the posterior mean to that of the prior, a high variance will make the prior useless and the estimates will be freely derived from the noisy data, i.e., the WNLLS solution. The variance of the priors is set to 0.5 (= equal to half the value of the estimates obtained from region-wise WNLLS) according to the results of a simulation study. The VB approach has also been customised to the peculiar characteristics of PET noise distribution. See (Castellaro et al. 2017) for a detailed explanation and mathematical derivation.

2.2 From regional estimates to between-region relationships: state of the art on 'metabolic connectivity'

'Metabolic connectivity' (MC), intended as the *across-subject* covariation of metabolic rates derived from [^{18}F]FDG PET, was introduced in the 1980s (Horwitz, Duara, and Rapoport 1984), but regained momentum in the last decade (Yakushev, Drzezga, and Habeck 2017), thanks to the emerging fields of 'connectomics' and network neuroscience, which conceive the brain as a network of *nodes* connected by structural or functional *links* (Betzel 2022).
MC has been studied both in healthy subjects and in pathological conditions, especially neurodegenerative disorders (Sala and Perani 2019), using approaches that range from seed-based correlation (Passow et al. 2015), to sparse inverse covariance estimation (Titov et al. 2017), and independent component analysis (ICA) (Di and B. B. Biswal 2012; Savio et al. 2017). The extracted patterns of brain regions whose metabolism covaries across subjects are then interpreted as [^{18}F]FDG RSNs.
Very few studies have instead attempted to exploit the dynamic PET signal to estimate *within-subject* MC, in a similar fashion to BOLD FC (see Chapter 3). Using ICA on human data, evidence was found for only two networks (cortical and cerebellar) negatively correlated with one another (D. G. Tomasi et al. 2017). Other works on animal models have reported a more structured pattern of con-

nections, and a good coupling between single-subject MC and FC (Amend et al. 2019; Ionescu et al. 2021).

In recent years, we have also witnessed a rise of a new PET experimental protocol, the so-called 'functional' PET (fPET), which substitutes the traditional *bolus* injection of $[^{18}F]$FDG with a *continuous infusion* protocol at a constant rate, allowing to image fluctuations of the PET signal around its baseline (R. E. Carson 2000; Villien et al. 2014; S. Li et al. 2020). This approach, designed mainly for improving task-related paradigms, has been successfully employed to compute single-subject MC via approaches already employed in rs-fMRI (e.g., correlation, ICA) (S. Li et al. 2020; Jamadar et al. 2021). However, rs-fMRI and PET signal time series are dramatically different, and usually some kind of standardization/normalization of the PET 'global signal' has been performed as a necessary means of assessing covarying fluctuations of the signals. This, however, can have important impact on the results, as we will discuss in Chapter 6.

The issue of MC in itself, therefore, requires further efforts, mainly in the accurate definition of what MC *means*, in the appropriate ways to *calculate* it, and in the *validation* of the results (Veronese et al. 2019; Sala, Lizarraga, et al. 2021).

Chapter 3

Resting-state Functional Magnetic Resonance Imaging

Based on the BOLD contrast, emerging the different magnetic properties of oxy- and deoxyhemoglobin, fMRI has been increasingly employed to image brain activity since its development in the 1990s (S. Ogawa, T. M. Lee, et al. 1990; Kwong et al. 1992). Its development was actually driven by evidence of temporary uncoupling of $CMRO_2$ and CBF during *task*-related activity, with increases in CBF and $CMRglc$ far exceeding the oxygen tissue demand (P. Fox et al. 1988): this uncoupling is the basis of the BOLD effect (P. T. Fox 2012). The BOLD signal is therefore shaped by $CMRO_2$ and CBF (with important contributions from CBV) (Kim and Seiji Ogawa 2012), and is considered as an indirect proxy of neuronal activity (Scholvinck et al. 2010) once the effect of the HRF filter has been considered (Buxton, Uludağ, et al. 2004); the relationship between the underlying neural activity and the vascular response measured with BOLD is called *neurovascular coupling* (Buxton and Frank 1997) (Figure 3.1). Typically, a T2*-weighted MR sequence is used to detect the BOLD effect, due to its sensitivity to the change in magnetic susceptibility of hemoglobin, from an increase in oxy- (diamagnetic) vs. deoxy- (paramagnetic) hemoglobin in response to neural activation (S. Ogawa, T. M. Lee, et al. 1990).

Studies using BOLD fMRI first concentrated on *task*-evoked activity, with seminal works which employed paradigms that had been developed using PET (M. E. Raichle 1998), and then their focus expanded to the exploration of the *resting state* of the brain (S. Ogawa, Menon, et al. 1993; B. Biswal et al. 1995).

BOLD fMRI is characterized by relatively good spatial (3 mm) and temporal resolution (1-2 s), it does not require the use of radiotracers or invasive blood sampling, and short scan durations can be easily achieved ($<$ 15 min). This is why it has become a widely popular functional imaging technique in recent decades, not only for research on healthy individuals, but also on neurological and psychiatric disorders (Sheline and Marcus E. Raichle 2013; Damaraju et al. 2014; Siegel, Shulman, and Corbetta 2017).

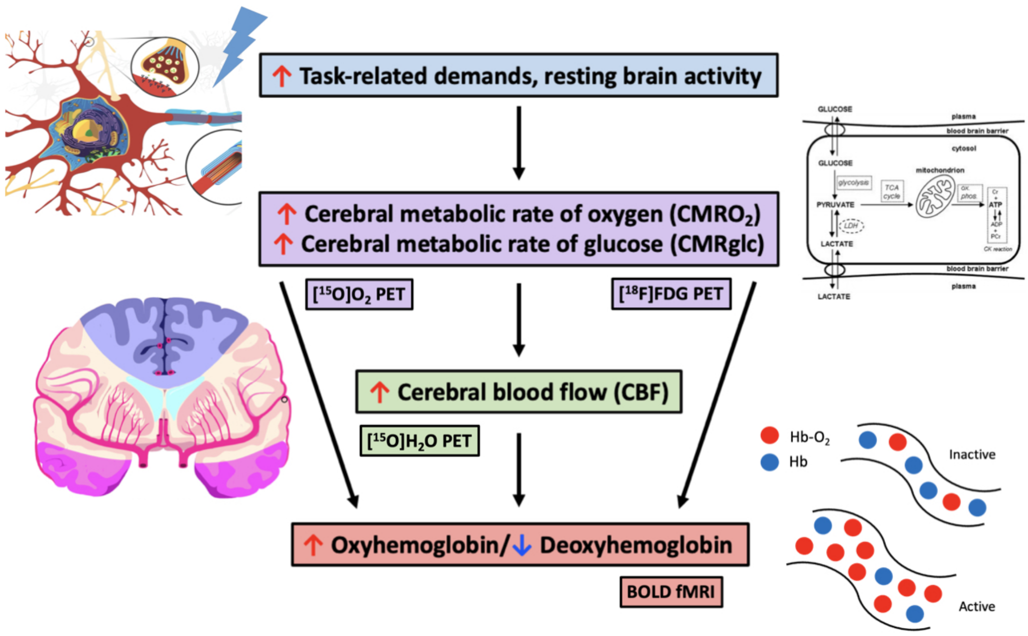

Figure 3.1: The complex chain of events linking $CMRglc$, $CMRO_2$ and CBF to neuronal activity. Local changes in brain activity are accompanied by changes in CBF and $CMRglc$ which far exceed changes in $CMRO_2$. The CBF-$CMRO_2$ uncoupling is the basis of the task-based BOLD effect. Adapted from (M. E. Raichle 1998).

3.1 Basic principles of resting-state fMRI

The paradigm shift towards rs-fMRI, i.e., imaging subjects with fMRI while the do not perform any specific task, began to happen in the 2000's, when more research began to focus on the spontaneous fluctuations of the BOLD signal, which had been considered just background noise during task studies (Greicius et al. 2003; M. D. Fox and Marcus E. Raichle 2007).
The spontaneous activity of distant brain areas, in particular homotopic sensorimotor cortices (homologous areas in the two hemispheres), was shown to be correlated, leading to the first rs-fMRI results on 'FC' (B. Biswal et al. 1995), defined as the statistical dependency between the BOLD time courses of differ-

ent regions. From these pivotal observations, many different RSNs began to be identified, as clusters of brain areas whose rs-fMRI spontaneous activity was more correlated than with the rest of the brain. The default mode network (DMN) was among the first to be identified (Marcus E. Raichle 2001), starting from observations on PET data; many others were later described (Yeo et al. 2011), leading to a high-level subdivision into 'task-positive', or 'extrinsic', i.e., RSNs related to sensorimotor and attention processing, vs. 'task-negative', or 'intrinsic', i.e., RSNs more related to cognitive control, memory and internally-driven processing (Doucet et al. 2011).

Notably, the BOLD signal significantly suffers from systemic contamination, in particular *motion*, *cardiac* and *respiratory* activity, whose low-frequency fluctuations can give rise to highly structured spatial patterns (J. E. Chen, Lewis, et al. 2020), as well as *vascular* biomechanics, being the BOLD signal heavily weighted towards draining veins and large pial vessels (Ugurbil 2016). Due to its high noise content, rs-fMRI is typically subjected to a multi-step preprocessing (Glasser, Sotiropoulos, et al. 2013), which, however, can vary significantly across research centers, leading to inconsistencies in the results.

Moreover, the *physiological* interpretation of the wide variety of results provided by BOLD fMRI, and resting-state fMRI in particular (T. T. Liu 2013), is problematic. The low-frequency fluctuations of the BOLD signal (0.01-0.1 Hz) are considered reflective of neuronal activity (N. K. Logothetis et al. 2001): seminal studies with simultaneous fMRI and electrophysiology in non-human primates have shown that BOLD signal fluctuations reflected local field potentials, assumed to represent peri-synaptic activity, much more than spikes (N. K. Logothetis et al. 2001; Nikos K. Logothetis 2008); however, much more complex and nuanced interplays between neural activity and BOLD have later been shown, making interpretations less straightforward (Gauthier and Fan 2019).

Notably, only a limited number of studies have directly tested the relationship between the BOLD-based features and $CMRglc$, CBF, $CMRO_2$, so exploring evidence of this coupling is still highly relevant.

3.2 The rs-fMRI signal and its many properties

Many different features can be extracted from the rs-fMRI signal, due to its richness in both space and time-frequency domains. While one must remember that a high degree of redundancy between BOLD-based features exists, with recent attempts trying to reach a parsimonious description (Bolt et al. 2022), we have chosen to organize BOLD-based properties into four main categories, i.e.,

1) rs-fMRI signal and its *local* properties
2) *HRF*-based information
3) *static* FC (sFC)
4) *time-varying* FC (tvFC)

which will be employed for comparison with PET-derived physiological parameters and MC networks in Chapter 4, 5, 6, and are briefly discussed below.

3.2.1 Local fMRI features

We can start from the most basic statistics of the BOLD time series, i.e., its mean, variance, and skewness. While the *absolute* value of the mean BOLD signal is arbitrary and scanner/sequence-dependent, its *relative* pattern across brain regions has been found to be related to cell density (Ulrich and Yablonskiy 2016; Wen et al. 2018). The variance of the BOLD signal is increasingly studied as it is known to carry significant physiological information on cellular properties (Garrett et al. 2010; Anderson et al. 2020) and also to be a correlate of cerebrovascular reactivity (Golestani, Wei, and J. J. Chen 2016). The skewness, which captures extreme BOLD events, has also been studied, and found to be related to structural connectivity (SC), with more connected regions having high negative skewness activity (Amor et al. 2015).

Moreover, nonlinear metrics of rs-fMRI temporal complexity have been also explored. Among them the *approximate entropy* (*ApEn*) (Sokunbi et al. 2011), which quantifies the mean negative log-probability that an m-dimensional state vector (template) will repeat itself at dimension (m + 1), and the *sample entropy* (*SampEn*) (Richman and Moorman 2000) which is instead defined without template matching, plus their modified versions, i.e., *range ApEn* and *range SampEn*, which are more robust to nonstationary signal amplitude changes and more appropriate to evaluate self-similarity in the signal (Omidvarnia, Mesbah, et al. 2018). Additionally, if the rs-fMRI time series is modelled as a first-order autoregressive AR(1) process, its exponents have been found to have physiological and cognitive relevance (G.-R. Wu, Liao, et al. 2013; Omidvarnia, Liégeois, et al. 2022).

Some local rs-fMRI measures which have enjoyed great popularity are the amplitude of low-frequency fluctuations (*ALFF*), which quantifies BOLD spectral

power within the [0.01; 0.1] Hz range, considered to be the richest frequency band in terms of neural information (Q.-H. Zou et al. 2008); its fractional counterpart, *fALFF*, i.e., *ALFF* normalized by the rs-fMRI signal amplitude over the entire frequency range, is considered to be a better index of the neural underpinnings of BOLD due to its lower sensitivity to the physiological noise corrupting the frequency range > 0.1 Hz (Q.-H. Zou et al. 2008).
The local coherence of the BOLD signal, computed as the concordance among one voxel's time series and its neighbors, and typically called 'regional homogeneity' (*ReHo*) (Zang et al. 2004), is expected to represent synchronization of local field potentials (Z. Li, Zhu, et al. 2012) and to be a proxy of local, short-range connectivity (Jiang and Zuo 2016).

3.2.2 The hemodynamic response function

While the role of the HRF has been extensively studied in the task-fMRI literature (K. Friston et al. 1998; Buxton, Uludağ, et al. 2004), in the last decade interest has also grown in its characterization in the resting state, using various deconvolution approaches for its estimation (Tagliazucchi et al. 2012; G.-R. Wu, Liao, et al. 2013; G.-R. Wu, Colenbier, et al. 2021). These methods typically build on a description of the rs-fMRI signal as a point process, where events that exceed a given threshold govern the dynamics, in this case called BOLD *pseudo-events* (Tagliazucchi et al. 2012; Zhang, Pan, and Keilholz 2020). Drawing from formalism on linear, time-invariant systems, the BOLD signal $y(t)$,

$$y(t) = s(t) \otimes h(t) + e(t) \tag{3.1}$$

is modeled as the convolution of the HRF, $h(t)$, and the underlying neural states, $s(t)$, with the addition of an error term, $e(t)$. The HRF can be estimated using the canonical model, i.e., two gamma functions with time and dispersion derivatives (K. Friston et al. 1998), or, more freely, as a linear combination of basis vectors for a smooth finite impulse response (sFIR) (Goutte, Nielsen, and Hansen 2000; G.-R. Wu and Marinazzo 2016). The HRF shape can be then described through various parameters, such as height, full-width-at-half-maximum (FWHM), time-to-peak etc., which were found to carry physiologically relevant information, in particular in relation to CBF (G.-R. Wu and Marinazzo 2016; G.-R. Wu, Colenbier, et al. 2021).

3.2.3 Static functional connectivity

When the statistical relationship between rs-fMRI signals of different brain regions is assessed across a single period of time, which usually corresponds to the entire fMRI scan, we talk about sFC. There are many different approaches to calculating sFC, going from simple correlations (at region or voxel level), to ICA (Calhoun et al. 2001), or clustering (Heuvel, Mandl, and Hulshoff Pol 2008).
When working at the region level, typically using a pre-defined atlas of brain areas, sFC matrices are usually calculated as pairwise Pearson's correlations between ROI-wise rs-fMRI time series, and then thresholded by retaining only connections associated with weights over a pre-defined connection density (Wijk, Stam, and Daffertshofer 2010).
A useful way to summarize sFC matrices at the region-level is to characterize their topological features using graph theory (Rubinov and Sporns 2010): the sparse FC matrix can be interpreted as a graph, $G = f(N, E)$, consisting of a set of nodes N (= regions), and edges E connecting node pairs (= the FC between those regions). A graph can be either weighted (if each edge is assigned a real number determining the strength of the connection), or unweighted/binary (representing only the presence or absence of a link).
For each graph, many summary measures can then be quantified to describe each node's role in the network in terms of centrality, integration or segregation. A brief description of the most representative nodal graph measures used in this thesis is presented here. Node degree (DEG), defined as the number of links connected to a node, is a node centrality measure used to characterize network structure and local connectivity:

$$DEG(i) = \sum_{j=1}^{N} \delta(i, j) \tag{3.2}$$

$$\delta(i, j) = \begin{cases} 1, & W(i, j) \neq 0 \\ 0, & W(i, j) = 0 \end{cases} \tag{3.3}$$

with $\delta(i, j)$ indicating the presence or absence of a connection between node i and node$j$.
Node strength (STR), i.e., the sum of all link weights $W(i, j)$ for each node, is used to complement node DEG as a measure of connectivity profile:

$$STR(i) = \sum_{j=1}^{N} W(i,j) \tag{3.4}$$

Eigenvector centrality (EC), which uses eigendecomposition of the FC matrix to measure if strong connections tend to link nodes with equally strong connections, accounting for the importance of indirect pathways (Lohmann et al. 2010), is another centrality measure:

$$EC(i) = \frac{1}{\lambda_1} \sum_{j=1}^{N} W(i,j)\mu_1(j) \tag{3.5}$$

with λ_1 as the largest eigenvalue and μ_1 as the largest eigenvector of the FC matrix.

Betweenness centrality (BC), calculated as the number of shortest paths between nodes passing through a specific node (Freeman 1977), is again a centrality measure:

$$BC(i) = \frac{1}{(n-1)(n-2)} \sum_{\forall j,k \neq i}^{N} \frac{\rho_{hj}(i)}{\rho_{hj}} \tag{3.6}$$

where ρ_{hj} is the shortest path connecting h and j, $\rho_{hj}(i)$ is the shortest path passing through h and connecting i and j, n is the number of nodes.

Network *segregation* can instead be assessed by the clustering coefficient (CC), which locally represents the number of triangles around an individual node over the number of connected triples in the network (Watts and Strogatz 1998; Onnela et al. 2005), and is calculated as:

$$CC(i) = \frac{2t_i}{k_i(k_i - 1)} \tag{3.7}$$

$$t_i = \frac{1}{2} \sum_{j,h \in N} (W(i,j)W(i,h)W(j,h))^{\frac{1}{3}} \tag{3.8}$$

where t_i is the number of triangles in the system in which the node i is one of the vertices, and k is the number of vertices.

A measure of network *integration* is the global efficiency (GE), which is the inverse shortest path length in the network (Latora and Marchiori 2001):

$$GE(i) = \frac{\sum_{j,h \in N} d_{i,j}^{-1}}{n-1} \tag{3.9}$$

where d_{ij} is the length of the shortest path between i and j. Finally, segregation can also be evaluated through local efficiency (LE), i.e., the ratio of the number of connections between a node's neighbors to the total number of possible links (Latora and Marchiori 2001), calculated as:

$$LE(i) = \frac{1}{M} \sum_{i \in N} GE(i) \tag{3.10}$$

where $GE(i)$ is the global efficiency of the subgraph composed of the neighbors of node i.

Another approach to summarize the information content of sFC matrices, which has gained substantial popularity in recent years, is the '*functional gradients*' analysis (Margulies et al. 2016; Tian et al. 2020). This framework works by applying linear or nonlinear dimensionality reduction techniques (principal component analysis (PCA), Laplacian eigenmaps etc.) to FC to extract 'gradients' or 'manifolds'. These components allow to separate higher-order networks (DMN) from the VIS networks (along gradient 1), and the VIS from the SMN (along gradient 2) (Margulies et al. 2016; Vos de Wael et al. 2020).

3.2.4 Time-varying functional connectivity

The underlying assumption behind sFC approaches is that FC does not change over time. Despite the presence of some controversy on the non-stationarity of FC (Laumann et al. 2016), an increasing amount of literature has explored the FC dynamics over time, using different approaches to estimate tvFC (Hutchison et al. 2013; Lurie et al. 2020). These approaches can be either *model-based*, if they explicitly model the neural processes putatively underlying the changes in the FC, or *data-driven*, if they simply try to estimate FC changes directly from the observed rs-fMRI signal (Lurie et al. 2020).

One of the most popular is the *sliding windows* approach, which estimates multiple time-resolved FC matrices over a number of overlapping time windows of length W. The selection of the W is a crucial hyperparameter, to avoid introducing spurious fluctuations in the tvFC if the window is too small, or being unable to capture relevant FC changes if the window is too large (Hutchison et al. 2013; Leonardi and Van De Ville 2015). Commonly employed values for the W range between 30 and 60 s, and the step size between adjacent windows is quite variable (Preti, Bolton, and Van De Ville 2017).

Typically, sliding-windows tvFC matrices are clustered into brain 'states', i.e.,

transient patterns of whole-brain FC (Allen et al. 2014). However, another possible way of summarizing the FC temporal variability would be to compute nodal graph metrics (DEG, STR, EC, etc) for each window, as in sFC analysis, thus obtaining graph metrics' time series, and then assess their node-wise variability across time (Chang and Glover 2010; Hellyer et al. 2017; Pedersen et al. 2017).
Importantly, tvFC has been characterized not only as changes in the covariation of BOLD signal *magnitudes*, but also in the coherence of their *phase* (Chang and Glover 2010): an example of this type of approach is the Leading Eigenvector Dynamic Analysis (LEiDA) framework (Cabral et al. 2017; Lord et al. 2019). In particular, BOLD signal phases, $\theta(n,t)$ are first estimated using the Hilbert transform, which expresses a given signal $y(t)$ as

$$y(t) = A(t)\cos\theta(t) \tag{3.11}$$

where $A(t)$ is the time-varying amplitude and θ is the time-varying phase. Instantaneous BOLD phase coherence is calculated at each single time point t (corresponding to a single TR), resulting in a time series of phase-locking values (PLV) between each pair of brain areas n and p at each time t:

$$PLV(n,p,t) = \cos(\theta(n,t) - \theta(p,t)) \tag{3.12}$$

Two regions with no phase difference have a $PLV(n,p,t) = \cos(0°) = 1$, while a 180° phase difference corresponds to a $PLV(n,p,t) = \cos(180°) = -1$. The leading eigenvector ($LEig$) of the $PLV(t)$ matrix at time t is then computed to capture the main orientation of regional BOLD phases over all other brain areas (Cabral et al. 2017; Lord et al. 2019).

Chapter 4

Modelling the complex spatial relationship between $[^{18}\text{F}]$FDG $SUVR$ and rs-fMRI features

4.1 Introduction

As already discussed in Chapter 1, brain glucose consumption, which can be assessed *in vivo* by $[^{18}\text{F}]$FDG PET, displays significant *regional variability* in the healthy brain, but the precise factors controlling this spatial heterogeneity are incompletely understood.

Since most of the remarkable metabolic budget of the brain is spent during *rest* (Clarke and Louis Sokoloff 1999; Marcus E. Raichle 2006), we expect the regional differences in brain glucose consumption to be explained by variability in spontaneous activity, which can be described by rs-fMRI (M. D. Fox and Marcus E. Raichle 2007). In addition to local *activity* alone, the functional *relationships* between resting-state activity patterns of different brain regions, i.e., their FC, may play a relevant part as well (Marcus E. Raichle 2015).

Some evidence on this relationship has started to emerge from both sequential and simultaneous $[^{18}\text{F}]$FDG PET/fMRI acquisitions (Cecchin et al. 2017). In particular, among *local activity* measures, *ALFF* and *fALFF* have been found to be associated with $[^{18}\text{F}]$FDG uptake (Nugent et al. 2015), especially in specific brain regions (Marco Aiello et al. 2015; S. Deng et al. 2022). Moderate associations between $[^{18}\text{F}]$FDG PET and *large-scale FC* metrics were also detected (Marco Aiello et al. 2015; D. Tomasi, G. J. Wang, and Volkow 2013), while stronger and more consistent correlations emerge for *ReHo*, an index of *local syn-*

chronization (J. Wang et al. 2021). The topological role of brain network nodes was also found to be important, with more central regions, according to fMRI FC, having a stronger relationship between their FC and metabolic consumption (Marco Aiello et al. 2015; Palombit et al. 2022). In addition, some evidence for nonlinearity (exponential or power law models) in the spatial relationship with local and large-scale FC has been reported (D. Tomasi, G. J. Wang, and Volkow 2013; Shokri-Kojori et al. 2019).

Notably, when the [18F]FDG vs. rs-fMRI associations are tested *across subjects*, instead of *across space* (regions or voxels), very low correlations are detected in most studies (Marco Aiello et al. 2015; J. Wang et al. 2021). This complicates the picture: the spatial agreement between [18F]FDG and rs-fMRI, which is present for an average brain, seems to be weakened/lost if one wants to describe region by region the inter-subject variability of one modality with that of the other.

Overall, somewhat inconsistent results emerge from the literature, with bivariate spatial correlations between [18F]FDG PET and rs-fMRI metrics ranging from 0 to 64% in explained variance, and substantial differences across brain *networks* (Marco Aiello et al. 2015; Shokri-Kojori et al. 2019), as well as low correlations across *subjects* even in simultaneous acquisitions (Marco Aiello et al. 2015; J. Wang et al. 2021). Moreover, only a handful of rs-fMRI features (*ALFF*, *ReHo*, FC *STR*) has been tested.

Notably, no study has ever attempted a *multivariable* integration of rs-fMRI features to explain local metabolism, which might allow to reach a higher explanatory power for the regional variability in [18F]FDG uptake, as well as a clearer description of the multiple functional contributors to glucose consumption.

We set out to fill these gaps with a fully data-driven approach, using simultaneously acquired [18F]FDG PET and rs-fMRI data of 26 subjects from two published datasets (Riedl et al. 2014; Marco Aiello et al. 2015), which we have already analyzed in previous work (Palombit et al. 2022).

We chose this dataset for a number of reasons:

1. It consists of simultaneously acquired [18F]FDG PET and rs-fMRI data, allowing us to probe the relationship between glucose metabolism and BOLD while minimizing within-subject variability between sessions (Cecchin et al. 2017);

2. The [18F]FDG parameter of choice is $SUVR$, which, despite its limitations, is the easiest to obtain from clinical PET imaging and thus has the highest availability (Hamberg et al. 1994);

3. The [18F]FDG tracer is administered via *bolus injection*, which again is

the most frequently employed PET imaging protocol, unlike *constant infusion* protocols which have now been (re)discovered for task experiments (Hahn et al. 2020) and 'MC' studies (Jamadar et al. 2021);

4. Both the [^{18}F]FDG and rs-fMRI data are of sufficient quality in terms of SNR and whole-brain brain coverage, while remaining in the context of clinically available sequences.

After preliminary assessment of a wide variety of rs-fMRI-derived variables (50), pooled into 4 categories, i.e., 1) signal, 2) HRF, 3) sFC, and 4) tvFC (see Table 4.1 for the list of the features), we set out to address these questions:

1. which is the strength of the *bivariate* association between each rs-fMRI feature and $SUVR$ across regions? And does this coupling change according to the ranking of brain nodes based on [^{18}F]FDG uptake?

2. can we explain group-average SUVR variance across regions by combining a group of rs-fMRI features in a *multivariable* regression model? Is the group of selected fMRI predictors more populated by *local* or *large-scale* brain network metrics? How well do the features, chosen at group-average level, account for between-*subject* variability (BSV) (Hox, Moerbeek, and Schoot 2017) in this spatial association? Finally, are the previously identified rs-fMRI features still important to explain $SUVR$ when multilevel modelling (MLM) is performed across fMRI RSNs, i.e., which is the between-*network* variability (BNV) of the $SUVR$-fMRI spatial coupling?

Notably, the MLM approach, which is carried out across *regions*, not *subjects*, is expected to be robust and statistically sound even in spite of the relatively low sample size (n subjects = 26) (Hox, Moerbeek, and Schoot 2017).

4.2 Materials and Methods

4.2.1 Imaging protocols

The dataset includes 26 healthy subjects from two studies: 11 subjects (8 males; 52.2 ± 10.4 years) from dataset 1 (Riedl et al. 2014), and 15 subjects (6 males; 64.7 ± 7.9 years) from dataset 2 (Marco Aiello et al. 2015). Subjects were scanned in *eyes open* condition. The subjects provided their informed written consent according to the Code of Ethics of the World Medical Association and the Institutional Review Board and Ethics Committee at the Technische Universität München (Riedl et al. 2014) and the SDN Foundation (Marco Aiello et al. 2015).

Pools	**rs-fMRI variables**
Signal	*med-BOLD*: median of the BOLD time series *MAD-BOLD*: median absolute deviation (MAD) of the BOLD time series [Garrett et al. 2010] *skew-BOLD*: skewness of the BOLD time series [Amor et al. 2015] *ApEn-BOLD*: approximate entropy (ApEn) of the BOLD time series [Sokunbi et al. 2011] *rApEn-BOLD* range ApEn of the BOLD time series [Omidvarnia, Mesbah, et al. 2018] *AR-BOLD*: reflection coefficient of the AR(1) model fit to BOLD time series [Omidvarnia, Mesbah, et al. 2018] *ALFF*: amplitude of low-frequency fluctuations (ALFF) of BOLD time series [Q.-H. Zou et al. 2008] *ReHo*: regional homogeneity of BOLD time series [Zang et al. 2004] *MAD-ReHo*: MAD of the time-varying ReHo (tvReHo) [L. Deng et al. 2016] *CV-ReHo*: CV% of tvReHo [L. Deng et al. 2016] *peaks-BOLD*: number of BOLD pseudo-events [G.-R. Wu, Liao, et al. 2013]
HRF	*peak-HRF*: height of HRF peak [G.-R. Wu, Liao, et al. 2013] *hrf-DEG*: degree (DEG) of HRF correlation matrix [*original*] *hrf-STR*: strength (STR) of HRF correlation matrix [*original*] *hrf-CC*: clustering coefficient (CC) of HRF correlation matrix [*original*] *hrf-BC*: betweenness centrality (BC) of HRF correlation matrix [*original*] *hrf-EC*: eigenvector centrality (EC) of HRF correlation matrix [*original*] *hrf-LE*: local efficiency (LE) of HRF correlation matrix [*original*] *hrf-GE*: local efficiency (GE) of HRF correlation matrix [*original*]]
sFC	*s-DEG*: DEG of sFC [Rubinov and Sporns 2010] *s-STR*: STR of sFC [Rubinov and Sporns 2010] *s-CC*: CC of sFC [Rubinov and Sporns 2010] *s-BC*: BC of sFC [Rubinov and Sporns 2010] *s-EC*: EC of sFC [Rubinov and Sporns 2010] *s-LE*: LE of sFC [Rubinov and Sporns 2010] *s-GE*: GE of sFC [Rubinov and Sporns 2010] *med-LEig*: median of the Leading Eigenvector (LEig)'s time series [Cabral et al. 2017]
tvFC	*mdiff-DEG*: temporal median of the differentials (mdiff) of DEG time series [*original*] *mdiff-STR*: mdiff of STR time series [*original*] *mdiff-CC*: mdiff of CC time series [*original*] *mdiff-BC*: diff of BC time series [*original*] *mdiff-EC*: mdiff of EC time series [*original*] *mdiff-LE*: mdiff of LE time series [*original*] *mdiff-GE*: mdiff of GE time series [*original*] *CV-DEG*: coefficient of variation (CV%) of DEG time series [Hellyer et al. 2017] *CV-STR*: CV% of STR time series [Hellyer et al. 2017] *CV-CC*: CV% of CC time series [Hellyer et al. 2017] *CV-BC*: CV% of BC time series [Hellyer et al. 2017] *CV-EC* CV% of EC time series [Hellyer et al. 2017] *CV-LE*: CV% of LE time series [Hellyer et al. 2017] *CV-GE*: CV% of GE time series [Hellyer et al. 2017] *SampEn-DEG*: sample entropy (SampEn) of DEG time series [Pedersen et al. 2017] *SampEn-STR*: SampEn of STR time series [Pedersen et al. 2017] *SampEn-CC*: SampEn of CC time series [Pedersen et al. 2017] *SampEn-BC*: SampEn of BC time series [Pedersen et al. 2017] *SampEn-LE*: SampEn of LE time series [Pedersen et al. 2017] *SampEn-GE*: SampEn of GE time series [Pedersen et al. 2017] *MAD-LEig*: MAD of LEig time series [Cabral et al. 2017] *CV-LEig*: CV% of LEig time series [Cabral et al. 2017] *mdiff-LEig*: mdiff of LEig time series [Cabral et al. 2017]

Table 4.1: Extracted rs-fMRI features and their categories Fifty fMRI-derived variables, divided according to the pool to which they belong: 1) signal, 2) HRF, 3) sFC, 4) tvFC. See Chapter 3 and Section 4.2 for full description of the features.

Both centers simultaneously collected $[^{18}F]$FDG PET and rs-fMRI data accompanied by a structural MR image on two identical Biograph mMR 3T scanners (Siemens Healthcare, Erlangen, Germany) equipped with the standard-supply head-neck coil (12-channel). The interested reader should refer to the respective papers (Riedl et al. 2014; Marco Aiello et al. 2015) for more detailed information on each dataset.

Dataset 1: MRI data consisted in a magnetization prepared rapid acquisition gradient echo (MPRAGE) T1-weighted (T1w) structural image (TR/TE = 2300/2.98 ms, FA = 9°, 1 mm isotropic voxel size with 0.5 mm gap), 300 volumes of T2*-weighted gradient-echo echo-planar imaging (GE-EPI) with TR/TE = 2000/30 ms and voxel size of 3 mm isotropic (0.6 mm inter-slice gap). PET acquisition started 30 minutes post-injection (175 ± 12 MBq), and consisted in a 10 min scan, reconstructed with voxel size of $3.7 \times 2.3 \times 2.7$ mm^3.

Dataset 2: MRI data consisted in a similar T1w MPRAGE structural image and 240 volumes of GE-EPI for rs-fMRI with 4 mm isotropic voxel and TR/TE = 1920/32 ms. Simultaneous PET/fMRI measurements started 30 min post-injection (5 MBq/kg for whole-body scan), and static PET images were acquired for 15 min and reconstructed with voxel size of $1.12 \times 1.12 \times 2.0$ mm^3.

4.2.2 Data preprocessing

All subjects were identically pre-processed to obtain local metabolism from $[^{18}F]$FDG PET data, and BOLD-based measures from rs-fMRI data, employing a pipeline similar to the Human Connectome Project (HCP) minimal preprocessing pipeline (Glasser, Sotiropoulos, et al. 2013).

Structural imaging pre-processing

Structural T1w images were N4 bias field-corrected (N. J. Tustison et al. 2010), skull-stripped (N. Tustison et al. 2013), and segmented into grey matter (GM), white matter (WM) and cerebrospinal fluid (CSF) using SPM12 (Ashburner and K. J. Friston 2005). The brain cortex was delineated with Freesurfer (*recon-all* volume and surface reconstruction pipelines) (Fischl, Sereno, and Dale 1999), obtaining pial and GM-WM interface surfaces. Manual editing was performed to correct for surface delineation errors. Generated surfaces were resampled over the *fs_LR* mesh provided by *Conte69* atlas (symmetric-hemisphere mesh of 32k nodes) to obtain aligned cortical surfaces for each subject.

The Schaefer functional atlas (Schaefer et al. 2018) was used to parcellate cortical surfaces into 200 parcels, grouped according to Yeo's 17 RSNs scheme (Yeo et al. 2011) into Central Visual (VIS(A)), Peripheral Visual (VIS(B)), Somato-Motor A (SM(A)), Somato-Motor B (SM(B)), Temporal Parietal (TP), Dorsal Attention A (DAN(A)), Dorsal Attention B (DAN(B)), Salience/Ventral Attention A (VAN(A)), Salience/Ventral Attention B (VAN(B)), Control A (CTR(A)), Control B (CTR(B)), Control C (CTR(C)), Default Mode A (DMN(A)), Default Mode B (DMN(B)), Default Mode C (DMN(C)), Limbic A (LIMBIC(A)) and Limbic B (LIMBIC(B). The cortical regions were supplemented by 18 subcortical regions (bilaterally: Caudate, Putamen, Accumbens, Pallidum, Amygdala, Hippocampus, Thalamus, Ventral diencephalon, Cerebellar cortex) delineated in single-subject space employing the Multi-Atlas Label Fusion (MALF) method (H. Wang and Yushkevich 2013). Parcels corresponding to subcortical regions were assigned to the Subcortical (SUB) group.

PET data pre-processing

PET images were normalized to injected dose and subject's body weight into standard uptake value (SUV) images (Equation 2.7). SUV images were linearly resampled to T1w space with FSL's *flirt* (Jenkinson, Beckmann, et al. 2012) and on top of the mid-thickness cortical surface mesh with Connectome Workbench (Marcus et al. 2011), then intensity-normalized into $SUVR$ by dividing each voxel's SUV value by the whole-brain average SUV (mean of GM, WM, CSF) (Byrnes et al. 2014) (Equation 2.8).

$SUVR$ maps were then parcellated according to the Schaefer cortical atlas and the subcortical MALF parcels as previously described, and parcel-wise $SUVR$ was computed as the median value of the vertices inside a region. All pre-processing steps avoided any further spatial smoothing on [18F]FDG data (beyond coregistration), to minimize PVEs, as also suggested in many recent metabolism-flow coupling reports (Hyder et al. 2016; Wesolowski et al. 2019; Henriksen, Gjedde, et al. 2021; Narciso, Ssali, L. Liu, Biernaski, et al. 2021; S. Deng et al. 2022).

Functional MRI data pre-processing

The first four rs-fMRI volumes were discarded to avoid non-equilibrium magnetization effects. The remaining volumes were corrected for slice timing differences (Smith, Jenkinson, et al. 2004) and magnetic field distortion (Andersson, Skare, and Ashburner 2003), and realigned to the median volume using FSL's *mcflirt* (Jenkinson, Beckmann, et al. 2012). A template EPI volume was obtained with

antsBuildTemplate (Avants et al. 2011) from realigned rs-fMRI data and used to estimate an affine transform (*flirt*, FSL), subsequently employed to map main tissue segmentations obtained from the pre-processed T1w image to the native EPI space. Nuisance signals consisted in motion traces and their first order derivatives complemented by the first five temporal principal components, obtained after PCA of WM and CSF EPI signals, explaining 70% and 50% of the average variance across subjects, respectively (Behzadi et al. 2007), which were regressed out from all brain voxels in native EPI space (Ciric et al. 2017). Regression residuals were finally resampled first to T1w space and then on top of the mid-thickness cortical surface mesh with Connectome Workbench (Marcus et al. 2011). Finally, the BOLD signal was high-pass filtered with a cut-off of 0.008 Hz. No low-pass filter was applied, as the higher frequency components (0.1-0.25 Hz) of BOLD are likely to provide relevant neural information (J. E. Chen and Glover 2015).
Motion correction was adapted to the features to be extracted. For features where it was important to preserve the temporal structure of the BOLD signal (e.g., tvFC, time-varying *ReHo*, HRF), motion-corrupted volumes were corrected by *despiking* with a cubic and spline interpolation, using the *icatb_despike_tc* function from the Group ICA Toolbox GIFT (Calhoun et al. 2001) in order to avoid extreme censoring methods that would interrupt the temporal autocorrelation structure of the data (Hutchison et al. 2013). For features that are more robust to *censoring* (e.g., sFC, *ReHo*), motion-corrupted volumes with frame-wise displacement (FD) higher than 0.3 mm were discarded before sFC calculation (Power et al. 2014). Mean FD and the number of censored volumes were evaluated for every subject, to ensure that a sufficient number of viable frames was available. The vertex-wise BOLD signals were parcellated in the same way as the PET data.

4.2.3 Resting-state fMRI feature extraction

Feature extraction as well as subsequent analyses were performed in MATLAB (ver. 2020a, The Mathworks, Natick, MA). 50 different features were obtained from the rs-fMRI signal, either at the vertex level or directly at the parcel level. The extracted features were chosen as descriptors of different aspects of the BOLD 1) *signal*, 2) *HRF*, 3) *sFC*, and 4) *tvFC*. A list of the features and their acronyms is reported in Table 4.1. More context on the interpretation of these features is reported in Chapter 3.2.

Signal and local features

Pre-processed EPI signals were averaged within each parcel to obtain a representative time course, then z-scored across parcels. The temporal *median*, median absolute deviation (*MAD*) and *skewness* of the parcel-wise BOLD signal, i.e., the nonparametric first-, second-, and third-moment statistics of the BOLD time series distribution, were calculated.

Nonlinear metrics of BOLD signal *complexity* were computed, in particular *approximate entropy* (*ApEn*) (Sokunbi et al. 2011) and *range approximate entropy* (*rApEn*) (Omidvarnia, Mesbah, et al. 2018). For ApEn calculation, the embedding dimension m was set equal to 2, and the tolerance r was set to 0.2 multiplied by the SD of the signal (Sokunbi et al. 2011).

An AR(1) model was also fit to the windowed BOLD time series by minimizing the forward prediction error in the least squares sense; the Yule-Walker equations were solved by the Levinson-Durbin recursion, obtaining the AR(1) reflection coefficients, whose absolute value was taken as the time dependence between $y(n)$ and $y(n–1)$ (Omidvarnia, Mesbah, et al. 2018).

At the vertex level, the BOLD signal's spectral content was quantified by *ALFF* (Q.-H. Zou et al. 2008), and the local coherence of the BOLD signal was described by *ReHo* (Zang et al. 2004), computed as Kendall's W coefficient of concordance among the time series of one vertex and its 27 neighbors. Parcel-wise *ReHo* and *ALFF* values were then extracted as the median of the vertices within the region. *Time-varying ReHo* was computed with a sliding windows approach (window size: 30 TRs, step: 1 TR), as Kendall's coefficient of concordance amongst neighboring vertices within each time window (L. Deng et al. 2016). *ReHo* time courses were extracted at the parcel level by averaging vertices within a region. Regional *ReHo* variability was calculated as nonparametric *MAD* and coefficient of variation ($CV\%$) of the parcel-wise time series, i.e., $CV_{nonpar} = \frac{MAD}{median} \cdot 100$.

HRF features

The parcel-wise BOLD signal was subjected to a blind deconvolution algorithm (G.-R. Wu, Liao, et al. 2013; G.-R. Wu and Marinazzo 2015) employing the rs-HRF toolbox v2.0 (`https://www.nitrc.org/projects/rshrf`). Before deconvolution, the high-pass filtered BOLD signal was despiked using a hyperbolic tangent squashing function. The HRF was estimated as the linear combination of basis vectors for a smooth finite impulse response (sFIR) (Goutte, Nielsen, and Hansen 2000; G.-R. Wu and Marinazzo 2016). BOLD pseudo-events were detected using a threshold, which was set to the default value of 1 SD from the mean of the BOLD signal, and their parcel-wise number was calculated (*peaks-BOLD*). Serial correlations in BOLD time series due to aliasing of biorhythms and unmodelled neuronal activity were accounted for using an AR(1) model during parameter estimation (G.-R. Wu, Liao, et al. 2013). The outputs of the deconvolution process were: A) three parcel-wise HRF parameters (height, FWHM, time-to-peak); B) the time course of the parcel-wise HRFs (16 time points, with time bins of 2 seconds, each corresponding to one TR); C) the time course of the deconvolved BOLD signal.

For each subject, a pairwise Spearman's correlation matrix was calculated from the parcel-wise HRFs, as the matrix of zero-lag temporal correlations between HRF time series of each pair of regions, interpreted as signals of vascular origin. The subject-wise "HRF connectivity" matrices were Fisher r-to-z transformed, and then thresholded retaining only connections associated with weights over a pre-defined connection density, set to the 80^{th} percentile (Wijk, Stam, and Daffertshofer 2010).

Topological features were estimated from these matrices using the Brain Connectivity Toolbox (Rubinov and Sporns 2010): node *DEG*, *STR*, *EC*, *BC*, *CC*, *LE*, *GE*.

Static FC features

sFC matrices were obtained as pairwise Pearson's correlations of the BOLD time series across brain regions, which were subsequently Fisher r-to-z transformed. Subject-level sFC matrices were thresholded (80^{th} percentile (Wijk, Stam, and Daffertshofer 2010)).

Topological features of sFC matrices (node *DEG*, *STR*, *EC*, *BC*, *CC*, *LE*, *GE*) were estimated using the Brain Connectivity Toolbox (Rubinov and Sporns 2010).

In addition to the more frequently employed *magnitude* FC approach, we also characterized FC as BOLD *phase* coherence, employing the LEiDA framework (Cabral et al. 2017; Lord et al. 2019).

After demeaning and detrending the BOLD time series, the parcel-wise BOLD signal phases were estimated using the Hilbert transform. BOLD phase coherence was calculated at each single time point. Then, the leading eigenvector (LEig) of each matrix is computed, and the parcel-wise value of the LEigs' median across time was obtained in every subject (*med-LEig*).

Time-varying FC features
Magnitude tvFC was computed with a sliding window approach (window size: 30 TRs, step: 1 TR), as Fisher r-to-z transformed Pearson's correlation. Sliding windows were thresholded using the connection density threshold approach (80th percentile): FC weights were selected on the population sFC matrix, and then propagated to the single sliding windows, to assess the temporal variability of the connections that are most likely to be significant at the population level. The same nodal graph metrics used in the sFC analysis (*DEG*, *STR*, *EC*, *BC*, *CC*, *LE*, *GE*) were computed for each window in every subject. Three metrics to quantify temporal variability across sliding windows were selected and applied to the graph metrics' time series at the parcel level: a) *CV%*, as a measure of fluctuation of the graph metric around its average value (Arachchige, Prendergast, and Staudte 2020; Hellyer et al. 2017); b) temporal median of the absolute value of first order differentials (*mdiff*) between graph metrics' values in adjacent sliding windows $|x_{it} - x_{it-1}|$, divided by the absolute value of the previous window ($|x_{it-1}|$) ; c) *sample entropy* of graph metrics' time series as a measure of graph metrics' time series complexity (Pedersen et al. 2017).
In addition to this, the regional *MAD*, *CV%* and *mdiff* of the LEigs were calculated as metrics of temporal variability of *phase* coherence.

4.2.4 Bivariate analysis of $SUVR$ vs. rs-fMRI

Spatial coupling across all brain regions
The bivariate relationship between node-wise $SUVR$ and rs-fMRI properties was assessed at the group level, in the naïve average data approach (NAD), employing the region-wise across-subject median values for $SUVR$ and for each of the 50 extracted features. Since the rs-fMRI properties were not normally distributed in most cases (Shapiro-Wilk test (Shapiro and Wilk 1965), p value > 0.05), the association between fMRI features and metabolism across nodes was tested via Spearman's rank bivariate correlation (significance level 0.05, corrected for multiple comparisons using the Benjamini-Hochberg false discovery rate (FDR) approach (Benjamini and Hochberg 1995)). The relationship between $SUVR$ and each of the 50 rs-fMRI properties ($fMRI_{ip}$, for $i = 1, \ldots, 218$ regions, and $p = 1, \ldots, 50$ features) was tested with four different bivariate models:

1) a *linear* model,

$$SUVR_i = \alpha_p + \beta_p \cdot fMRI_{ip} \tag{4.1}$$

2) a *mono-exponential* model,

$$SUVR_i = \alpha_p \cdot \mathrm{e}^{\beta_p \cdot fMRI_{ip}} \tag{4.2}$$

3) a *power law* model,

$$SUVR_i = \alpha_p \cdot fMRI_{ip}^{\beta_p} \tag{4.3}$$

4) a *log-linear* model,

$$SUVR_i = \alpha_p + \beta_p \cdot \log fMRI_{ip} \tag{4.4}$$

Model selection was performed according to the residual sum of squares (RSS) (Müller, Scealy, and Welsh 2013) to evaluate whether the $SUVR$-fMRI association was better described by a linear or a nonlinear model for each of the 50 features, as an expansion of previous assessments (D. Tomasi, G. J. Wang, and Volkow 2013; Shokri-Kojori et al. 2019). The percentualized difference in RSS values between the nonlinear models (*exp*, *power*, *log*) and the linear model (*lin*) were expressed as follows:

$$\Delta RSS_1 = \frac{RSS_{lin} - RSS_{exp}}{RSS_{lin}} \cdot 100 \tag{4.5}$$

$$\Delta RSS_2 = \frac{RSS_{lin} - RSS_{power}}{RSS_{lin}} \cdot 100 \tag{4.6}$$

$$\Delta RSS_3 = \frac{RSS_{lin} - RSS_{log}}{RSS_{lin}} \cdot 100 \tag{4.7}$$

Importantly, the number of model parameters is equal for the four model structures that were examined (i.e., two, intercept/amplitude α_p and slope β_p).

Spatial coupling in specific clusters of nodes

The spatial heterogeneity in the [^{18}F]FDG PET-fMRI relationship was probed by selecting clusters of nodes with increasingly high or low $SUVR$, and re-assessing correlations across those nodes only. The threshold levels were determined by considering linearly *increasing* percentiles of the $SUVR$ distribution over all nodes, in the range going from the 1^{st} to 85^{th} percentiles, with step 1 (from 218 to 33 nodes); moreover, in the opposite direction, nodes were selected according to linearly *decreasing* percentiles of $SUVR$, from the 100^{th} to the 15^{th} percentile (again, from 218 to 33 nodes). For each threshold level, Spearman's correlation between $SUVR$ and all fMRI-derived features was calculated across the selected nodes, and FDR-corrected for multiple comparisons across thresholds and rs-fMRI features (significance level 0.05) (Benjamini and Hochberg 1995). Finally, the absolute values of Spearman's correlations were summed column-wise for each percentile, to determine which percentile threshold led to the maximum PET-fMRI correlation across features.

4.2.5 Multivariable $SUVR$ vs. rs-fMRI modelling at group level

At the NAD level, a multiple linear regression approach was employed to assess how much of the group-wise $SUVR$ variance across regions could be explained by the linear combination of different fMRI-based features. The ordinary least squares (OLS) problem was formulated as follows:

$$y = X\beta + \varepsilon \tag{4.8}$$

where y and ε are n×1 vectors of the response/dependent variable (i.e., $SUVR$) and the model error, and $X \in \mathbb{R}^{nxp}$ is the matrix of p regressors (i.e., log-transformed rs-fMRI predictors, see chapter 4.3.3), or design matrix. Before performing OLS regression, all predictors were z-scored, i.e., centered and scaled by their SD across brain regions. The outcome variable, i.e., $SUVR$, was z-scored as well, so no model intercept needed to be estimated. The solution to the OLS problem was obtained as

$$\hat{\beta} = (X^T X)^{-1} X^T y \tag{4.9}$$

The model design matrix initially consisted of 50 parameters. The model was formulated as follows:

$$SUVR_i = \beta_1 \cdot \log fMRI_{i1} + \beta_2 \cdot \log fMRI_{i2} + ... + \beta_p \cdot \log fMRI_{ip} + \varepsilon_i \tag{4.10}$$

for each observation i=1,. . . ,n. The relationships amongst the predictors were evaluated by Spearman's correlation, to assess the presence of strong correlations (i.e., multicollinearity). Since high multicollinearity amongst predictors is known to result in lower precision, switched signs of the coefficients, and a lack of statistical significance of the multivariable model (Belsley 1991), the ill-conditioning of the design matrix was quantified using the condition number, i.e.,

$$\kappa(X) = \frac{\sigma_{max}(X)}{\sigma_{min}(X)} \tag{4.11}$$

with $\sigma_{max}(X)$ and $\sigma_{min}(X)$ as the highest and lowest singular values of X, respectively. As a rule of thumb, $\kappa(X)$ requires attention if higher than 30 (Belsley 1991). Moreover, the variance inflation factors (VIFs) were calculated to assess how much each individual predictor contributed to the multicollinearity of the final model (Belsley 1991). The OLS fit was obtained with all the rs-fMRI variables and interpreted as the highest possible predictive power that could be extracted from the available features. However, it is well-known that, in the case of overparameterized linear models, OLS is generally not useful, as many CVs%, (i.e., percent error SD divided by the absolute value of the parameter estimates) are too high (CVs% $>$ 100%) and the model is not *a posteriori* identifiable, so it should be rejected (E. Carson 2013). As discussed, performing feature selection at the individual level would lead to unstable estimates, so we continued to work at the group (i.e., NAD) level.

Feature selection

Eleven feature selection strategies were employed to identify the best multivariable model at the group level, with $SUVR$ as the dependent variable, and the rs-fMRI variables as predictors.

The employed approaches were: a) non-negative least squares (NNLS), b) elastic net regression, c) hierarchical clustering (Ward method), d) stepwise selection, e) general-to-specific (GETS) modelling. The following combinations of methods were employed: 1) Ward clustering, 2) NNLS, 3) GETS, 4) Ward + NNLS, 5) Ward + GETS, 6) Ward + stepwise, 7) Ward + elastic net, 8) NNLS + GETS, 9) NNLS + elastic net, 10) GETS + NNLS, 11) GETS + elastic net.

NNLS (a) and *elastic net regression* (b), which were in the chosen feature selection procedure, i.e., method 9), are detailed in the following.

A *NNLS* algorithm was implemented in methods 2), 4), 8), 9), 10), using the Lawson-Hanson active-set method for convex optimization (Lawson and Hanson 1974) (*lsqnonneg* function in MATLAB). NNLS estimation has been shown to be as effective in obtaining sparse estimates as the well-known LASSO (Tibshirani 1996), thanks to the non-negativity constraint, but without the need to perform

the delicate choice of the regularization parameter (Meinshausen 2013). As a preprocessing step, singular value decomposition (SVD) was performed (Golub and Reinsch 1970): in order to meet the NNLS assumption that βs are non-negative, the values of the z-scored predictors with negative weights on the first right-singular vector V_1 were multiplied by -1.
Elastic net regression (H. Zou and Hastie 2005) was implemented as a second step in methods 7), 9) and 11). The α parameter value was set as 0.7, i.e., leaning towards LASSO, but with the inclusion of the L2 penalty in order to better handle the predictors' multicollinearity. The selection of the regularization parameter $\lambda \in \{\lambda_1, \ldots, \lambda_m\}$ over 100 possible values, geometrically spaced between 0 and the highest value giving a non-null model, was performed through k-fold cross-validation (k-CV) (Stone 1974). k-CV was implemented with repeated random sub-sampling with 1,000 Monte Carlo independent realizations.
Hierarchical cluster analysis (c), used in methods 1), 4), 6), 7), was performed on the Spearman's correlation matrix of the rs-fMRI predictors using Ward's linkage method (Ward 1963) and Euclidean distance. The dendrogram structure was evaluated by means of the cophenetic correlation coefficient. The cluster solution was chosen by means of a cut-off determined by an inconsistency coefficient of 1 (Jain and Dubes 1988). After choosing the cluster cut, for each cluster only the feature with the highest Spearman's correlation with $SUVR$ was selected.
Stepwise selection (Hocking 1976) (d) was implemented in method 6) by starting from the model provided by Ward clustering and using both forward and backward stepwise regression to determine the final model. The *general-to-specific* (GETS) modelling strategy (e) was employed in methods 3), 5), 8), 10), 11), to overcome limitations of stepwise (Hoover and Perez 1999), such as the fact it proceeds along a single path without back-testing, its sensitivity to multicollinearity, and its usually resulting in R^2 that are biased towards high values (Desboulets 2018; Smith and Nichols 2018).
The implementation in R (R Core Team, 2018) by the package *gets* (Pretis, Reade, and Sucarrat 2018) was used.
The results obtained with each feature selection strategy were evaluated (Müller, Scealy, and Welsh 2013) in terms of: 1) number of selected features; 2) condition number $\kappa(X)$ of the design matrix after selection; 3) ordinary R^2, as an indicator of goodness of fit; 4) Bayesian Information Criterion (BIC), which proves useful when models to compare result in different number of parameters; 5) RSS, as another indicator of goodness of fit; 6) parameter CVs% as indicators of the

precision of the estimates; 7) signs of β estimates, i.e., the concordance with the signs of Spearman's correlation of the rs-fMRI predictors with $SUVR$.

4.2.6 Full hierarchical modelling of $SUVR$ vs. rs-fMRI

As a NAD approach like the one described so far is statistically sound and unbiased only in case of low BSV, a MLM approach (i.e., population modelling, linear mixed-effects (LME) modelling) was employed to characterize in a single stage both the group-level (*fixed*) and individual-level (*random*) effects (Hox, Moerbeek, and Schoot 2017) contributing to the relationship between the selected rs-fMRI variables and $SUVR$. First, the link between model and $SUVR$ was described at *individual* level by the following equations:

$$y_{Si} = F_{Si}(X_{Si}, \psi_{Si}) \tag{4.12}$$

$$z_{Si} = y_{Si} + v_{Si} \tag{4.13}$$

with y_{Si} as the $SUVR$ model prediction for the i^{th} subject (i=1,...,m), which is a function of X_{Si} (the fixed-effects design matrix composed by the features extracted from the rs-fMRI data of subject i), and the parameters ψ_{Si} to be estimated for subject i; z_{Si} is the vector of the measured $SUVR$ data of subject i and v_{Si} is the *within-subject variability*, or residual unexplained variability, assumed to be normally distributed with zero mean and variance σ_i^2.

Second, at *population* level, ψ_{Si} was described by a function combining population parameters (or fixed effects, θ_S), and the random variability of individual parameters around the population mean (or random effects, η_{Si}), according to the following assumptions:

$$\eta_{Si} \sim N(0, \Omega_S) \tag{4.14}$$

$$\psi_{Si} = \theta_{Si} + \eta_{Si} \tag{4.15}$$

where η_{Si} is assumed to be Gaussian, with zero mean, independent across individuals and with covariance matrix Ω_S; as a consequence, ψ_{Si} have a normal distribution as well. The matrix Ω_S was assumed to be full. The *intra-individual* (first-level) model structure was composed by the nine features selected with the NAD approach, here at single-subject level. Data normalization was per-

formed within subjects via z-scoring across regions. The *inter-individual* model (second-level) describing the BSV of the parameters was set according to the aforementioned assumptions.
The normality of the model residuals v_{Si} (or a reasonable approximation thereof) was assessed at each level by inspecting their histograms, boxplots, and Q-Q plots. The normality of the random effects η_{Si} was inspected with histograms and boxplots. This estimation requires solving a penalized least squares problem, i.e., the penalized weighted residual sum of squares,

$$PWRSS(\Omega_S, \theta, y_{Si}|Z_{Si}) = WRSS(\Omega_S, \theta, y_{Si}|Z_{Si}) + \parallel y_{Si}|Z_{Si} \parallel^2 \tag{4.16}$$

with Z_{Si} as the random-effects design matrix. The optimization problem was solved using the restricted maximum likelihood estimation method (Laird and Ware 1982). The standard errors (SEs) were calculated for each θ_{Si} parameter estimate as the square root of the diagonal of their covariance matrix. The overall (naïve pooled data, NPD) and subject-wise MLM R^2 were also evaluated. The residual unexplained variability v_{Si} was evaluated by calculating its median and variability (CV%) across subjects.
The hierarchical modelling approach was also performed across *networks* (N) in order to characterize BNV. RSNs were used as the grouping (or random) factor instead of subjects, in a model formulated as follows:

$$y_{Nj} = F_{Nj}(X_{Nj}, \psi_{Nj}) \tag{4.17}$$

$$z_{Nj} = y_{Nj} + v_{Nj} \tag{4.18}$$

with j as the j^{th} network (j=1,...,q). Normalization of $SUVR$ and rs-fMRI variables was performed via z-scoring within RSNs.
The random effects $\boldsymbol{\eta_N}$ and the resulting individual parameters $\boldsymbol{\psi_N}$ were evaluated in terms of their similarity structure, both across RSNs (first dimension of $\boldsymbol{\eta_N}$) and across the nine predictors (second dimension of $\boldsymbol{\psi_N}$), by using cosine similarity (with an arbitrary threshold equal to the 80^{th} percentile to emphasize high similarity values). The Gaussianity of residuals v_{Nj} and random effects η_{Nj} was assessed as described before.

Relative importance analysis

Relative importance analysis (Luo and Azen 2013; Tonidandel and LeBreton 2011) was employed as a supplement to the results of hierarchical modelling. This type of analysis allows to appropriately partition the model's explained variance amongst multiple predictors when there is still significant multicollinearity, which makes typical indicators of importance (e.g., standardized regression coefficients) flawed. Dominance analysis (DA), in particular, works by rank-ordering the predictors in term of relative importance by comparing the additional contributions they make to the R^2 of all possible subset models. Specifically, we assessed the *general dominance* of the variables, which is established for one predictor over another when the average of its conditional contributions over all model sizes is greater than that of the other. The obtained general dominance weights are also measures of relative effect sizes, as they sum to the model R^2: the percent contribution to the model R^2 was therefore calculated and reported. While DA was originally proposed for OLS models, it was later extended to MLM (Luo and Azen 2013). In order to apply DA to hierarchical models, a null model with no predictors must be provided, and the slopes of first-level models must be considered fixed even when they are random in the identified model, to simplify dominance evaluation. DA was used to assess the extent to which each selected variable was driving the prediction in the context of the LME models with subjects (S) and networks (N) as random factors, as they were still affected by non-negligible multicollinearity.

4.3 Results

4.3.1 Resting-state fMRI feature extraction and correlation structure

A flowchart describing the preprocessing and preliminary analysis of the [^{18}F]FDG PET and rs-fMRI data is shown in Figure 4.1.

The [^{18}F]FDG variable of interest is the $SUVR$, calculated at individual level for every region of the Schaefer cortical atlas (Schaefer et al. 2018), supplemented by 18 subcortical regions (H. Wang and Yushkevich 2013), which will be considered as the *dependent*variable from here onward.

We extracted 50 rs-fMRI variables at the single-subject level for the same 218 regions, and subdivided them into 4 *a priori*-defined pools, as reported in Table 4.1 .

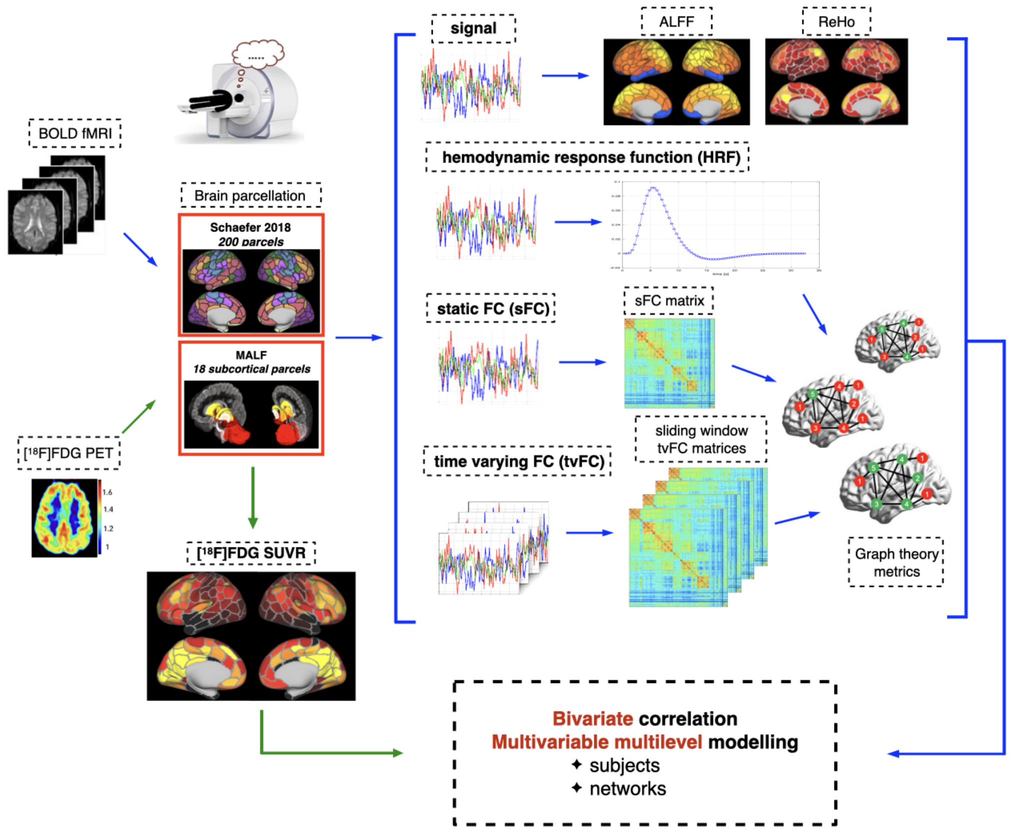

Figure 4.1: Flowchart of rs-fMRI and [18F]FDG PET processing, feature extraction and analysis. Both rs-fMRI time series and [18F]FDG $SUVR$ data were parceled using the Schaefer cortical atlas and 18 subcortical ROIs. The parcel-wise rs-fMRI data were used to extract fifty features representative of four "pools", i.e., 1) *signal*, 2) *HRF*, 3) *sFC*, 4) *tvFC*. The PET-fMRI spatial coupling was investigated using bivariate correlation and multivariable MLM across subjects and across fMRI-based RSNs.

To briefly recapitulate, the *signal* pool (1) contains features related to the basic statistics of the regional BOLD time series, its complexity/entropy, its low-frequency fluctuations ($ALFF$), local coherence (*ReHo*) and high-amplitude events (*peaks-BOLD*); the *HRF* pool (2) includes the amplitude of the HRF peak, and the correlation between regions in terms of HRF shape (introduced here for the first time), summarized by means of graph properties; the *sFC* pool (3) characterizes sFC with graph theory metrics at ROI-level; the *tvFC* pool (4) assesses graph metrics' temporal variability across sliding windows (Allen et al. 2014), and, notably, is very rich in features, because of our desire to characterize tvFC from multiple, complementary viewpoints (variance, entropy etc.).

These metrics are expected to be representative of the vast majority of properties that can be extracted from the rs-fMRI signal and its FC in a standard EPI acquisition.

Preliminarily, the Spearman's correlation matrix between the 50 rs-fMRI variables at group average level (i.e., by taking the parcel-wise median value of each feature across subjects) was computed (Figure 4.2a), in order to assess the spatial relationships between the extracted features and their degree of redundancy.
The clustering into 4 pools provided by *a priori* knowledge was fairly consistent with the observed correlation structure, with signal, HRF and sFC features (*upper block*) being clearly distinguished from tvFC features (*lower block*), which they are negatively correlated with. It was also noticeable that strong correlations between many variables were present, especially for the tvFC pool, and that a feature selection step was going to be necessary to use these variables in a numerically sound fMRI-based multivariable model of SUVR: the condition number $\kappa(X)$, which quantifies the level of correlation between predictors in a multiple regression context (i.e., their multicollinearity), was high ($\kappa(X) = 70.58$), way beyond the acceptability range (Belsley 1991), which is known to result in unstable and unreliable models.

4.3.2 $SUVR$ vs. rs-fMRI: bivariate spatial relationships

Before moving to the multiple regression framework, we began by investigating bivariate associations between $SUVR$ and the extracted rs-fMRI variables at the group level, in the so-called NAD approach, as frequently done by previous studies (D. Tomasi, G. J. Wang, and Volkow 2013; Marco Aiello et al. 2015). Here, notably, a much wider range of fMRI-derived variables was explored. Many significant spatial associations between $SUVR$ and rs-fMRI features were detected across the 218 analyzed regions, as assessed through Spearman's rank correlation ($p = 0.05$ significance level) with FDR multiple comparison correction (Benjamini and Hochberg 1995). The correlation coefficients are reported in Figure 4.2b.
The strongest *positive* associations were with 1) *ReHo* (ρ = 0.45, $p < 0.001$), 2) *s-BC* (ρ = 0.4, $p < 0.001$), and 3) *SampEn-BC* (ρ = 0.44, $p < 0.001$), respectively 1) a measure of local synchronization of BOLD, 2) a sFC graph metric, i.e., betweenness centrality (BC), which describes a region in terms of its global connections in the network (Rubinov and Sporns 2010), and 3) a tvFC measure of temporal complexity of the BC time series. The strongest *negative* correlations were *mdiff-BC* (ρ = -0.42, $p < 0.001$) and *CV-BC* (ρ = -0.42, $p < 0.001$) in the tvFC pool, both measures of temporal variability of BC.
In general, it can be noted that *positive* associations emerged for the majority of the signal-based, HRF and sFC-related features, while tvFC metrics, which

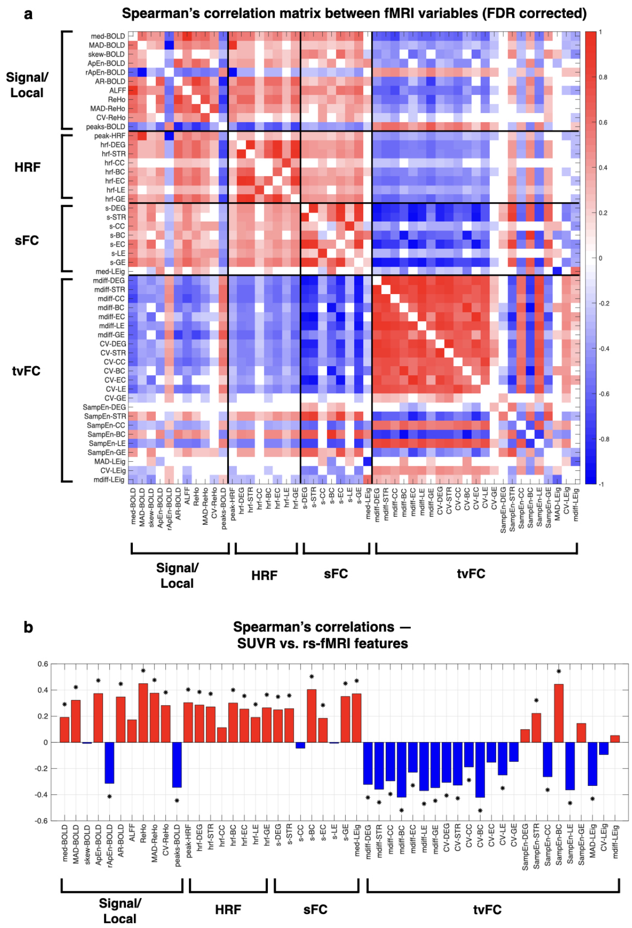

Figure 4.2: Bivariate correlations among rs-fMRI variables, and between rs-fMRI variables and $SUVR$. The pattern of Spearman's correlations (FDR-corrected, non-significant values in white) among rs-fMRI features, assessed at the group level and divided according to the pool to which they have been assigned (1) *signal*, 2) *HRF*, 3) *sFC*, 4) *tvFC*), is shown in (a). The rs-fMRI features are tested for association with group median $SUVR$ across 218 regions via Spearman's correlation (significant values after FDR correction indicated with an asterisk) (b).

highlight the variability of the FC profile of each brain region, displayed a consistent and never previously reported *negative* association with $SUVR$ (Figure 4.2b). Exceptions amongst signal-based features are *rApEn-BOLD* (ρ = -0.31, p < 0.001), a measure of rs-fMRI signal complexity, and *peaks-BOLD* (ρ = -0.34, p < 0.001), which quantifies the number of signal peaks exceeding one standard deviation from the baseline: both exhibited negative relationships with $SUVR$. Among tvFC features, *SampEn-BC* (ρ = 0.44, p < 0.001) shows a strong positive coupling with $SUVR$, in contrast to the behavior of the other tvFC metrics. Interestingly, the dynamics of local synchronization measures, i.e., *MAD-ReHo* and *CV-ReHo*, displays a positive association with $SUVR$, in contrast with the tvFC pool.

$SUVR$-fMRI associations are strengthened in low $SUVR$ nodes

Since from previous evidence we suspected the relationship between [^{18}F]FDG PET and rs-fMRI to be heterogeneous across regions, Spearman's correlations were also re-evaluated across groups of nodes selected according to linearly increasing percentiles of the SUVR distribution, i.e., by retaining the nodes with progressively higher and higher $SUVR$values, from the 1^{st} (all parcels) up to the 85^{th} percentile (33 parcels), as well as decreasing percentiles, i.e., by retaining nodes with lower and lower $SUVR$ values, from the 100^{th} to the 15^{th}. The purpose of using this data-driven approach was to verify whether $SUVR$-fMRI associations would be strengthened in high $SUVR$ nodes or, conversely, in low $SUVR$ nodes, since [^{18}F]FDG PET provides a ranking of brain regions that is expected to be related to important structural and functional properties (L. Sokoloff et al. 1977; Clarke and Louis Sokoloff 1999).

Spearman's correlations (p = 0.05 significance level, FDR-corrected) across regions between $SUVR$ and all 50 rs-fMRI features (*rows*) are shown in Figure 4.3a, for each threshold level along the $SUVR$ distribution (*columns*). Assessing the correlation in nodes with progressively higher $SUVR$ (right side of Figure 4.3a) does not lead to any relevant effect (except for few measures): therefore, hardly any strengthening of $SUVR$-fMRI relationships is detected in regions with high [^{18}F]FDG uptake.

Unexpectedly, however, a marked increase in many associations can be observed by assessing correlations over nodes with progressively lower values of $SUVR$ (left side of Figure 4.3a), with highly significant correlations even after FDR correction.

We identified the threshold corresponding to the highest total correlation across features: the spatial pattern of the 87 nodes that have a $SUVR$ below the 40th percentile is shown in Figure 4.3b. These parcels, where the $SUVR$-fMRI association is emphasized, mainly belong to temporal/limbic areas (including hippocampus), sensorimotor cortices, and subcortical regions, such as cerebellum and globus pallidus.

This finding suggests the presence of nonlinear relationships between [^{18}F]FDG $SUVR$ and most rs-fMRI features: tighter and more linear associations are present across a limited range of brain regions with low-medium [^{18}F]FDG up-

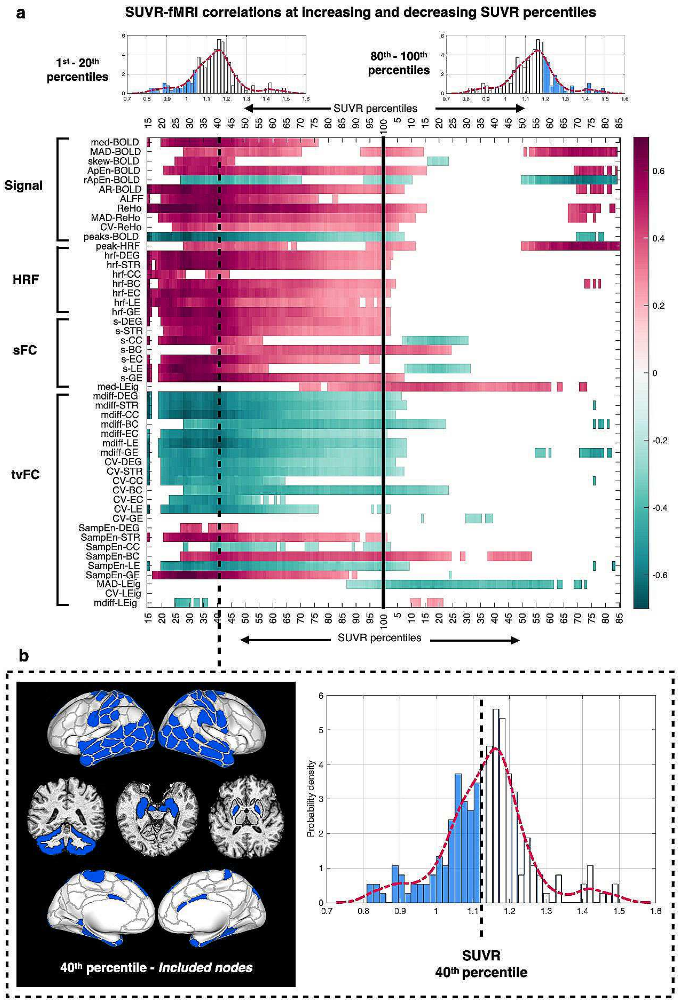

Figure 4.3: The $SUVR$-fMRI correlation changes strongly in low $SUVR$ nodes. Spearman's correlations (FDR-corrected, non-significant values in white) between $SUVR$ and all rs-fMRI features (y *axis*), evaluated across nodes selected by increasing (x *axis* - *right*) and decreasing (x *axis* - *left*) percentiles of $SUVR$ (a). The dashed black line shows the percentile with maximum correlation across features (i.e., nodes in the 1^{st} - 40^{th} percentile range). The histogram on the right highlights the range of percentiles included in the correlation. The brain regions shown on the left are the parcels over which correlations are assessed (b).

take, with weaker coupling as $SUVR$ gets higher.

This nonlinearity in the association was thus further tested by performing model selection for all variables, expanding on previous studies which were focused on specific networks and features (D. Tomasi, G. J. Wang, and Volkow 2013; Shokri-Kojori et al. 2019). In particular, we explored which model structure, amongst four options with equal number of parameters (linear, mono-exponential, power law, log-linear), was the best at fitting each of the 50 bivariate $SUVR$-fMRI associations. Notably, a nonlinear relationship was identified as the winning model for most (86%) of the $SUVR$-fMRI associations, with the power law as the model of choice for 72% of them (36/50 features). Since the log-linear model (i.e., a logarithmic transformation of the rs-fMRI variables):

1) would be easier to integrate in a multiple regression + feature selection framework than a fully nonlinear model like the power law, allowing us to use a (more robust) linear estimator;

2) was still superior to the linear model in 62% of the cases (31/50 associations);

3) displayed very small differences in RSS with respect to the power law, in the range of [-0.05; 0.01];

we chose to perform multivariable model selection using the log-linear model.

4.3.3 $SUVR$ vs. rs-fMRI: multivariable multilevel model

We then set out to assess which combination of rs-fMRI features was better able to explain $SUVR$ across brain regions, using multiple regression and MLM.
In MLM, the model structure is usually known, or selected at the lower level, i.e., at the individual level (Hox, Moerbeek, and Schoot 2017). However, as significant BSV in the $SUVR$-fMRI association is expected, we chose to identify the predictors at the population level (again, in a NAD approach), thus exploiting the denoising properties of averaging. The model structure selected at the group median level was then used on individual-level data to characterize the BSV of the $SUVR$-fMRI spatial association, trying to capitalize on the fact that [^{18}F]FDG and rs-fMRI data were acquired in the same subjects.

Maximum rs-fMRI explanatory power for $SUVR$ variability

To do a preliminary assessment of the maximum explanatory power provided by the rs-fMRI features, we began by fitting an OLS regression model employing all the available features in log-linear form (i.e., exploring the relationship between $SUVR$ and the log-transformed rs-fMRI explanatory variables), to account for the detected nonlinearity. From now we will call this *log-linear model*.
The OLS model had an R^2 value of 0.62: the maximum explanatory power the rs-fMRI variables provide reaches around 60% of the $SUVR$ variance, without full saturation despite a marked overparameterization (i.e., 50 rs-fMRI predictors). Due to the high number of predictors and the presence of multicollinearity, the precision of numerous parameter estimates was, as expected, very low (CVs $>$ 100%) (E. Carson 2013).

Modelling approach	number of features	Condition Number	Ordinary R^2	BIC	Model RSS	CV% ($\mu \pm \sigma$)	Switched signs
OLS	50	75.72	0.630	670.03	80.25	533.68 ± 1092.1	YES
Ward	50 → 12	13.23	0.472	543.02	114.57	124.27 ± 246.41	YES
NNLS	50 → 13	8.08	0.420	568.82	122.67	778.24 ± 1674.6	NO
GETS	50 → 11	12.93	0.564	495.84	94.58	26.73 ± 6.11	YES
Ward+NNLS	12 → 6	13.23 → 4.71	0.394	540.82	131.53	77.68 ± 17.89	NO
Ward+GETS	12 → 4	13.23 → 3.44	0.428	517.26	124.04	21.57 ± 3.34	YES
Ward+stepwise	12 → 6	13.23 → 5.06	0.436	525.05	122.35	42.07 ± 17.92	YES
Ward+elastic net	12 → 12	13.23 → 13.10	0.461	545.37	115.81	203.26 ± 509.03	YES
NNLS+GETS	13 → 3	8.08 → 2.39	0.390	526.23	132.48	27.62 ± 8.06	YES
NNLS+elastic net	**13 → 9**	**8.08 → 6.56**	**0.411**	**550.01**	**127.40**	**66.73 ± 17.79**	**NO**
GETS+NNLS	11 → 6	12.93 → 3.51	0.396	539.91	130.98	64.58 ± 35.15	NO
GETS+elastic net	11 → 11	12.93 → 12.93	0.561	497.92	95.48	28.86 ± 6.52	YES

Table 4.2: Feature selection strategies for the log-linear model at group level. For each of the eleven feature selection methods, the table's columns display 1) number of features after selection, 2) condition number of design matrix after selection, 3) ordinary R^2, 4) Bayesian Information Criterion (BIC), 5) model residual sum of squares (RSS), 6) mean (μ) and standard deviation (σ) of CVs% of estimates, 7) presence of switched signs of the coefficients. The feature selection strategy that was chosen as the most informative (NNLS + elastic net) is highlighted in red.

A parsimonious and informative group-level multivariable model

Multiple feature selection approaches (11 methods) were then tested to reach a mathematically sound regression model. These were compared in terms of number of selected features, condition number $\kappa(X)$ of the predictor matrix after selection, goodness-of-fit indices (R^2, RSS), parsimony criteria (BIC), precision of the estimates (mean and SD of CVs%), and presence of coefficients with switched signs (with respect to bivariate correlations with $SUVR$). We also considered other aspects of the solutions, i.e., the number of features from each rs-fMRI pool (trying to avoid too parsimonious solutions) The details of the results are reported in (Figure 4.4, Table 4.2).

The chosen feature selection process was performed in two stages. First, a sign-constrained NNLS estimator (Meinshausen 2013) was employed; then, the NNLS estimates were refined with a second stage of feature selection via elastic net regression (H. Zou and Hastie 2005). The reached solution was optimal in comparison with the other ten methods, in terms of both goodness of fit ($R^2 = 0.411$) and precision of the estimates (CVs% $\mu \pm \sigma = 66.73 \pm 17.79$ %).

The selected rs-fMRI predictors are: 1) *ApEn-BOLD*, 2) *rApEn-BOLD*, 3) *ReHo*, 4) *CV-ReHo*, 5) *peaks-BOLD*, 6) *hrf-LE*, 7) *s-BC*, 8) *med-LEig*, 8) *CV-BC*. The first five predictors belong to the signal and local synchronization pool, while the other four to the remaining groups of rs-fMRI features, suggesting a clear and direct [18F]FDG-fMRI spatial relationship mostly for local features. Notably, most of the identified rs-fMRI predictors were chosen with high consistency across the tested feature selection methods (*ReHo* in particular, in 10/11 cases), which highlights the robustness of their association with $SUVR$ (Figures 4.4).

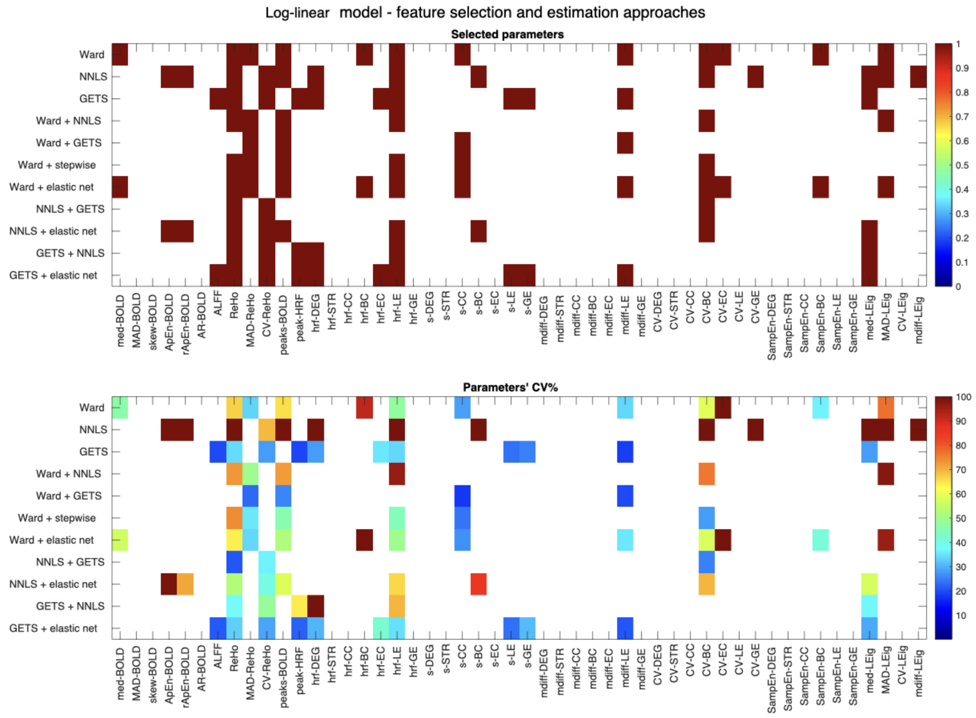

Figure 4.4: Feature selection results for the group-level log-linear model. Selected rs-fMRI variables (top matrix, in red) and CVs% of the estimated parameters (bottom matrix, ceiling at 100%). The employed selection strategies (*y axis*) are: 1) Ward hierarchical clustering, 2) NNLS, 3) GETS, 4) Ward, then NNLS, 5) Ward, then GETS, 6) Ward, then stepwise, 7) Ward, then elastic net, 8) NNLS, then GETS, 9) NNLS, then elastic net, 10) GETS, then NNLS, 11) GETS, then elastic net. The rs-fMRI features are shown on the *x axis*.

Multivariable multilevel model – subjects as random factor

The hierarchical modelling framework was then applied to the individual data using the nine selected predictors, to fully characterize the BSV of the $SUVR$-fMRI association. The log-linear model identified at the group level was re-estimated using a MLM approach (Hox, Moerbeek, and Schoot 2017). The*fixed-effect* (θ_S) parameter estimates, which represent the equivalent of the parameters estimated at the group level, are reported in (Figure 4.5a) with their SEs. To get an accurate ranking of the most relevant predictors in explaining $SUVR$, the estimated θ_S were ordered by their relative contribution to the model explanatory power using *dominance analysis* (DA) (Luo and Azen 2013) (Figure 4.5b). In terms of general dominance, at the top was *ReHo* (48% of the total R^2), followed by *peaks-BOLD* (19%), *CV-ReHo* (11.74%), *CV-BC* (10.50%), *s-BC* (8.02%), *ApEn-BOLD* (3.67%), *med-LEig* (2.60%), *hrf-LE* (1.47%), *rApEn-BOLD* (0.02%). Notably, the features belonging to the signal pool collectively accounted for 76.17% of the hierarchical model R^2.

The *random* effects (η_{Si}) describe the deviation of the parameters for a specific subject i from the group value, i.e., how much the parameters of each subject i are distant from the group-level estimates θ_S. We found that the BSV in the $SUVR$-fMRI association is clearly non-negligible: the explained variance of the overall model, i.e., considering the individual-level data in a NPD approach, was lower ($R^2 = 0.245$). The R^2 values of the subject-level models display high variability (from 0.05 to 0.45).
The across-subject average of the model's residuals υ_{Si}, which highlight how well the $SUVR$ of each region is explained by the identified model, can be visualized in Figure 4.5c. Notably, high positive values are present in posteromedial cortex (posterior cingulate cortex (PCC) in particular) and subcortex (putamen): these areas identify nodes with high [18F]FDG uptake which are not satisfactorily explained by the available rs-fMRI features. Importantly, this deficiency in explanatory power is highly consistent across subjects, as evidenced by the low BSV of the residuals in those areas (Figure 4.5d).

Multivariable multilevel model – networks as random factor

Finally, the nine rs-fMRI features, selected for their ability to *globally* explain $SUVR$ across all brain regions, were tested as predictors to describe the BNV of the $SUVR$-fMRI association. Parcels were grouped according to RSNs of the Schaefer atlas in its 17-RSN partition (Schaefer et al. 2018), supplemented by a subcortical "network" with 18 subcortical anatomical regions (H. Wang and Yushkevich 2013). A suboptimal way to do this would be to use a single-network approach, i.e., to estimate the weights of each of the nine BOLD predictors for each network separately, and then to consider the average and variability of the results across networks. A more appropriate approach is the full MLM framework, but this time with RSNs as the random/grouping factor for individual-level data, instead of subjects.
The *fixed* effects θ_N and their SEs for the between-network model are reported in (Figure 4.6a): *ReHo* and *peaks-BOLD* are still important parameters in describing $SUVR$, together with *ApEn-BOLD* and *CV-BC*; *rApEn-BOLD* and *hrf-LE*, instead, lose importance, and their fixed effect θ_N becomes irrelevant (with their SE range crossing the zero-line). To confirm the ranking, DA was performed in this context as well: *ReHo* was still the most important predictor in terms of general dominance (explaining 23.24% of the model's R^2), followed closely by *CV-BC* (19.85%), *peaks-BOLD* (16.39%), *s-BC* (15.19%), *ApEn-BOLD* (11.46%),

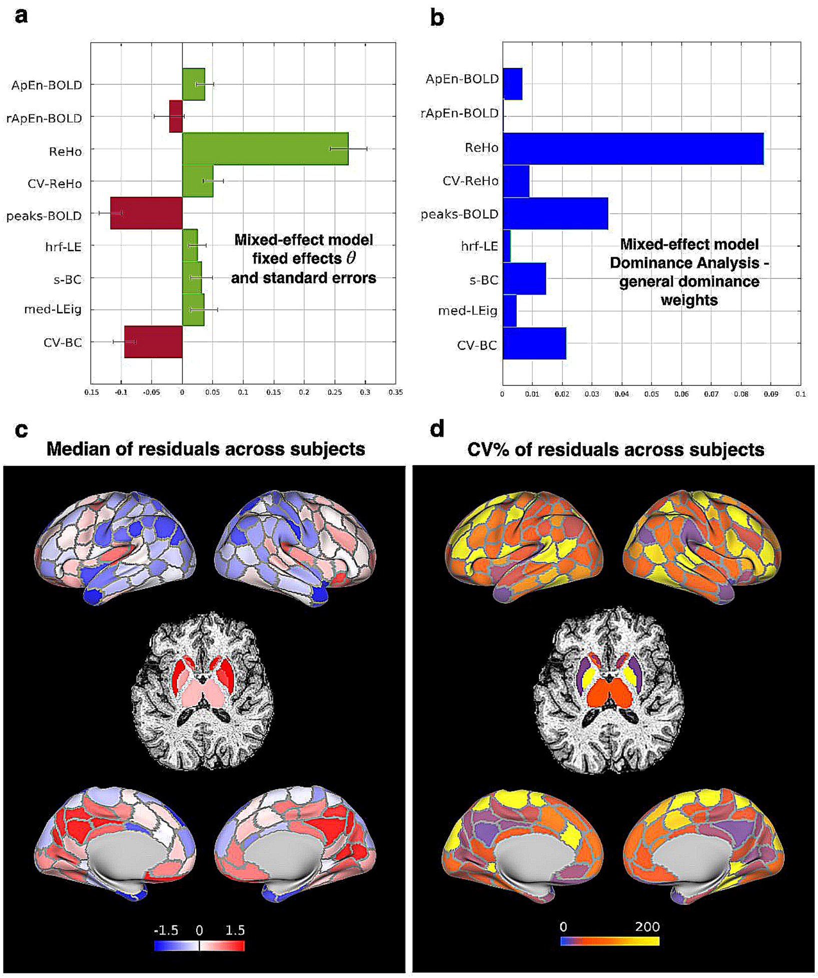

Figure 4.5: Multilevel $SUVR$ modelling and its BSV. Parameter estimates and SEs for the *fixed* effects θ_S, which represent the parameters that best explain $SUVR$ across the regions of the whole brain at group level (a). The relative importance weights derived from *dominance analysis*, highlighting the proportion of the multivariable MLM R^2 explained by each predictor (b). Across-subject median (c) and variability (d) of weighted residuals v_{Si} of the multilevel model.

med-LEig (9.65%), *CV-ReHo* (2.55%), *hrf-LE* (1.80%), *rApEn-BOLD* (0.13%) (Figure 4.66b).

Notably, the R^2 of model prediction considering network-wise estimates is markedly lower than when subjects are the random factor. As shown in (Figure 4.6c), the single RSNs are highly heterogeneous in terms of model R^2, ranging from around 0 to 0.32, with an overall NPD prediction of $R^2 = 0.147$.

The individual RSN estimates (i.e., weights of the nine rs-fMRI features) can be obtained by combining the fixed effects with the specific variation of each RSN: more specifically, the variability of the $SUVR$-fMRI association across networks (BNV) is measured by the *random* effects η_{Nj} for each network, with some RSNs displaying marked distance from the *fixed*-effect estimates θ_N of the "average network". To better assess this variability, the parameter estimates ψ_{Nj} (i.e., sum of fixed effects θ_N and random effects η_{Nj} for every network j) of the nine rs-fMRI predictors were plotted (Figure 4.7a).

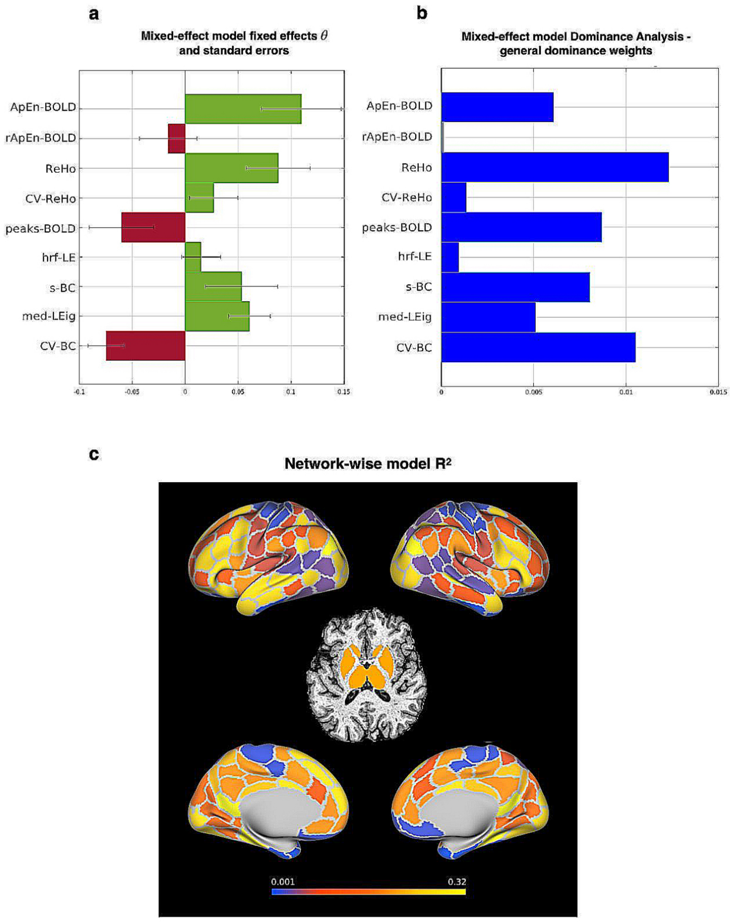

Figure 4.6: Multilevel $SUVR$ modelling and its BNV – parameter estimates and explained variance. Parameter estimates and SEs for the *fixed* effects θ_N, which represent the parameters that best explain $SUVR$ across regions in an average network (a). Relative importance weights produced by DA in terms of the proportion of the between-network model R^2 explained by each predictor (b). Network-wise R^2 values, representing the percentage of $SUVR$ variance explained by the mixed-effect model at the network level (c).

We can observe that most predictors included in the model display heterogeneity across networks in their relationship with $SUVR$, with either positive or negative associations depending on the specific RSN, which cannot be captured by the average description given by the fixed effects θ_N of Figure 4.6a.

As some predictors seemed to show very similar spatial patterns with one another, we assessed this consistency by calculating the cosine similarity between their random effects across networks (Figure 4.7b). Notably, high similarity ($> 80^{th}$ percentile) can be found between the patterns of *ReHo*, *CV-ReHo*, *hrf-LE* and

med-LEig, with strong positive weights for somatomotor network B (SM(B)) and also control network (CTR(C)). Another interesting pattern emerges for CV-BC, which displays both positive (CTR(A), VIS(B)) and negative weights (TEMP/-PAR, LIMBIC(A), SAL/VAN(A), DMN(B)), highlighting the presence of both *positive* and *negative* associations with $SUVR$.
Finally, the cosine similarity of the network-wise ψ_{Nj} values was evaluated across the nine predictors this time, to assess how similar the RSNs are to one another in terms of their multivariable $SUVR$-fMRI coupling (Figure 4.7c). When considering the high similarity values ($> 80^{th}$ percentile), an interesting pattern emerges: some RSNs are fairly isolated from the rest of the brain in their $SUVR$-fMRI association pattern (e.g. DMN(A), DMN(C), VIS(A), VIS(B), SM(A), CTR(A)), with only 1-2 strong associations with other RSNs; other RSNs, instead, have many associations, and thus are similar to many other networks in their $SUVR$-fMRI coupling (SAL/VAN(A), DAN(A), DAN(B), CTR(C), DMN(B), SUB).

4.4 Discussion

In this work, we have thoroughly investigated and modelled the spatial coupling between features extracted from rs-fMRI and simultaneously acquired [^{18}F]FDG PET, while also accounting for the variability across *subjects* (i.e., BSV) and *networks*(i.e., BNV) in this relationship.

4.4.1 New associations between [^{18}F]FDG PET and rs-fMRI

In addition to the few rs-fMRI variables that have already been associated to [^{18}F]FDG uptake, i.e., *ALFF*, *ReHo*, sFC *DEG/STR* (D. Tomasi, G. J. Wang, and Volkow 2013; Nugent et al. 2015; Marco Aiello et al. 2015; S. Deng et al. 2022; Palombit et al. 2022), we have assessed to a wider variety of previously unexplored features, such as those related to time-varying functional connectivity (tvFC) and the hemodynamic response (HRF) of rs-fMRI.
To our knowledge, in particular, the relationship between [^{18}F]FDG metabolism and FC temporal variability has never been tested before. It is known that regions with stronger sFC tend to have higher CBF (Liang et al. 2013) and $CMRglc$ (D. Tomasi, G. J. Wang, and Volkow 2013; Palombit et al. 2022), possibly reflecting the fact that they are also more strongly connected anatomically (Honey et al.

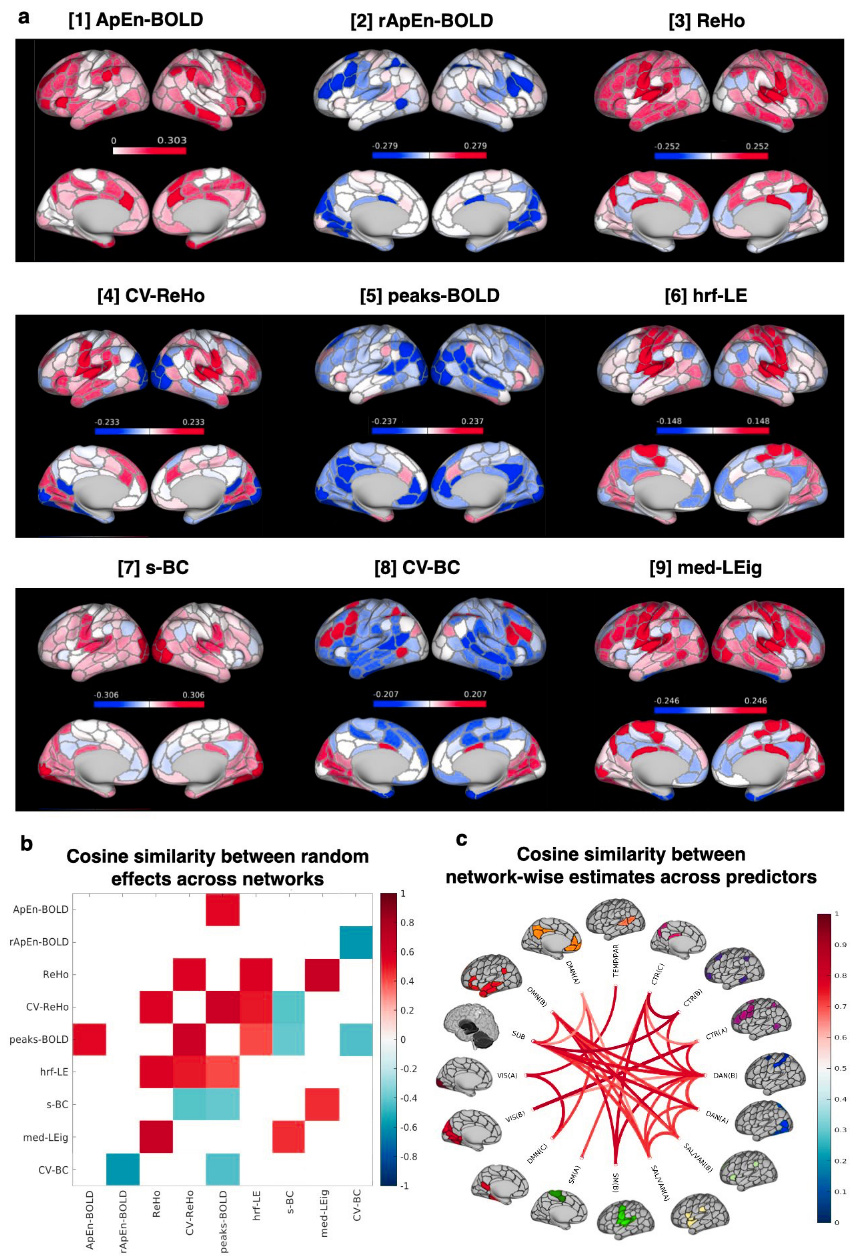

Figure 4.7: Multilevel $SUVR$ modelling and its BNV – multivariable network-level estimates. Individual network parameter estimates (ψ_{Nj}, sum of *fixed* effects θ_N and *random* effects η_{Nj}, which describe the variability from the fixed effect for each RSN j) for each predictor (a). Cosine similarity matrix (values above the 10^{th} and below the 80^{th} percentile set to zero – in white) between the nine predictors' random effects η_{Nj} across *RSNs* (b). Circular graph of the cosine similarity (values below 80^{th} percentile set to zero) among RSNs in terms of their parameter estimates ($\psi_{Nj} = \theta_N + \eta_{Nj}$) for the nine *predictors* (c).

2009), but the tvFC coupling with glucose metabolism is not established.

We found that graph metrics' temporal variability is *negatively* related to $SUVR$. The interpretation of this finding can be supported by knowing that sFC and tvFC graph metrics are also negatively correlated, as shown by the correlation betwen

rs-fMRI measures (Figure 4.2a); in fact, the higher the strength of a correlation across the entire rs-fMRI acquisition, the lower its temporal variability across time windows from the *same* acquisition (Thompson and Fransson 2015). However, when examining the correlations of tvFC metrics vs. sFC metrics with $SUVR$, different patterns emerge, suggesting that tvFC-$SUVR$ associations are not simply the *inverse* of the sFC findings. Similarly to our findings with [^{18}F]FDG, tvFC has been previously linked to cerebral protein levels assessed with L-[1-^{11}C]leucine PET, with regions having higher protein turnover displaying lower temporal variability of their graph properties (Hellyer et al. 2017).
Additionally, one of the strongest negative relationships is found between $SUVR$ and the number of BOLD pseudo-events (*peaks-BOLD*), a metric that is related to the description of the rs-fMRI signal as a point process, with sparse neural events governing its dynamics (Zhang, Pan, and Keilholz 2020).
One interpretation might come from considering that higher local oxygen consumption by active neurons has been found to be associated with decreased positive BOLD fluctuations (Howarth, Mishra, and Hall 2021), and therefore the higher the number of BOLD peaks and extreme events, the lower the oxidative metabolism (and $SUVR$) might be in that region, but further investigation is required. Additionally, one might also consider a recent hypothesis on metabolic resources representing an anticipatory allocation of energy for neural expenditure, as discussed in (Mann et al. 2021) in Drosophila using calcium imaging as a marker of neural activity and pyruvate and ATP concentration as metabolic sensors. Under this vision, our results reporting lower glucose consumption in parcels with more BOLD peaks and higher time-varying FC might be explained with a decreased ability of these regions to allocate energy due to a difficulty in anticipating higher-frequency and more variable neuronal activity. However, while these hypotheses could be intriguing, more complex experimental settings are required to make these assessments in human neuroimaging data.

4.4.2 The $SUVR$-fMRI associations are stronger in low $SUVR$ nodes

We then examined how these relationships are modulated by selecting parcels according to their ranking in terms of [^{18}F]FDG uptake. Since the spatial relationship between $SUVR$ and rs-fMRI was previously found to be heterogeneous across the brain (Marco Aiello et al. 2015; Shokri-Kojori et al. 2019), we chose to evaluate the changes in correlations when selecting nodes from the $SUVR$ standpoint. Unexpectedly, when choosing nodes with progressively higher $SUVR$ we found no increases in the the associations, which instead became significantly stronger when progressively selecting nodes with lower and lower $SUVR$ (Figure 4.3).

This finding suggests that only in nodes with lower glucose metabolism is the [^{18}F]FDG-fMRI spatial relationship emphasized, implying the presence of a *non-linear* association for most of the rs-fMRI features, not just for the previously explored metrics (D. Tomasi, G. J. Wang, and Volkow 2013; Shokri-Kojori et al. 2019). Regions with high [^{18}F]FDG uptake remaining unexplained by the available features.

This nonlinear spatial relationship was also directly tested, and either an exponential, a power law or a log-linear relationship was attributed to the majority (86%) of the evaluated bivariate associations. The nonlinearity of the coupling between glucose consumption and BOLD is partly expected: 1) known nonlinearities exist in the associations between BOLD and neuronal activity (Kim and Seiji Ogawa 2012), to which glucose metabolism is instead linearly related (Louis Sokoloff 1999); 2) nonlinear models (e.g., power laws) are commonly detected in biological data, and in particular in metabolic budget (D. Tomasi, G. J. Wang, and Volkow 2013); 3) the [^{18}F]FDG coupling with local and large-scale FC (D. Tomasi, G. J. Wang, and Volkow 2013; Shokri-Kojori et al. 2019) has been described with a power law within specific areas; 4) nonlinear relationships between CBF, a main ingredient of BOLD, and $CMRglc$ have also been reported (Henriksen, Vestergaard, et al. 2018).

What seems clear is that the nodes with the *highest [^{18}F]FDG uptake* are poorly described by rs-fMRI features, possibly implying that they are richer in properties that are not easily captured by rs-fMRI (e.g., receptor density, structural connections, neural activity etc.?).

Further investigation on the few features that increase their correlations in high $SUVR$ nodes (i.e., *MAD-BOLD*, *rApEn-BOLD*, *peak-HRF*) might also provide some insight, as these are expected to be related to CBF.

4.4.3 The multivariable multilevel model: local fMRI features are the strongest predictors

To our knowledge, this is the first study to model the [^{18}F]FDG-fMRI coupling using a *multivariable* approach, attempting to identify the best subset of metrics, among a wide range of candidate fMRI variables, to explain $SUVR$ variability across regions, and then describe their relative contributions to overall glucose consumption. Moreover, to fully capitalize on the fact that PET and fMRI data were acquired in the same subjects, we employed a *MLM* approach, with feature selection performed at the group level, and modelling performed at the individual level, to characterize the BSV of the $SUVR$-fMRI association. The selected model consisted of nine rs-fMRI variables (Figure 4.5) representing each of the 4 a priori-defined pools of features: signal (*ApEn-BOLD*, *rApEn-BOLD*, *peaks-BOLD*, *ReHo*, *CV-ReHo*), HRF (*hrf-LE*), sFC (*s-BC*, *med-LEig*), tvFC (*CV-BC*).

Importantly, the strongest predictors of the $SUVR$ spatial distribution are found to be related to the BOLD *signal* and its local synchronization properties (*ReHo* in particular), which consistently emerged as relevant across all feature selection methods.

The fact that the $SUVR$-fMRI spatial coupling is emphasized when *local* BOLD variables are involved might reflect the interplay between excitatory and inhibitory neural populations (Muthukumaraswamy et al. 2012), and their regulation of local CBF, which could play a relevant role in these rs-fMRI features (Kim and Seiji Ogawa 2012; Tong et al. 2017). *ReHo*, in particular, which emerges as important also in past PET-fMRI work (Bernier et al. 2017; J. Wang et al. 2021), is expected to represent synchronization of local field potentials (Z. Li, Zhu, et al. 2012) and to be a proxy of local, short-range connectivity (Jiang and Zuo 2016).

Overall, the explanatory power provided by rs-fMRI features reached only a 40% of the $SUVR$ variance at the group level (and 24% at individual subject level). Zones of polarization in the model residuals emerged in subcortical, posteromedial, and lateral frontal regions, which could mainly be attributed to the aforementioned "outliers" with higher metabolism, which are poorly explained by the available rs-fMRI features in a consistent manner across subjects (Figure 4.5).

These results point to the idea that the BOLD signal and FC reflect the metabolic architecture established by [^{18}F]FDG only partially, even in simultaneously acquisitions, and that *large-scale* FC and its graph metrics, in particular, cannot be considered as good proxies of brain glucose metabolism.

Although most major neuroimaging initiatives (e.g., HCP, ABCD, UK Biobank) only acquire MRI data (Elam et al. 2021), we argue that [^{18}F]FDG PET still provides non-redundant information that are of great value.

4.4.4 The high variability of the [^{18}F]FDG-fMRI coupling across subjects

An issue that clearly emerged from MLM is that, while the group-level model R^2 is moderately high (~ 0.4), the individual model R^2 values were remarkably variable across subjects, ranging from 0.05 to 0.45: this highlights the fact that the $SUVR$-fMRI relationship displays significant BSV, with subjects whose BOLD signal and FC architecture are more related to $SUVR$ across regions, and others where there is hardly any [^{18}F]FDG-fMRI relationship.

Why this is the case is not fully clear. Simultaneous [^{18}F]FDG PET/fMRI acquisitions are expected to reduce the within-subject variability affecting non-simultaneous studies (e.g., (D. Tomasi, G. J. Wang, and Volkow 2013)), and also improve the match between modalities (Cecchin et al. 2017). However, PET measures are also known to have higher test-retest stability with respect to fMRI (Cecchin et al. 2017), which would point to the higher variability in fMRI-derived features being the reason for the better match in some subjects, and worse in others. Previous work has also called into play the 'non-ergodicity' of neuroimaging measurements (Jamadar et al. 2021), with group-level measures not being representative of what happens at the subject level: with regard to this, we chose to employ the mixed-effects population modelling approach since, despite its limitations, it might help find a balance between noisier individual-level associations and more robust group-level information.

4.4.5 The [^{18}F]FDG-fMRI coupling changes across networks

Finally, we used the MLM approach and the identified predictors to try to characterize BNV of the [^{18}F]FDG-fMRI association, exploiting the fMRI-derived RSNs to group the individual data in a network-by-network fashion, i.e., the parcels within a given network for all the subjects; this approach adds to and enriches previous work on such network-related variability (Marco Aiello et al. 2015; Shokri-Kojori et al. 2019).

The rs-fMRI predictors selected in the previous step are shown to be mostly relevant, but their ranking changes noticeably, with static and time-varying *large-scale* FC features (*CV-BC* in particular) gaining more importance in the model. Moreover, when the network-wise variability in the model parameters is considered, one can identify patterns of predictors with some similarity across networks, with a group of RSNs (subcortical, salience, dorsal attention etc.) sharing a similar $SUVR$-fMRI association pattern, while other networks seem to be more isolated (part of the default mode, visual, somatomotor etc.).

The first take-home message is that, while the spatial coupling across the whole brain tends to favor more local fMRI features (e.g., *ReHo*), the fMRI FC properties do gain more relevance in explaining local metabolism within specific networks. While the spatial model estimated across the whole brain, gives an "average" representation of the [^{18}F]FDG-fMRI relationship, when we focus on the single networks, which by definition are more homogeneous in terms of FC, it is possible for the association between [^{18}F]FDG and large-scale network properties (sFC, tvFC) to change and become stronger.

For what concerns the two groups of RSNs that are identified based on their [^{18}F]FDG-fMRI association patterns, the more peripheral role, from a topological standpoint (Rubinov and Sporns 2010), of networks like VIS and SM, or the enrichment in high $SUVR$ nodes for DMN and VIS, might explain the identified 'clusters'. Notably, the regions where $SUVR$-fMRI *bivariate* correlations are higher (Figure 4.3b) tend to fall into networks with high R^2 values in the *multivariable* model (Figure 4.6c). Other physiological variables (blood flow, neuronal or connection density etc.), might be important to explain these differences between networks.

Overall, we find a low explanatory power (R^2 from 0 to 0.32) in the network model: this is line with the previously reported weak or absent correlations between [^{18}F]FDG PET and rs-fMRI when assessed *across subjects* and not *across space* (Marco Aiello et al. 2015; J. Wang et al. 2021). In our analysis, the parcels of all subjects are pooled together within each network, and the [^{18}F]FDG-fMRI association is tested *across both space and subjects*: this might be behind the weaker performance of fMRI measures in explaining $SUVR$, with respect to spatial modelling across *all* brain regions. The reasons behind the poor match between the inter-subject variability of [^{18}F]FDG and rs-fMRI measures might be multifactorial (differences in time scales, spatial resolutions, sensitivity to artefacts, normalization strategies, between-subject reproducibility etc. among the two modalities (J. Wang et al. 2021)).

Notably, only a significant region-by-region coupling between [^{18}F]FDG and rs-fMRI measures *across subjects* would make one modality a "replacement" of the other at the individual level, especially for clinical purposes. Further investigation with a higher number of subjects is thus highly warranted to confirm this (lack of) association (see Chapter 5).

4.4.6 Limitations

A comprehensive understanding of the relationship between [^{18}F]FDG PET and rs-fMRI is likely to require assessing other features, such as CBF and $CMRO_2$ (S. Deng et al. 2022) (Chapter 5).
Additionally, while the dataset employed here consists of standard *rs-fMRI* acquisitions (single-echo, TR of 2s, voxel size 3-4 mm), more advanced fMRI denoising methods (e.g., multi-echo imaging (Kundu et al. 2017), recordings of respiratory volume and heart rate (J. E. Chen, Lewis, et al. 2020), and regression of the CBF contribution (Tong et al. 2017) out of the BOLD signal features) might significantly improve the BOLD-[^{18}F]FDG coupling.
For what concerns *[^{18}F]FDG PET*, it must of course be remembered that $SUVR$, which was employed here as well as in the majority of the literature on [^{18}F]FDG-fMRI coupling (Nugent et al. 2015; Marco Aiello et al. 2015; J. Wang et al. 2021), may offer a biologically confounded view of glucose consumption (Chapter 2). PET kinetic modelling is likely to help disentangle the biological processes underlying both rs-fMRI features and static PET estimates (Chapter 5).
To find better matching between [^{18}F]FDG and fMRI measures, it is also possible that PET measurements should be brought into a *large-scale 'connectivity'* framework as well, with ongoing research on 'MC' offering new perspectives on this multimodal integration (Amend et al. 2019; Jamadar et al. 2021) (Chapter 6).
As to the dataset employed in the analysis, the age range of the subjects (40-80 years old) may limit the generalizability of the findings, due to known age-related modifications of CBF and $CMRglc$. Future work reassessing these findings in a younger cohort is highly warranted.
With regard to the number of subjects (n = 26), increasing the sample size is clearly important, especially to better assess across-*subject* associations between [^{18}F]FDG and fMRI measures. However, as the MLM modelling framework employed here was tailored to *spatial* associations, either across the whole brain (i.e., 218 regions), or across regions within a network for all subjects (i.e., 26 multiplied by the number of regions in each network), we do believe our statistical analysis to be sufficiently powered for its purposes.

4.5 Conclusions

In conclusion, for the first time we thoroughly investigated and modelled the spatial relationship between [^{18}F]FDG $SUVR$ and a wide range of features derived from rs-fMRI, pooled into 1) signal, 2) HRF, 3) sFC, and 4) tvFC-based features, using simultaneous PET/fMRI data. Selection of low $SUVR$ parcels led to a strengthening of $SUVR$-fMRI associations, implying the presence of a nonlinear spatial relationship. Moreover, a novel multivariable MLM framework was employed to identify the best subset of rs-fMRI predictors able to explain$SUVR$ variance across regions, highlighting that predictors based on the BOLD signal local properties (*ReHo* and BOLD pseudo-events, in particular) are the ones that are more tightly related to [^{18}F]FDG $SUVR$ across regions spanning the whole brain.

Notably, the overall explanatory power provided by rs-fMRI on the regional metabolic variability did not exceed 40% of the variance at the group level, with significant variability across subjects. When MLM of the $SUVR$-fMRI coupling was carried out across networks, the selected predictors were still relevant for description of RSN metabolism, but noticeable between-network variability was present: new positive and negative associations emerged, and large-scale sFC and tvFC network features gained importance. In conclusion, [^{18}F]FDG variability across parcels is only partly expression of brain network organization described by rs-fMRI.

This work has been published as (Tommaso Volpi, Erica Silvestri, Marco Aiello, et al. 2021b; Tommaso Volpi, Marco Aiello, et al. 2021; Tommaso Volpi, Erica Silvestri, Marco Aiello, et al. 2021a; Volpi, Silvestri, Aiello, et al. 2022).

Chapter 5

[^{18}F]FDG uptake, delivery and phosphorylation: what changes in the coupling with fMRI?

5.1 Introduction

The complex interplay between the brain's glucose ($CMRglc$) and oxygen ($CMRO_2$) metabolism, CBF, and brain activity has been the subject of investigation for a long time (Roy and Sherrington 1890; M. E. Raichle 1998; Louis Sokoloff et al. 1955), with one of the most interesting findings being the role that spontaneous activity plays for neural metabolism (Clarke and Louis Sokoloff 1999; Marcus E. Raichle 2006). One would thus expect a tight coupling between indices of brain metabolism ($CMRglc$, $CMRO_2$), as derived from PET experiments ([^{18}F]FDG, [^{15}O]H_2O, [^{15}O]O_2) (Marcus E. Raichle 1976; Hyder et al. 2016; S. Deng et al. 2022), and measures of resting-state brain activity, such as those derived from rs-fMRI (Riedl et al. 2014; Marco Aiello et al. 2015; J. Wang et al. 2021; Tommaso Volpi, Erica Silvestri, Marco Aiello, et al. 2021b; Palombit et al. 2022; S. Deng et al. 2022). Notably, while a large amount of work has focused on relating fMRI to electrophysiological signals (N. K. Logothetis et al. 2001; Nikos K. Logothetis 2008; Scholvinck et al. 2010), only a limited number of studies have directly tested how BOLD-based features can be mapped to hemodynamic and metabolic physiology as measured by PET-derived $CMRglc$ (Bernier et al. 2017; S. Deng et al. 2022), CBF, $CMRO_2$ (S. Deng et al. 2022).
Moreover, one must remember that the physiology of glucose metabolism as it can be tracked by [^{18}F]FDG is more complex than what is captured by simple semi-

quantitative measures like $SUVR$ (Chapter 2). While through [^{18}F]FDG PET we can only follow the initial steps of glucose metabolism, i.e., up to the first biochemical reaction of glycolysis, we can still use compartmental modelling to separate its delivery (K_1) across the BBB through glucose transporters, from its efflux into the venous blood (k_2), and its phosphorylation rate by the hexokinase enzyme (k_3), as well as to estimate the irreversible uptake rate (K_i) microparameter (L. Sokoloff et al. 1977; S. C. Huang et al. 1980; Alessandra Bertoldo, Rizzo, and Veronese 2014), (see Equation 2.5).

The K_1 of [^{18}F]FDG, in particular, is related to CBF (Renkin 1959; Crone 1963)

$$K_1 = EF \cdot CBF \tag{5.1}$$

but since the single-pass capillary extraction fraction (EF) of [^{18}F]FDG is low (around 18% in total GM), and variable across brain regions (Huisman et al. 2012), this coupling is not necessarily going to be strong or homogenous across the brain. On the other hand, [^{18}F]FDG k_3 is expected to be closely related to K_i, being weighted towards the late-phase metabolic information (L. Sokoloff et al. 1977; S. C. Huang et al. 1980), but there may still be regions where removing the impact of tracer delivery K_1 may prove very relevant.

The spatial distribution of these parameters has been investigated for the first time in the 1980's (Heiss et al. 1984), and in some later works (Piert et al. 1996; Hermanides et al. 2021), but a more fine-grained assessment of the microparameters regional variability, and their different roles in the association with rs-fMRI, as well as with CBF and $CMRO_2$, is warranted. Additionally, it has been demonstrated that, while most of the glucose metabolism in the brain is oxidative (as assessed by $CMRO_2$), there is a non-negligible portion of glucose that undergoes a purely glycolytic pathway (without oxidative phosphorylation) even in the presence of oxygen, the so-called '*aerobic glycolysis*' (AG). Through combined $CMRglc$ and $CMRO_2$ measurements, AG has been found to be spatially heterogeneous across the brain, with stronger presence in DMN regions and absence in visual cortex and cerebellum (Vaishnavi et al. 2010; Goyal, Vlassenko, et al. 2017; Blazey et al. 2019). Assessing the relationship between the spatial distribution of [^{18}F]FDG parameters and AG, as well as their interplay with rs-fMRI, might provide interesting insights.

In this chapter, we fully exploit the physiological information that can be extracted from [^{18}F]FDG PET data in a large dataset of healthy controls (n = 47), to expand on our previous assessment focused on the coupling between rs-fMRI and [^{18}F]FDG $SUVR$, which concluded that only a moderate portion of variance of regional glucose metabolism could be explained by rs-fMRI measures, mainly coming from local features such as *ReHo* (Tommaso Volpi, Erica Silvestri, Marco Aiello, et al. 2021b) (Chapter 4).

The main questions and aims driving our work in this chapter are:

1. as a preliminary step, assessing how reproducible the fMRI-$SUVR$ associations reported in chapter 4 are on a new dataset with different characteristics (non-simultaneous PET-fMRI acquisitions on different scanners);
2. estimating [^{18}F]FDG kinetic parameters (K_i, K_1, k_3), using an IDIF approach (K. Chen et al. 1998) and VB inference at voxel level (Castellaro et al. 2017), to assess their spatial distribution across brain regions in a large dataset of healthy subjects, focusing on the unique information provided by microparameters K_1 and k_3;
3. evaluating how much the spatial relationship between rs-fMRI and [^{18}F]FDG PET changes when considering kinetic parameters instead of $SUVR$, employing bivariate, multivariable and full mixed-effects modelling (= MLM) as in Chapter 4;
4. evaluating if (and how much) CBF and $CMRO_2$ add to the [^{18}F]FDG-fMRI coupling.

5.2 Materials and Methods

5.2.1 Participants

Forty-seven healthy adults (mean age 57.4 $\pm$ 14.8 years, 17 males) underwent [^{18}F]FDG PET, rs-fMRI and ^{15}O scans. Subjects were excluded if they had contraindications to MRI, history of mental illness, possible pregnancy, or medication use that could interfere with brain function. The interested reader should refer to (Goyal, Blazey, et al. 2022) for more detailed information on this dataset.

All assessments and imaging procedures were approved by Human Research Protection Office and Radioactive Drug Research Committee at Washington University in St. Louis. Written consent was provided from each participant.

5.2.2 Imaging protocols

For each participant, high-resolution structural images were acquired on a Siemens Magnetom Prisma scanner using a 3D sagittal T1-weighted magnetization-prepared

180° radio-frequency pulses and rapid gradient-echo (MPRAGE) multi-echo sequence (TE = 1.81, 3.6, 5.39, 7.18 ms, TR = 2,500 ms), TI = 1,000 ms, voxel size 0.8 × 0.8 × 0.8 mm). The final T1w image was obtained as the average of the first two echoes (Elam et al. 2021). Additionally, T2* gradient-echo echo planar imaging (GE-EPI) data were acquired (TR/TE=800/33 ms, flip angle 52°, voxel size 2.4 × 2.4 × 2.4 mm, MB 6, 375 volumes for total scan time of 5 min), together with two spin-echo (SE) acquisitions (TR/TE=6000/60 ms, flip angle 90°) with opposite phase encoding directions (AP, PA).

All subjects underwent one [^{18}F]FDG PET scan and two sets of ^{15}O scans ([^{15}O]CO, [^{15}O]H_2O, and [^{15}O]O_2).

The [^{18}F]FDG scans were performed on a Siemens model 962 ECAT EXACT HR+ PET scanner (Siemens/CTI) (Brix et al. 1997), as previously described (Vaishnavi et al. 2010), after i.v. bolus injection of 5.2 ± 0.4 mCi (192.4 ± 14.2 MBq) of [^{18}F]FDG. Dynamic acquisition of PET emission data continued for 60 min.

The [^{15}O]H_2O and [^{15}O]O_2 scans were also performed on the Siemens EXACT HR+ scanner, as previously described (Vaishnavi et al. 2010), after i.v. bolus injection of 49.6 ± 2.3 mCi (1835.2 ± 85.1 MBq) for [^{15}O]H_2O, and inhalation in room air of 66.5 ± 6.7 mCi (2460.5 ± 247.9 MBq) for [^{15}O]O_2. Dynamic acquisition of PET emission data continued for 3 min for both [^{15}O]H_2O and [^{15}O]O_2. Subject head movements during scanning were restricted by a thermoplastic facial mask. All PET images were acquired in the eyes-closed waking state. No specific instructions were given regarding cognitive activity during scanning other than to remain awake. PET data were reconstructed via filtered back-projection as 128x128x63 matrices. Attenuation correction was performed using the subject's own transmission scan.

The chosen reconstruction grid for [^{18}F]FDG consisted of 52 frames of increasing duration (24 x 5 s, 9 x 20 s, 10 x 1 min, and 9 x 5 min frames), while for [^{15}O]H_2O and [^{15}O]O_2 it consisted of 49 frames (35 x 2 s, 6 x 5 s, 8 x 10 s frames).

In the case of [^{18}F]FDG, venous samples for plasma glucose determination were obtained just before and at the midpoint of the scan to verify that glucose levels were within normal range throughout the study. Also, venous samples were collected to assess [^{18}F]FDG plasma concentration, with two possible sampling schedules: for most subjects, sampling occurred 20, 30, 45 minutes after injection of the radiotracer, whereas, for a minority of subjects (n = 9), samples were acquired after 30, 40 and 50 minutes. Each sample consisted of about 2 ml, half of which was used to measure radioactivity in plasma. Radioactivity counter measurements was given in counts per 12 seconds. The counter's efficiency (0.2707 cps/Becquerels) was experimentally determined (Tommaso Volpi, J. J. Lee, et al. 2022).

5.2.3 MRI preprocessing

Structural T1w images were N4 bias field-corrected (N. J. Tustison et al. 2010), skull-stripped (N. Tustison et al. 2013), and segmented into GM, WM and CSF (Ashburner and K. J. Friston 2005). T1w images were normalized to the symmetric MNI152 2009c atlas (Fonov et al. 2011) via nonlinear diffeomorphic registration (Avants et al. 2011). The Schaefer functional atlas (200 parcels, 17 networks) (Schaefer et al. 2018) was registered to T1w space by inverting the obtained nonlinear transformation. The Schaefer ROIs were supplemented by 16 subcortical ROIs taken from the Hammers atlas (Hammers et al. 2003) (bilateral hippocampus, amygdala, caudate, accumbens, putamen, pallidum, thalamus, cerebellum). The fMRI data were analyzed in a similar way to the HCP minimal preprocessing pipeline (Glasser, Sotiropoulos, et al. 2013): the first four volumes were discarded to avoid non-equilibrium effects, while the remaining volumes underwent 1) slice timing correction (Smith, Jenkinson, et al. 2004), 2) distortion correction (Andersson, Skare, and Ashburner 2003), 3) regression of nuisance signals (motion parameters and their first order derivatives, plus the first 5 temporal principal components of WM and CSF EPI signals (Behzadi et al. 2007), 4) high-pass filtering (cut-off of 0.008 Hz). The rs-fMRI preprocessing was identical to what reported in Chapter 4.2.2), except for the resampling onto cortical surfaces (Freesurfer, Connectome Workbench).
ROI-level pre-processed EPI signals were obtained within each parcel from the Schaefer + Hammers atlas (linearly mapped from T1w to EPI space), by averaging over voxels within the GM segmentation (probability > 0.8 of belonging to GM). Motion correction was adapted to the rs-fMRI features to be extracted (Chapter 4.2.2).

5.2.4 PET kinetic modelling

[^{18}F]FDG PET

Dynamic PET data were motion-corrected using an in-house combination of PMOD (`www.pmod.com`) and FSL's *mcflirt* (Jenkinson, Bannister, et al. 2002).

A static PET image was obtained by summing late PET frames (40-60 min) after motion correction. The static image was linearly registered to T1w space using FSL's *flirt* (Jenkinson, Bannister, et al. 2002), and normalized by injected dose and weight into a SUV image (Equation 2.7). The SUV image was intensity-normalized into $SUVR$ by dividing each voxel's value (SUV_{target}) by the whole-brain [^{18}F]FDG average uptake ($SUV_{reference}$) (Byrnes et al. 2014) (Equation 2.8). To perform PET kinetic modelling, an IDIF was extracted from dynamic PET data using a semi-automatic pipeline (Erica Silvestri et al. 2022):

- segmentation of the internal carotid arteries is performed on a pseudo-angiography image (obtained by summing dynamic PET frames up to an adaptive threshold of one frame before the peak time for venous vessels), on which a *vesselness* algorithm (Jerman filter) (Jerman et al. 2016) is run to generate a vessel mask;
- selection of "hot voxels" within the mask, according to their peak amplitude and time-to-peak;
- parametric clustering (Peruzzo et al. 2011) (k-means algorithm, k = 2, squared Euclidean distance, 500 replicates) on seven parameters calculated on the TAC of each voxel (peak amplitude, slope of rising part before peak, slope of tail, area under the curve before and after the peak, tail average value, TAC standard deviation), with the cluster having the highest peak centroid being selected and used to derive the raw IDIF;
- IDIF model fitting is performed using a modified version of Feng's model (D. Feng, S.-C. Huang, and X. Wang 1993; Tonietto et al. 2015) with maximum a posteriori estimation of the exponential decay parameters;
- Chen's spillover correction (K. Chen et al. 1998) is applied to the fitted IDIF curves using three venous samples (obtained after arteriovenous equilibration, i.e., after 20 min post-injection) and a background tissue TAC, obtained as the highest activity cluster centroid within a background mask (obtained from morphological dilation of the *vesselness* mask);
- IDIF shift correction, to correct for delay between the carotids and the voxel of interest.

Notably, Chen's approach is still the 'gold-standard' approach for [^{18}F]FDG IDIF calibration with older scanners like HR+, and was found to be the only one

with the recognized potential for calculating accurate microparameters (Zanotti-Fregonara, Fadaili, et al. 2009).
Voxel-wise estimation of Sokoloff's model parameters was performed using the VB approach (Chapter 2.1.2) (Castellaro et al. 2017), according to the following pipeline:

- a k-means clustering approach is applied to the dynamic PET data, extracting 6 GM and 5 WM clusters (as from the tissue segmentations linearly mapped to PET space);
- conventional nonlinear estimation of Sokoloff's model using WNLLS, with weights chosen as the inverse of the variance of the PET measurement error (Alessandra Bertoldo, Rizzo, and Veronese 2014), is performed at the region level, i.e., on the 11 cluster centroids;
- voxel-wise estimation of the model parameters via VB inference using prior distributions derived from cluster-wise estimates.

Parametric maps of K_1, k_2, k_3, V_b were obtained for each subject. The parametric map of K_i was obtained by the solving Equation 2.5) at the voxel level. The group-average voxel-wise maps of $SUVR$, K_i, K_1, k_3 are reported in Figure 5.2). From the K_i estimate we also derived the $CMRglc$ (Equation 2.6), with the LC set at 0.65 (H. Wu 2003).
The $SUVR$, K_i, K_1, k_3 parametric maps were parceled at the subject level with the Schaefer + Hammers atlas: ROI-level parameter estimates were extracted from the Schaefer and Hammers parcels, which had been linearly mapped from T1w to PET space, by averaging over voxels within the GM segmentation (probability > 0.8). Importantly, the GM segmentation provided by SPM, being quite conservative, allows to extract an average TAC which is as free of PVEs as possible (Rousset et al. 2007). Moreover, spatial smoothing of the PET data during processing was avoided, further minimizing PVEs.
The region-wise $SUVR$, K_i, K_1, k_3 values were within-subject normalized via z-scoring, i.e., centered with respect to their mean and divided by the standard deviation across ROIs (Yan et al. 2013). Their averages across subjects, rescaled to a [0;1] range, can be seen in (Figure 5.2).

$[^{15}O]H_2O$ and $[^{15}O]O_2$ PET

The differential equation of the $[^{15}O]H_2O$ tracer's one-tissue compartment model

(Kety and C. F. Schmidt 1945; M. E. Raichle et al. 1983)

$$\dot{C}_1(t) = K_1 C_p(t) - k_2 C_1(t) \tag{5.2}$$

with $C_1(t)$ as the tissue tracer concentration and $C_p(t)$ as the AIF, was linearized as follows:

$$C_1(t) = K_1 \int_0^t C_p(\tau)d\tau - k_2 \int_0^t C_1(\tau)d\tau \tag{5.3}$$

to identify the K_1 [ml/cm^3/min] (inflow of the tracer), which in the case of [^{15}O]H$_2$O corresponds to the CBF, and k_2 [min^{-1}] (efflux of the tracer).
Since arterial samples were not available, and the data were too noisy to extract an IDIF from the carotid signals like we did for [^{18}F]FDG, we used a model-based IDIF approach similar to (Ssali et al. 2018; Narciso, Ssali, L. Liu, Jesso, et al. 2022), which reconstructs the $C_p(t)$ by rearranging Equation 5.2 as follows:

$$C_p(t) = \frac{1}{CBF^{WB}} \dot{C}_1^{WB}(t) + \frac{k_2^{WB}}{CBF^{WB}} C_1^{WB}(t) \tag{5.4}$$

with $C_1^{WB}(t)$ as the whole-brain average tissue TAC from dynamic [^{15}O]H$_2$O data, CBF^{WB} as whole-brain average CBF value, and $\frac{k_2^{WB}}{CBF^{WB}}$ corresponding to $\frac{1}{\lambda}$ (λ is the blood-brain partition coefficient for water). The values for CBF^{WB} and λ are chosen *a priori* as 0.5 ml/cm^3/min and 0.9 ml/cm^3, respectively (M. E. Raichle et al. 1983). The raw IDIF curve was fit with a Gamma-variate function similarly to (J. J. Lee et al. 2010; Peruzzo et al. 2011; Rizzo et al. 2017) to regularize its noisy shape.
Since [^{15}O]H$_2$O K_1 is directly dependent on the amplitude of the $C_p(t)$ (Treyer 2003), the final mean CBF value will be approximately close to the chosen value for whole-brain K_1. This makes the result of this approach a *relative* CBF map. However, for our analyses, we do not need *absolute* estimates of CBF as we only aim to compare relative spatial distributions between [^{18}F]FDG parameters, fMRI variables, and CBF and $CMRO_2$.
To estimate $CMRO_2$, a reference-tissue modelling approach (Narciso, Ssali, Iida, et al. 2021; Narciso, Ssali, L. Liu, Biernaski, et al. 2021) was employed. Voxel-wise $CMRO_2$ values are obtained via the following equation:

$$CMRO_{2i} = CMRO_2^{WB} \frac{\int_0^T C_{1i}(t)dt + \frac{CBF_i}{\lambda} \int_0^T \int_0^t C_{1i}(u)dudt}{\int_0^T C_1^{WB}(t)dt + \frac{CBF^{WB}}{\lambda}) \int_0^T \int_0^t C_1^{WB}(u)dudt} \text{for } i = 1, ..., p \text{ voxels} \quad (5.5)$$

with $CMRO_2^{WB}$ as whole-brain average $CMRO_2$ value, C_{1i} as the voxel-wise $[^{15}O]O_2$ tissue TAC, CBF_i as the voxel-wise CBF values, obtained from $[^{15}O]H_2O$ PET modelling, C_1^{WB} as the whole-brain $[^{15}O]O_2$ tissue TAC. The $CMRO_2^{WB}$ value was obtained by

$$CMRO_2^{WB} = C_a^{O_2} CBF^{WB} \frac{(S_a^{O_2} - S_v^{O_2})}{S_a^{O_2}} \quad (5.6)$$

with $C_a^{O_2}$ as the O_2 arterial tension, set to the literature value of 90 mmHg, and $S_a^{O_2}$ as the O_2 arterial saturation, set to 98% (Narciso, Ssali, L. Liu, Jesso, et al. 2022). Due to the use of literature values for $C_a^{O_2}$, $S_a^{O_2}$, CBF^{WB}, the result of this approach is a *relative* $CMRO_2$ map as well.
The glycolytic index (GI), calculated as the residuals of the voxel-wise regression of $CMRO_2$ on $CMRglc$ standardized by the variance of $CMRglc$, was used as a measure of AG (Vaishnavi et al. 2010).
Since two runs of $[^{15}O]H_2O$ and $[^{15}O]O_2$ PET scans were available for each subject, the average CBF, $CMRO_2$, GI parametric maps across the two runs were used for further analysis.
The group-average maps of CBF, $CMRO_2$, GI are reported in Figure 5.1). The CBF, $CMRO_2$, GI parametric maps were parceled at the subject level with the Schaefer + Hammers atlas (GM-masked to minimize PVEs). Spatial smoothing of the PET data was avoided. The region-wise CBF, $CMRO_2$, GI values were within-subject normalized via z-scoring, i.e., centered with respect to their mean and divided by the standard deviation across ROIs (Yan et al. 2013). Their averages can again be visualized in Figure 5.2).

5.2.5 Resting-state fMRI feature extraction

The aforementioned 50 fMRI features, divided *a priori* into 4 categories, i.e., 1) signal, 2) HRF, 3) sFC, 4) tvFC, were extracted for all subjects.
For a detailed description of the extracted rs-fMRI features, see Chapter 4).

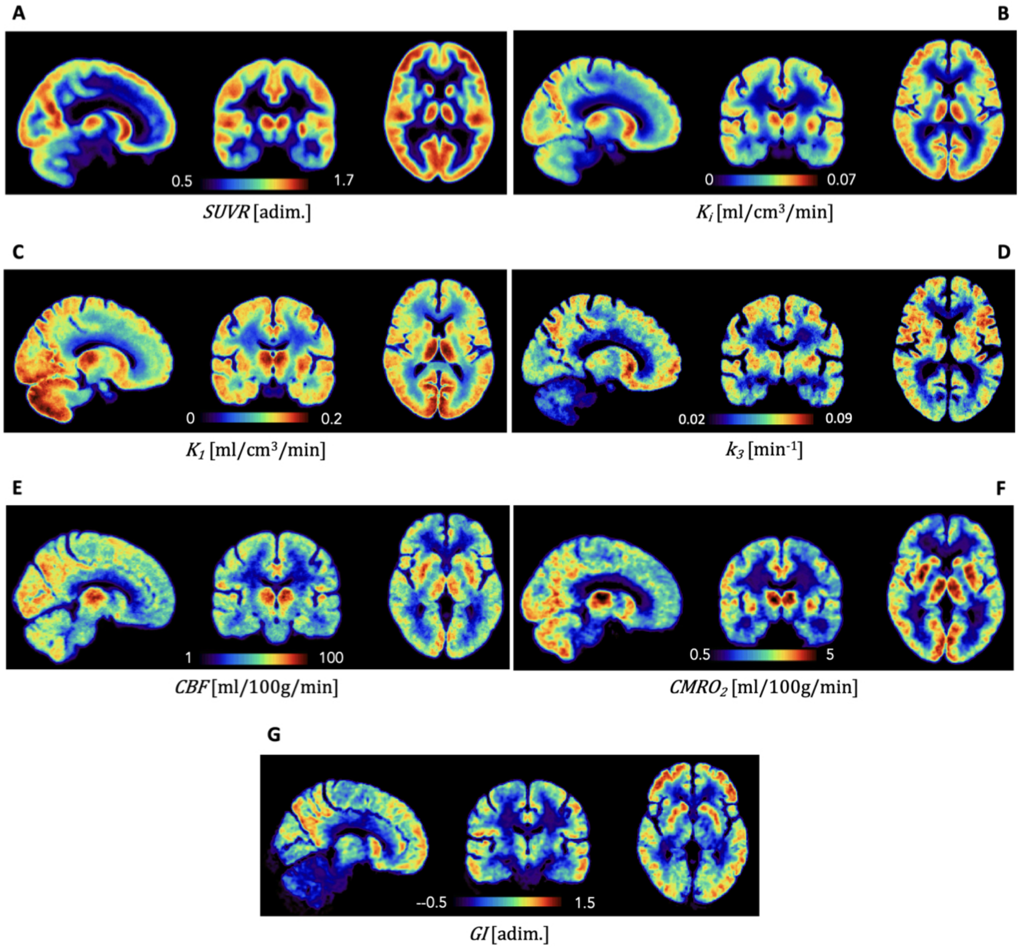

Figure 5.1: Group-average parametric maps (n = 47) for [18F]FDG $SUVR$ (A), K_i (B), K_1 (C), k_3 (D), [15O]H_2O-derived CBF (E), [15O]O_2-derived $CMRO_2$ (F), and GI (G).

5.2.6 Assessing the reproducibility of the $SUVR$-fMRI associations

First, we assessed similarities and differences between the new dataset (labelled as 'Dataset B') and the one described in chapter 4 ('Dataset A'), which are age-matched (A: 59.8 ± 10.9 yo, B: 57.4 ± 14.8 yo) and identically preprocessed for what concerns [18F]FDG $SUVR$ and rs-fMRI features. Only the 200 cortical regions of the Schaefer atlas were considered in this reproducibility study, in order to have direct comparability (subcortical regions are defined in slightly different ways in the two datasets).

Reproducibility of $SUVR$ and rs-fMRI features

The [18F]FDG $SUVR$ and each of the 50 rs-fMRI features from Dataset B

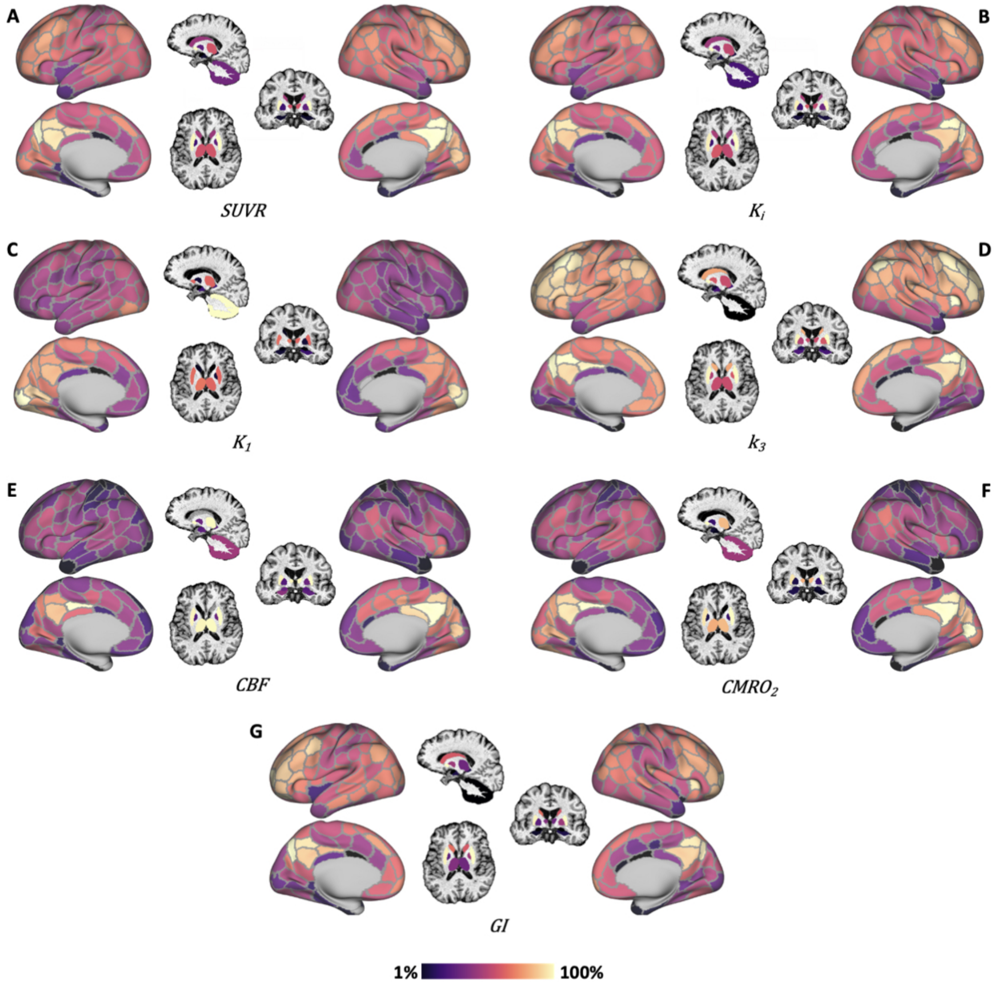

Figure 5.2: Group-average (n = 47) [^{18}F]FDG $SUVR$ (A), K_i (B), K_1 (C), k_3 (D), CBF (E), $CMRO_2$ (F), and GI (G) regional values plotted on the Schaefer cortical parcels and subcortex, and rescaled to the 1-100% relative range.

were correlated with their equivalent from Dataset A (Spearman's ρ correlation, $p < 0.05$). With regard to the 50 rs-fMRI features, the correlation p-values were FDR-corrected using the Benjamini-Hochberg approach (Benjamini and Hochberg 1995). The linear regression between $SUVR$ of Dataset A vs. Dataset B was used to assess the percentage of variance of $SUVR$ – A explained by $SUVR$ – B (ordinary R^2). The difference in amplitude of $SUVR$ values between the ROIs of Dataset A and Dataset B was assessed via the Wilcoxon rank sum test ($p < 0.05$), while the differences in $SUVR$ variability (expressed as MAD) were evaluated via the Brown-Forsythe test ($p < 0.05$) (Brown and Forsythe 1974). Outliers were identified in the $SUVR$ values of Dataset A and Dataset B, as nodes with values distant from the median $SUVR$ by more than

3 MADs), and divided into positive (above the median) and negative (below the median). The Spearman's correlation matrix among rs-fMRI features was also calculated and compared between the two datasets.

Reproducibility of bivariate $SUVR$-fMRI associations

Bivariate Spearman's correlations ($p < 0.05$, FDR-corrected) were computed across cortical regions between $SUVR$ and each of the 50 rs-fMRI features for both datasets. The similarity between the patterns of $SUVR$-fMRI Spearman's correlations from the two datasets was also assessed via Spearman's correlation ($p < 0.05$). $SUVR$-fMRI Spearman's correlations ($p < 0.05$, FDR-corrected) were also tested across nodes selected according to linearly increasing percentiles (from 1^{st} to 85^{th}) of the $SUVR$ distribution, as well as to decreasing percentiles (from 100^{th} to 15^{th}) (see chapter 4.2.4) for a more detailed description of this approach).

Model selection was performed both in Dataset A and B to compare a linear vs. nonlinear (exponential, power law) description of the $SUVR$ vs rs-fMRI bivariate spatial relationships. The differences in RSS between the linear model and both the power (Equation 4.6) and exponential model (Equation 4.5) were percentualized and used for model selection: in case of positive ΔRSS_1 and ΔRSS_2 values, a power law or exponential model, respectively, describes the data better than a linear model.

Reproducibility of multivariable MLM outcomes

Moving to the multivariable modelling scenario at the group-average level (i.e., taking the across-subject median of each feature), a logarithmic transformation of the fMRI predictors (*log-linear model*) was performed (see chapter 4.2.5). We first compared the ordinary R^2 of the multivariable model built using 1) *all* 50 rs-fMRI predictors, and 2) the 9 previously selected rs-fMRI features, in the two datasets. Then, we used the same 9 features in a full MLM framework (see chapter 4) for details). Both the MLM with *subjects* and the one with *networks* as random/grouping factors were tested. The fixed effects with their weights, signs, and SEs, the correlation amongst the random effects, the individual and NPD model R^2, and the Gaussianity of the residuals were evaluated for Dataset A and B in both cases.

5.2.7 The spatial distribution of [^{18}F]FDG parameters

To investigate the spatial distribution and regional variability of K_i, K_1 and k_3, the group-average vectors of the z-scored K_i, K_1 and k_3 values were obtained. The top and bottom 20% values of each vector were identified as 'high' and 'low' clusters of the related parameters. These parcels were visualized on the cortex and subcortex. The percentage of 'top' and 'bottom' nodes belonging to each RSN was also computed.

Across-*region* Spearman's correlations ($p < 0.05$) between the group-average parameters (z-scored) were computed, as were the linear regression models between K_i and the two microparameters K_1 and k_3. The models' weighted residuals (WRES) were plotted to assess the presence of regional mismatches, showing only the values exceeding the [-1; 1] range.

Across-*subject* Spearman's correlations ($p < 0.05$, FDR-corrected) between each pair of [^{18}F]FDG parameters were also calculated region by region (after within-subject z-scoring); the average and variability (median $\pm$ MAD) of the absolute values of these correlations were computed, after Fisher r-to-z transformation, as indices of the overall strength of association across brain regions.

Similarly, group-average GI was related to K_i, K_1 and k_3 via 1) group-average across-region Spearman's correlation ($p < 0.05$), 2) linear regression model by plotting the WRES, 3) region-wise across-subject correlations (Spearman's, $p < 0.05$, FDR-corrected) and their median $\pm$ MAD absolute value.

5.2.8 Bivariate and multivariable [^{18}F]FDG vs. rs-fMRI analysis

Bivariate across-*region* Spearman's correlations ($p < 0.05$, FDR-corrected) between [^{18}F]FDG kinetic parameters and rs-fMRI features were calculated across regions. The average and variability (median $\pm$ MAD) of the correlation absolute values were computed, after Fisher r-to-z transformation, as indices of the overall strength of association across fMRI variables. The differences among [^{18}F]FDG kinetic parameters in the amplitude of their correlation with rs-fMRI features were assessed via the Wilcoxon rank sum test ($p < 0.05$), while differences in variability were evaluated via the Brown-Forsythe test, ($p < 0.05$). Spearman's correlations ($p < 0.05$, FDR-corrected) were also tested across nodes selected according to linearly increasing percentiles (from 1^{st} to 85^{th}) of the K_i, K_1 and k_3 distribution, as well as to decreasing percentiles (from 100^{th} to 15^{th}).

Model selection was performed to compare a linear vs. nonlinear (exponential, power law) description of the bivariate spatial relationships between rs-fMRI and [^{18}F]FDG K_i, K_1 and k_3. The differences in RSS of the linear vs. power (ΔRSS_1), and linear vs. exponential model (ΔRSS_2) were percentualized and used for model selection as previously described.

Across-*subject* Spearman's correlations ($p < 0.05$, FDR-corrected) between [^{18}F]FDG parameters and rs-fMRI features were computed region by region (after within-subject z-scoring). The number of regions with significant [^{18}F]FDG-fMRI associations was calculated for each feature.

Multivariable modelling was performed at the group-average level with log-transformed rs-fMRI features as predictors, and each [^{18}F]FDG kinetic parameter (K_i, K_1 and k_3) as outcome, separately.

Two different feature selection strategies (chapter 4.2.5) were tested:

- sign-constrained NNLS followed by elastic net regression;
- sign-constrained NNLS followed by GETS modelling;

and compared in terms of 1) number of selected features; 2) condition number $\kappa(X)$ of the design matrix after selection; 3) ordinary R^2; 4) BIC; 5) RSS; 6) parameter precision (CVs%); 7) signs of the estimated coefficients. We opted for the more parsimonious NNLS+GETS approach, and only its results are therefore presented.

A full MLM approach, using the features selected in the previous step, was employed to explain the spatial distribution of K_i, K_1 and k_3, with *subjects* as the grouping factor. The fixed effects θ_S with their weights, signs, and SEs, the correlation amongst the random effects η_{Si}, the individual and NPD model R^2, and the Gaussianity of the residuals v_{Si} were evaluated. We refer to chapter 4.2.6) for further details. The individual-level R^2 were tested for association with the subjects' age (Spearman's correlation, $p < 0.05$). The group average of each model's v_{Si} was computed and standardized to the variance of the outcomes (i.e., K_i, K_1 and k_3) to make it comparable to other explanatory models of the same outcome parameter. The average of v_{Si} were plotted on the brain cortex and subcortex, highlighting the regions outside the [-1;1] range to verify which regions are strong outliers not fully interpreted by the chosen rs-fMRI features.

5.2.9 Including CBF and $CMRO_2$ in the [^{18}F]FDG-fMRI model

Bivariate across-*region* Spearman's correlations ($p < 0.05$, FDR-corrected) between group-average CBF, $CMRO_2$, and the [^{18}F]FDG kinetic parameters were calculated, as well as with the 50 rs-fMRI features ($p < 0.05$, FDR-corrected).
Across-*subject* Spearman's correlations ($p < 0.05$, FDR-corrected) between [^{18}F]FDG parameters and CBF, $CMRO_2$ were computed region by region; the average and variability (median ± MAD) of the correlation absolute values were computed, after Fisher r-to-z transformation. The number of regions with significant CBF vs. [^{18}F]FDG or $CMRO_2$ vs. [^{18}F]FDG associations was calculated.
Addition of CBF or $CMRO_2$ to the group-level multivariable model, with the previously selected rs-fMRI features, was tested and assessed according to the aforementioned criteria. Addition of CBF or $CMRO_2$ to the full MLM framework for K_i, K_1 and k_3 was also tested. The fixed effects, the correlation amongst the random effects, the individual and NPD model R^2, and the Gaussianity of the residuals were evaluated. As before, the group average of each model's v_{Si} was standardized to the variance of the outcomes (i.e., K_i, K_1 and k_3), to make it comparable to the fMRI-only model.

5.3 Results

5.3.1 The reproducibility of the $SUVR$ vs. rs-fMRI spatial model

As a first step, we moved to assess similarity and differences between the new dataset (Dataset B, 47 subjects) and the previous one (Dataset A, 26 subjects, see chapter 4), by attempting to replicate some of the key steps of our $SUVR$ vs. fMRI study. Importantly, both [^{18}F]FDG PET and rs-fMRI data were identically (pre)processed in Dataset A and B. The similarity of the findings was assessed for the 200 Schaefer cortical regions to ensure the regions were exactly the same.

Reproducibility of $SUVR$ and rs-fMRI features

To start with, we assessed the reproducibility of $SUVR$ and rs-fMRI features at the group-average level (Figure 5.3). The 50 rs-fMRI features are pooled into 4 categories, i.e., 1) signal, 2) HRF, 3) sFC, 4) tvFC, as in chapter 4.

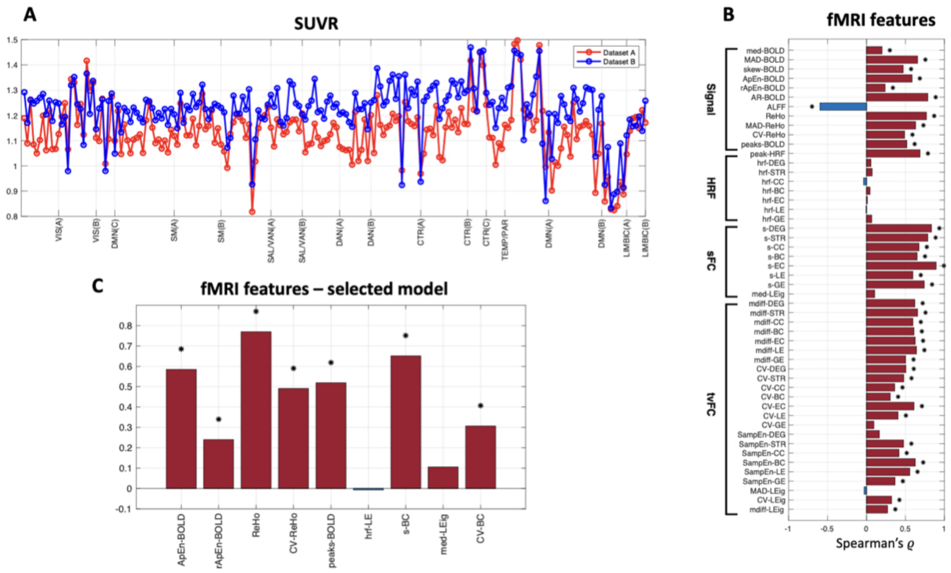

Figure 5.3: Reproducibility of group-level $SUVR$ and rs-fMRI features for the 200 Schaefer cortical regions. Plot of the group-average regional $SUVR$ values for Dataset A (red) and Dataset B (blue) (A). Spearman's correlation values between each group-average rs-fMRI feature from Dataset A vs. Dataset B. Significant correlations (p < 0.05, FDR-corrected) are highlighted with an asterisk (B). The correlation values from the features of the model selected on Dataset A are highlighted in (C).

The Spearman's correlation across regions between $SUVR$ of Dataset A and B is 0.62 ($p < 10^{-9}$), Pearson's correlation is 0.78 ($p < 10^{-9}$) with an R^2 value of 0.61. When comparing the $SUVR$ values from the two datasets (Figure 5.3A), there is overall good agreement in the relative spatial distribution, but a clear difference in amplitude, with Dataset B having higher $SUVR$ values (Wilcoxon rank sum test, $p < 10^{-9}$). Moreover, there are more high $SUVR$ nodes (positive outliers, distant from the median by more than 3 MADs) in Dataset A ($n = 11$) than in B ($n = 8$), while there are more low $SUVR$ (negative outliers, distant from the median by more than 3 MADs) in Dataset B ($n = 19$) than in A ($n = 12$).
With regard to rs-fMRI features (Figure 5.3B), we find overall good group-level reproducibility for signal, sFC and tvFC features, despite varying degrees of correlation. Interestingly, *ALFF* of Dataset B is moderately but negatively correlated with the one of Dataset A. HRF features, on the other hand, have very low reproducibility, with the exception of *peak-HRF*.
When focusing on the 9 features selected for the previously presented $SUVR$ model (chapter 4.3.3), we find good to high reproducibility (ρ 0.5) for *ApEn-BOLD*, *ReHo*, *CV-ReHo*, *peaks-BOLD*, *s-BC*. However, lower reproducibility is found for *rApEn-BOLD* and *CV-BC*, while *hrf-LE* and *med-LEig* are completely uncorrelated in the two datasets. These discrepancies are also evident when com-

paring the Spearman's correlation matrix between the 50 group-average rs-fMRI features in Dataset A and B (Figure 5.4). The correlations both within and between *signal* and *HRF* features are weaker in Dataset B. The HRF features, in particular, have a different pattern of correlations with the rest of the variables. The tvFC features have overall similar correlations in the two datasets, with the exception of the graph metrics CV% and the phase coherence-derived variables, which have weaker and stronger correlations with the rest of the variables, respectively.

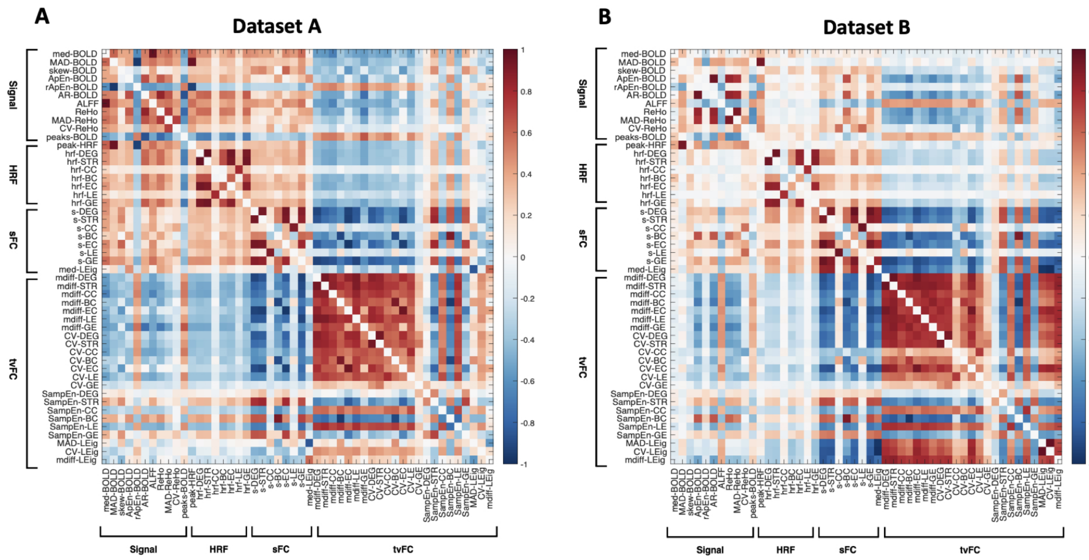

Figure 5.4: Spearman's correlation matrices among rs-fMRI features in Dataset A (A) and Dataset B (B).

<u>*Reproducibility of bivariate SUVR-fMRI associations*</u>

We then moved to evaluate the associations between group-level $SUVR$ and rs-fMRI features in the two datasets.

We first evaluated Spearman's correlations (p $<$ 0.05, FDR-corrected) across all 200 cortical regions (Figure 5.5A): the pattern of correlations in the two datasets is very similar (Spearman's correlation 0.88, p $< 10^{-9}$), but their amplitude is different in some cases. In Dataset B we find stronger positive and negative correlations in the signal and tvFC pools, in particular. The HRF pool, as seen in the previous paragraph, is markedly different in the two datasets: the moderate positive correlations with $SUVR$ in Dataset A are missing in Dataset B (again, with the exception of *peak-HRF*).

Then, we assessed $SUVR$-fMRI Spearman's correlations (FDR-corrected, $p < 0.05$) across nodes selected according to increasing (from 1^{st} to 85^{th}) as well as decreasing percentiles (from 100^{th} to 15^{th}) of the $SUVR$ distribution: this is to verify whether the $SUVR$-fMRI coupling is stronger in lower $SUVR$ nodes, as already demonstrated in Dataset A (chapter 4.3.2). We replicated our previous findings that the strongest spatial correlations between $SUVR$ and rs-fMRI tend to emerge when high $SUVR$ nodes are removed, i.e., when moving to the left, away from the centerline in both matrices of (Figure 5.5B). HRF features are again uncorrelated with $SUVR$ across all percentiles in Dataset B, while even stronger correlations emerge for signal-related (see *ApEn-BOLD*, *ReHo*, *peaks-BOLD*) and tvFC features (including the block of phase coherence measures).
Finally, we performed model selection for both Dataset A and B to assess whether a linear or nonlinear (exponential, power law) model would better describe the $SUVR$ vs rs-fMRI bivariate spatial relationships across cortical regions. The model selection procedure was performed by evaluating the difference in residual sum of squares between the linear model and both the power (ΔRSS_1) and exponential model (ΔRSS_2). In 70% of the cases for Dataset B (80% for Dataset A), positive ΔRSS_1 and ΔRSS_2 values are detected, representing the cases when the nonlinear models describe the data better than the linear. This confirms a tendency towards nonlinearity in the $SUVR$ vs. rs-fMRI bivariate associations.

Reproducibility of multivariable MLM outcomes

We finally moved to the multivariable modelling scenario, testing how well the linear combination of rs-fMRI features could explain the regional $SUVR$ variability, both at the group level and in individual data, after logarithmic transformation of the predictors (log-linear model).
First, we checked the R^2 of the multivariable model built using *all* 50 rs-fMRI predictors at group level, which is 0.675 for Dataset A, and 0.84 for Dataset B. This would imply that, in the case of Dataset B, either the rs-fMRI features have more overall explanatory power, or the group-wise $SUVR$ variability is lower. However, there was no significant difference in $SUVR$ variability between Dataset A and B (Brown-Forsythe test, $p = 0.407$), which leads to think that indeed the rs-fMRI variables may be more informative.
When the 9 previously selected rs-fMRI features were used as predictors, the R^2 of the group level multivariable model becomes 0.70 for the Dataset B, while it is 0.48 for Dataset A, again with a marked difference in explanatory power (Figure

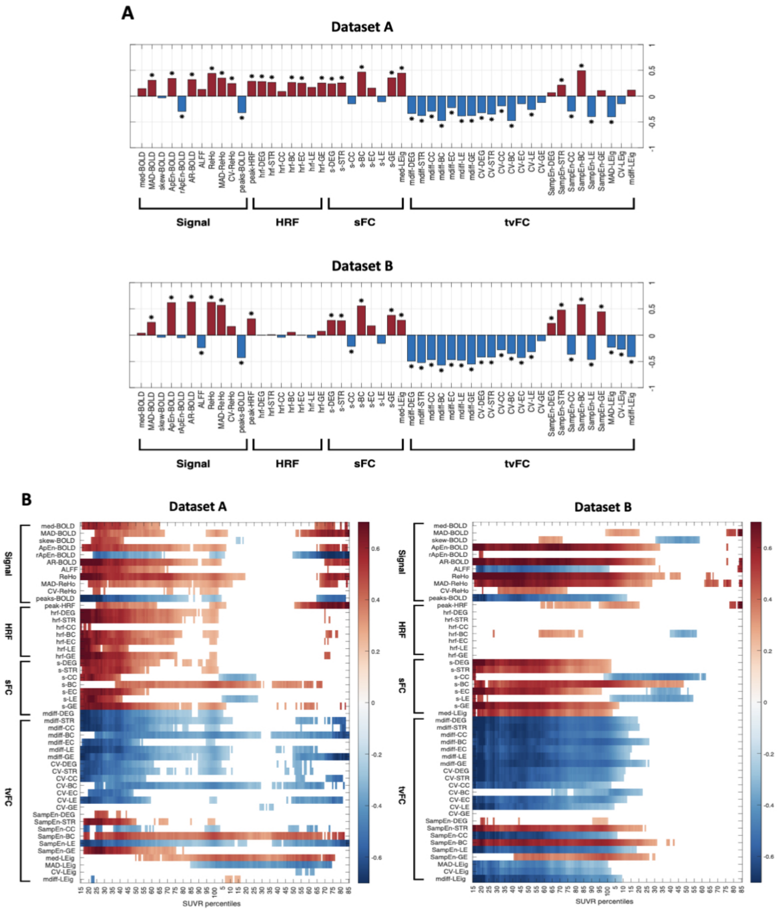

Figure 5.5: Bivariate Spearman's correlations between group-average $SUVR$ and rs-fMRI features assessed in Dataset A and B: correlations ($p < 0.05$, FDR-corrected) are assessed both across all cortical regions (A), and across nodes selected according to increasing and decreasing percentiles of the $SUVR$ distribution (B).

5.6A).

When the same features were included in the full MLM, the NPD R^2 was 0.25 for Dataset A, and 0.35 for Dataset B. In Dataset B, the model is therefore able to explain more of the $SUVR$ information across all individual data. When looking at the the fixed effects (Figure 5.6B), we can appreciate that *ReHo* clearly has the highest weight in both datasets; most other features maintain similar roles, with the exception of *CV-BC* (which changes its sign) and *rApEn-BOLD* (which becomes non-significant in Dataset B).

We also assessed how the MLM changes when the grouping factor is chosen to be the RSN: in this case, the NPD R^2 is 0.145 for Dataset A, and 0.148 for Dataset B, thus demonstrating poor explanatory power in both datasets. Among the fixed effects (Figure 5.6C), *ReHo* is again quite important in both datasets, but in the case of Dataset B many parameters become non-significant (*rApEn-BOLD*, *CV-ReHo*, *hrf-LE*, *med-LEig*).

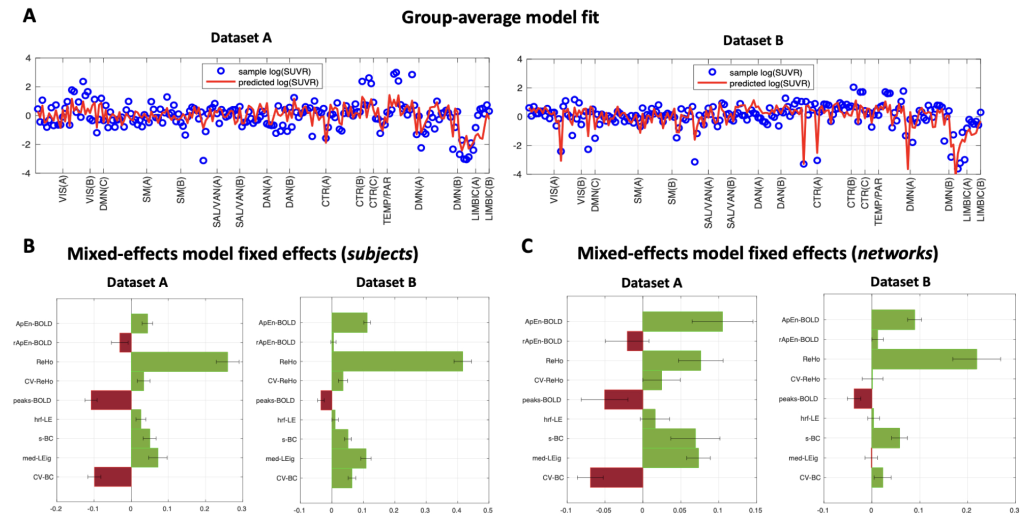

Figure 5.6: Assessment of the multivariable multilevel log-linear model, using the 9 fMRI predictors selected on Dataset A: model fit of group-average $SUVR$ (A), fixed effects (and their SEs) for the MLM with *subjects* as the grouping factor (B) and with *networks* as the grouping factor (C).

5.3.2 The spatial distribution of [18F]FDG uptake rate, delivery and phosphorylation

We then moved to the kinetic model parameters estimated from [18F]FDG dynamic data, i.e., K_i, K_1 and k_3. We decided to assess their spatial distribution and regional variability across the chosen parcellation, to better understand where they map in the brain and which additional and unique information they can provide.

First, we looked at the parcels representing the top and bottom 20% values of the averaged z-score maps of K_i, K_1 and k_3 (Figure 5.7), as well as which fMRI-based RSNs these nodes fall into.

Both K_i and k_3 have many top nodes in lateral prefrontal areas (CTR(A), CTR(B)), inferior parietal and posteromedial cortex (DMN(A)), while K_1 has mainly a strong distribution of top posteromedial nodes in both DMN and VIS networks, but also in the medial sensorimotor areas (SM(A)). When looking at the bottom nodes, limbic areas, both at the level of the temporal poles and anterior cingulate cortex, are represented for all three parameters; however, k_3 has strong presence of bottom nodes in the visual cortex, and presents additional low

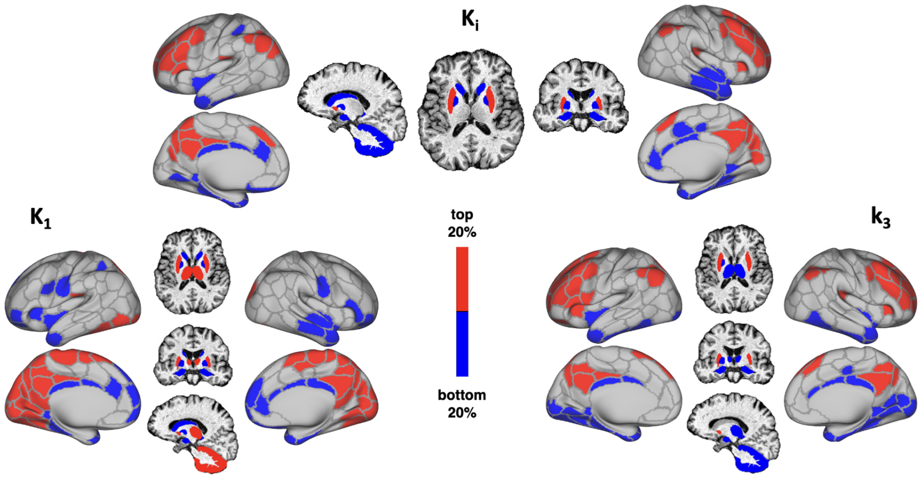

Figure 5.7: Binary representation of top (*red*) and bottom (*blue*) 20% weights of the group-average maps of K_i, K_1 and k_3.

nodes in the frontal cortex (both motor and cognitive areas) and insula. When focusing on the subcortex, we again find a similar pattern for K_i and k_3, with the putamen as a top parcel, and cerebellum as a bottom one. However, the caudates are bottom nodes only for K_i, and the thalamus is for k_3. In the case of K_1, we find agreement in the putamina, which are top parcels, and the caudate, which is a bottom node like in the case of K_i; the thalamus and cerebellum are instead among the top regions.

Also, when partitioning brain functional RSNs into *extrinsic* (VIS, SMN) vs. *intrinsic* (DMN, CTR), which respectively indicate lower order sensorimotor areas vs. higher order cognitive regions (Doucet et al. 2011), another marked distinction between K_1 and k_3 emerges: while K_1 is significantly higher in extrinsic RSNs (Wilcoxon rank sum, p = 4.2 10^{-4}), k_3 is higher in intrinsic RSNs (Wilcoxon rank sum, p = 2.1 10^{-4}), as is K_i, albeit with lower significance (Wilcoxon rank sum, p = 0.01).

The *spatial* correlations (Spearman's ρ) between the group-average [^{18}F]FDG parameters (z-scored) across the chosen parcellation are as follows:

- K_i vs. K_1: $\rho = 0.489$ (p $< 10^{-9}$);
- K_i vs. k_3: $\rho = 0.809$ (p $< 10^{-9}$);
- K_1 vs. k_3: $\rho = 0.151$ (p = 0.026);

To better quantify the extent of the regional mismatch between the macroparameter K_i and the microparameters K_1 and k_3, we plotted the WRES of the two linear regression models (K_1 or k_3 as predictor, K_i as outcome), by showing only the positive or negative residual values exceeding the [-1; 1] range, to emphasize the strongest distances from K_i (Figure 5.8).

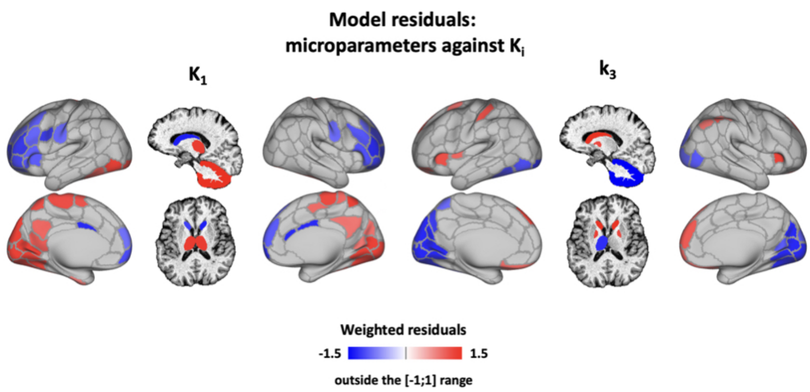

Figure 5.8: Weighted residuals of the linear regression of group-average K_1 (*left*) and k_3 (*right*) on K_i; weighted residual values in the $[-1; 1]$ range are set to zero.

This again confirms that K_1 has very high values in posteromedial areas (motor cortex, posterior cingulate, visual cortex, thalamus and cerebellum), while it fails to follow the high K_i values in lateral frontal areas and caudate nuclei. As to k_3, it has markedly lower values in visual cortex and cerebellum than expected by K_i, but also in thalamus; instead k_3 values exceed K_i mainly in the caudate nuclei, but also in insular and lateral cortical areas. This shows that, although K_i and k_3 are highly correlated at group level, there is an interesting spatial distribution that makes the quantification of k_3 non-redundant.
We also assessed the across-*subject* correlations (Spearman's ρ) amongst the [^{18}F]FDG parameters region by region (Figure 5.9). The correlations of K_i with the microparameters are moderate to high, both for K_i-K_1 (median $\pm$ MAD of absolute ρ values: 0.561 $\pm$ 0.089) and K_i-k_3 (0.636 $\pm$ 0.078). The microparameters, instead, are overall uncorrelated with one another (K_1-k_3: 0.128 $\pm$ 0.109).

Finally, we also had the possibility to evaluate how indices of aerobic glycolysis (e.g., GI) could map onto the [^{18}F]FDG kinetic parameters, which represent the overall glucose metabolism, both *oxidative* and *glycolytic*.
The Spearman's correlations between group-average GI and K_i, K_1 and k_3 are 0.78 ($p < 10^{-9}$), 0.185 ($p = 0.006$) and 0.828 ($p < 10^{-9}$), respectively ($R^2 = 0.746$ for K_i, 0.07 for K_1, 0.795 for k_3). The WRES of the linear regression between GI and k_3 show how the glycolytic index exceeds what predicted by k_3 in regions of the peripheral VIS and DMN networks, as well as in the putamen; instead the k_3 overestimates GI in regions of SMN, SAL e CTR.

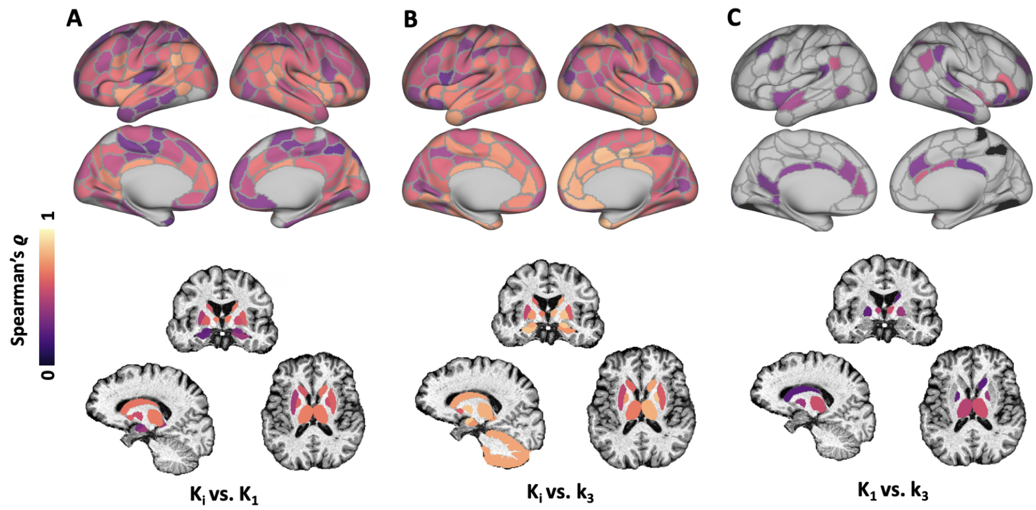

Figure 5.9: Across-subject Spearman's correlations ($p < 0.05$, FDR-corrected) between [^{18}F]FDG parameters (K_i, K_1 and k_3) assessed region by region

As to region-wise across-subject correlations (Spearman's ρ, $p < 0.05$ FDR-corrected), K_1-*GI* associations (median $\pm$ MAD of absolute ρ values: 0.353 ± 0.122) peak in DMN and caudate, while k_3-GI associations are high in DMN, VIS, SAL, and most subcortical regions (0.513 ± 0.103).

5.3.3 The different fMRI-based models for [^{18}F]FDG K_i, K_1 and k_3

Bivariate associations with rs-fMRI

The Spearman's correlations ($p < 0.05$, FDR-corrected) between group-average [^{18}F]FDG kinetic parameters and rs-fMRI features are presented in Figure 5.10. In the signal pool, moderate-to-strong positive or negative correlations are present for K_i and k_3 with *ALFF*, *ReHo* and its variability, and *peaks-BOLD*, while K_1 shows weaker coupling with these features related to rs-fMRI local properties. Notably, *peak-HRF*, which represents a blood flow-related information, is significantly, though weakly correlated with K_1 and K_i, but not with k_3. Moreover, the HRF network features are only related to K_1, while they lack any significant associations with K_i and k_3. Interestingly, all sFC measures display significant associations with K_1, but not with k_3, while K_i presents a mixed situation, as expected. Finally, in the case of the tvFC pool, the pattern of correlations is similar for the three [^{18}F]FDG parameters, albeit with stronger correlations for K_i. When assessing the absolute values of correlations (median $\pm$ MAD), K_i (0.328 $\pm$ 0.158) and K_1 (0.339 $\pm$ 0.074) have similar magnitudes, while k_3 (0.229 $\pm$

0.137) has significantly lower correlations with rs-fMRI features (Wilcoxon rank sum test, p = 0.008). However, K_i and K_1 correlation distributions have different dispersion (Brown-Forsythe test, p = 0.002).

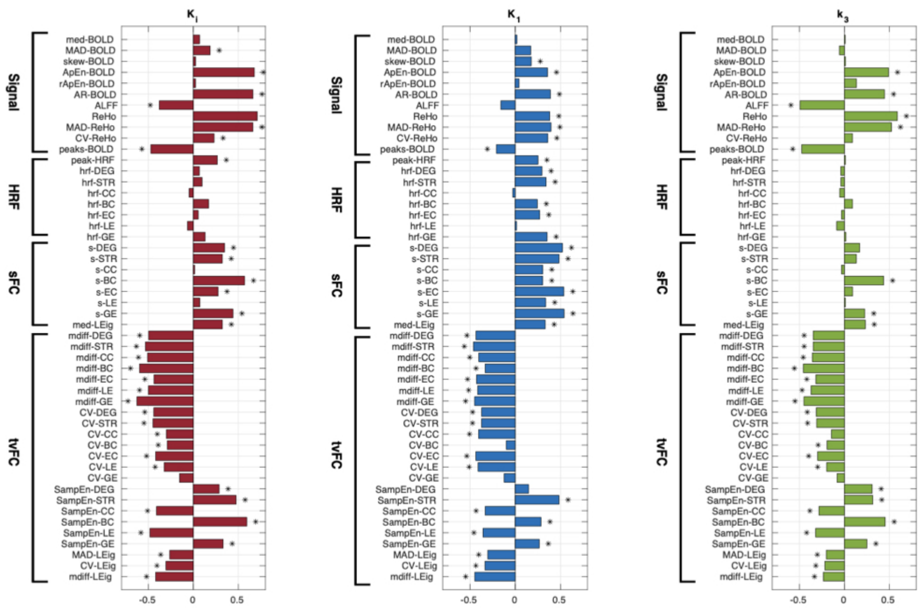

Figure 5.10: Spearman's correlations ($p < 0.05$, FDR-corrected) between group-average [18F]FDG parameters (K_i, K_1 and k_3) and rs-fMRI features across all brain regions.

Then we reassessed [18F]FDG-fMRI Spearman's correlations ($p < 0.05$, FDR-corrected) across nodes selected according to linearly increasing (from 1^{st} to 85^{th}) as well as decreasing (from 100^{th} to 15^{th}) percentiles of each parameter's distribution (K_i, K_1 and k_3: this was done to expand our finding that the $SUVR$-fMRI coupling is stronger in lower $SUVR$ nodes (see chapter 4 and Figure 5.5B).
The $SUVR$ pattern is faithfully reproduced by K_i, with strong and significant correlations mainly in the left portion of the matrix (Figure 5.11, *left panel*), linearly decreasing percentiles of K_i, i.e., after removing more and more high K_i nodes). A similar, although noticeably weaker, pattern of correlations emerges for k_3 (Figure 5.11, *right panel*), while K_1 is enriched by significant correlations with $ALFF$ and CBF-related features (*MAD-BOLD*, *peak-HRF*) in the high-K_1 area, i.e., on the right of the K_1 matrix (Figure 5.11, *middle panel*), as well as with the other HRF features. Overall, this is a confirmation that a nonlinearity exists in the relationship between [18F]FDG kinetic parameters and rs-fMRI features across brain regions.
So, we again performed model selection to assess whether a linear, exponential, or power law model would best describe the bivariate spatial relationships between

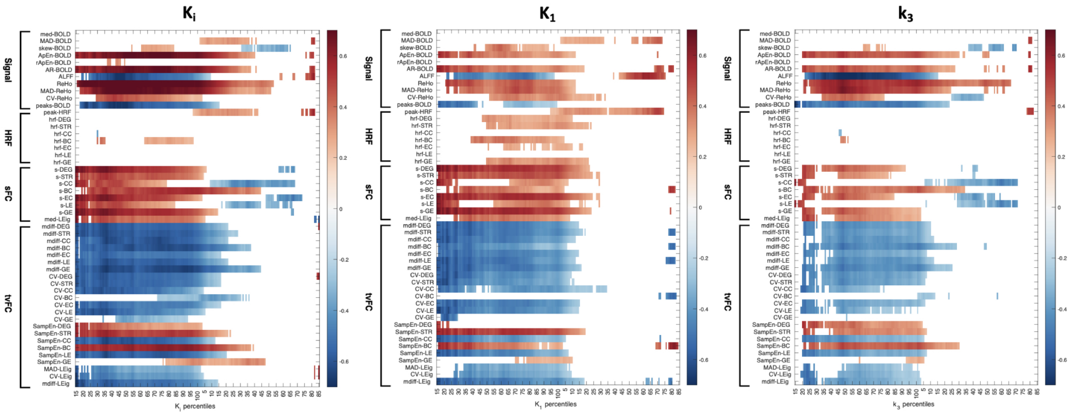

Figure 5.11: Spearman's correlations (FDR-corrected) between group-average [^{18}F]FDG parameters (K_i, K_1 and k_3) and rs-fMRI features across brain regions selected by linearly increasing and decreasing percentiles of the corresponding [^{18}F]FDG parameters.

group-average [^{18}F]FDG kinetic parameters and rs-fMRI features (Figure 5.12). The model selection procedure was performed by evaluating the percentualized differences in RSS between the linear model and both the power (ΔRSS_1) and exponential model (ΔRSS_2). The positive ΔRSS_1 and ΔRSS_2 values (%) are shown in Figure 5.12A for K_i (left), K_1 (middle), and k_3 (right): the nonlinear models describe the data better than the linear in 48% of the cases for K_i, 56% for K_1, and 54% for k_3 (Figure 5.12B). This confirms a tendency towards nonlinearity in the [^{18}F]FDG vs. rs-fMRI bivariate associations in around half of the features, with the strongest nonlinear (power law) associations coming from the sFC and tvFC pools. For this reason, we employed a nonlinear (log) transformation of all the features, as in chapter 4.

Multivariable modelling at group level

We then moved to evaluating which combinations of rs-fMRI features could best explain the regional variability of K_i, K_1 and k_3. Using a more restrictive feature selection approach (NNLS + GETS modelling) than in chapter 4, motivated by the higher condition number of the predictors' design matrix ($\kappa(X) = 107.98$), we reached the following log-linear multivariable models:

- for group-average K_i: $R^2 = 0.724$, with 6 chosen fMRI features (*ApEn-BOLD*, *ReHo*, *CV-ReHo*, *CV-BC*, *SampEn-GE*, *MAD-LEig*);

- for group-average K_1: $R^2 = 0.386$, with 4 chosen fMRI features (*AR-BOLD*, *s-EC*, *CV-BC*, *SampEn-GE*);

- for group-average k_3: $R^2 = 0.509$, with 4 chosen fMRI features (*ReHo*, *s-LE*,

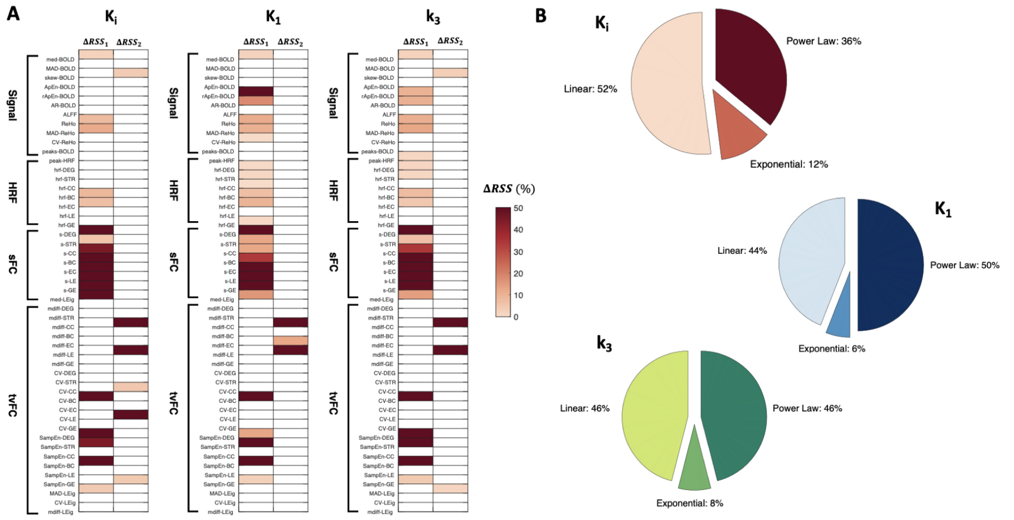

Figure 5.12: Assessment of nonlinearities in the bivariate associations between [18F]FDG parameters (K_i, K_1 and k_3) and rs-fMRI features: percentualized differences between linear and power model (ΔRSS_1) and between linear and exponential model (ΔRSS_2) for each rs-fMRI feature (A), and pie chart with the percentage of features (out of 50) whose association with each [18F]FDG parameter is best described by a linear, exponential, or power law model (B).

CV-BC, *SampEn-GE*).

All parameter estimates had acceptable precision (CVs $< 100\%$). Interestingly, *CV-BC* and *SampEn-GE* are selected in all three cases, while *ReHo* is a chosen features for both K_i and k_3.

Full mixed-effects modelling

The full MLM approach (Figure 5.13) with the features selected in the previous step allowed to explain a significant proportion of subject-level variability in the spatial distribution of K_i (NPD $R^2 = 0.35$), but less so in the case of K_1 (NPD $R^2 = 0.147$) and k_3 (NPD $R^2 = 0.19$). Overall, our finding that there is high between-subject variability in individual R^2 values for $SUVR$ is also confirmed here for K_i, K_1 and k_3 (Figure 5.13C). The individual R^2 do not correlate significantly with subjects' age for any of the parameters ($p > 0.05$). *AR-BOLD* (a parameter describing the autocorrelation structure of the rs-fMRI signal), which has a positive weight in the group-level model of K_1 (0.31), inverts its sign in the full MLM. *ReHo* is confirmed as the most important explanatory parameter in the case of K_i and k_3 (Figure 5.13A). Importantly, at the group-average level, *ReHo* explains a large proportion of variance for both K_i ($R^2 = 0.552$) and k_3 ($R^2 = 0.407$). If we recompute the MLM estimates using only *ReHo* as a predictor, we obtain a NPD R^2 of 0.302 for K_i, and 0.177 for k_3: this implies that, for these two parameters, *ReHo* explains the vast majority of the variance in the multivariable model.

If we look at the group average of the model residuals v_{Si}, focusing on the regions outside the [-1;1] range (Figure 5.13B), we can see that they still bear significant resemblance to the top and bottom 20% regions of each parameter (Figure 5.7): this implies that the high and low outlier nodes are not well interpreted by the chosen rs-fMRI features. This is true especially for K_1, which shows high residual values (> 2) in posteromedial cortex and cerebellum, but also for K_i and k_3, with high values in the putamina and low ($<$ -2) in the cerebellum.

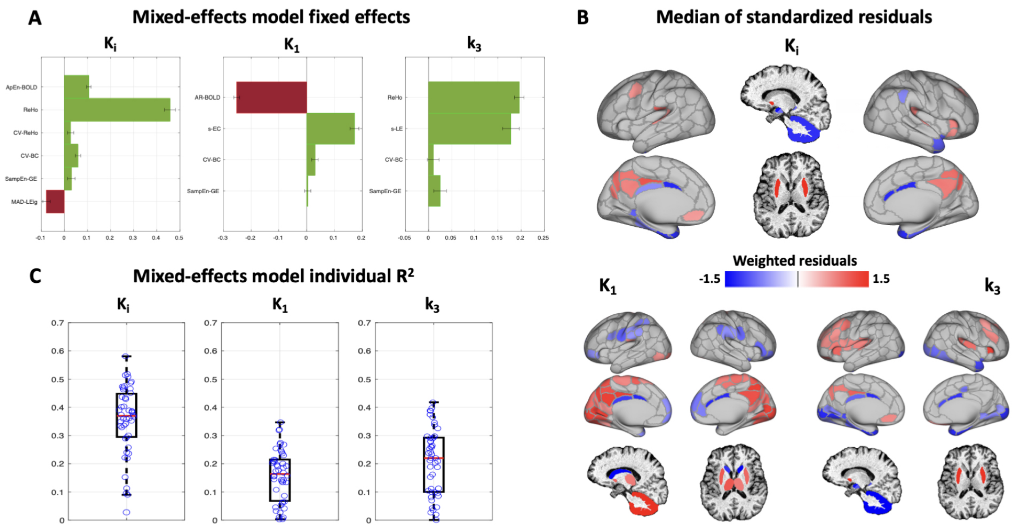

Figure 5.13: Assessment of the fMRI-based MLM results for the [^{18}F]FDG parameters (K_i, K_1 and k_3): fixed effects and their SE (A), group average of the standardized residuals (values outside the $[-1;1]$ range are shown) (B), and boxplots of the individual subjects' R^2 (C), for each [^{18}F]FDG parameter.

5.3.4 The role of CBF and $CMRO_2$ in the [^{18}F]FDG vs. fMRI model

Bivariate associations with CBF and $CMRO_2$

We finally moved to evaluating the impact of including PET-derived estimates of CBF and $CMRO_2$ into the fMRI-based models explaining the regional variability of [^{18}F]FDG kinetic parameters.

The spatial correlation (Spearman's ρ) of group-average CBF vs. $CMRO_2$ is 0.857 ($p < 10^{-9}$). The group-average spatial correlations (Spearman's ρ) with the [^{18}F]FDG kinetic parameters (K_i, K_1 and k_3) are:

- for CBF, 0.362 ($p < 10^{-6}$), 0.311 ($p < 10^{-6}$), 0.175 ($p = 0.01$), respectively;

- for $CMRO_2$, 0.525 (p $< 10^{-9}$), 0.515 (p $< 10^{-9}$) and 0.204 (p $= 0.003$), respectively;

while the linear model R^2 for the same associations are:

- for CBF, 0.182, 0.147, 0.061, respectively;
- for $CMRO_2$, 0.364, 0.371, 0.105, respectively.

We thus find only moderate correlations with CBF and $CMRO_2$ when K_i and K_1 are considered, while k_3 has low correlations with both.
The group-average spatial correlations (Spearman's ρ) of CBF and $CMRO_2$ with the 50 rs-fMRI features (p < 0.05, FDR-corrected) are shown in Figure 5.14.

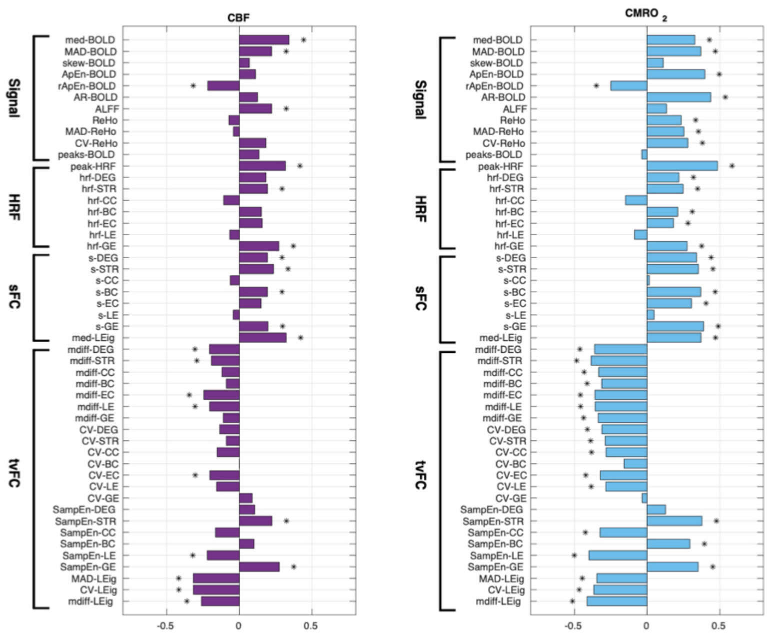

Figure 5.14: Spearman's correlations (p < 0.05, FDR-corrected) between group-average CBF (*left*), $CMRO_2$ (*right*) and rs-fMRI features across all brain regions.

Interestingly, if drawing comparisons with Figure 5.10, some key differences emerge. CBF and $CMRO_2$ are significantly correlated with *med-BOLD*, which describes the average rs-fMRI signal of each region, while [^{18}F]FDG kinetic parameters are not; also, CBF is significantly positively correlated with *ALFF*, which has negative associations with [^{18}F]FDG K_i and k_3. *ReHo* is correlated only with $CMRO_2$ (though weakly), but not with CBF. Moreover, moderate significant correlations are present between CBF, $CMRO_2$, and *MAD-BOLD* and *peak-HRF*, both blood flow-related indices (G.-R. Wu and Marinazzo 2016). Overall, correlations with the HRF and sFC pool are significant and stronger than for [^{18}F]FDG K_i and k_3, while a similar pattern is present for tvFC. Notably, the $CMRO_2$-fMRI correlations are higher (0.312 ± 0.058) than the CBF-fMRI correlations (0.174 ± 0.057), as assessed via the Wilcoxon rank sum test ($p < 10^{-6}$). We then assessed the across-subject correlations (Spearman's ρ, $p < 0.05$, FDR-corrected) between the [18F]FDG parameters and CBF, $CMRO_2$ region by region. Again, K_i and K_1 have higher and more significant correlations (K_i vs. CBF: 0.242 ± 0.117; K_1 vs. CBF: 0.198 ± 0.105; K_i vs. $CMRO_2$: 0.243 ± 0.094; K_1 vs. $CMRO_2$: 0.234 ± 0.091) with respect to k_3 (k_3 vs. CBF: 0.111 ± 0.068; k_3 vs. $CMRO_2$: 0.099 ± 0.066), as assessed via Wilcoxon rank sum test. This finding was also assessed in comparison to rs-fMRI (Figure 5.15).

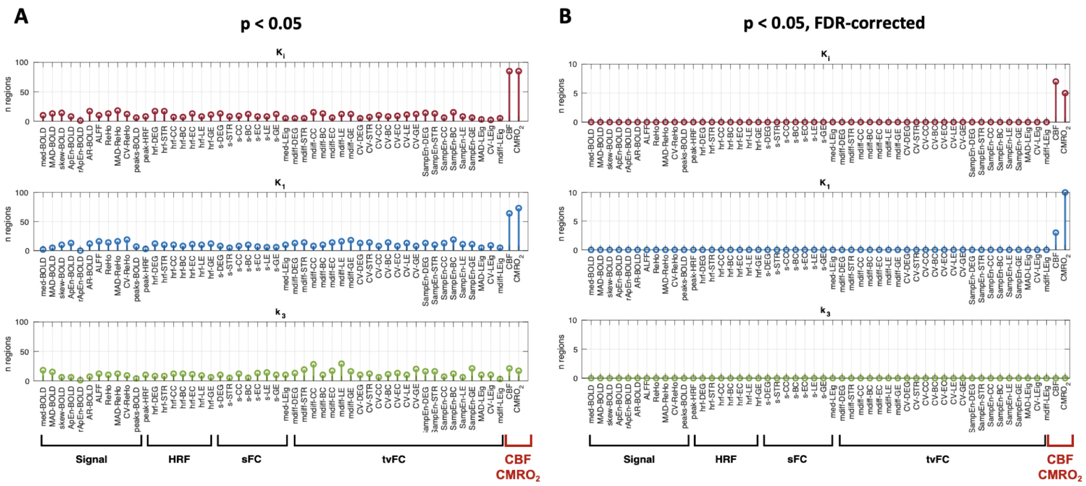

Figure 5.15: Number of significant region-wise across-subject Spearman's correlations between [18F]FDG parameters (K_i, K_1 and k_3 and rs-fMRI features (plus CBF or $CMRO_2$): $p < 0.05$, uncorrected (range of y axis: 0-100) (A) and after FDR correction (range of y axis: 0-10) (B).

In the case of across-subject correlations between rs-fMRI and [18F]FDG parameters, no regions have any significant associations ($p < 0.05$, FDR-corrected), independently of the pool to which rs-fMRI features belong, or the chosen [18F]FDG parameter (Figure 5.15B). Instead, when associations with CBF and $CMRO_2$ are considered, around 5-10 regions have significant correlations, both for K_i and K_1 (but not k_3). This trend is even clearer when considering the uncorrected results (Figure 5.15A), with a number of 50-100 regions with $p < 0.05$ only in the case of CBF, $CMRO_2$ vs. K_i and K_1 associations.

Multivariable MLM with CBF and $CMRO_2$

We conclude our assessment by including CBF or $CMRO_2$ into out multivariable modelling framework with rs-fMRI features as predictors of the spatial distribution of [18F]FDG parameters.

At group-average level, the addition of CBF increases the R^2 of K_i from 0.724

to 0.795, the R^2 of K_1 from 0.386 to 0.446, and the R^2 of k_3 from 0.509 to 0.536. Parameters' precision remains within an acceptable range (CVs < 150%). The inclusion of $CMRO_2$, on the other hand, increases the R^2 of K_i from 0.724 to 0.786, the R^2 of K_1 from 0.386 to 0.519, and the R^2 of k_3 from 0.509 to 0.514. Parameters' precision remains within an acceptable range (CVs < 150%), with the exception of *SampEn-GE* (CV = 307%), which would be eliminated from the K_1 model.

Overall, CBF and $CMRO_2$ lead to similar improvements in the K_i and k_3 models (moderate and minor, respectively). However, $CMRO_2$ importantly improves the K_1 model.

We then assessed how these improvements impact the full MLM framework.

Notably, the addition of $CMRO_2$ to the previously selected models leads to a marked increase in explained variance of the individual-level data for K_i (from a NPD R^2 of 0.35 to 0.468) and K_1 (from 0.147 to 0.268), with minor improvement also for k_3 (from 0.19 to 0.22). The individual subjects' model R^2 can be visualized in Figure 5.16C, and their improvements with respect to Figure 5.13C can be appreciated. When we look at the fixed effects, *ReHo* and $CMRO_2$ have the strongest weights in the K_i model, while in the k_3 model, *ReHo* becomes the most relevant parameter, as does $CMRO_2$ in the K_1 model (Figure 5.16A). If we look at the group average of the model residuals v_{Si}, focusing on the regions outside the [-1;1] range (Figure 5.16B), we can see the improvement in explanatory power with respect to the fMRI-only model (Figure 5.13B). This is true for K_i, which no longer shows high residual values in posteromedial cortex, as well as for K_1, with improvements in posterior DMN, thalamus and putamen.

Adding CBF, on the other hand, leads to a similar increase in explained variance of the individual-level data for K_i (R^2 = 0.456) and k_3 (R^2 = 0.245), while the benefit is lower for K_1 (R^2 = 0.222), as anticipated by the group-average multivariable modelling results.

Importantly, if we minimize the number of predictor variables, using only *ReHo* (previously shown to be the strongest rs-fMRI predictor) and $CMRO_2$, we reach a NPD R^2 of 0.434 for K_i, and 0.212 for k_3; using only *ReHo* and CBF, the NPD R^2 of K_i is 0.42, and the R^2 of k_3 is 0.202.

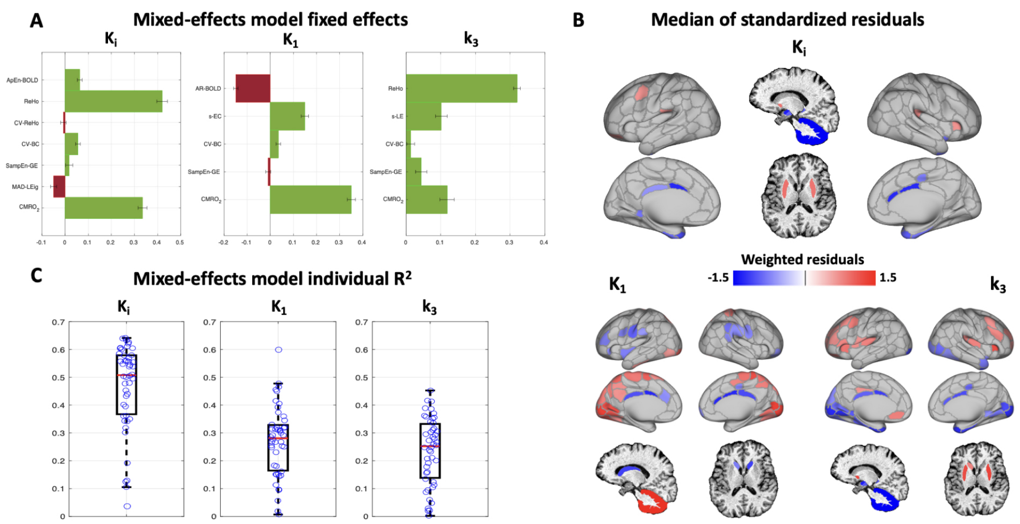

Figure 5.16: Assessment of the fMRI-based MLM results for the [^{18}F]FDG parameters (K_i, K_1 and k_3) after $CMRO_2$ is added to each set of selected rs-fMRI predictors: fixed effects and their SE (A), group average of the standardized residuals (values outside the $[-1; 1]$ range are shown) (B), and boxplots of the individual subjects' R^2 (C), for each [^{18}F]FDG parameter.

5.4 Discussion

In this work, we have evaluated the regional variability of [^{18}F]FDG kinetic model parameters (K_i, K_1 and k_3) describing different kinetic events of glucose metabolism, for the first time at a fine-grained spatial resolution. Furthermore, we have fully investigated the relationships of K_i, K_1 and k_3 with CBF and $CMRO_2$, as well as with a plethora of rs-fMRI measures of both spontaneous activity and FC, to better understand if the peculiar spatial patterns of [^{18}F]FDG K_i, K_1 and k_3 can be explained by combination of information on oxygen metabolism, blood flow, and spontaneous activity.

5.4.1 Reproducibility of $SUVR$-fMRI coupling

We started by assessing how reproducible the $SUVR$-fMRI spatial coupling, described in chapter 4 (Tommaso Volpi, Erica Silvestri, Marco Aiello, et al. 2021b), is on a new dataset.
First, it must be noted that, despite similar subject age and application of the same preprocessing pipelines, key differences in the two datasets are present, i.e., Dataset A (chapter 4) was obtained through simultaneous PET-fMRI acquisitions on a Siemens Biograph mMR scanner, while Dataset B was derived through sequential measurements (PET on a ECAT HR+ scanner, MRI on a

Siemens Prisma scanner).

With regard to $SUVR$ regional values, we found a good overall match between Dataset A and B. However, we noticed how Dataset A has lower average $SUVR$, but more high-$SUVR$ outlier nodes, while Dataset B has more low-$SUVR$ outliers. Why this is the case might be related to the different scanners and related PVEs. Further work applying region-wise partial volume correction (PVC), e.g., via the geometric transfer matrix approach (Sattarivand et al. 2012), and quantitatively assessing the spatial autocorrelation of the $SUVR$ maps (Markello and Misic 2021) will be carried out to better understand these effects.

With regard to rs-fMRI features, which underwent identical preprocessing in the two datasets, we found varying degrees of reproducibility depending on the variable under investigation.

Importantly, rs-fMRI data from the two datasets are different in terms of spatial resolution (Dataset A: voxel size = 3/4 mm iso-voxel; Dataset B: voxel size = 2.4 mm iso-voxel), sampling frequency (Dataset A: TR = 2s; Dataset B: TR = 0.8 s), and scan duration (Dataset A: 7.5/10 min; Dataset B: 5 min). This seems to have had a strong impact on HRF-related variables in particular, but also on other feature pools, such as entropy measures (e.g., *rApEn-BOLD*) and phase-based FC (e.g., *med-LEig*).

Further work is required to better understand the reasons. Possibly, the use of band-pass (instead of high-pass) filtered data might change the match with PET-derived variables. Also, averaging features across multiple EPI runs might strengthen the estimate of the features' spatial distribution, making them more similar to those of Dataset A.

When attempting to reproduce the multivariable modelling at group and individual level using the MLM framework, we found that the new rs-fMRI features had higher explanatory power (up to 70% of the $SUVR$ variance at group level). This seems to suggest that the higher quality of the rs-fMRI data in Dataset B (Prisma vs. Biograph mMR scanner) improves the match between regional glucose metabolism and BOLD-derived information, despite the acquisitions not being simultaneous. A reassessment of this relationship after PVC is, however, warranted.

5.4.2 A fine-grained assessment of [^{18}F]FDG K_i, K_1, k_3 spatial distributions

We want to point out again that this is the first time that [^{18}F]FDG kinetic parameters, in particular the microparameters (K_1 and k_3) have been obtained and studied at this level of spatial resolution. Most frequently, only $SUVR$ is employed as an index of glucose consumption; despite it being a good proxy of K_i in healthy subjects, it is both relative and semi-quantitative, and is known to be susceptible to bias for multiple technical and physiological reasons (Hamberg et al. 1994; S.-C. Huang 2000).

Only early studies in the 1980s have attempted to characterize the different spatial distributions of K_1 and k_3 (Heiss et al. 1984). Actually, there is some agreement between our results and what was described on much more coarse-grained regions (Heiss et al. 1984), e.g., on the markedly posterior distribution of K_1. However, we can find more fine-grained differences, such as in the subcortex, where the putamina are top parcels for all kinetic parameters, while the adjacent caudate appears to be among the lowest K_1 and K_i regions. At the cortical level, there does not seem to be a clear RSN hierarchy for these parameters, as previously determined for $SUVR$ (Palombit et al. 2022). High K_i and k_3 nodes are however enriched in 'intrinsic', or task-negative networks (DMN, CTR), while K_1 has many top nodes in 'extrinsic', or task-positive areas (VIS, SMN), as also previously described for *aerobic glycolysis* indices (Glasser, Goyal, et al. 2014). Limbic areas (including hippocampus and amygdala) are consistently among the bottom nodes.

We also regressed the spatial map of k_3 on K_i, to better show which additional information k_3 is providing: this showed that not only k_3 relatively underestimates K_i in visual cortex (VIS(A) and VIS(B)), cerebellum, and thalamus, but also overestimates K_i in the caudate, insular and frontoparietal cortex. Despite group-average K_i and k_3 being highly correlated across regions (0.8), k_3 is differently expressed in a series of areas, where the impact of K_1 and k_2 make K_i a biased predictor of the glucose phosphorylation events. The repercussions of these findings remain to be thoroughly understood, as these parameters have never been previously assessed in more than a handful of subjects with low-resolution PET data.

We believe the maps of [^{18}F]FDG kinetic parameters we obtained to be faithful representations of the physiological parameters' spatial distribution, at least at the group level. Despite the low spatial resolution of the HR+ scanner and high noise level in the data, the Variational Bayesian approach (Castellaro et al. 2017) is capable of retrieving accurate and precise estimates at the voxel level (provided that the input function is reliable). Of course, re-assessing these results in a more ideal framework, using a PET scanner with higher spatiotemporal resolution, will be important to assess the reproducibility of these spatial distributions and possibly capture higher detail in these maps (see preliminary results on a Biograph mMR PET/MR dataset from Padova, Figure 5.17).

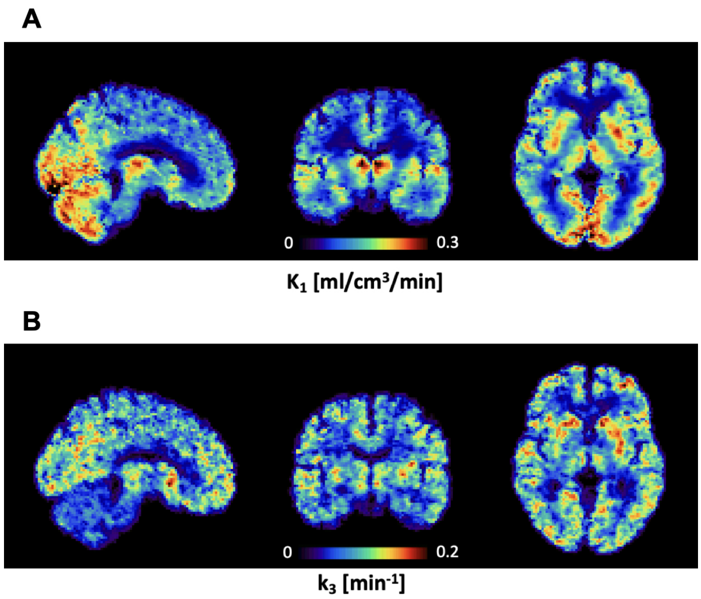

Figure 5.17: Average K_1 (A) and k_3 (B) parametric maps in a small sample of healthy subjects (n = 4) acquired on a Siemens Biograph mMR in Padova.

Different physiological drivers could be called into play to explain the peculiar spatial patterns of K_1 and k_3, which is more marked than could be naïvely expected for two putatively coupled processes (i.e., delivery and utilization of glucose). Some hypotheses might include

- the vascular distribution (K_1 has higher values in the posterior cerebral artery territory, as already noted by (Heiss et al. 1984);

- the expression of different isoforms of glucose transporters (GLUT1, mainly expressed at the BBB, and GLUT3, mainly present in neurons (Pessin and Bell 1992), but also SGLT transporters expressed almost exclusively in the cerebellum (Barrio et al. 2020)) for K_1, and of the hexokinase enzyme (HK1, HK2) for k_3, but possibly also genes related to cell proliferation (e.g., CDK2, VEGF-A (Strauss et al. 2011));

- the expression of specific gradients of histological and molecular phenotypes (Paquola et al. 2021);

- the dominance of different electrophysiological rhythms (higher vs. lower frequencies in EEG/MEG) in different brain networks (e.g. posterior dominance of the alpha rhythm).

We have started to investigate some of these possibilities, but a clear answer is still lacking.

Despite the difficulties associated with longer dynamic PET acquisitions, the microparameters might have significant importance and impact on different types of neurological and psychiatric disorders (see e.g., (Piert et al. 1996) on Alzheimer's disease; (Hermanides et al. 2021) on traumatic brain injury), and the increasingly high spatial resolution of new PET scanners (Meikle et al. 2021) will allow for more accurate assessment of specific deficits in glucose delivery (K_1) and phosphorylation (k_3). Glucose phosphorylation by hexokinase, being the rate limiting step for glucose utilization, is of particular pathophysiological relevance (Furler et al. 1991; Piert et al. 1996).

We have also studied the differences between k_3, representative of both *oxidative* and *glycolytic* metabolism, and GI, which describes only the glycolytic portion. Interestingly, the GI has a slightly stronger spatial consistency with k_3 rather than K_i (80% explained variance, against 75% for K_i), despite being the result of regressing $CMRglc$ (= scaled K_i) against $CMRO_2$. However, when across-subject correlations are tested, we find high consistency in many, but not all, brain areas.

Substituting indices of aerobic glycolysis, which require the burdensome acquisition of [^{18}F]FDG plus ^{15}O tracers, with parameters obtained by [^{18}F]FDG only (e.g., k_3) would be an interesting endeavor to pursue, but the same sensitivity to pathology and age-related changes (Goyal, Vlassenko, et al. 2017) should first be demonstrated.

5.4.3 [^{18}F]FDG uptake and phosphorylation are spatially coupled to fMRI local coherence

When we assessed the spatial relationships of [^{18}F]FDG parameters with rs-fMRI variables, we found an overall consistency with our previous findings on $SUVR$ (chapter 4):

1) variable degrees of association with rs-fMRI variables was present, with strongest match for signal-related features (Figure 5.10);

2) evidence of nonlinearity emerges from [^{18}F]FDG-fMRI correlations across clusters of nodes selected according to increasing and decreasing percentiles of each parameter (Figure 5.11), which is confirmed by linear vs. nonlinear model selection (Figure 5.12);

3) when moving to multivariable and full MLM context, we find that the top and bottom regions of each [^{18}F]FDG parameter are still difficult to interpret using only rs-fMRI features (Figure 5.13B); also, there is significant between-subject variability in the [^{18}F]FDG-fMRI spatial association (Figure 5.13C), which is not easily explainable by subject-specific covariates (e.g., age, sex).
However, there are many aspects which are peculiar this work.
First, the model R^2 are overall higher in this case than in our previous work (i.e., Dataset A), as already seen in the $SUVR$-fMRI reproducibility analysis, so the same considerations apply (fMRI data quality, higher smoothing/PVE levels in the HR+ [^{18}F]FDG data).
ReHo emerges as the rs-fMRI variable having the strongest spatial match with [^{18}F]FDG kinetic parameters, as for $SUVR$, which is also consistent with various publications (Marco Aiello et al. 2015; Nugent et al. 2015; J. Wang et al. 2021), two of which actually comparing *ReHo* to fully quantitative K_i (Bernier et al. 2017; S. Deng et al. 2022). Here, *ReHo* alone is capable of explaining 55% of K_i variance at group level, and 30% on individual subject data (for k_3: 40% at group level, 18% at individual-subject level). This confirms the moderate-to-strong spatial coupling between glucose metabolism and features of BOLD fMRI local signal coherence, as recently and thoroughly discussed by (S. Deng et al. 2022) for *ReHo* and $fALFF$; sFC and tvFC features, instead, provide much weaker contribution, especially in multivariable associations (Figure 5.10, Figure 5.13).
However, despite being remarkably reproducible (Z. Li, Kadivar, et al. 2012), *ReHo* does not escape the lack of across-*subject* (instead of across-*region*) associations between [^{18}F]FDG and rs-fMRI assessed for each region separately (Figure 5.15). This absence of across-subject coupling has already been previously reported for $SUVR$ (Marco Aiello et al. 2015; J. Wang et al. 2021). More careful assessment of [^{18}F]FDG microparameters vs. fMRI across-subject associations and possible confounding factors (e.g., data normalization) at the voxel level (S. Deng et al. 2022) is highly warranted.
When focusing on K_1 and its relationship with BOLD, the picture changes. In terms of bivariate associations, it is the only parameter that has significant associations with most HRF and sFC features. This is a nice confirmation of the

relationship between features of the HRF and CBF, since K_1, as the delivery rate of [^{18}F]FDG, is a proxy of perfusion (though biased) (Huisman et al. 2012). More interesting is the consistent relationship with sFC, which seems to imply that the large-scale FC network structure is more dependent on CBF rather than on glucose metabolism. In the same direction, sFC features have the most marked *nonlinear* associations with [^{18}F]FDG parameters, especially K_i and k_3. Notably, a sFC feature (eigenvector centrality, *s-EC*), which has a high correlation with K_1 ($\rho > 0.5$) (Figure 5.10), is also selected in the multivariable model, and displays one of the most relevant weights together with the exponent of rs-fMRI signal autocorrelation (*AR-BOLD*) (Figure 5.13). Nonetheless, BOLD-based information does not seem to provide extensive explanation of the spatial distribution of K_1 (group-average $R^2 \sim 0.4$, naïve pooled $R^2 \sim 0.15$).

5.4.4 [^{18}F]FDG uptake and delivery are partially coupled to $CMRO_2$ and CBF

Finally, we tested the hypothesis that the independent addition of CBF and/or $CMRO_2$ to the models of the [^{18}F]FDG parameters' spatial variability would significantly improve on the explanatory power given by rs-fMRI alone. Our hypothesis was that the [^{18}F]FDG delivery (K_1) would have a relatively strong relationship with CBF, while k_3 might possibly better match with $CMRO_2$ (representing oxidative glucose metabolism), and K_i would have a high similarity with both CBF and $CMRO_2$, as predicted by previous studies (Vaishnavi et al. 2010; Hyder et al. 2016).

At group-average level, we find only moderate spatial correlations for K_i and K_1 with $CMRO_2$ ($\rho \sim 0.5$) and even lower with CBF ($\rho \sim$ 0.3-0.4). On the other hand, k_3 has low correlations with both ($\rho \sim 0.2$). When moving to across-subject correlations, no k_3 vs. CBF or k_3 vs. $CMRO_2$ correlations survive FDR correction (and very few are even significant when uncorrected p-values are considered, exactly like the rs-fMRI vs. [^{18}F]FDG across-subject correlations), while K_i and K_1 do have higher and more significant correlations with both CBF and $CMRO_2$ (Figure 5.15). When we try adding CBF or $CMRO_2$ to the fMRI-only models, an important impact is obtained on K_i and K_1, with an increase of more than 10% in the explained variance of the individual data, and a marked amelioration of the pattern of the average residuals, especially in the areas with the strongest positive values, i.e., posterior cingulate for K_i, and posteromedial cortex for K_1 (Figure 5.16).

The strong role of $CMRO_2$ in explaining [^{18}F]FDG K_1 is interesting and deserves attention. From a physiological standpoint it represents a match between the delivery of glucose (K_1) and the delivery and consumption of oxygen ($CMRO_2$), with highest values in medial and posterior regions. This finding is also consistent with previous reports of [^{18}F]FDG K_1 and $CMRO_2$ spatial distribution (Glasser, Goyal, et al. 2014; Hermanides et al. 2021). However, some key differences emerge, especially in the subcortical areas and cerebellum, which is one of the highest hotspots only for K_1. In the case of the cerebellum, peculiar physiological characteristics might come into play to explain its very high [^{18}F]FDG delivery, such as its different glia-to-neuron ratio (Herculano-Houzel 2014), density and type of glucose transporters (Barrio et al. 2020), different LC (Graham et al. 2002; Barrio et al. 2020), higher EF (Huisman et al. 2012) and permeability-surface product (*preliminary data*), etc.

It also interesting to underline that the informative power provided by rs-fMRI, both alone and supplemented by CBF and $CMRO_2$, is not enough to satisfactorily explain the spatial distribution of k_3 (maximum R^2 values: ~ 0.5 at group level, ~ 0.25 at NPD level).

For what concerns the relationship of CBF and $CMRO_2$ with k_3, our results are consistent with what recently described by (Hermanides et al. 2021), who showed that k_3 remained relatively constant for the healthy range of CBF and $CMRO_2$ values. Only local rs-fMRI indices (i.e., $ReHo$), possibly tracking some features of synaptic activity, seem to satisfactorily describe the hexokinase activity. In the future, investigating the match of k_3 with markers of synaptic density, e.g., [^{11}C]UCB-J (Aalst et al. 2021), or mitochondrial distribution, e.g., [^{18}F]FCPP-EF (Venkataraman et al. 2022), might provide additional insights on the physiological underpinnings of this parameter.

Notably, the correlations between CBF, $CMRO_2$ and [^{18}F]FDG K_i were somewhat weaker than expected, especially for CBF (e.g., Glasser, Goyal, et al. 2014; Hyder et al. 2016; S. Deng et al. 2022). This could be due to a number of reasons, including the use of different quantification approaches for CBF (and also $CMRO_2$), i.e., the absolute quantitative parameter (Hyder et al. 2016), a relative quantitative parameter (as in our case), or a semiquantitative $SUVR$ (as in Vaishnavi et al. 2010). As a next step on this, we are going to explore the match between our relative CBF, $CMRO_2$ parameters and [^{15}O]H_2O and [^{15}O]O_2 $SUVR$. When checking group-average associations with [^{18}F]FDG $SUVR$, nonetheless, a higher match was detected ($SUVR$ vs. CBF $R^2 = 0.26$; $SUVR$ vs. $CMRO_2$ R^2

= 0.432), especially when the $SUVR$ from Dataset A was considered ($SUVR_A$ vs. CBF R^2 = 0.488; $SUVR_A$ vs. $CMRO_2$ R^2 = 0.487). Moreover, recent reports in the quantitative PET literature talk of a moderate (Spearman's $\rho = 0.56$) and *nonlinear* association between $CMRglc$ ($= K_i$) and CBF, with higher CBF in thalamus, cerebellum and medial temporal lobe than predicted by $CMRglc$ (Henriksen, Vestergaard, et al. 2018).

On a final note, we have also assessed the spatial relationships between CBF, $CMRO_2$ and rs-fMRI features expanding on previous assessments (S. Deng et al. 2022).

Interestingly, both CBF and $CMRO_2$ are significantly correlated with the baseline rs-fMRI signal of each region, while [^{18}F]FDG kinetic parameters are not, and CBF is positively correlated with $ALFF$), which has negative associations with [^{18}F]FDG K_i (as in S. Deng et al. 2022) and k_3. We find *ReHo* to be weakly correlated with CBF, differently from (S. Deng et al. 2022); however, this is still in line with their hypothesis of a stronger coupling of *ReHo* with $CMRglc$ than with CBF.

Importantly, significant correlations are present between CBF and blood flow-related indices such as *MAD-BOLD* and *peak-HRF* (G.-R. Wu and Marinazzo 2016). Moreover, similarly to [^{18}F]FDG K_1, correlations with the HRF and sFC pool are significant and stronger than for K_i and k_3, which again seems to imply that FC network measures are more supported by blood flow and blood oxygenation than by glucose metabolism.

5.4.5 Limitations

There are some limitations in this work that need to be considered.

First, the PET and rs-fMRI data were not acquired simultaneously. While simultaneous PET/fMRI acquisitions are expected to provide superior performance in integrating multiple modalities by reducing between-scan variability (Cecchin et al. 2017; Z. Chen et al. 2018), sequential scans have been employed in many PET vs. fMRI studies (e.g., D. Tomasi, G. J. Wang, and Volkow 2013; S. Deng et al. 2022). In our case, a higher spatial match between PET and rs-fMRI variables was actually found in the non-simultaneous case (Chapter 5) with respect to the simultaneous case (Chapter 4), possibly due to higher-quality fMRI acquisitions.

Secondly, despite our extensive efforts, the PET modelling estimates on this dataset cannot be considered fully quantitative.

With regard to [^{18}F]FDG, our image-derived input function approach, fully de-

tailed in (Erica Silvestri et al. 2022), and fine-tuned here to the peculiarities of this dataset, allows to retrieve an input function that is sufficiently accurate, but is likely to still be affected by PVEs due to the limited spatial resolution of the ECAT HR+ scanner (FWHM 5 mm) (Zanotti-Fregonara, K. Chen, et al. 2011). This makes the K_i, K_1 and k_3 estimates biased. However, we believe their *relative* spatial distribution to be accurate, which is what is required for the spatial modelling approach we have presented, where demeaned or z-scored input data are employed. The bigger impact is on across-*subject* associations, since within-subject z-scoring of the parameters is removing the individual-level effects, making it possible to only evaluate PET-fMRI correspondences in terms of how similar the *relative ranking* of a given region across different subjects is for the two modalities. Hopefully, in the future we will have the opportunity to analyze fully quantitative data (i.e., with arterial sampling, or IDIF extraction on a high-resolution PET scanner) and be able to avoid within-subject normalization altogether. PVC of the $[^{18}F]$FDG parametric maps is ongoing, to minimize the effects related to the low spatial resolution of the scanner.
With regard to $[^{15}O]H_2O$ and $[^{15}O]O_2$ data, the same reasoning applies. Further assessment of the $[^{15}O]H_2O$ and $[^{15}O]O_2$ quantification results is required to evaluate their reliability.
With regard to the rs-fMRI analysis, we have opted for a granular assessment of the different fMRI features, as in chapter 4, to have the best chance of discovering a relevant coupling with $[^{18}F]$FDG, but, especially in light of new perspectives on a more unitary representation of the rs-fMRI features (Bolt et al. 2022), we are also exploring other summary features such as FC gradients (Margulies et al. 2016; Vos de Wael et al. 2020) (Figure 5.18) to verify if they improve the match with glucose metabolic parameters.

5.5 Conclusions

In this chapter, we have fully assessed the physiological information contained in $[^{18}F]$FDG dynamic PET data from a large dataset of ~ 50 healthy subjects, estimating both the macroparameter K_i (uptake rate), and the single rate constants K_1 and k_3, describing the delivery and phosphorylation of glucose, with unprecedented spatial detail.
The combination of rs-fMRI (mainly local features, i.e., $ReHo$) and CBF, $CMRO_2$ allows to explain a significant portion of spatial variance for $[^{18}F]$FDG K_i, while

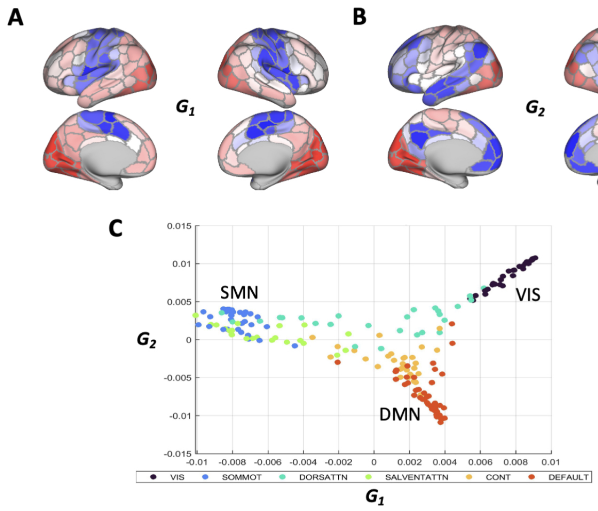

Figure 5.18: Representation of the first (A) and second (B) gradients (G_1 and G_2) of the group-average FC matrix (n = 47) of the dataset in question, plotted on the cortical surface; scatter plot of G_1 vs. G_2, with nodes divided according to RSN (C).

K_1 is mostly sensitive to the information provided by $CMRO_2$, and k_3 by $ReHo$. Overall, this work enriches the landscape of research on the interplay between PET- and BOLD-derived variables, as well as on the interactions between brain metabolism ($CMRglc$, $CMRO_2$), blood flow (CBF), and neural activity.
Future assessment of glucose delivery (K_1) and hexokinase activity (k_3) via [^{18}F]FDG PET, in healthy and pathological populations, is promising thanks to the improvements in both hardware and software which make parameter estimates more reliable and sensitive.
Part of this work has been published as (Volpi, J. Lee, et al. 2022).

Chapter 6

Bringing [^{18}F]FDG PET to the 'brain connectivity' framework to explore its match with FC

6.1 Introduction

The rise of the field of 'connectomics', which aims at characterizing the structural and functional connections between brain areas, typically using diffusion magnetic resonance imaging (dMRI) and fMRI (Betzel 2022), has opened new scenarios for brain [^{18}F]FDG PET, which has been employed to obtain estimates of the so-called 'MC', defined as the similarity between different brain regions in terms of their metabolic activity.

In most studies, only a *group*-level MC estimate is obtained, as the covariation of [^{18}F]FDG PET uptake across subjects (Yakushev, Drzezga, and Habeck 2017; Veronese et al. 2019). This '*subject series* MC' (ss-MC) approach (Jamadar et al. 2021) differs significantly, both in the calculation and in the interpretation, from what is typically done to calculate fMRI FC (Smith, Miller, et al. 2011), where adjacency matrices are derived at the single-subject level.

As we have shown in chapter 4 and 5, FC measures tend display a somewhat weak similarity with *regional* [^{18}F]FDG kinetic parameters: this is why applying a '*large-scale connectivity*' framework to PET data instead might improve the match with fMRI-based connectomes.

As anticipated in Chapter 2, only a handful of studies have attempted to use dynamic PET data to derive MC from the PET signal TACs at the individual level, i.e., *time series* MC (ts-MC), in humans (D. G. Tomasi et al. 2017; Jamadar et al. 2021) and animal models (Wehrl et al. 2013; Amend et al. 2019; Ionescu et al. 2021).

Importantly, handling dynamic PET time series comes with peculiar challenges as compared to fMRI time series or static PET *subject series* (Tommaso Volpi, Erica Silvestri, Corbetta, et al. 2021): the strong collinearity amongst tissue TACs, which all share a positive trend related to the tracer irreversible uptake, makes it difficult to directly employ simple correlation analysis. To overcome this issue, it was suggested to perform some sort of TAC *standardization*, or *detrending*, both for traditional *bolus injection* and for *continuous infusion* fPET protocols; the detrending approach has been especially employed on the latter, where MC is becoming very popular due to the higher temporal resolution fPET data are reconstructed to (Amend et al. 2019; S. Li et al. 2020; Jamadar et al. 2021; Voigt et al. 2022). This approach, however, is problematic, as it removes the main signal in PET TACs leaving only the fluctuations around it, which may be related more to physical and statistical noise than to biologically informative variability. Another relevant point to address is that, in virtually all previous MC studies, only a semi-quantitative measure of [^{18}F]FDG uptake is employed, i.e., SUV or $SUVR$. Resorting to full kinetic modelling, instead, might provide important physiological information, such as the tracer's K_i and microparameters K_1, k_2, k_3 (L. Sokoloff et al. 1977; S. C. Huang et al. 1980; Alessandra Bertoldo, Rizzo, and Veronese 2014). Interestingly, by using kinetic modelling we can also reconstruct the TACs of the first (C_1) and second compartment (C_2), i.e., the tissue concentration of unphosphorylated and phosphorylated [^{18}F]FDG, respectively. This multi-parametric information, which allows to separate tracer delivery from its actual metabolism in the PET signal, might prove relevant for more accurate MC estimation, but this has never been tested so far.

With these premises, we set out to provide a more comprehensive framework for [^{18}F]FDG PET MC, using traditional bolus injection data from a large dataset ($>$ 50 subjects) of dynamic [^{18}F]FDG PET studies in healthy individuals.

To obtain single-subject ts-MC estimates, we started by comparing different TAC standardization strategies and similarity metrics to select the best approach, and then we proceeded to derive ts-MC matrices not only from the *full* tissue TACs (0-60 min), but also from their *early* part (0-10 min) and *late* part (40-60 min), to characterize MC networks more related to inflow (early) or metabolism (late) (see Figure 6.1, *bottom*). Then, we carried out [^{18}F]FDG kinetic modelling, using an IDIF calibrated with venous plasma samples (K. Chen et al. 1998) (Chapter

5), and the reconstructed TACs of C_1 and C_2 were also used to derive ts-MC estimates.
Then, ts-MC (group average) were compared to ss-MC matrices, derived not only from $SUVR$, but also from macro- (K_i) and microparameters (K_1, k_3) (see Figure 6.1, *top*). The comparison was run at multiple levels, i.e., a) similarity of matrix structure, b) similarity of 'hub' nodes (Rubinov and Sporns 2010), c) match with [^{18}F]FDG kinetic parameters, d) match with other connectivity estimates, i.e., SC (from an average template (Yeh et al. 2018)) and, in particular, FC from rs-fMRI data acquired in the same subjects.

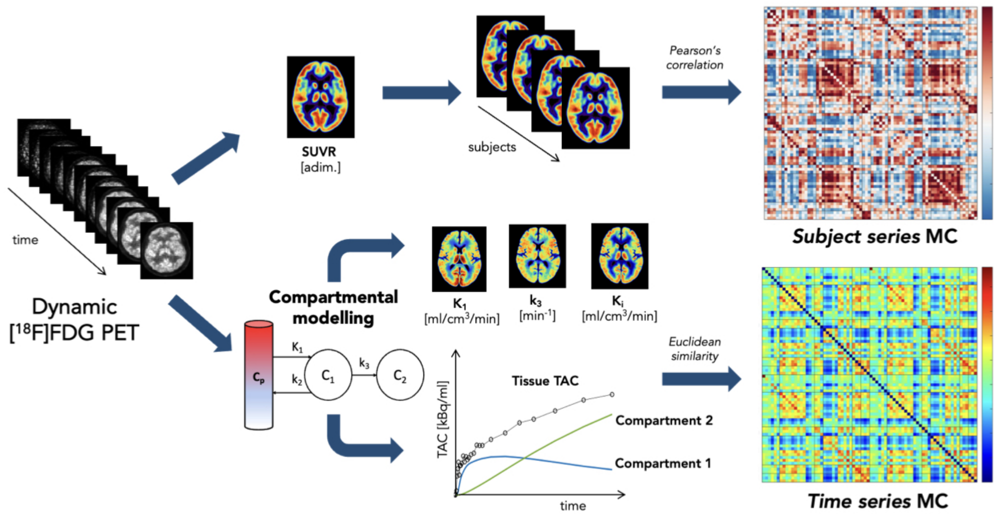

Figure 6.1: Analysis pipeline for estimating single-subject (ts-MC) and across-subject (ss-MC) MC. A static $SUVR$ image (*top left*) is derived from the 40-60 min window of the [^{18}F]FDG PET dynamic data; in parallel, compartmental modelling is applied to dynamic PET data to estimate [^{18}F]FDG kinetic parameters, in particular K_i, K_1 and k_3 (*center*) and reconstruct the time courses of compartments 1 and 2 (*bottom center*). From the *subject series* of parameters $SUVR$, K_i, K_1 and k_3 we calculate across-subject MC via Pearson's correlation (*top right*), while from the *time series* of the tissue TAC, compartments 1 and 2, single-subject MC is obtained via Euclidean similarity (*bottom right*).

6.2 Materials and Methods

6.2.1 Participants

Fifty-four healthy adults (mean age 57.4 $\pm$ 14.8 years, 24 males) underwent [^{18}F]FDG PET scans. Subjects were excluded if they had contraindications to MRI, history of mental illness, possible pregnancy, or medication use that could interfere with brain function. All assessments and imaging procedures were approved by Human Research Protection Office and Radioactive Drug Research Committee at Washington University in St. Louis. Written consent was provided from each participant.

6.2.2 Imaging protocols

For each participant, a multi-echo T1w MRI scan, T2* GE-EPI scan, two SE scans were acquired on a Siemens Magnetom Prisma scanner. One-hour dynamic [^{18}F]FDG scans were performed on a Siemens ECAT EXACT HR+ scanner, after i.v. bolus injection of 5.1 ± 0.3 mCi (187.7 ± 12.1 MBq) of [^{18}F]FDG. The reconstruction grid consisted of 52 frames (24 x 5 s, 9 x 20 s, 10 x 1 min, and 9 x 5 min frames). Venous samples were collected to assess [^{18}F]FDG plasma concentration.
For all the additional details on these acquisitions, see chapter 5.

6.2.3 MRI preprocessing

Structural T1w images underwent the same pre-processing as in chapter 5.
The Hammers anatomical atlas (Hammers et al. 2003) and the Schaefer functional atlas (100 parcels, 7 networks) (Schaefer et al. 2018) were registered to T1w space by inverting the obtained nonlinear transformation.
For the *Hammers* atlas, 74 ROIs (out of the original 83) were kept for further analysis, after removing WM- and CSF-only ROIs. For simpler visualization and interpretation, the regions were divided into 7 anatomical clusters, i.e., 1) frontal lobe, 2) temporal lobe, 3) parietal lobe, 4) occipital lobe, 5) insula and cingulate gyri, 6) subcortical structures, 7) cerebellum.
For the *Schaefer* atlas, the 100 ROIs were supplemented by 12 subcortical ROIs taken from the Hammers atlas (bilateral caudate, accumbens, putamen, pallidum, thalamus, cerebellum).
As to rs-fMRI data, GE-EPI images underwent the same pre-processing as in chapter 5.
Pre-processed EPI signals were obtained within each parcel from the Hammers and Schaefer atlases, which had been linearly mapped from T1w to EPI space, by averaging over voxels within the SPM (Ashburner and K. J. Friston 2005) GM segmentation (probability > 0.8 of belonging to GM).

6.2.4 PET kinetic modelling

For detailed steps of PET data analysis and kinetic modelling on this dataset, see chapter 5.
A static PET image was obtained by summing late PET frames (40-60 min) after motion correction, and normalized first into a SUV image, then into an $SUVR$ dividing by the whole-brain average uptake (Byrnes et al. 2014).
To perform full kinetic modelling, an IDIF was extracted from dynamic PET data using a semi-automatic pipeline (Volpi, Silvestri 2022) and corrected for spillover (K. Chen et al. 1998). Voxel-wise estimation of Sokoloff's model parameters was performed using a VB approach (Castellaro et al. 2017). Parametric maps of K_1, k_2, k_3, V_b were obtained for each subject. The parametric map of K_i was computed by the solving Equation 2.5 at the voxel level.
The voxel-wise time courses of C_1 and C_2 were reconstructed with the following equations (L. Sokoloff et al. 1977; Phelps et al. 1979):

$$C_1(t) = \frac{K_1 k_2}{k_2 + k_3} + \mathrm{e}^{-(k_2+k_3)t} \otimes C_p(t) \tag{6.1}$$

$$C_2(t) = K_i \int_0^t C_p(t)dt \tag{6.2}$$

6.2.5 *Time series* metabolic connectivity (ts-MC)

ROI-level PET signals ([^{18}F]FDG tissue TACs, C_1 and C_2 TACs) were extracted from the Hammers and Schaefer parcels, which had been linearly mapped from T1w to PET space, by averaging over voxels within the GM segmentation (probability > 0.8 of belonging to GM).
The first 24 5 s frames (120 s in total) of the parcel-wise tissue TACs were filtered in the temporal dimension by averaging them in triplets, due to their high noise content. Denoising was not performed on the TACs of C_1 and C_2, as they are noise-free by construction. The signals (tissue TACs, C_1 and C_2 TAC) were interpolated on a uniform virtual grid (5 s step), obtaining a subject-wise matrix $\mathbf{X} \in \mathbb{R}^{p \times T}$, where p is the feature size (72 parcels) and T is the sample size (690 time points).
To calculate ts-MC, we tested and compared several methods for

- TAC standardization (detailed in Figure 6.2):
  1. Dividing by the whole-brain average TAC, i.e., mean TAC across ROIs (D. G. Tomasi et al. 2017; Amend et al. 2019), to emphasize the fluctuations

of the signal of each ROI with respect to the metabolic baseline;
2. Z-scoring across regions (i.e., subtracting the mean TAC across ROIs and dividing by the SD TAC across ROIs), followed by demeaning across time points (i.e., subtracting the mean across time, ROI by ROI), again to emphasize the fluctuations of the signal with respect to the baseline;
3. Demeaning across regions (i.e., subtracting the mean TAC across ROIs), followed by z-scoring across time points (i.e., subtracting the mean across time and dividing by the SD across time, ROI by ROI), to emphasize the fluctuations of the signal with respect to itself;
4. Dividing by the $C_p(t)$, i.e., by the IDIF time course, to remove the vascular information from the tissue TACs;
5. Dividing by the integral of $C_p(t)$, $\int_0^t C_p(t)$, to emphasize the vascular information in the TACs;

- MC matrix estimation (Pearson's correlation, Cosine Similarity, Euclidean distance).

The selected MC estimation approach is based on Euclidean distance d_{x_1,x_2}:

$$d_{x_1,x_2} = \sqrt{\sum_{i=1}^{T}(x_{i,1} - x_{i,2})^2 \text{ with } T = \text{ number of time points}} \tag{6.3}$$

between each pair of TACs $x_{i,1}$ and $x_{i,2}$. From d_{x_1,x_2} we derived a measure of Euclidean similarity (ES), as the complement to 1 of the normalized d_{x_1,x_2} (divided by its maximum). Due to the markedly heavy-tailed (left-skewed) distribution of ES values, a Fisher z-transformation was applied, and then the values were again rescaled to the [0;1] range dividing by their maximum.
To fully evaluate the different physiological information contained within PET TACs, ts-MC matrices were calculated at the single-subject level from

a) the *full* tissue TACs (0-60 min)
b) the *early* part of the tissue TAC (0-10 min)
c) the *late* part of the tissue TAC (40-60 min)
d) the *full* TACs of C_1
e) the *full* TACs of C_2

and then averaged across subjects into 5 group-level MC matrices.
The BSV of a)-e) ts-MC was calculated edge by edge as the CV%, i.e., the percentualized MAD/median ratio across subjects. An overall index of the BSV was obtained from the median $\pm$ MAD of the CVs% for each matrix.

The association between each pair of ts-MC matrices was tested via Pearson's correlation coefficients, calculated between the upper triangular portions of each matrix, both without sparsification and after imposing a threshold (80^{th} percentile), as is typical in connectivity studies (Wijk, Stam, and Daffertshofer 2010). The significance of the Pearson's correlation values was assessed via the Mantel's test, which is used to evaluate the correlation between two symmetric similarity matrices obtained from multivariate data (Mantel and Haenszel 1959). Mantel statistics were tested for significance by 15,000 permutations, and then p-values were Bonferroni-corrected (10 comparisons) (Shaffer 1986).

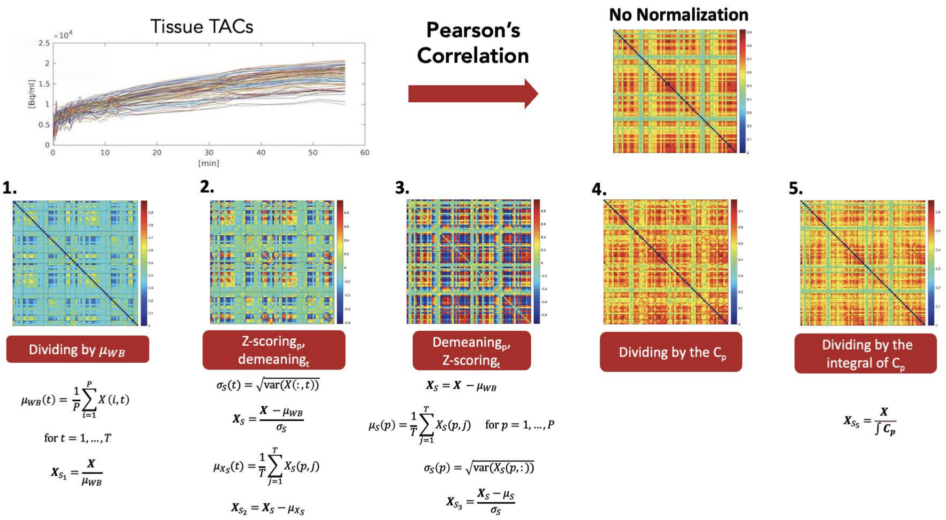

Figure 6.2: Group-average *time series* MC matrices (Hammers atlas) obtained at individual level from the full tissue TAC, using Pearson's correlation as a similarity metric. The non-normalized case is compared with five different normalizations: division by mean TAC μ_{WB} (1), z-scoring across regions followed by demeaning across time points (2), demeaning across regions (removing μ_{WB}) followed by z-scoring across time (3), division by IDIF (C_p) curve (4), division by IDIF integral curve (5).

6.2.6 *Subject series* metabolic connectivity (ss-MC)

The $SUVR$, K_i, K_1, k_3 parametric maps were parceled at the subject level with the Hammers and Schaefer atlas as described in chapter 5. The region-wise $SUVR$, K_i, K_1, k_3 values were within-subject normalized via z-scoring, i.e., centered with respect to their mean and divided by the standard deviation across ROIs, in accordance with previous PET connectivity work (Veronese et al. 2019). ss-MC matrices for $SUVR$, K_i, K_1, k_3 were computed with Pearson's correlation (see Figure 6.1, *top*). The association between each pair of ss-MC matrices was tested via Pearson's correlation coefficients (upper triangle), both without sparsification and after imposing a threshold (80^{th} percentile). The significance of the p-values was assessed via the Mantel's test: Mantel statistics were tested for significance by 15,000 permutations, and then p-values were Bonferroni corrected (6 comparisons).

6.2.7 Multilevel comparison of ts-MC vs. ss-MC

We now have five average ts-MC matrices, i.e., a) full TAC, b) early TAC, c) late TAC, d) C_1, e) C_2 MC, and four ss-MC matrices, i.e., a) $SUVR$, b) K_i, c) K_1, d) k_3-based MC. The complementary information provided by the *time series* vs. *subject series* approaches was assessed via multiple strategies: at *edge* level by calculating the Pearson's correlation between the matrix elements, and at *region* level by comparing the graph metrics and derived hub nodes of each MC matrix. Moreover, the match with a SC template (Yeh et al. 2018) and group-average FC was assessed.

Comparing ts-MC vs. ss-MC: matrices

For direct matrix-to-matrix comparison, Pearson's correlation coefficients were calculated between the upper triangular portions of each ts-MC vs. ss-MC matrix, both without sparsification and after imposing a threshold (80^{th} percentile). The significance of the p-values was assessed via the Mantel's test: Mantel statistics were tested for significance by 15,000 permutations, and p-values were Bonferroni corrected (20 comparisons).

Comparing ts-MC vs. ss-MC: graph metrics and hub nodes

To identify hub nodes, all matrices were thresholded at the 80^{th} percentile. Region-wise graph metrics were computed, i.e., DEG and EC (see chapter 3).
The regional EC values from both ts-MC and ss-MC matrices were plotted against the across-subject mean [^{18}F]FDG parameters ($SUVR$, K_i, K_1, k_3) to assess their relationships.
Then, hubs were identified on each matrix as the nodes belonging to the top 20% of the distribution of the two graph metrics (DEG and EC) simultaneously, thus highlighting nodes with both high local and global connectivity (Rubinov and Sporns 2010).
For comparison of hubs across matrices, the Dice Similarity coefficient (DSC) between pairs of binary hub vectors of ts-MC and ss-MC was computed.

Comparing ts-MC vs. ss-MC: match with structural and functional connectivity

A publicly available tractography atlas was used to create a group-level SC matrix (Yeh et al. 2018), whose entries represent the number of white matter tracts between each pair of parcels. As for MC, the sparsity level of the matrix was set to 20%. To assess the agreement between the estimated metabolic connections and the underpinning structural connections, the DSC between the binarized SC and each binarized ts-MC (group average) and ss-MC network was computed.
For each subject, the FC matrix was obtained by means of Pearson's correlation computed between the pre-processed fMRI time series of each pair of parcels. FC matrices were then Fisher z-transformed and averaged across subjects to obtain the group-averaged FC (see chapter 5). As for MC, the sparsity level was set at 20%.
To assess the agreement between the estimated metabolic connections and the FC structure, the DSC between binarized FC and each binarized ts-MC (group average) and ss-MC network was computed.

6.3 Results

6.3.1 *Time series* MC maps from PET time-activity curves

When we compared different MC estimation (ES, Pearson's correlation, Cosine Similarity) and TAC standardization approaches (Figure 6.2), the ES method emerged as the only one capable of retrieving structured MC matrices even without any signal normalization: in particular, in all the matrices reported in Figure 6.3 (Hammers anatomical atlas) and Figure 6.4 (Schaefer functional atlas), both a) a block-diagonal structure along the main matrix diagonal, and b) enhanced secondary diagonals are clearly present, representing within-'network' connections and interhemispheric homotopic connections (i.e., between homologous regions) respectively. Therefore, the ts-MC matrices obtained via the ES approach will be presented and used for further analysis.
Representative examples of ts-MC derived via Pearson's correlation are shown in Figure 6.2. Similar results were obtained with Cosine similarity (*not shown*). A discussion of the issues related to TAC normalizations and other MC estimation approaches can be found in (Tommaso Volpi, Erica Silvestri, Corbetta, et al. 2021).

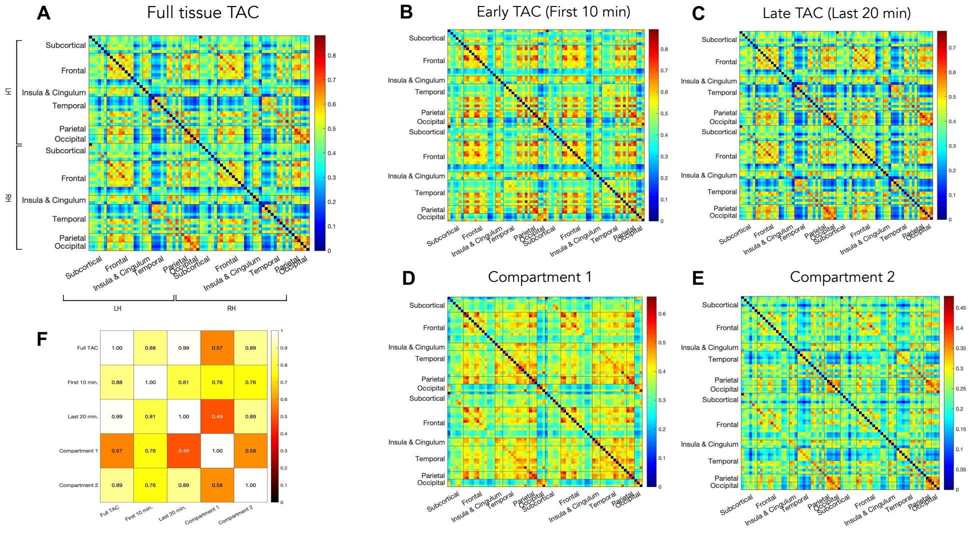

Figure 6.3: *Time series* MC matrices (Hammers atlas). We report the group-average (n = 54) MC matrices obtained at the individual level from the *full* tissue TAC (A), its *early* part (B) and *late* part (C), the kinetics of C_1 (D) and C_2 (E), via the Euclidean similarity metric. We also report the Pearson's correlation matrix between the edges of the 5 ts-MC matrices (upper triangle) (F).

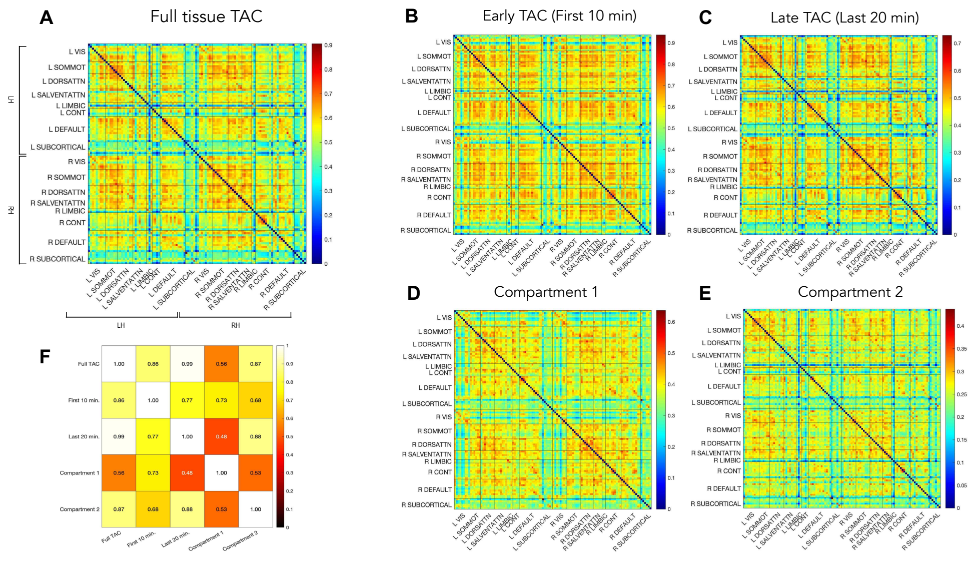

Figure 6.4: *Time series* MC matrices (Schaefer atlas). We report the group-average (n = 54) MC matrices obtained at the individual level from the *full* tissue TAC (A), its *early* part (B) and *late* part (C), the kinetics of C_1 (D) and C_2 (E), via the Euclidean similarity metric. We also report the Pearson's correlation matrix between the edges of the 5 ts-MC matrices (upper triangle) (F).

When visually assessing the ts-MC matrices from the full TAC (Figure 6.3A), the late part (Figure 6.3C), and C_2 (Figure 6.3E), areas of strong within-'network' connections are located in the frontal and occipital cortex, but also in medial temporal lobe regions.

However, this network structure is clearly modified in the ts-MC from the early part of the TAC (Figure 6.3B), and C_1 (Figure 6.3D): the occipital lobe loses 'connectivity', and the temporal and parietal areas become highly connected both within and between 'network'.
Notably, subcortical structures tend to always display lower ts-MC than cortical areas.
The BSV of the obtained ts-MC matrices, shown at the single edge level in Figure 6.5, is overall low for all approaches, being lowest for the full TAC (CVs% median $\pm$ MAD: 8.3 $\pm$ 28.9), and highest for C_2 (CVs% median $\pm$ MAD: 47.7 $\pm$ 9.4).

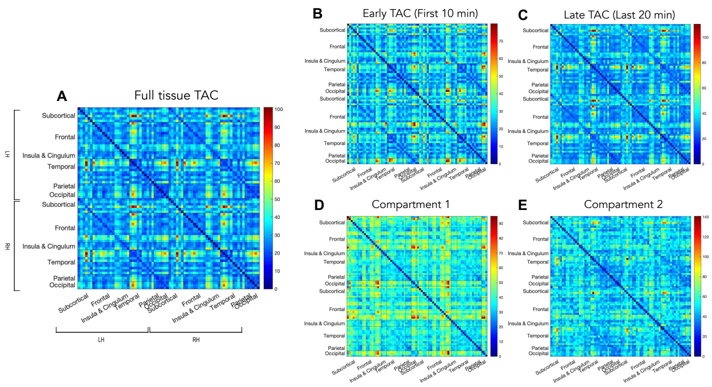

Figure 6.5: Across-subject variability of *time series* MC matrices (Hammers atlas). report the edge-level across-subject coefficients of variation (%) of MC matrices obtained from the *full* tissue TAC (A), its *early* part (B) and *late* part (C), the kinetics of C_1 (D) and C_2 (E).

If we assess the Pearson's correlation between the edges of average ts-MC matrices, we can see how the full TAC ts-MC has strong correlations with the early part, C_2 and especially the late part of the TAC. Notably, the C_1 MC has weaker relationships with the other ts-MC matrices, except for a high correlation (r = 0.73, Mantel's test, p $< 10^{-9}$, Bonferroni corrected) with the early TAC MC (Figure 6.3F).
To sum up, by using dynamic PET TACs and the ES metric, it is possible to obtain single-subject MC estimates characterized by within-network and homotopic connections, a low BSV, and to highlight different physiological information (i.e., full signal, early vs. late portions, and the kinetics of the model compartments). Overall, these results are consistent across different atlases.

6.3.2 *Subject series* MC maps: $SUVR$ and kinetic parameters

The ss-MC matrices are displayed in Figure 6.6 (Hammers) and Figure 6.7 (Schaefer). The ss-MC of [^{18}F]FDG kinetic model parameters (K_i, K_1, k_3) is presented here for the first time, extending on typical ss-MC approaches based on $SUVR$. From a visual standpoint, some similarities are shared between the different parameters, especially between $SUVR$ and K_i MC (r = 0.82, Mantel's test, $p < 10^{-9}$, Bonferroni corrected), as expected due to their high spatial correlation, with strong within-'network' connections are present in temporolimbic areas. The k_3 ss-MC is instead quite different, with enhanced 'connectivity' in frontal areas and also subcortical structures, and is in fact the least correlated with the others, especially with $SUVR$ MC (r = 0.43, Mantel's test, $p < 10^{-9}$, Bonferroni corrected).

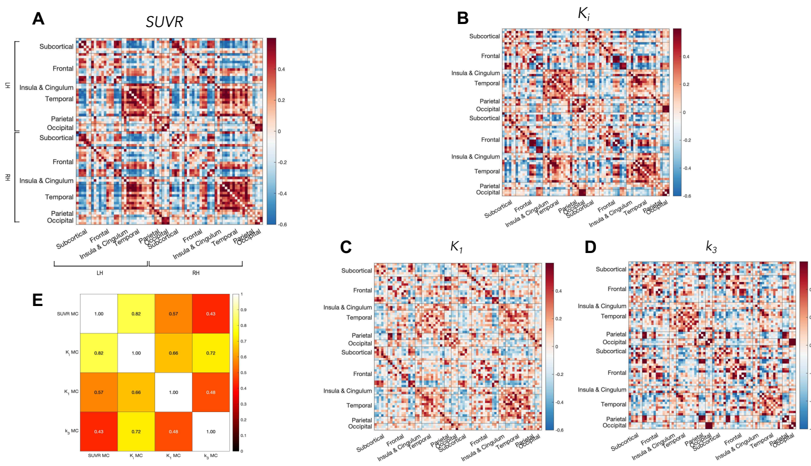

Figure 6.6: *Subject series* MC matrices (Hammers atlas). We report the across-subject Pearson's correlation matrices for $SUVR$ (A), K_i (B), K_1 (C) and k_3 (D). We also report the Pearson's correlation matrix between the edges of the 4 ss-MC matrices (upper triangle) (E).

6.3.3 Similarity of ts-MC and ss-MC matrices and hubs

When the ts-MC and ss-MC networks were related to each other via Pearson's correlation (Table 6.1), some significant correlations are found, especially between ts-MC matrices and K_1 and k_3 ss-MC. However, the correlation values are generally low, with a maximum of 0.37. Even lower correlations are found for the Schaefer atlas (maximum 0.28). $SUVR$ ss-MC seems to carry no meaningful relationships with ts-MC approaches.

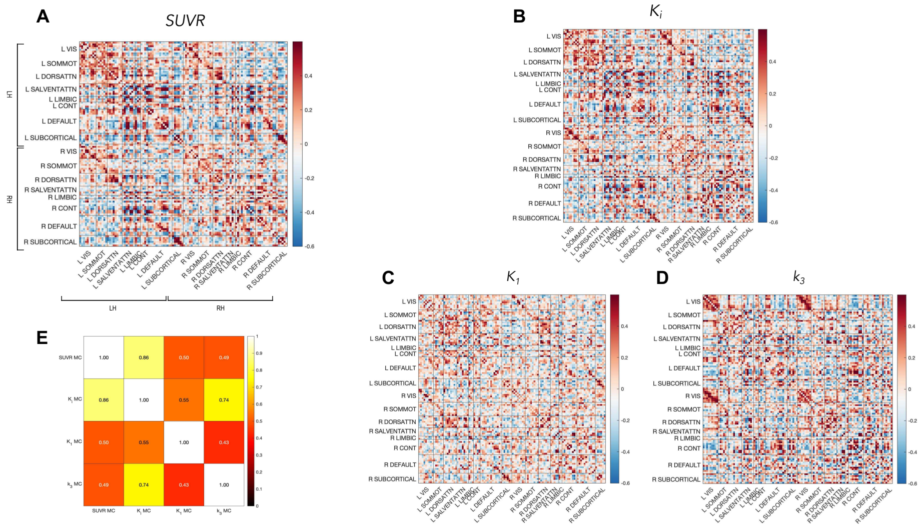

Figure 6.7: *Subject series* MC matrices (Schaefer atlas). We report the across-subject Pearson's correlation matrices for $SUVR$ (A), K_i (B), K_1 (C) and k_3 (D). We also report the Pearson's correlation matrix between the edges of the 4 ss-MC matrices (upper triangle) (E).

Pearson's R	$SUVR$ **ss-MC**	K_i **ss-MC**	K_1 **ss-MC**	k_3 **ss-MC**
Full TAC ts-MC	0.17*	0.2*	0.29*	0.29*
First 10' ts-MC	0.06	0.11*	0.26*	0.25*
Last 20' ts-MC	0.16*	0.17*	0.26*	0.25*
C_1 **ts-MC**	0.18*	0.22*	0.37*	0.33*
C_2 **ts-MC**	0.2*	0.23*	0.29*	0.33*

Table 6.1: Across-edge Pearson's correlations between group-average *time series* (rows) and *subject series* (columns) MC matrices (Hammers atlas, upper triangle, 80^{th} percentile threshold). Significant correlations (Mantel's test, $p < 0.05$, Bonferroni corrected) are reported as *.

We then moved to identifying 'hub' nodes, i.e., highly connected and representative nodes in each MC network, as is typically done in the field of connectomics. With regard to ts-MC hubs (Hammers atlas), they are mainly located in frontal and temporal areas, with the exception of C_1 with more parietal involvement (Figure 6.8A). As to the ss-MC hubs, while $SUVR$, K_i and K_1 have a similar hub distribution, mainly in temporal, insular and cingulate cortices, k_3 hubs fall in frontal and subcortical areas (Figure 6.8B). When we look at the DSC between hub vectors of ts-MC vs. ss-MC matrices, again we find a lack of match between $SUVR$ MC and ts-MC hubs, with higher overlap in the case of K_1 and especially k_3.

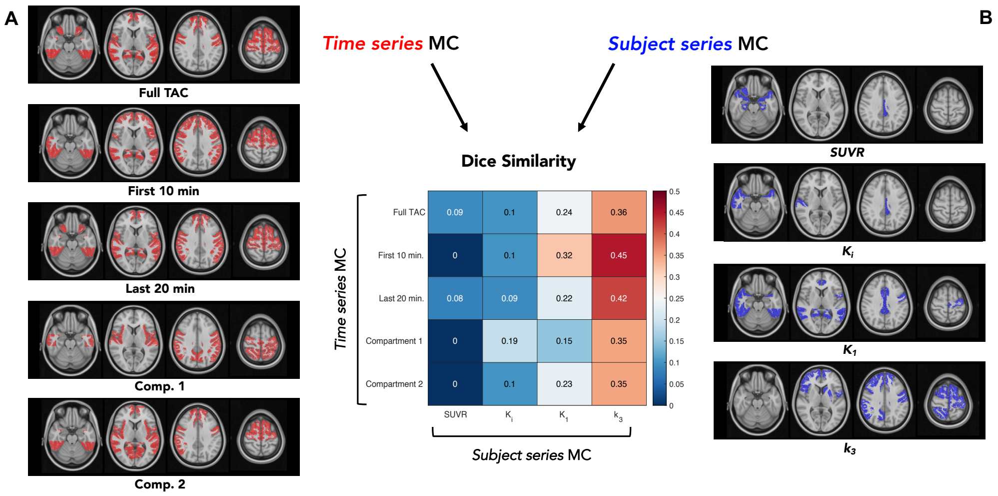

Figure 6.8: Comparison of ts-MC (A) vs. ss-MC (B) 'hubs', identified as the top *DEG* and *EC* nodes for each matrix. Hub nodes are shown on the Hammers atlas regions in red (A) and blue (B) respectively. The Dice Similarity matrix between ts-MC and ss-MC hubs is reported in the central panel.

6.3.4 Relationship with [^{18}F]FDG kinetic parameters

After relating the ts-MC and ss-MC results to one another, we tried to assess the level of similarity between summary measures derived from these networks and the [^{18}F]FDG kinetic parameters, which are more directly interpretable from a physiological standpoint. In particular, the regional values of the EC graph metric of all ts-MC and ss-MC matrices, which describe the level of 'connectedness' of a region in each MC network, were plotted against the across-subject mean values of [^{18}F]FDG $SUVR$, K_i, K_1, k_3 (Figure 6.9).

While the EC of ss-MC matrices (Figure 6.9B) have overall weak relationships with [^{18}F]FDG parameters, typically with a negative sign, the EC of ts-MC matrices (Figure 6.9A) have positive relationships with the parameters, which are highly nonlinear especially for the full TAC, late part, and C_2 vs. $SUVR$ (well described by a quadratic fit, as reported in Figure 6.9A).

6.3.5 Relationship with structural and functional connectivity

Finally, we assessed the similarity between the ts-MC and ss-MC networks and a) a SC template (Yeh et al. 2018), b) the group-average FC from the same subjects, to understand if underlying a) structural or b) fMRI functional connections might

relate to the identified metabolic relationships.
When looking at SC (Figure 6.10A), the Dice similarity values are higher for ts-MC matrices, especially for the early part of the TAC (DSC = 0.47), C_1 (DSC = 0.39) and C_2 (DSC = 0.39). Amongst the ss-MC matrices, k_3 has the highest similarity (DSC = 0.37), while $SUVR$ the lowest (DSC = 0.27). In the case of the Schaefer atlas, the ts-MC vs. ss-MC difference is instead not present (DSC values ranging from 0.24 to 0.3).
Notably, when we look at the match with FC, the ts-MC matrices have even higher similarity (early TAC: DSC = 0.63, C_1: DSC = 0.54, C_2: DSC = 0.55), while ss-MC maintain lower values (k_3: DSC = 0.39, $SUVR$: DSC = 0.24) (Figure 6.10B). Importantly, this result on the Hammers atlas is reproduced also with the Schaefer atlas (full TAC: DSC = 0.44; early TAC: DSC = 0.38, C_1: DSC = 0.42, C_2: DSC = 0.40; $SUVR$: DSC = 0.35; k_3: DSC = 0.33).

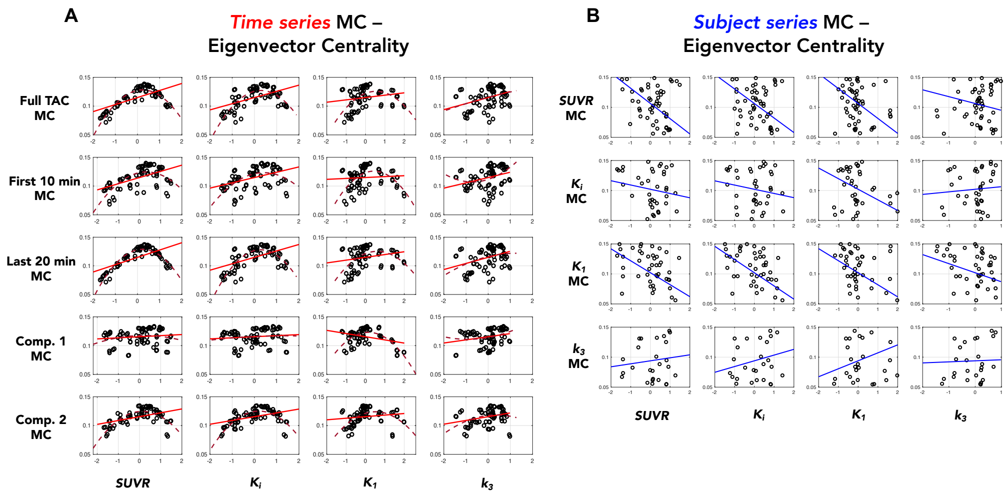

Figure 6.9: Scatter plots of the across-region associations (Hammers atlas) between group-average values of $SUVR$, K_i, K_1 and k_3 (on the x axis) and the *EC* of *time series* (A) and *subject series* MC (B) matrices (on the y axis). A linear fit line is shown in both A (red) and B (blue); a quadratic fit is shown as a red dashed line in A.

6.4 Discussion

In this chapter, we have reassessed the concept of 'MC' from a PET kinetic modelling perspective, trying to capitalize on the multifaceted information provided by dynamic [^{18}F]FDG data.

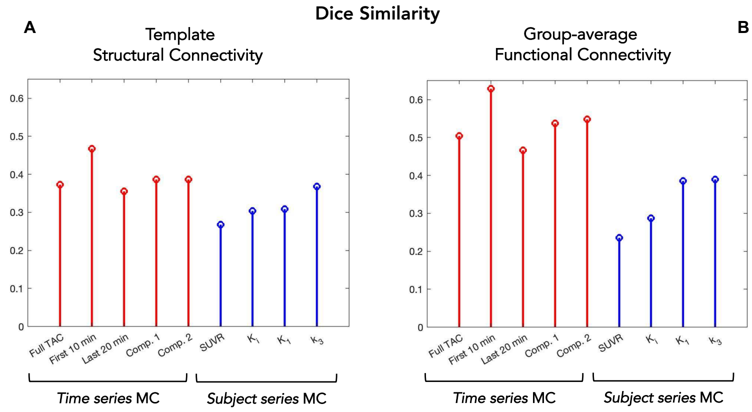

Figure 6.10: Stem plot of the Dice Similarity values between the group-average ts-MC (*red*) and ss-MC (*blue*) binarized matrices (80^{th} percentile) and the SC template (A) and group-average FC matrix (B), for the Hammers atlas.

6.4.1 A new approach for single-subject MC estimation from dynamic PET data

The first issue we wanted to tackle was to select a feasible approach to estimate single-subject MC from PET time series (i.e., ts-MC). The methods used in the fMRI literature to assess single-subject FC conventionally rely on correlation/covariance, i.e., variance-based methods, designed to identify signals that vary together over time (Smith, Miller, et al. 2011). These approaches, directly borrowed from fMRI, are used in the small amount of works which estimate single-subject MC from dynamic PET (Amend et al. 2019; Ionescu et al. 2021; Jamadar et al. 2021). However, variance-based methods tend to perform poorly on dynamic PET data (Figure 6.2), where signal fluctuations are likely to be related to noise without relevant physiological value, while the positive trend in the signal and its amplitude, which are used for kinetic modelling, are clearly more biologically informative (R. E. Carson 2000; Alessandra Bertoldo, Rizzo, and Veronese 2014).

On the other hand, Euclidean similarity, i.e., our method of choice for ts-MC calculation, identifies signals that are close to one another in a Euclidean sense. Notably, when used on dynamic PET data at the voxel level (both in chapter 5 and 6 as pre-steps to VB estimation), Euclidean distance/similarity has already proven to be effective at identifying biologically meaningful clusters (Liptrot et al. 2004). Here, we have repurposed it from a hard cluster assignment to a continuous space, in order to highlight *pharmacokinetic similarities* across brain regions, producing matrices with 1) a block-diagonal structure on the main diagonal and 2) secondary diagonals for homotopic connections, which are considered the hallmarks of brain connectivity (Betzel 2022).

Importantly, the BSV of the MC matrices estimated via ES is remarkably low, which highlights the robustness of the chosen approach and its potential for application as a biomarker.

Another relevant advancement in the presented ts-MC matrices was the emphasis on the different kinds of physiological information that dynamic PET data can provide: in particular, the early TAC and the time course of C_1 are more related to inflow and blood-to-tissue exchanges, while the late TAC and C_2 are more associated with metabolic exchanges. This was aimed to overcome the limitation of ts-MC approaches based solely on the raw tissue TAC, which combines the tracer's specific binding with non-specific binding and delivery information (Veronese et al. 2019). Overall we find good overlap between the late tissue TAC and C_2, i.e., concentration of phosphorylated [^{18}F]FDG, while the C_1 ts-MC is the least similar to the other approaches, implying that full compartmental modelling might still provide additional information for single-subject MC calculation with respect to simpler tissue TAC analysis.

6.4.2 The many faces of *subject series* MC: $SUVR$ vs. kinetic model parameters

An additional aim was to use kinetic modelling to provide a new look on *subject series* MC, which has always been based on $SUVR$, i.e., the easiest parameter to obtain from a single static scan (Yakushev, Drzezga, and Habeck 2017; Veronese et al. 2019): as we have shown, there are relevant differences in the estimated matrices when the chosen [^{18}F]FDG parameter is not $SUVR$, but K_i, K_1 and especially k_3, which produces a remarkably unique ss-MC matrix.

Notably, in the case of other PET tracers, kinetic model parameters (e.g., V_T, BP_{ND}) have already been employed to assess ss-MC (Veronese et al. 2019; Fang et al. 2021) but this has never been tried before with [^{18}F]FDG. While $SUVR$ and K_i are typically considered to be the most important [^{18}F]FDG parameters to summarize [^{18}F]FDG metabolism, there is evidence that the long-forgotten microparameters (e.g., K_1 and k_3) might bear additional meaning, both in physiology (Heiss et al. 1984) and in pathology (Piert et al. 1996; Sari et al. 2022), as we have thoroughly discussed in chapter 5.

6.4.3 *Time series* and *subject series* MC information are not redundant

A crucial point was the evaluation of how similar the two MC frameworks (ts-MC and ss-MC) are to one another. Since the ss-MC approach, with the $SUVR$ parameter in particular, is the most frequently employed in the literature, it is highly relevant to confirm whether the *across-subject* estimates also reflect the *single-subject* information.
When we assess the match between across-subject (ss-MC) and within-subject (ts-MC) matrices, some weak-to-moderate correlations are found, especially with K_1 and k_3 MC, which is consistent with the microparameters being more sensitive to the physiological processes probed by ts-MC. The correlation with $SUVR$ MC is instead very low.
Moreover, when we move to identifying the putative 'hubs' of the MC networks, again we find different distributions for ts-MC and ss-MC: while ts-MC hubs are more concentrated in frontotemporal areas, the ss-MC hubs are temporal and limbic for $SUVR$, K_i and K_1.
Notably, ts-MC hubs identified with fPET (albeit obtained via correlation between PET signal fluctuations) were also located in frontotemporal regions (Jamadar et al. 2021). Notably, again $SUVR$ hubs do not match at all with the structure of ts-MC matrices.
Additionally, when relating the EC graph metric of MC matrices to the mean values of the [^{18}F]FDG parameters across regions, we find a positive correlation for ts-MC, while ss-MC matrices have negative correlations.
When we look at the scatter plots of the ts-MC EC vs. [^{18}F]FDG parameters (especially $SUVR$, K_i and K_1), we find a nonlinear, non-monotonic relationship which seems to imply that the regions whose TACs are similar to the rest of the brain signals also have average glucose metabolism and transport, while nodes with tissue TACs that are very dissimilar from the rest (and thus have low EC) have very high or very low metabolism.
While further investigation is necessary to understand if there is a viable physiological interpretation to this unusual pattern, what is clearer is that ss-MC graph measures have no interesting relationship with the original [^{18}F]FDG parameters.
In summary, as already shown with fPET (Jamadar et al. 2021), across-subject approaches do not seem to be well representative of single-subject MC.

6.4.4 Matching metabolic networks to structural and functional connectomes

As a final step, we provided a 'validation' of our MC connectomes by comparing them to other typical measures of brain connectivity, i.e., SC and FC.
While it is clear that, at least at a global level, there is not a high overlap between MC and SC, we found a higher match for ts-MC (especially C_1 and C_2), at least for the Hammers atlas. Among the ss-MC matrices, the highest overlap was with k_3, while $SUVR$ MC, which is the most frequently reported in the literature, and has already been related to SC (Yakushev, Ripp, et al. 2022), is actually the one with the *lowest* similarity with the underlying structural network. This seems to additionally cast doubt on the widespread use of this index of MC. The reasons of the different readout given by the Hammers vs. Schaefer parcellation will be thoroughly investigated, possibly using different SC templates.
Importantly, the match with FC is higher for ts-MC, both in the Hammers and Schaefer atlases, and, notably, higher than the ts-MC vs. ss-MC match itself (Table 6.1). This echoes previous findings for both bolus and fPET protocols in rodents (Amend et al. 2019), as well as fPET results in humans (Jamadar et al. 2021). While this will require further investigation of the FC-MC coupling at a finer scale (e.g., region by region, network by network), our findings suggest the individual-level MC captures more of the functional network information than its across-subject counterpart.
As anticipated, the match between metabolism, as described by [^{18}F]FDG PET, and fMRI *large-scale* FC, which seems to be somewhat limited when considering only *local* metabolic measures like $SUVR$ (Tommaso Volpi, Erica Silvestri, Marco Aiello, et al. 2021b) (chapter 4, 5), seems to become stronger when both [^{18}F]FDG and fMRI are brought to a 'connectivity' framework.

6.4.5 Limitations

This work is not without limitations.
With regard to absolute quantification of Sokoloff's model parameters, and the problems associated with the input function in this dataset, we refer to Chapter 5.4.5. Moreover, one must remember that in the case of across-subject MC estimates, it is not the *absolute* value of the parameters that is of interest (as it would be for drug development or clinical studies), but their *relative* spatial distribution across regions, which is likely to be preserved.

Also, our approach does not solve the inherent problem of connectomic analyses: while one can retrieve networks with plausible structure, their biological underpinnings and physiological interpretation remain elusive. The attempts at 'validation' presented here (relating MC to SC/FC, and MC graph measures to [^{18}F]FDG parameters) provide only a partial understanding of the underlying mechanisms. Further efforts aimed at validating these connectomes are highly warranted, possibly using interventional approaches in animal models to better elucidate *causative* links.

6.5 Conclusions

In this work, we provided a new distance-based approach to calculate single-subject MC from dynamic PET data, and evaluated different portions of the signal and the underlying compartment kinetics, to build metabolic connectomes related to the multiple aspects of the [^{18}F]FDG tracer physiology (inflow vs. metabolism). The same idea was applied to across-subject covariation of [^{18}F]FDG parameters, building four different ss-MC matrices.

We thoroughly assessed the relationships between ts-MC and ss-MC at multiple levels, i.e., in terms of matrix and hub similarity, and match with [^{18}F]FDG parameters and FC and SC matrices. We found the two MC frameworks (ts-MC and ss-MC) to provide different and somewhat complementary information, with ts-MC having higher match with FC networks from the same individuals.

In the future, we will attempt to further explore the promising match with fMRI functional networks, as well as apply ts-MC approaches to clinical populations to verify if they can provide useful biomarkers.

Part of this work has been published as (Tommaso Volpi, Erica Silvestri, Corbetta, et al. 2021; Tommaso Volpi, Erica Silvestri, Hammers, et al. 2021; Volpi, De Francisci, et al. 2022; Tommaso Volpi, Vallini, et al. 2022).

Chapter 7

Conclusions

The remarkable metabolic budget spent at rest by the human brain, famously called '*the brain's dark energy*', was an intriguing discovery which motivated our work trying to integrate resting-state measurements of glucose metabolism, as assessed by [^{18}F]FDG PET, with fMRI imaging of the brain's spontaneous activity fluctuations.
Acquisition of [^{18}F]FDG dynamic PET data, combined with appropriate mathematical modelling, can provide physiologically informative parameters describing the initial steps of glucose metabolism, from simpler indices like $SUVR$ to the more refined microparameters K_1 and k_3. Additionally, estimates of 'metabolic connectivity' can be obtained from [^{18}F]FDG PET studies, typically as a group-level measure only.
On the other hand, rs-fMRI studies have painted a rich characterization of brain's functional architecture during rest, but the interpretation of these results has been made difficult but a lack of full understanding of their physiological and metabolic underpinnings.
Starting from these premises, we have explored the coupling between [^{18}F]FDG PET- and BOLD fMRI-derived parameters under multiple frameworks:

- first, we assessed the spatial coupling between $SUVR$ and a range of both local and large-scale fMRI variables, trying to increase the amount of $SUVR$ explained variance with a multivariable combination of fMRI features;

- secondly, we extended our exploration to [^{18}F]FDG microparameters, to achieve a richer physiological description of glucose consumption in relation to BOLD, while also considering the role of additional metabolic information from CBF and $CMRO_2$;

- finally, we brought [^{18}F]FDG PET from a local activity to a large-scale connectivity scenario, working on a method to estimate single-subject MC to directly compare it with fMRI FC.

A brief summary of the results we obtained in these chapters is reported.

- In Chapter 4, we used a new integration framework between $SUVR$ and fMRI-based variables, with feature selection at group level, and multilevel modelling at individual level. We found an overall moderate spatial coupling using a combination of 9 fMRI predictors, in particular *local* fMRI variables (e.g., *ReHo*), but with significant between-*subject* and between-*network* differences.

- in Chapter 5, besides assessing the reproducibility of the $SUVR$ vs. fMRI model on a new dataset, we described the spatial distribution of [^{18}F]FDG delivery and phosphorylation for the first time at this level of spatial resolution. While the overall metabolic rate K_i is nicely explained by the combination of fMRI (again, *ReHo*) and CBF or $CMRO_2$ information (around 50% of the individual-level variance), the delivery and phosphorylation rates are more difficult to describe: K_1 is found to be mainly related to $CMRO_2$, and k_3 to *ReHo*.

- in Chapter 6, we explored the 'connectivity' framework on [^{18}F]FDG, with the hope to ameliorate its match with the *large-scale* fMRI FC information which was shown to have a somewhat weaker coupling with $SUVR$ and kinetic parameters. In this work, we devised a new method to estimate single-subject MC from dynamic PET time series, using not only the raw signal but also model-based kinetics of tissue compartments, effectively separating delivery from metabolic information in the PET signal and in the resulting MC matrices. We then compared *time series* MC with conventional across-subject correlations of $SUVR$, but also K_i and microparameters. We found a limited match between individual-level and group-level MC, and the single-subject approach was shown to have a higher similarity with fMRI FC, as we had hypothesized.

Overall, these results confirm the strong spatial association between regional glucose metabolism and local coherence of the BOLD signal, with the additional comfort given by findings on the direct measure of tracer phosphorylation (k_3), which we have provided for the first time. *ReHo* is thus a promising feature to

be explored even further as a simple, non-invasive and fast readout of metabolic processes. Nonetheless, the marked between-subject variability in the association, already highlighted in the literature with different approaches, continues to underline how the two modalities are complementary rather than substitutive, and how [^{18}F]FDG PET still provides additional, non-trivial information.
Moreover, we believe voxel-wise [^{18}F]FDG microparameter estimates, the application of which has so far been limited due to lack of appropriate methods for input function extraction and voxel-level parameter identification, could provide important insights into healthy function and pathological mechanisms, and the new technological advances in PET imaging, such as total-body and brain-dedicated PET scanners with superior sensitivity and spatial resolution, are going to allow to finally exploit this unexplored potential.
With regard to the research on 'metabolic connectivity', we have provided a rigorous framework based on PET kinetic modelling and used it to obtain physiology-based MC networks, separating tracer delivery from metabolic events. Potentially, this approach can be applied to any PET tracer, allowing to obtain single-subject connectomes of receptor density, enzyme activity, synaptic density, and so on. Also, using Euclidean distance, we have chosen a metric that allows to obtain PET connectivity matrices without any brute-force signal normalization, even with a limited number of time points; with the high temporal resolution of new PET scanners, it will be interesting to reassess whether a variance-based approach like correlation can provide more valuable results. Overall, the match found with FC seems very promising, and requires further exploration.
On a final note, the story of the studies on the interactions between brain metabolism ($CMRglc$, $CMRO_2$), blood flow (CBF), and neuronal activity, and how these physiological variables are captured by [^{18}F]FDG PET and BOLD fMRI, has been long and complex, and it has not reached a satisfying conclusion yet. With our comprehensive assessment of the many features that can be extracted from the two imaging modalities, working both at a *local* and *large-scale network* level, we believe we have opened up new perspectives and provided useful tools to reach a better understanding of this problem.

Chapter 8

Appendix: other activities

In this section, we briefly present three additional projects that were carried out during the PhD.

8.1 Image-derived input functions in brain $[^{18}F]$FDG PET studies: comparing three extraction sites

The aim of this work was to develop an innovative automatic pipeline to extract IDIF from three vascular sites, i.e., internal carotids (syphon portion), as is typical in the literature, and two alternative sites, i.e., common carotids, available thanks to the large axial FOV of the Siemens Biograph hybrid PET/MR scanner, and the superior sagittal sinus (a venous site).
The three IDIFs were extracted from a large dataset of 39 glioma patients undergoing dynamic $[^{18}F]$FDG PET acquisitions on a hybrid PET/MR scanner. The extracted IDIFs were compared in terms of their between-subject variability, peak and tail amplitude, and impact on quantification of K_i. The common carotid, which is easy to segment and surrounded by low-activity tissue, is found to have less spillover and lower between-subject variability, and is a promising vascular extraction site for IDIF in new, larger FOV PET scanners.
This work was presented as an Oral Presentation at IEEE EMBC 2022 (https://embc.embs.org/2022/), and published as (Erica Silvestri et al. 2022).

8.2 Predicting venous [^{18}F]FDG plasma samples for IDIF calibration with Nonlinear Mixed-Effects Modelling

Venous plasma samples are used for IDIF calibration and spillover correction in [^{18}F]FDG PET studies. These are, however, not always available, and, when they are, they may be noisy and sparse measurements.
Analyzing a large dataset of venous samples from 54 healthy individuals, we applied nonlinear mixed-effects modeling (NLMEM) to obtain robust estimates in the presence of sparse sampling and, most importantly, to relate the BSV of the model parameters to participant-specific covariates (e.g., age, sex, weight etc.), allowing to predict missing venous data at the individual level, with the aim of avoiding blood sampling altogether.
With this NLMEM approach, we show that the variability in the amplitude of venous plasma [^{18}F]FDG concentration is explained mainly by sex and body surface area, allowing us to predict venous plasma data in healthy subjects with good reliability.
This work was presented as an Oral Presentation at IEEE EMBC 2022 ((https://embc.embs.org/2022/), chosen as finalist for the Student Paper Competition, and published as (Tommaso Volpi, J. J. Lee, et al. 2022).

8.3 The role of neuroreceptor systems in explaining regional glucose utilization: evidence from brain PET studies

Research is increasing on the complex organization of neurotransmitter systems across brain regions, as well as their relationship with other structural and functional properties of the brain.
In this work, we have related [^{18}F]FDG metabolic rates, i.e., $SUVR$, K_i, K_1, k_3, to a range of PET templates covering 8 different neurotransmitter systems, to understand how macroscale neurotransmitter organization relates to regional variability in glucose metabolism. We explored this relationship using bivariate and multivariate approaches to understand which pattern of receptor systems could explain a significant amount of variance of [^{18}F]FDG parameters. While gluta-

mate receptors (NMDAR, $mGluR_5$) emerge as relevant predictors of tracer delivery (K_1), the metabolic rates (K_i, k_3) are more tightly coupled with cannabinoid receptors (CB_1) and, negatively, with the inhibitory $5HT_{1A}$ serotonin receptor. Further exploration is required to overcome issues related mainly to PET templates with different image quality and kinetic parameters ($SUVR$, V_T, BP_{ND}). This work was presented as an Oral Presentation at Brain and Brain PET 2022 (https://brain2022.scot), and published in (Volpi, Silvestri, J. Lee, et al. 2022).

Bibliography

Aalst, June van et al. (Jan. 14, 2021). “In vivo synaptic density relates to glucose metabolism at rest in healthy subjects, but is strongly modulated by regional differences”. In: *Journal of Cerebral Blood Flow & Metabolism*, p. 0271678X2098150. ISSN: 0271-678X, 1559-7016. DOI: 10.1177/0271678X20981502. URL: http://journals.sagepub.com/doi/10.1177/0271678X20981502 (visited on 04/03/2021).

Aiello, Marco et al. (2015). “Relationship between simultaneously acquired resting-state regional cerebral glucose metabolism and functional MRI: A PET/MR hybrid scanner study”. In: *NeuroImage* 113, pp. 111–121. DOI: 10.1016/j.neuroimage.2015.03.017.

Allen, Elena A. et al. (Mar. 2014). “Tracking whole-brain connectivity dynamics in the resting state”. In: *Cerebral Cortex* 24.3, pp. 663–676. DOI: 10.1093/cercor/bhs352.

Amend, Mario et al. (2019). “Functional resting-state brain connectivity is accompanied by dynamic correlations of application-dependent [18 F]FDG PET-tracer fluctuations”. In: *NeuroImage* 196, pp. 161–172. DOI: 10.1016/j.neuroimage.2019.04.034.

Amor, T. A. et al. (2015). “Extreme brain events: Higher-order statistics of brain resting activity and its relation with structural connectivity”. In: *EPL* 111.6. DOI: 10.1209/0295-5075/111/68007.

Anderson, Kevin M. et al. (2020). “Transcriptional and imaging-genetic association of cortical interneurons, brain function, and schizophrenia risk”. In: *Nature Communications* 11.1. DOI: 10.1038/s41467-020-16710-x.

Andersson, Jesper L.R., Stefan Skare, and John Ashburner (Oct. 2003). “How to correct susceptibility distortions in spin-echo echo-planar images: application to diffusion tensor imaging”. In: *NeuroImage* 20.2, pp. 870–888. ISSN: 10538119. DOI: 10.1016/S1053-8119(03)00336-7. URL: https://linkinghub.elsevier.com/retrieve/pii/S1053811903003367 (visited on 08/16/2022).

Arachchige, Chandima N. P. G., Luke A. Prendergast, and Robert G. Staudte (Aug. 20, 2020). "Robust analogs to the coefficient of variation". In: *Journal of Applied Statistics*, pp. 1–23. ISSN: 0266-4763, 1360-0532. DOI: 10.1080/02664763.2020.1808599. URL: https://www.tandfonline.com/doi/full/10.1080/02664763.2020.1808599 (visited on 04/03/2021).

Ashburner, John and Karl J. Friston (July 2005). "Unified segmentation". In: *NeuroImage* 26.3, pp. 839–851. ISSN: 10538119. DOI: 10.1016/j.neuroimage.2005.02.018. URL: https://linkinghub.elsevier.com/retrieve/pii/S1053811905001102 (visited on 08/16/2022).

Avants, Brian B. et al. (Feb. 2011). "A reproducible evaluation of ANTs similarity metric performance in brain image registration". In: *NeuroImage* 54.3, pp. 2033–2044.

Barrio, Jorge R. et al. (June 2020). "Does 2-FDG PET Accurately Reflect Quantitative In Vivo Glucose Utilization?" In: *Journal of Nuclear Medicine* 61.6, pp. 931–937. ISSN: 0161-5505, 2159-662X. DOI: 10.2967/jnumed.119.237446. URL: http://jnm.snmjournals.org/lookup/doi/10.2967/jnumed.119.237446 (visited on 04/05/2021).

Behzadi, Yashar et al. (2007). "A component based noise correction method (CompCor) for BOLD and perfusion based fMRI". In: *NeuroImage* 37.1, pp. 90–101. DOI: 10.1016/j.neuroimage.2007.04.042.

Belsley, David A. (1991). *Conditioning diagnostics: collinearity and weak data in regression*. Probability and mathematical statistics. New York: Wiley. 396 pp. ISBN: 978-0-471-52889-0.

Benjamini, Yoav and Yosef Hochberg (Jan. 1995). "Controlling the False Discovery Rate: A Practical and Powerful Approach to Multiple Testing". In: *Journal of the Royal Statistical Society: Series B (Methodological)* 57.1, pp. 289–300. ISSN: 00359246. DOI: 10.1111/j.2517-6161.1995.tb02031.x. URL: http://doi.wiley.com/10.1111/j.2517-6161.1995.tb02031.x (visited on 04/04/2021).

Bernier, Michaël et al. (2017). "Spatial distribution of resting-state BOLD regional homogeneity as a predictor of brain glucose uptake: A study in healthy aging". In: *NeuroImage* 150. Publisher: Academic Press Inc., pp. 14–22. ISSN: 10959572. DOI: 10.1016/j.neuroimage.2017.01.055.

Bertoldo, A., P. Peltoniemi, et al. (Sept. 1, 2001). "Kinetic modeling of [^{18} F]FDG in skeletal muscle by PET: a four-compartment five-rate-constant model". In: *American Journal of Physiology-Endocrinology and Metabolism* 281.3, E524–

E536. ISSN: 0193-1849, 1522-1555. DOI: 10.1152/ajpendo.2001.281.3.E524. URL: https://www.physiology.org/doi/10.1152/ajpendo.2001.281.3.E524 (visited on 04/05/2021).

Bertoldo, A., P. Vicini, et al. (Dec. 1998). "Evaluation of compartmental and spectral analysis models of [/sup 18/F]FDG kinetics for heart and brain studies with PET". In: *IEEE Transactions on Biomedical Engineering* 45.12, pp. 1429–1448. ISSN: 00189294. DOI: 10.1109/10.730437. URL: http://ieeexplore.ieee.org/document/730437/ (visited on 04/03/2021).

Bertoldo, Alessandra, Gaia Rizzo, and Mattia Veronese (2014). "Deriving physiological information from PET images: From SUV to compartmental modelling". In: *Clinical and Translational Imaging* 2.3, pp. 239–251. DOI: 10.1007/s40336-014-0067-x.

Betzel, Richard F. (2022). "Network neuroscience and the connectomics revolution". In: *Connectomic Deep Brain Stimulation*. Elsevier, pp. 25–58. ISBN: 978-0-12-821861-7. DOI: 10.1016/B978-0-12-821861-7.00002-6. URL: https://linkinghub.elsevier.com/retrieve/pii/B9780128218617000026 (visited on 07/02/2022).

Biswal, Bharat et al. (1995). "Functional Connectivity in the Motor Cortex of Resting Human Brain Using Echo-Planar MRI". In: *Magnetic Resonance in Medicine* 34.4, pp. 537–541. DOI: 10.1002/mrm.1910340409.

Blazey, Tyler et al. (2019). "Quantitative positron emission tomography reveals regional differences in aerobic glycolysis within the human brain". In: *Journal of Cerebral Blood Flow and Metabolism* 39.10. Publisher: SAGE Publications Ltd, pp. 2096–2102. DOI: 10.1177/0271678X18767005.

Blomqvist, G. et al. (July 1990). "Positron Emission Tomographic Measurements of Cerebral Glucose Utilization Using [1- 11 C]D-Glucose". In: *Journal of Cerebral Blood Flow & Metabolism* 10.4, pp. 467–483. ISSN: 0271-678X, 1559-7016. DOI: 10.1038/jcbfm.1990.89. URL: http://journals.sagepub.com/doi/10.1038/jcbfm.1990.89 (visited on 04/05/2021).

Boellaard, Ronald (May 2009). "Standards for PET Image Acquisition and Quantitative Data Analysis". In: *Journal of Nuclear Medicine* 50 (Suppl 1), 11S–20S. ISSN: 0161-5505, 2159-662X. DOI: 10.2967/jnumed.108.057182. URL: http://jnm.snmjournals.org/lookup/doi/10.2967/jnumed.108.057182 (visited on 08/26/2022).

Bolt, Taylor et al. (Aug. 2022). "A parsimonious description of global functional brain organization in three spatiotemporal patterns". In: *Nature Neuroscience*

25.8, pp. 1093–1103. ISSN: 1097-6256, 1546-1726. DOI: 10.1038/s41593-022-01118-1. URL: https://www.nature.com/articles/s41593-022-01118-1 (visited on 08/27/2022).

Britz-Cunningham, Scott H. and S. James Adelstein (Dec. 2003). "Molecular targeting with radionuclides: state of the science". In: *Journal of Nuclear Medicine: Official Publication, Society of Nuclear Medicine* 44.12, pp. 1945–1961. ISSN: 0161-5505.

Brix, G. et al. (Oct. 1997). "Performance evaluation of a whole-body PET scanner using the NEMA protocol. National Electrical Manufacturers Association". In: *Journal of Nuclear Medicine: Official Publication, Society of Nuclear Medicine* 38.10, pp. 1614–1623. ISSN: 0161-5505.

Brown, Morton B. and Alan B. Forsythe (June 1974). "Robust Tests for the Equality of Variances". In: *Journal of the American Statistical Association* 69.346, pp. 364–367. ISSN: 0162-1459, 1537-274X. DOI: 10.1080/01621459.1974.10482955. URL: http://www.tandfonline.com/doi/abs/10.1080/01621459.1974.10482955 (visited on 08/29/2022).

Buxton, Richard B. and Lawrence R. Frank (Jan. 1997). "A Model for the Coupling between Cerebral Blood Flow and Oxygen Metabolism during Neural Stimulation". In: *Journal of Cerebral Blood Flow & Metabolism* 17.1, pp. 64–72. ISSN: 0271-678X, 1559-7016. DOI: ca. URL: http://journals.sagepub.com/doi/10.1097/00004647-199701000-00009 (visited on 04/05/2021).

Buxton, Richard B., Kâmil Uludağ, et al. (Jan. 2004). "Modeling the hemodynamic response to brain activation". In: *NeuroImage* 23, S220–S233. ISSN: 10538119. DOI: 10.1016/j.neuroimage.2004.07.013. URL: https://linkinghub.elsevier.com/retrieve/pii/S1053811904003787 (visited on 04/05/2021).

Byrnes, Kimberly R. et al. (2014). "FDG-PET imaging in mild traumatic brain injury: a critical review". In: *Frontiers in Neuroenergetics* 5. ISSN: 1662-6427. DOI: 10.3389/fnene.2013.00013. URL: http://journal.frontiersin.org/article/10.3389/fnene.2013.00013/abstract (visited on 04/03/2021).

Cabral, Joana et al. (2017). "Cognitive performance in healthy older adults relates to spontaneous switching between states of functional connectivity during rest". In: *Scientific Reports* 7.1. DOI: ce.

Calhoun, V D et al. (2001). "A Method for Making Group Inferences from Functional MRI Data Using Independent Component Analysis". In: *Human Brain Mapping* 14.3, pp. 140–151. DOI: 10.1002/hbm.1048.

Carson, Ewart (2013). *Modelling methodology for physiology and medicine*. Waltham, MA: Elsevier. ISBN: 978-0-12-411557-6.

Carson, Richard E (Oct. 2000). "PET physiological measurements using constant infusion". In: *Nuclear Medicine and Biology* 27.7, pp. 657–660. ISSN: 09698051. DOI: 10.1016/S0969-8051(00)00138-4. URL: https://linkinghub.elsevier.com/retrieve/pii/S0969805100001384 (visited on 04/05/2021).

Castellaro, M. et al. (2017). "A Variational Bayesian inference method for parametric imaging of PET data". In: *NeuroImage* 150 (October 2016). Publisher: Elsevier, pp. 136–149. ISSN: 10959572. DOI: 10.1016/j.neuroimage.2017.02.009. URL: http://dx.doi.org/10.1016/j.neuroimage.2017.02.009.

Catana, Ciprian (May 2017). "Principles of Simultaneous PET/MR Imaging". In: *Magnetic Resonance Imaging Clinics of North America* 25.2, pp. 231–243. ISSN: 10649689. DOI: 10.1016/j.mric.2017.01.002. URL: https://linkinghub.elsevier.com/retrieve/pii/S1064968917300028 (visited on 04/05/2021).

Cecchin, Diego et al. (2017). "Brain PET and functional MRI: Why simultaneously using hybrid PET/MR systems?" In: *Quarterly Journal of Nuclear Medicine and Molecular Imaging* 61.4, pp. 345–359. DOI: 10.23736/S1824-4785.17.03008-4.

Chang, Catie and Gary H. Glover (Mar. 2010). "Time–frequency dynamics of resting-state brain connectivity measured with fMRI". In: *NeuroImage* 50.1, pp. 81–98. ISSN: 10538119. DOI: 10.1016/j.neuroimage.2009.12.011. URL: https://linkinghub.elsevier.com/retrieve/pii/S1053811909012981 (visited on 08/28/2022).

Chen, Jingyuan E. and Gary H. Glover (Feb. 2015). "BOLD fractional contribution to resting-state functional connectivity above 0.1 Hz". In: *NeuroImage* 107, pp. 207–218. ISSN: 10538119. DOI: 10.1016/j.neuroimage.2014.12.012. URL: https://linkinghub.elsevier.com/retrieve/pii/S1053811914010040 (visited on 05/22/2021).

Chen, Jingyuan E., Laura D. Lewis, et al. (2020). "Resting-state "physiological networks"". In: *NeuroImage* 213. DOI: 10.1016/j.neuroimage.2020.116707.

Chen, Kewei et al. (July 1998). "Noninvasive Quantification of the Cerebral Metabolic Rate for Glucose Using Positron Emission Tomography, ^{18}F-Fluoro-2-Deoxyglucose, the Patlak Method, and an Image-Derived Input Function". In: *Journal of Cerebral Blood Flow & Metabolism* 18.7, pp. 716–723. ISSN:

0271-678X, 1559-7016. DOI: 10.1097/00004647-199807000-00002. URL: http://journals.sagepub.com/doi/10.1097/00004647-199807000-00002 (visited on 10/12/2021).

Chen, Zhaolin et al. (Dec. 2018). "From simultaneous to synergistic MR-PET brain imaging: A review of hybrid MR-PET imaging methodologies". In: *Human Brain Mapping* 39.12, pp. 5126–5144. ISSN: 1065-9471, 1097-0193. DOI: 10.1002/hbm.24314. URL: https://onlinelibrary.wiley.com/doi/abs/10.1002/hbm.24314 (visited on 04/05/2021).

Ciric, Rastko et al. (2017). "Benchmarking of participant-level confound regression strategies for the control of motion artifact in studies of functional connectivity". In: *NeuroImage* 154, pp. 174–187. DOI: 10.1016/j.neuroimage.2017.03.020.

Clarke, Donald D and Louis Sokoloff (1999). "Circulation and energy metabolism in the brain". In: *Basic Neurochemistry: Molecular, Cellular and Medical Aspects. 6th edition. Philadelphia: Lippincott-Raven*. Vol. 81. URL: https://fordham.bepress.com/chem_facultypubshttps://fordham.bepress.com/chem_facultypubs/81.

Cobelli, Claudio and Ewart R. Carson (2008). *Introduction to modeling in physiology and medicine*. 1. ed. Academic Press series in biomedical engineering. OCLC: 253916250. Amsterdam: Elsevier, Acad. Press. 324 pp. ISBN: 978-0-12-160240-6.

Cornford, Eain M. et al. (June 1998). "Dynamic [^{18}F]fluorodeoxyglucose positron emission tomography and hypometabolic zones in seizures: Reduced capillary influx". In: *Annals of Neurology* 43.6, pp. 801–808. ISSN: 03645134. DOI: 10.1002/ana.410430615. URL: http://doi.wiley.com/10.1002/ana.410430615 (visited on 04/05/2021).

Crone, Christian (Aug. 1963). "The Permeability of Capillaries in Various Organs as Determined by Use of the 'Indicator Diffusion' Method". In: *Acta Physiologica Scandinavica* 58.4, pp. 292–305. ISSN: 00016772, 1365201X. DOI: 10.1111/j.1748-1716.1963.tb02652.x. URL: http://doi.wiley.com/10.1111/j.1748-1716.1963.tb02652.x (visited on 04/05/2021).

Cumming, Paul (Jan. 2014). "PET Neuroimaging: The White Elephant Packs His Trunk?" In: *NeuroImage* 84, pp. 1094–1100. ISSN: 10538119. DOI: 10.1016/j.neuroimage.2013.08.020. URL: https://linkinghub.elsevier.com/retrieve/pii/S1053811913008744 (visited on 04/05/2021).

Cunningham, Vincent J. and Terry Jones (Jan. 1993). "Spectral Analysis of Dynamic PET Studies". In: *Journal of Cerebral Blood Flow & Metabolism* 13.1, pp. 15–23. ISSN: 0271-678X, 1559-7016. DOI: 10.1038/jcbfm.1993.5. URL: http://journals.sagepub.com/doi/10.1038/jcbfm.1993.5 (visited on 09/19/2022).

Damaraju, E. et al. (2014). "Dynamic functional connectivity analysis reveals transient states of dysconnectivity in schizophrenia". In: *NeuroImage: Clinical* 5, pp. 298–308. DOI: 10.1016/j.nicl.2014.07.003.

Deng, Lifu et al. (May 2016). "Characterizing dynamic local functional connectivity in the human brain". In: *Scientific Reports* 6. DOI: 10.1038/srep26976.

Deng, Shengwen et al. (Apr. 2022). "Hemodynamic and metabolic correspondence of resting-state voxel-based physiological metrics in healthy adults". In: *NeuroImage* 250, p. 118923. ISSN: 10538119. URL: https://linkinghub.elsevier.com/retrieve/pii/S1053811922000350 (visited on 03/02/2022).

Desboulets, Loann David Denis (2018). "A review on variable selection in regression analysis". In: *Econometrics* 6.4. DOI: 10.3390/econometrics6040045.

Di, Xin and Bharat B. Biswal (Oct. 2012). "Metabolic Brain Covariant Networks as Revealed by FDG-PET with Reference to Resting-State fMRI Networks". In: *Brain Connectivity* 2.5, pp. 275–283. ISSN: 2158-0014, 2158-0022. DOI: 10.1089/brain.2012.0086. URL: http://www.liebertpub.com/doi/10.1089/brain.2012.0086 (visited on 04/05/2021).

Di, Xin, Suril Gohel, et al. (Nov. 2017). "Do all roads lead to Rome? A comparison of brain networks derived from inter-subject volumetric and metabolic covariance and moment-to-moment hemodynamic correlations in old individuals". In: *Brain Structure and Function* 222.8. Publisher: Springer Verlag, pp. 3833–3845. DOI: 10.1007/s00429-017-1438-7.

Doucet, Gaëlle et al. (2011). "Brain activity at rest: a multiscale hierarchical functional organization". In: *J Neurophysiol* 105, pp. 2753–2763. DOI: 10.1152/jn.00895.2010.-Spontaneous. URL: www.jn.org.

Elam, Jennifer Stine et al. (Dec. 2021). "The Human Connectome Project: A retrospective". In: *NeuroImage* 244, p. 118543. ISSN: 10538119. DOI: 10.1016/j.neuroimage.2021.118543. URL: https://linkinghub.elsevier.com/retrieve/pii/S1053811921008168 (visited on 03/27/2022).

Fang, Xiaotian T. et al. (Aug. 2021). "Identifying brain networks in synaptic density PET (11C-UCB-J) with independent component analysis". In: *NeuroImage* 237, p. 118167. ISSN: 10538119. DOI: 10.1016/j.neuroimage.

2021.118167. URL: https://linkinghub.elsevier.com/retrieve/pii/S1053811921004444 (visited on 08/15/2022).

Feng, Dagan, Sung-Cheng Huang, and Xinmin Wang (Mar. 1993). "Models for computer simulation studies of input functions for tracer kinetic modeling with positron emission tomography". In: *International Journal of Bio-Medical Computing* 32.2, pp. 95–110. ISSN: 00207101. DOI: 10.1016/0020-7101(93)90049-C. URL: https://linkinghub.elsevier.com/retrieve/pii/002071019390049C (visited on 10/12/2021).

Feng, Tao et al. (May 10, 2021). "Total-Body Quantitative Parametric Imaging of Early Kinetics of ^{18} F-FDG". In: *Journal of Nuclear Medicine* 62.5, pp. 738–744. ISSN: 0161-5505, 2159-662X. DOI: 10.2967/jnumed.119.238113. URL: http://jnm.snmjournals.org/lookup/doi/10.2967/jnumed.119.238113 (visited on 08/28/2022).

Fischl, Bruce, Martin I Sereno, and Anders M Dale (1999). *Cortical Surface-Based Analysis II: Inflation, Flattening, and a Surface-Based Coordinate System.* URL: http://www.idealibrary.com.

Fonov, Vladimir et al. (Jan. 2011). "Unbiased average age-appropriate atlases for pediatric studies". In: *NeuroImage* 54.1, pp. 313–327. ISSN: 10538119. DOI: 10.1016/j.neuroimage.2010.07.033. URL: https://linkinghub.elsevier.com/retrieve/pii/S1053811910010062 (visited on 03/27/2022).

Fox, Michael D. and Marcus E. Raichle (Sept. 2007). "Spontaneous fluctuations in brain activity observed with functional magnetic resonance imaging". In: *Nature Reviews Neuroscience* 8.9, pp. 700–711. ISSN: 1471-003X, 1471-0048. DOI: 10.1038/nrn2201. URL: http://www.nature.com/articles/nrn2201 (visited on 04/03/2021).

Fox, P. et al. (July 22, 1988). "Nonoxidative glucose consumption during focal physiologic neural activity". In: *Science* 241.4864, pp. 462–464. ISSN: 0036-8075, 1095-9203. DOI: 10.1126/science.3260686. URL: https://www.sciencemag.org/lookup/doi/10.1126/science.3260686 (visited on 04/05/2021).

Fox, Peter T. (Aug. 2012). "The coupling controversy". In: *NeuroImage* 62.2, pp. 594–601. ISSN: 10538119. DOI: 10.1016/j.neuroimage.2012.01.103. URL: https://linkinghub.elsevier.com/retrieve/pii/S1053811912001218 (visited on 04/05/2021).

Freeman, Linton C. (Mar. 1977). "A Set of Measures of Centrality Based on Betweenness". In: *Sociometry* 40.1, p. 35. ISSN: 00380431. DOI: 10.2307/

3033543. URL: https://www.jstor.org/stable/3033543?origin=crossref (visited on 04/03/2021).

Friston, K.J. et al. (Jan. 1998). "Event-Related fMRI: Characterizing Differential Responses". In: *NeuroImage* 7.1, pp. 30–40. ISSN: 10538119. DOI: 10.1006/nimg.1997.0306. URL: https://linkinghub.elsevier.com/retrieve/pii/S1053811997903062 (visited on 04/03/2021).

Furler, S. M. et al. (Sept. 1, 1991). "In vivo location of the rate-limiting step of hexose uptake in muscle and brain tissue of rats". In: *American Journal of Physiology-Endocrinology and Metabolism* 261.3, E337–E347. ISSN: 0193-1849, 1522-1555. DOI: 10.1152/ajpendo.1991.261.3.E337. URL: https://www.physiology.org/doi/10.1152/ajpendo.1991.261.3.E337 (visited on 04/05/2021).

Garrett, D. D. et al. (Apr. 7, 2010). "Blood Oxygen Level-Dependent Signal Variability Is More than Just Noise". In: *Journal of Neuroscience* 30.14, pp. 4914–4921. ISSN: 0270-6474, 1529-2401. DOI: 10.1523/JNEUROSCI.5166-09.2010. URL: http://www.jneurosci.org/cgi/doi/10.1523/JNEUROSCI.5166-09.2010 (visited on 04/04/2021).

Gauthier, C.J. and A.P. Fan (Feb. 2019). "BOLD signal physiology: Models and applications". In: *NeuroImage* 187, pp. 116–127. ISSN: 10538119. DOI: 10.1016/j.neuroimage.2018.03.018. URL: https://linkinghub.elsevier.com/retrieve/pii/S1053811918302222 (visited on 04/05/2021).

Glasser, Matthew F., Manu S. Goyal, et al. (June 2014). "Trends and properties of human cerebral cortex: Correlations with cortical myelin content". In: *NeuroImage* 93, pp. 165–175. ISSN: 10538119. DOI: 10.1016/j.neuroimage.2013.03.060. URL: https://linkinghub.elsevier.com/retrieve/pii/S1053811913003108 (visited on 09/19/2022).

Glasser, Matthew F., Stamatios N. Sotiropoulos, et al. (Oct. 2013). "The minimal preprocessing pipelines for the Human Connectome Project". In: *NeuroImage* 80, pp. 105–124. ISSN: 10538119. DOI: h. URL: https://linkinghub.elsevier.com/retrieve/pii/S1053811913005053 (visited on 04/03/2021).

Golestani, Ali M., Luxi L. Wei, and J. Jean Chen (Sept. 2016). "Quantitative mapping of cerebrovascular reactivity using resting-state BOLD fMRI: Validation in healthy adults". In: *NeuroImage* 138, pp. 147–163. ISSN: 10538119. DOI: 10.1016/j.neuroimage.2016.05.025. URL: https://linkinghub.elsevier.com/retrieve/pii/S1053811916301458 (visited on 04/03/2021).

Golub, G. H. and C. Reinsch (Apr. 1970). "Singular value decomposition and least squares solutions". In: *Numerische Mathematik* 14.5, pp. 403–420. ISSN: 0029-599X, 0945-3245. DOI: 10.1007/BF02163027. URL: http://link.springer.com/10.1007/BF02163027 (visited on 04/03/2021).

Goutte, C., F.A. Nielsen, and K.H. Hansen (Dec. 2000). "Modeling the hemodynamic response in fMRI using smooth FIR filters". In: *IEEE Transactions on Medical Imaging* 19.12, pp. 1188–1201. ISSN: 02780062. DOI: 10.1109/42.897811. URL: http://ieeexplore.ieee.org/document/897811/ (visited on 04/03/2021).

Goyal, Manu S., Tyler Blazey, et al. (June 23, 2022). *Brain aerobic glycolysis and resilience in Alzheimer disease*. preprint. Neuroscience. DOI: 10.1101/2022.06.21.497006. URL: http://biorxiv.org/lookup/doi/10.1101/2022.06.21.497006 (visited on 10/25/2022).

Goyal, Manu S., Andrei G. Vlassenko, et al. (Aug. 2017). "Loss of Brain Aerobic Glycolysis in Normal Human Aging". In: *Cell Metabolism* 26.2, 353–360.e3. ISSN: 15504131. DOI: 10.1016/j.cmet.2017.07.010. URL: https://linkinghub.elsevier.com/retrieve/pii/S155041311730431X (visited on 04/03/2021).

Graham, Michael M. et al. (Sept. 2002). "The FDG lumped constant in normal human brain". In: *Journal of Nuclear Medicine: Official Publication, Society of Nuclear Medicine* 43.9, pp. 1157–1166. ISSN: 0161-5505.

Greicius, M. D. et al. (Jan. 7, 2003). "Functional connectivity in the resting brain: A network analysis of the default mode hypothesis". In: *Proceedings of the National Academy of Sciences* 100.1, pp. 253–258. ISSN: 0027-8424, 1091-6490. DOI: 10.1073/pnas.0135058100. URL: http://www.pnas.org/cgi/doi/10.1073/pnas.0135058100 (visited on 04/03/2021).

Hahn, Andreas et al. (Apr. 21, 2020). "Reconfiguration of functional brain networks and metabolic cost converge during task performance". In: *eLife* 9, e52443. ISSN: 2050-084X. DOI: 10.7554/eLife.52443. URL: https://elifesciences.org/articles/52443 (visited on 04/05/2021).

Hamberg, L. M. et al. (Aug. 1994). "The dose uptake ratio as an index of glucose metabolism: useful parameter or oversimplification?" In: *Journal of Nuclear Medicine: Official Publication, Society of Nuclear Medicine* 35.8, pp. 1308–1312. ISSN: 0161-5505.

Hammers, Alexander et al. (Aug. 2003). "Three-dimensional maximum probability atlas of the human brain, with particular reference to the temporal lobe".

In: *Human Brain Mapping* 19.4, pp. 224–247. ISSN: 1065-9471, 1097-0193. DOI: 10.1002/hbm.10123. URL: https://onlinelibrary.wiley.com/doi/10.1002/hbm.10123 (visited on 08/18/2021).

Hattori, Naoya et al. (Nov. 2003). "Correlation of regional metabolic rates of glucose with glasgow coma scale after traumatic brain injury". In: *Journal of Nuclear Medicine: Official Publication, Society of Nuclear Medicine* 44.11, pp. 1709–1716. ISSN: 0161-5505.

Heiss, W.-D. et al. (June 1984). "Regional Kinetic Constants and Cerebral Metabolic Rate for Glucose in Normal Human Volunteers Determined by Dynamic Positron Emission Tomography of [^{18} F]-2-Fluoro-2-Deoxy-D-Glucose". In: *Journal of Cerebral Blood Flow & Metabolism* 4.2, pp. 212–223. ISSN: 0271-678X, 1559-7016. DOI: 10.1038/jcbfm.1984.30. URL: http://journals.sagepub.com/doi/10.1038/jcbfm.1984.30 (visited on 04/05/2021).

Hellyer, Peter J. et al. (July 2017). "Protein synthesis is associated with high-speed dynamics and broad-band stability of functional hubs in the brain". In: *NeuroImage* 155, pp. 209–216. ISSN: 10538119. DOI: 10.1016/j.neuroimage.2017.04.062. URL: https://linkinghub.elsevier.com/retrieve/pii/S1053811917303828 (visited on 04/03/2021).

Henriksen, Otto M., Albert Gjedde, et al. (June 1, 2021). "Regional and interindividual relationships between cerebral perfusion and oxygen metabolism". In: *Journal of Applied Physiology* 130.6, pp. 1836–1847. ISSN: 8750-7587, 1522-1601. DOI: 10.1152/japplphysiol.00939.2020. URL: https://journals.physiology.org/doi/10.1152/japplphysiol.00939.2020 (visited on 08/31/2022).

Henriksen, Otto M., Mark B. Vestergaard, et al. (Oct. 1, 2018). "Interindividual and regional relationship between cerebral blood flow and glucose metabolism in the resting brain". In: *Journal of Applied Physiology (Bethesda, Md.: 1985)* 125.4, pp. 1080–1089. ISSN: 1522-1601. DOI: ho.

Herculano-Houzel, Suzana (Sept. 2014). "The glia/neuron ratio: How it varies uniformly across brain structures and species and what that means for brain physiology and evolution: The Glia/Neuron Ratio". In: *Glia* 62.9, pp. 1377–1391. ISSN: 08941491. DOI: 10.1002/glia.22683. URL: http://doi.wiley.com/10.1002/glia.22683 (visited on 04/05/2021).

Hermanides, Jeroen et al. (Dec. 16, 2021). "Metabolic derangements are associated with impaired glucose delivery following traumatic brain injury". In: *Brain* 144.11, pp. 3492–3504. ISSN: 0006-8950, 1460-2156. DOI: 10.1093/

brain/awab255. URL: https://academic.oup.com/brain/article/144/11/3492/6317666 (visited on 08/25/2022).

Heuvel, Martijn van den, Rene Mandl, and Hilleke Hulshoff Pol (Apr. 23, 2008). "Normalized Cut Group Clustering of Resting-State fMRI Data". In: *PLoS ONE* 3.4. Ed. by Björn Brembs, e2001. ISSN: 1932-6203. DOI: 10.1371/journal.pone.0002001. URL: https://dx.plos.org/10.1371/journal.pone.0002001 (visited on 08/28/2022).

Hocking, R. R. (Mar. 1976). "A Biometrics Invited Paper. The Analysis and Selection of Variables in Linear Regression". In: *Biometrics* 32.1, p. 1. ISSN: 0006341X. DOI: 10.2307/2529336. URL: https://www.jstor.org/stable/2529336?origin=crossref (visited on 04/03/2021).

Honey, C. J. et al. (Feb. 10, 2009). "Predicting human resting-state functional connectivity from structural connectivity". In: *Proceedings of the National Academy of Sciences* 106.6, pp. 2035–2040. ISSN: 0027-8424, 1091-6490. DOI: 10.1073/pnas.0811168106. URL: http://www.pnas.org/lookup/doi/10.1073/pnas.0811168106 (visited on 04/04/2021).

Hoover, Kevin D. and Stephen J. Perez (Dec. 1, 1999). "Data mining reconsidered: encompassing and the general-to-specific approach to specification search". In: *The Econometrics Journal* 2.2, pp. 167–191. ISSN: 1368-4221, 1368-423X. DOI: 10.1111/1368-423X.00025. URL: https://academic.oup.com/ectj/article/2/2/167-191/5071697 (visited on 04/03/2021).

Horwitz, Barry, Ranjan Duara, and Stanley I. Rapoport (Dec. 1984). "Intercorrelations of Glucose Metabolic Rates between Brain Regions: Application to Healthy Males in a State of Reduced Sensory Input". In: *Journal of Cerebral Blood Flow & Metabolism* 4.4, pp. 484–499. ISSN: 0271-678X, 1559-7016. DOI: 10.1038/jcbfm.1984.73. URL: http://journals.sagepub.com/doi/10.1038/jcbfm.1984.73 (visited on 04/06/2021).

Howarth, Clare, Anusha Mishra, and Catherine N. Hall (Jan. 4, 2021). "More than just summed neuronal activity: how multiple cell types shape the BOLD response". In: *Philosophical Transactions of the Royal Society B: Biological Sciences* 376.1815, p. 20190630. ISSN: 0962-8436, 1471-2970. DOI: 10.1098/rstb.2019.0630. URL: https://royalsocietypublishing.org/doi/10.1098/rstb.2019.0630 (visited on 04/03/2021).

Hox, J. J., Mirjam Moerbeek, and Rens van de Schoot (2017). *Multilevel analysis: techniques and applications*. Third edition. Quantitative methodology series. New York, NY: Routledge. ISBN: 978-1-138-12140-9 978-1-138-12136-2.

Huang, S. C. et al. (Jan. 1, 1980). "Noninvasive determination of local cerebral metabolic rate of glucose in man". In: *American Journal of Physiology-Endocrinology and Metabolism* 238.1, E69–E82. ISSN: 0193-1849, 1522-1555. DOI: 10.1152/ajpendo.1980.238.1.E69. URL: https://www.physiology.org/doi/10.1152/ajpendo.1980.238.1.E69 (visited on 08/11/2022).

Huang, Sung-Cheng (Oct. 2000). "Anatomy of SUV". In: *Nuclear Medicine and Biology* 27.7, pp. 643–646. ISSN: 09698051. DOI: 10.1016/S0969-8051(00)00155-4. URL: https://linkinghub.elsevier.com/retrieve/pii/S0969805100001554 (visited on 04/06/2021).

Huisman, Marc C et al. (2012). "Cerebral blood flow and glucose metabolism in healthy volunteers measured using a high-resolution PET scanner". In: *EJNMMI Research* 2.1, p. 63. ISSN: 2191-219X. DOI: 10.1186/2191-219X-2-63. URL: http://ejnmmires.springeropen.com/articles/10.1186/2191-219X-2-63 (visited on 04/06/2021).

Hutchison, R. Matthew et al. (Oct. 2013). "Dynamic functional connectivity: Promise, issues, and interpretations". In: *NeuroImage* 80, pp. 360–378. ISSN: 10538119. DOI: 10.1016/j.neuroimage.2013.05.079. URL: https://linkinghub.elsevier.com/retrieve/pii/S105381191300579X (visited on 04/03/2021).

Hyder, Fahmeed et al. (May 2016). "Uniform distributions of glucose oxidation and oxygen extraction in gray matter of normal human brain: No evidence of regional differences of aerobic glycolysis". In: *Journal of Cerebral Blood Flow & Metabolism* 36.5, pp. 903–916. ISSN: 0271-678X, 1559-7016. DOI: 10.1177/0271678X15625349. URL: http://journals.sagepub.com/doi/10.1177/0271678X15625349 (visited on 04/04/2021).

Ionescu, Tudor M. et al. (Apr. 2021). "Elucidating the complementarity of resting-state networks derived from dynamic [18F]FDG and hemodynamic fluctuations using simultaneous small-animal PET/MRI". In: *NeuroImage*, p. 118045. ISSN: 10538119. DOI: 10.1016/j.neuroimage.2021.118045. URL: https://linkinghub.elsevier.com/retrieve/pii/S1053811921003220 (visited on 04/14/2021).

Jain, Anil K. and Richard C. Dubes (1988). *Algorithms for clustering data*. Prentice Hall advanced reference series. Englewood Cliffs, N.J: Prentice Hall. 320 pp. ISBN: 978-0-13-022278-7.

Jamadar, Sharna D et al. (Feb. 3, 2021). "Metabolic and Hemodynamic Resting-State Connectivity of the Human Brain: A High-Temporal Resolution Simultaneous BOLD-fMRI and FDG-fPET Multimodality Study". In: *Cerebral Cortex*, bhaa393. ISSN: 1047-3211, 1460-2199. DOI: 10.1093/cercor/bhaa393. URL: https://academic.oup.com/cercor/advance-article/doi/10.1093/cercor/bhaa393/6126755 (visited on 04/06/2021).

Jenkinson, Mark, Peter Bannister, et al. (2002). "Improved Optimization for the Robust and Accurate Linear Registration and Motion Correction of Brain Images". In: *NeuroImage* 17.2. Publisher: Elsevier BV, pp. 825–841. ISSN: 10538119. DOI: 10.1006/nimg.2002.1132.

Jenkinson, Mark, Christian F. Beckmann, et al. (2012). "FSL". In: *NeuroImage* 62.2, pp. 782–790. ISSN: 1095-9572 (Electronic). DOI: 10.1016/j.neuroimage.2011.09.015.

Jerman, Tim et al. (Sept. 2016). "Enhancement of Vascular Structures in ¡?Pub _newline ?¿ 3D and 2D Angiographic Images". In: *IEEE Transactions on Medical Imaging* 35.9, pp. 2107–2118. ISSN: 0278-0062, 1558-254X. DOI: 10.1109/TMI.2016.2550102. URL: http://ieeexplore.ieee.org/document/7446363/ (visited on 10/12/2021).

Jiang, Lili and Xi-Nian Zuo (Oct. 2016). "Regional Homogeneity: A Multimodal, Multiscale Neuroimaging Marker of the Human Connectome". In: *The Neuroscientist* 22.5, pp. 486–505. ISSN: 1073-8584, 1089-4098. DOI: 10.1177/1073858415595004. URL: http://journals.sagepub.com/doi/10.1177/1073858415595004 (visited on 04/06/2021).

Kety, Seymour S. (1957). "Determinants of tissue oxygen tension". In: *Federation Proceedings* 16.3, pp. 666–671.

Kety, Seymour S. and Carl F. Schmidt (Jan. 1, 1945). "THE DETERMINATION OF CEREBRAL BLOOD FLOW IN MAN BY THE USE OF NITROUS OXIDE IN LOW CONCENTRATIONS". In: *American Journal of Physiology-Legacy Content* 143.1, pp. 53–66. ISSN: 0002-9513. DOI: 10.1152/ajplegacy.1945.143.1.53. URL: https://www.physiology.org/doi/10.1152/ajplegacy.1945.143.1.53 (visited on 08/16/2022).

Keyes, J. W. (Oct. 1995). "SUV: standard uptake or silly useless value?" In: *Journal of Nuclear Medicine: Official Publication, Society of Nuclear Medicine* 36.10, pp. 1836–1839. ISSN: 0161-5505.

Kim, Seong-Gi and Seiji Ogawa (July 2012). "Biophysical and Physiological Origins of Blood Oxygenation Level-Dependent fMRI Signals". In: *Journal of Cerebral Blood Flow & Metabolism* 32.7, pp. 1188–1206. ISSN: 0271-678X, 1559-7016. DOI: 10.1038/jcbfm.2012.23. URL: http://journals.sagepub.com/doi/10.1038/jcbfm.2012.23 (visited on 04/03/2021).

Kundu, Prantik et al. (July 2017). “Multi-echo fMRI: A review of applications in fMRI denoising and analysis of BOLD signals”. In: *NeuroImage* 154, pp. 59–80. ISSN: 10538119. DOI: 10.1016/j.neuroimage.2017.03.033. URL: https://linkinghub.elsevier.com/retrieve/pii/S1053811917302410 (visited on 04/04/2021).

Kwong, K K et al. (June 15, 1992). “Dynamic magnetic resonance imaging of human brain activity during primary sensory stimulation.” In: *Proceedings of the National Academy of Sciences* 89.12, pp. 5675–5679. ISSN: 0027-8424, 1091-6490. DOI: 10.1073/pnas.89.12.5675. URL: https://pnas.org/doi/full/10.1073/pnas.89.12.5675 (visited on 11/24/2022).

Laird, N. M. and J. H. Ware (Dec. 1982). “Random-effects models for longitudinal data”. In: *Biometrics* 38.4, pp. 963–974. ISSN: 0006-341X.

Lammertsma, Adriaan A. (July 2017). “Forward to the Past: The Case for Quantitative PET Imaging”. In: *Journal of Nuclear Medicine* 58.7, pp. 1019–1024. ISSN: 0161-5505, 2159-662X. DOI: 10.2967/jnumed.116.188029. URL: http://jnm.snmjournals.org/lookup/doi/10.2967/jnumed.116.188029 (visited on 01/16/2022).

Latora, Vito and Massimo Marchiori (Oct. 17, 2001). “Efficient Behavior of Small-World Networks”. In: *Physical Review Letters* 87.19, p. 198701. ISSN: 0031-9007, 1079-7114. DOI: 10.1103/PhysRevLett.87.198701. URL: https://link.aps.org/doi/10.1103/PhysRevLett.87.198701 (visited on 04/03/2021).

Laumann, Timothy O. et al. (Sept. 2, 2016). “On the Stability of BOLD fMRI Correlations”. In: *Cerebral Cortex*, cercor, bhw265v1. ISSN: 1047-3211, 1460-2199. DOI: 10.1093/cercor/bhw265. URL: http://cercor.oxfordjournals.org/cgi/doi/10.1093/cercor/bhw265 (visited on 04/03/2021).

Lawson, Charles L. and Richard J. Hanson (Jan. 1, 1974). *Solving least squares problems*. Prentice-Hall Series in Automatic Computation. Englewood Cliffs:Prentice-Hall.

Lee, John J. et al. (May 2010). “Dynamic susceptibility contrast MRI with localized arterial input functions”. In: *Magnetic Resonance in Medicine* 63.5, pp. 1305–1314. ISSN: 07403194. DOI: 10.1002/mrm.22338. URL: https://onlinelibrary.wiley.com/doi/10.1002/mrm.22338 (visited on 08/16/2022).

Leonardi, Nora and Dimitri Van De Ville (Jan. 2015). "On spurious and real fluctuations of dynamic functional connectivity during rest". In: *NeuroImage* 104, pp. 430–436. ISSN: 10538119. DOI: 10.1016/j.neuroimage.2014.09.007. URL: https://linkinghub.elsevier.com/retrieve/pii/S1053811914007496 (visited on 04/03/2021).

Li, Shenpeng et al. (June 2020). "Analysis of continuous infusion functional PET (fPET) in the human brain". In: *NeuroImage* 213, p. 116720. ISSN: 10538119. DOI: 10.1016/j.neuroimage.2020.116720. URL: https://linkinghub.elsevier.com/retrieve/pii/S105381192030207X (visited on 04/06/2021).

Li, Zhengjun, Aniseh Kadivar, et al. (Aug. 2012). "Test-retest stability analysis of resting brain activity revealed by blood oxygen level-dependent functional MRI". In: *Journal of Magnetic Resonance Imaging* 36.2, pp. 344–354. ISSN: 10531807. DOI: 10.1002/jmri.23670. URL: https://onlinelibrary.wiley.com/doi/10.1002/jmri.23670 (visited on 08/31/2022).

Li, Zhengjun, Yisheng Zhu, et al. (Sept. 21, 2012). "Relations between BOLD fMRI-Derived Resting Brain Activity and Cerebral Blood Flow". In: *PLoS ONE* 7.9. Ed. by Emmanuel Andreas Stamatakis, e44556. ISSN: 1932-6203. DOI: 10.1371/journal.pone.0044556. URL: https://dx.plos.org/10.1371/journal.pone.0044556 (visited on 04/06/2021).

Liang, X. et al. (Jan. 29, 2013). "Coupling of functional connectivity and regional cerebral blood flow reveals a physiological basis for network hubs of the human brain". In: *Proceedings of the National Academy of Sciences* 110.5, pp. 1929–1934. ISSN: 0027-8424, 1091-6490. DOI: 10.1073/pnas.1214900110. URL: http://www.pnas.org/cgi/doi/10.1073/pnas.1214900110 (visited on 04/03/2021).

Liptrot, Matthew et al. (Feb. 2004). "Cluster analysis in kinetic modelling of the brain: a noninvasive alternative to arterial sampling". In: *NeuroImage* 21.2, pp. 483–493. ISSN: 10538119. DOI: 10.1016/j.neuroimage.2003.09.058. URL: https://linkinghub.elsevier.com/retrieve/pii/S1053811903006086 (visited on 03/27/2022).

Liu, Thomas T. (Oct. 2013). "Neurovascular factors in resting-state functional MRI". In: *NeuroImage* 80, pp. 339–348. ISSN: 10538119. DOI: 10.1016/j.neuroimage.2013.04.071. URL: https://linkinghub.elsevier.com/retrieve/pii/S1053811913004187 (visited on 04/03/2022).

Logothetis, N. K. et al. (2001). "Neurophysiological investigation of the basis of the fMRI signal." In: *Nature* 412.6843, pp. 150–157. ISSN: 0028-0836 (Print). DOI: 10.1038/35084005.

Logothetis, Nikos K. (June 2008). "What we can do and what we cannot do with fMRI". In: *Nature* 453.7197, pp. 869–878. ISSN: 0028-0836, 1476-4687. DOI: 10.1038/nature06976. URL: http://www.nature.com/articles/nature06976 (visited on 04/06/2021).

Lohmann, Gabriele et al. (Apr. 27, 2010). "Eigenvector Centrality Mapping for Analyzing Connectivity Patterns in fMRI Data of the Human Brain". In: *PLoS ONE* 5.4. Ed. by Olaf Sporns, e10232. ISSN: 1932-6203. DOI: 10.1371/journal.pone.0010232. URL: https://dx.plos.org/10.1371/journal.pone.0010232 (visited on 04/03/2021).

Lord, Louis-David et al. (Oct. 2019). "Dynamical exploration of the repertoire of brain networks at rest is modulated by psilocybin". In: *NeuroImage* 199, pp. 127–142. ISSN: 10538119. DOI: 10.1016/j.neuroimage.2019.05.060. URL: https://linkinghub.elsevier.com/retrieve/pii/S1053811919304525 (visited on 04/03/2021).

Luo, Wen and Razia Azen (Feb. 2013). "Determining Predictor Importance in Hierarchical Linear Models Using Dominance Analysis". In: *Journal of Educational and Behavioral Statistics* 38.1, pp. 3–31. ISSN: 1076-9986, 1935-1054. DOI: 10.3102/1076998612458319. URL: http://journals.sagepub.com/doi/10.3102/1076998612458319 (visited on 05/16/2021).

Lurie, Daniel J. et al. (Jan. 2020). "Questions and controversies in the study of time-varying functional connectivity in resting fMRI". In: *Network Neuroscience* 4.1, pp. 30–69. ISSN: 2472-1751. DOI: 10.1162/netn_a_00116. URL: https://direct.mit.edu/netn/article/4/1/30-69/95807 (visited on 04/06/2021).

Magistretti, P. J. and L. Pellerin (1999). "Cellular mechanisms of brain energy metabolism and their relevance to functional brain imaging." In: *Philosophical transactions of the Royal Society of London. Series B, Biological sciences* 354.1387, pp. 1155–1163. DOI: 10.1098/rstb.1999.0471.

Mann, Kevin et al. (May 13, 2021). "Coupling of activity, metabolism and behaviour across the Drosophila brain". In: *Nature* 593.7858, pp. 244–248. ISSN: 0028-0836, 1476-4687. DOI: 10.1038/s41586-021-03497-0. URL: http://www.nature.com/articles/s41586-021-03497-0 (visited on 03/02/2022).

Mantel, Nathan and William Haenszel (Apr. 1, 1959). "Statistical Aspects of the Analysis of Data From Retrospective Studies of Disease". In: *JNCI: Journal of the National Cancer Institute* 22.4, pp. 719–748. ISSN: 0027-8874. DOI: 10.1093/jnci/22.4.719. URL: https://doi.org/10.1093/jnci/22.4.719 (visited on 07/30/2022).

Marcus, Daniel S. et al. (2011). "Informatics and Data Mining Tools and Strategies for the Human Connectome Project". In: *Frontiers in Neuroinformatics* 5. ISSN: 1662-5196. DOI: 10.3389/fninf.2011.00004. URL: http://journal.frontiersin.org/article/10.3389/fninf.2011.00004/abstract (visited on 04/03/2021).

Margulies, Daniel S. et al. (2016). "Situating the default-mode network along a principal gradient of macroscale cortical organization". In: *Proceedings of the National Academy of Sciences of the United States of America* 113.44. Publisher: National Academy of Sciences, pp. 12574–12579. ISSN: 10916490. DOI: 10.1073/pnas.1608282113.

Markello, Ross D. and Bratislav Misic (Aug. 2021). "Comparing spatial null models for brain maps". In: *NeuroImage* 236, p. 118052. ISSN: 10538119. DOI: 10.1016/j.neuroimage.2021.118052. URL: https://linkinghub.elsevier.com/retrieve/pii/S1053811921003293 (visited on 09/19/2022).

Meikle, Steven R et al. (Mar. 21, 2021). "Quantitative PET in the 2020s: a roadmap". In: *Physics in Medicine & Biology* 66.6, 06RM01. ISSN: 0031-9155, 1361-6560. DOI: 10.1088/1361-6560/abd4f7. URL: https://iopscience.iop.org/article/10.1088/1361-6560/abd4f7 (visited on 08/26/2022).

Meinshausen, Nicolai (2013). "Sign-constrained least squares estimation for high-dimensional regression". In: *Electronic Journal of Statistics* 7.1, pp. 1607–1631.

Müller, Samuel, J. L. Scealy, and A. H. Welsh (May 1, 2013). "Model Selection in Linear Mixed Models". In: *Statistical Science* 28.2. ISSN: 0883-4237. DOI: 10.1214/12-STS410. URL: https://projecteuclid.org/journals/statistical-science/volume-28/issue-2/Model-Selection-in-Linear-Mixed-Models/10.1214/12-STS410.full (visited on 04/03/2021).

Muthukumaraswamy, Suresh D. et al. (Feb. 2012). "Individual variability in the shape and amplitude of the BOLD-HRF correlates with endogenous GABAergic inhibition". In: *Human Brain Mapping* 33.2, pp. 455–465. ISSN: 10659471. DOI: 10.1002/hbm.21223. URL: http://doi.wiley.com/10.1002/hbm.21223 (visited on 04/04/2021).

Narciso, Lucas, Tracy Ssali, Hidehiro Iida, et al. (Mar. 21, 2021). “A non-invasive reference-based method for imaging the cerebral metabolic rate of oxygen by PET/MR: theory and error analysis”. In: *Physics in Medicine & Biology* 66.6, p. 065009. ISSN: 0031-9155, 1361-6560. DOI: 10.1088/1361-6560/abe737. URL: https://iopscience.iop.org/article/10.1088/1361-6560/abe737 (visited on 08/16/2022).

Narciso, Lucas, Tracy Ssali, Linshan Liu, Heather Biernaski, et al. (Dec. 2021). “A Noninvasive Method for Quantifying Cerebral Metabolic Rate of Oxygen by Hybrid PET/MRI: Validation in a Porcine Model”. In: *Journal of Nuclear Medicine* 62.12, pp. 1789–1796. ISSN: 0161-5505, 2159-662X. DOI: 10.2967/jnumed.120.260521. URL: http://jnm.snmjournals.org/lookup/doi/10.2967/jnumed.120.260521 (visited on 08/16/2022).

Narciso, Lucas, Tracy Ssali, Linshan Liu, Sarah Jesso, et al. (Feb. 28, 2022). “Non-invasive Quantification of Cerebral Blood Flow Using Hybrid ¡span style=”font-variant:small-caps;”¿PET¡/span¿ / ¡span style=”font-variant:small-caps;”¿MR¡/span¿ Imaging to Extract the [¡span style=”font-variant:small-caps;”¿ ^{15} O ¡/span¿] ¡span style=”font-variant:small-caps;”¿ H $_{2}$ O ¡/span¿ Image-Derived Input Function Free of Partial Volume Errors”. In: *Journal of Magnetic Resonance Imaging*, jmri.28134. ISSN: 1053-1807, 1522-2586. DOI: 10.1002/jmri.28134. URL: https://onlinelibrary.wiley.com/doi/10.1002/jmri.28134 (visited on 08/16/2022).

Nugent, Allison C et al. (Apr. 2015). “The Relationship between Glucose Metabolism, Resting-State fMRI BOLD Signal, and GABA $_{A}$ -Binding Potential: A Preliminary Study in Healthy Subjects and Those with Temporal Lobe Epilepsy”. In: *Journal of Cerebral Blood Flow & Metabolism* 35.4, pp. 583–591. ISSN: 0271-678X, 1559-7016. URL: http://journals.sagepub.com/doi/10.1038/jcbfm.2014.228 (visited on 04/04/2021).

Ogawa, S., T. M. Lee, et al. (Dec. 1, 1990). “Brain magnetic resonance imaging with contrast dependent on blood oxygenation.” In: *Proceedings of the National Academy of Sciences* 87.24, pp. 9868–9872. ISSN: 0027-8424, 1091-6490. DOI: 10.1073/pnas.87.24.9868. URL: http://www.pnas.org/cgi/doi/10.1073/pnas.87.24.9868 (visited on 04/06/2021).

Ogawa, S., R.S. Menon, et al. (Mar. 1993). “Functional brain mapping by blood oxygenation level-dependent contrast magnetic resonance imaging. A comparison of signal characteristics with a biophysical model”. In: *Biophysical Journal* 64.3, pp. 803–812. ISSN: 00063495. DOI: 10.1016/S0006-3495(93)

81441-3. URL: https://linkinghub.elsevier.com/retrieve/pii/S0006349593814413 (visited on 04/06/2021).

Omidvarnia, Amir, Raphaël Liégeois, et al. (Aug. 18, 2022). "On the Spatial Distribution of Temporal Complexity in Resting State and Task Functional MRI". In: *Entropy* 24.8, p. 1148. ISSN: 1099-4300. DOI: 10.3390/e24081148. URL: https://www.mdpi.com/1099-4300/24/8/1148 (visited on 08/27/2022).

Omidvarnia, Amir, Mostefa Mesbah, et al. (Dec. 13, 2018). "Range Entropy: A Bridge between Signal Complexity and Self-Similarity". In: *Entropy* 20.12, p. 962. ISSN: 1099-4300. DOI: 10.3390/e20120962. URL: http://www.mdpi.com/1099-4300/20/12/962 (visited on 04/03/2021).

Onnela, Jukka-Pekka et al. (June 13, 2005). "Intensity and coherence of motifs in weighted complex networks". In: *Physical Review E* 71.6, p. 065103. ISSN: 1539-3755, 1550-2376. DOI: 10.1103/PhysRevE.71.065103. URL: https://link.aps.org/doi/10.1103/PhysRevE.71.065103 (visited on 04/03/2021).

Palombit, Alessandro et al. (May 2022). "Variability of regional glucose metabolism and the topology of functional networks in the human brain". In: *NeuroImage*, p. 119280. ISSN: 10538119. DOI: 10.1016/j.neuroimage.2022.119280. URL: https://linkinghub.elsevier.com/retrieve/pii/S1053811922004013 (visited on 05/04/2022).

Paquola, Casey et al. (Aug. 25, 2021). "The BigBrainWarp toolbox for integration of BigBrain 3D histology with multimodal neuroimaging". In: *eLife* 10, e70119. ISSN: 2050-084X. DOI: 10.7554/eLife.70119. URL: https://elifesciences.org/articles/70119 (visited on 08/25/2022).

Passow, Susanne et al. (June 2015). "Default-mode network functional connectivity is closely related to metabolic activity". In: *Human Brain Mapping* 36.6, pp. 2027–2038. ISSN: 1065-9471, 1097-0193. DOI: 10.1002/hbm.22753. URL: https://onlinelibrary.wiley.com/doi/10.1002/hbm.22753 (visited on 04/03/2021).

Patlak, Clifford S., Ronald G. Blasberg, and Joseph D. Fenstermacher (Mar. 1983). "Graphical Evaluation of Blood-to-Brain Transfer Constants from Multiple-Time Uptake Data". In: *Journal of Cerebral Blood Flow & Metabolism* 3.1, pp. 1–7. ISSN: 0271-678X, 1559-7016. DOI: 10.1038/jcbfm.1983.1. URL: http://journals.sagepub.com/doi/10.1038/jcbfm.1983.1 (visited on 04/06/2021).

Pedersen, Mangor et al. (June 2017). "Spontaneous brain network activity: Analysis of its temporal complexity". In: *Network Neuroscience* 1.2, pp. 100–115.

ISSN: 2472-1751. DOI: 10.1162/NETN_a_00006. URL: https://direct.mit.edu/netn/article/1/2/100-115/5389 (visited on 04/03/2021).

Peruzzo, Denis et al. (Dec. 2011). "Automatic selection of arterial input function on dynamic contrast-enhanced MR images". In: *Computer Methods and Programs in Biomedicine* 104.3, e148–e157. ISSN: 01692607. DOI: 10.1016/j.cmpb.2011.02.012. URL: https://linkinghub.elsevier.com/retrieve/pii/S0169260711000447 (visited on 01/20/2022).

Pessin, J E and G I Bell (Oct. 1992). "Mammalian Facilitative Glucose Transporter Family: Structure and Molecular Regulation". In: *Annual Review of Physiology* 54.1, pp. 911–930. ISSN: 0066-4278, 1545-1585. DOI: 10.1146/annurev.ph.54.030192.004403. URL: https://www.annualreviews.org/doi/10.1146/annurev.ph.54.030192.004403 (visited on 08/25/2022).

Phelps, M. E. et al. (Nov. 1979). "Tomographic measurement of local cerebral glucose metabolic rate in humans with (F-18)2-fluoro-2-deoxy-D-glucose: Validation of method". In: *Annals of Neurology* 6.5, pp. 371–388. ISSN: 0364-5134, 1531-8249. DOI: 10.1002/ana.410060502. URL: http://doi.wiley.com/10.1002/ana.410060502 (visited on 04/06/2021).

Piert, M. et al. (Feb. 1996). "Diminished glucose transport and phosphorylation in Alzheimer's disease determined by dynamic FDG-PET". In: *Journal of Nuclear Medicine: Official Publication, Society of Nuclear Medicine* 37.2, pp. 201–208. ISSN: 0161-5505.

Power, Jonathan D. et al. (2014). "Methods to detect, characterize, and remove motion artifact in resting state fMRI." In: *NeuroImage* 84, pp. 320–341. ISSN: 1095-9572 (Electronic). DOI: 10.1016/j.neuroimage.2013.08.048.

Preti, Maria Giulia, Thomas AW Bolton, and Dimitri Van De Ville (Oct. 2017). "The dynamic functional connectome: State-of-the-art and perspectives". In: *NeuroImage* 160, pp. 41–54. ISSN: 10538119. DOI: 10.1016/j.neuroimage.2016.12.061. URL: https://linkinghub.elsevier.com/retrieve/pii/S1053811916307881 (visited on 04/03/2021).

Pretis, Felix, J. James Reade, and Genaro Sucarrat (2018). "Automated General-to-Specific (GETS) Regression Modeling and Indicator Saturation for Outliers and Structural Breaks". In: *Journal of Statistical Software* 86.3. ISSN: 1548-7660. DOI: 10.18637/jss.v086.i03. URL: http://www.jstatsoft.org/v86/i03/ (visited on 04/03/2021).

Raichle, M. E. (Feb. 3, 1998). "Behind the scenes of functional brain imaging: A historical and physiological perspective". In: *Proceedings of the National*

Academy of Sciences 95.3, pp. 765–772. ISSN: 0027-8424, 1091-6490. DOI: 10.1073/pnas.95.3.765. URL: http://www.pnas.org/cgi/doi/10.1073/pnas.95.3.765 (visited on 04/06/2021).

Raichle, M. E. et al. (Sept. 1983). "Brain blood flow measured with intravenous H2(15)O. II. Implementation and validation". In: *Journal of Nuclear Medicine: Official Publication, Society of Nuclear Medicine* 24.9, pp. 790–798. ISSN: 0161-5505.

Raichle, Marcus E. (Aug. 1, 1976). "Correlation Between Regional Cerebral Blood Flow and Oxidative Metabolism: In Vivo Studies in Man". In: *Archives of Neurology* 33.8, p. 523. ISSN: 0003-9942. DOI: 10.1001/archneur.1976.00500080001001. URL: http://archneur.jamanetwork.com/article.aspx?doi=10.1001/archneur.1976.00500080001001 (visited on 04/06/2021).

— (July 12, 2001). "Bold insights". In: *Nature* 412.6843, pp. 128–130. ISSN: 0028-0836, 1476-4687. DOI: 10.1038/35084300. URL: http://www.nature.com/articles/35084300 (visited on 04/06/2021).

— (2006). "The Brain's Dark Energy". In: *Science* 314.5803, pp. 1249–1250.

— (May 19, 2015). "The restless brain: how intrinsic activity organizes brain function". In: *Philosophical Transactions of the Royal Society B: Biological Sciences* 370.1668, p. 20140172. ISSN: 0962-8436, 1471-2970. DOI: 10.1098/rstb.2014.0172. URL: https://royalsocietypublishing.org/doi/10.1098/rstb.2014.0172 (visited on 04/03/2021).

Reivich, M. et al. (June 1985). "Glucose Metabolic Rate Kinetic Model Parameter Determination in Humans: The Lumped Constants and Rate Constants for [^{18} F]Fluorodeoxyglucose and [^{11} C]Deoxyglucose". In: *Journal of Cerebral Blood Flow & Metabolism* 5.2, pp. 179–192. ISSN: 0271-678X, 1559-7016. DOI: 10.1038/jcbfm.1985.24. URL: http://journals.sagepub.com/doi/10.1038/jcbfm.1985.24 (visited on 04/06/2021).

Renkin, Eugene M. (Dec. 1, 1959). "Transport of potassium-42 from blood to tissue in isolated mammalian skeletal muscles". In: *American Journal of Physiology-Legacy Content* 197.6, pp. 1205–1210. ISSN: 0002-9513. DOI: 10.1152/ajplegacy.1959.197.6.1205. URL: https://www.physiology.org/doi/10.1152/ajplegacy.1959.197.6.1205 (visited on 04/06/2021).

Richman, Joshua S. and J. Randall Moorman (June 1, 2000). "Physiological time-series analysis using approximate entropy and sample entropy". In: *American Journal of Physiology-Heart and Circulatory Physiology* 278.6, H2039–H2049. ISSN: 0363-6135, 1522-1539. DOI: 10.1152/ajpheart.2000.278.6.H2039.

URL: https://www.physiology.org/doi/10.1152/ajpheart.2000.278.6.H2039 (visited on 08/27/2022).

Riedl, V. et al. (Apr. 30, 2014). "Local Activity Determines Functional Connectivity in the Resting Human Brain: A Simultaneous FDG-PET/fMRI Study". In: *Journal of Neuroscience* 34.18, pp. 6260–6266. ISSN: 0270-6474, 1529-2401. DOI: 10.1523/JNEUROSCI.0492-14.2014. URL: http://www.jneurosci.org/cgi/doi/10.1523/JNEUROSCI.0492-14.2014 (visited on 04/03/2021).

Rizzo, Gaia et al. (Apr. 2017). "Bayesian Quantification of Contrast-Enhanced Ultrasound Images With Adaptive Inclusion of an Irreversible Component". In: *IEEE Transactions on Medical Imaging* 36.4, pp. 1027–1036. ISSN: 0278-0062, 1558-254X. DOI: 10.1109/TMI.2016.2637698. URL: http://ieeexplore.ieee.org/document/7778162/ (visited on 08/16/2022).

Rousset, Olivier et al. (Apr. 2007). "Partial Volume Correction Strategies in PET". In: *PET Clinics* 2.2, pp. 235–249. ISSN: 15568598. DOI: 10.1016/j.cpet.2007.10.005. URL: https://linkinghub.elsevier.com/retrieve/pii/S1556859807000338 (visited on 08/15/2022).

Roy, C. S. and C. S. Sherrington (Jan. 1, 1890). "On the Regulation of the Blood-supply of the Brain". In: *The Journal of Physiology* 11.1, pp. 85–158. ISSN: 00223751. DOI: 10.1113/jphysiol.1890.sp000321. URL: http://doi.wiley.com/10.1113/jphysiol.1890.sp000321 (visited on 04/06/2021).

Rubinov, Mikail and Olaf Sporns (2010). "Complex network measures of brain connectivity: uses and interpretations." In: *NeuroImage* 52.3, pp. 1059–1069. ISSN: 1095-9572 (Electronic). DOI: 10.1016/j.neuroimage.2009.10.003.

Sala, Arianna, Aldana Lizarraga, et al. (Aug. 19, 2021). "Static versus Functional PET: Making Sense of Metabolic Connectivity". In: *Cerebral Cortex*, bhab271. ISSN: 1047-3211, 1460-2199. DOI: 10.1093/cercor/bhab271. URL: https://academic.oup.com/cercor/advance-article/doi/10.1093/cercor/bhab271/6354619 (visited on 01/02/2022).

Sala, Arianna and Daniela Perani (June 14, 2019). "Brain Molecular Connectivity in Neurodegenerative Diseases: Recent Advances and New Perspectives Using Positron Emission Tomography". In: *Frontiers in Neuroscience* 13, p. 617. ISSN: 1662-453X. DOI: 10.3389/fnins.2019.00617. URL: https://www.frontiersin.org/article/10.3389/fnins.2019.00617/full (visited on 04/06/2021).

Sari, Hasan et al. (May 2022). "First results on kinetic modelling and parametric imaging of dynamic 18F-FDG datasets from a long axial FOV PET scanner in oncological patients". In: *European Journal of Nuclear Medicine and Molecular Imaging* 49.6, pp. 1997–2009. ISSN: 1619-7070, 1619-7089. DOI: 10.1007/s00259-021-05623-6. URL: https://link.springer.com/10.1007/s00259-021-05623-6 (visited on 08/16/2022).

Sattarivand, Mike et al. (Nov. 7, 2012). "Symmetric geometric transfer matrix partial volume correction for PET imaging: principle, validation and robustness". In: *Physics in Medicine and Biology* 57.21, pp. 7101–7116. ISSN: 0031-9155, 1361-6560. DOI: 10.1088/0031-9155/57/21/7101. URL: https://iopscience.iop.org/article/10.1088/0031-9155/57/21/7101 (visited on 09/19/2022).

Savio, Alexandre et al. (Aug. 2017). "Resting-State Networks as Simultaneously Measured with Functional MRI and PET". In: *Journal of Nuclear Medicine* 58.8, pp. 1314–1317. ISSN: 0161-5505, 2159-662X. DOI: 10.2967/jnumed.116.185835. URL: http://jnm.snmjournals.org/lookup/doi/10.2967/jnumed.116.185835 (visited on 04/06/2021).

Schaefer, Alexander et al. (Sept. 1, 2018). "Local-Global Parcellation of the Human Cerebral Cortex from Intrinsic Functional Connectivity MRI". In: *Cerebral Cortex* 28.9, pp. 3095–3114. ISSN: 1047-3211, 1460-2199. DOI: 10.1093/cercor/bhx179. URL: https://academic.oup.com/cercor/article/28/9/3095/3978804 (visited on 04/03/2021).

Schmidt, K. et al. (Sept. 1992). "Errors Introduced by Tissue Heterogeneity in Estimation of Local Cerebral Glucose Utilization with Current Kinetic Models of the [^{18}F]Fluorodeoxyglucose Method". In: *Journal of Cerebral Blood Flow & Metabolism* 12.5, pp. 823–834. ISSN: 0271-678X, 1559-7016. DOI: 10.1038/jcbfm.1992.114. URL: http://journals.sagepub.com/doi/10.1038/jcbfm.1992.114 (visited on 04/06/2021).

Scholvinck, M. L. et al. (June 1, 2010). "Neural basis of global resting-state fMRI activity". In: *Proceedings of the National Academy of Sciences* 107.22, pp. 10238–10243. ISSN: 0027-8424, 1091-6490. DOI: 10.1073/pnas.0913110107. URL: http://www.pnas.org/cgi/doi/10.1073/pnas.0913110107 (visited on 04/06/2021).

Shaffer, Juliet Popper (Sept. 1986). "Modified Sequentially Rejective Multiple Test Procedures". In: *Journal of the American Statistical Association* 81.395, pp. 826–831. ISSN: 0162-1459, 1537-274X. DOI: 10.1080/01621459.1986.10478341. URL: http://www.tandfonline.com/doi/abs/10.1080/01621459.1986.10478341 (visited on 08/15/2022).

Shapiro, S. S. and M. B. Wilk (Dec. 1, 1965). "An analysis of variance test for normality (complete samples)". In: *Biometrika* 52.3, pp. 591–611. ISSN: 0006-3444, 1464-3510. DOI: 10.1093/biomet/52.3-4.591. URL: https://academic.oup.com/biomet/article-lookup/doi/10.1093/biomet/52.3-4.591 (visited on 03/25/2022).

Sheline, Yvette I. and Marcus E. Raichle (Sept. 2013). "Resting State Functional Connectivity in Preclinical Alzheimer's Disease". In: *Biological Psychiatry* 74.5, pp. 340–347. ISSN: 00063223. DOI: 10.1016/j.biopsych.2012.11.028. URL: https://linkinghub.elsevier.com/retrieve/pii/S0006322312010591 (visited on 08/31/2022).

Shokri-Kojori, Ehsan et al. (Dec. 2019). "Correspondence between cerebral glucose metabolism and BOLD reveals relative power and cost in human brain". In: *Nature Communications* 10.1, p. 690. ISSN: 2041-1723. DOI: 10.1038/s41467-019-08546-x. URL: http://www.nature.com/articles/s41467-019-08546-x (visited on 04/03/2021).

Siegel, Joshua S, Gordon L Shulman, and Maurizio Corbetta (Aug. 2017). "Measuring functional connectivity in stroke: Approaches and considerations". In: *Journal of Cerebral Blood Flow & Metabolism* 37.8, pp. 2665–2678. ISSN: 0271-678X, 1559-7016. DOI: 10.1177/0271678X17709198. URL: http://journals.sagepub.com/doi/10.1177/0271678X17709198 (visited on 08/31/2022).

Silvestri, Erica et al. (July 11, 2022). "Image-derived Input Function in brain [^{18} F]FDG PET data: which alternatives to the carotid siphons?" In: *2022 44th Annual International Conference of the IEEE Engineering in Medicine & Biology Society (EMBC)*. 2022 44th Annual International Conference of the IEEE Engineering in Medicine & Biology Society (EMBC). Glasgow, Scotland, United Kingdom: IEEE, pp. 243–246. ISBN: 978-1-72812-782-8. DOI: 10.1109/EMBC48229.2022.9871200. URL: https://ieeexplore.ieee.org/document/9871200/ (visited on 09/09/2022).

Smith, Stephen M., Mark Jenkinson, et al. (2004). "Advances in functional and structural MR image analysis and implementation as FSL". In: *NeuroImage* 23 (SUPPL. 1), S208–S219. ISSN: 10538119. DOI: 10.1016/j.neuroimage.2004.07.051.

Smith, Stephen M., Karla L. Miller, et al. (Jan. 2011). "Network modelling methods for FMRI". In: *NeuroImage* 54.2, pp. 875–891. ISSN: 10538119. DOI: 10.

1016/j.neuroimage.2010.08.063. URL: https://linkinghub.elsevier.com/retrieve/pii/S1053811910011602 (visited on 03/27/2022).

Smith, Stephen M. and Thomas E. Nichols (Jan. 2018). “Statistical Challenges in “Big Data” Human Neuroimaging”. In: *Neuron* 97.2, pp. 263–268. ISSN: 08966273. DOI: 10.1016/j.neuron.2017.12.018. URL: https://linkinghub.elsevier.com/retrieve/pii/S0896627317311418 (visited on 04/03/2021).

Sokoloff, L. et al. (May 1977). “THE [^{14} C]DEOXYGLUCOSE METHOD FOR THE MEASUREMENT OF LOCAL CEREBRAL GLUCOSE UTILIZATION: THEORY, PROCEDURE, AND NORMAL VALUES IN THE CONSCIOUS AND ANESTHETIZED ALBINO RAT”. In: *Journal of Neurochemistry* 28.5, pp. 897–916. ISSN: 0022-3042, 1471-4159. DOI: 10.1111/j.1471-4159.1977.tb10649.x. URL: https://onlinelibrary.wiley.com/doi/10.1111/j.1471-4159.1977.tb10649.x (visited on 03/25/2022).

Sokoloff, Louis (1999). “Energetics of functional activation in neural tissues”. In: *Neurochemical Research* 24.2, pp. 321–329. ISSN: 03643190. DOI: 10.1023/A:1022534709672.

Sokoloff, Louis et al. (1955). “The effect of mental arithmetic on cerebral circulation and metabolism”. In: *Journal of Clinical Investigation* 34.7, pp. 1101–1108. DOI: 10.1172/jci103159.

Sokunbi, M. O. et al. (Nov. 2011). “Inter-individual Differences in fMRI Entropy Measurements in Old Age”. In: *IEEE Transactions on Biomedical Engineering* 58.11, pp. 3206–3214. ISSN: 0018-9294, 1558-2531. DOI: 10.1109/TBME.2011.2164793. URL: http://ieeexplore.ieee.org/document/5995157/ (visited on 04/03/2021).

Ssali, Tracy et al. (Aug. 2018). “A Noninvasive Method for Quantifying Cerebral Blood Flow by Hybrid PET/MRI”. In: *Journal of Nuclear Medicine* 59.8, pp. 1329–1334. ISSN: 0161-5505, 2159-662X. DOI: 10.2967/jnumed.117.203414. URL: http://jnm.snmjournals.org/lookup/doi/10.2967/jnumed.117.203414 (visited on 08/16/2022).

Stone, M. (Jan. 1974). “Cross-Validatory Choice and Assessment of Statistical Predictions”. In: *Journal of the Royal Statistical Society: Series B (Methodological)* 36.2, pp. 111–133. ISSN: 00359246. DOI: 10.1111/j.2517-6161.1974.tb00994.x. URL: http://doi.wiley.com/10.1111/j.2517-6161.1974.tb00994.x (visited on 04/03/2021).

Strauss, Ludwig G. et al. (Dec. 2011). “Impact of Cell-Proliferation-Associated Gene Expression on 2-Deoxy-2-[18F]fluoro-d-Glucose (FDG) Kinetics as Measured by Dynamic Positron Emission Tomography (dPET) in Colorectal Tumors". In: *Molecular Imaging and Biology* 13.6, pp. 1290–1300. ISSN: 1536-1632, 1860-2002. DOI: 10.1007/s11307-010-0465-z. URL: http://link.springer.com/10.1007/s11307-010-0465-z (visited on 08/26/2022).

Sundar, Lalith KS et al. (Aug. 2019). "Towards quantitative [18F]FDG-PET/MRI of the brain: Automated MR-driven calculation of an image-derived input function for the non-invasive determination of cerebral glucose metabolic rates". In: *Journal of Cerebral Blood Flow & Metabolism* 39.8, pp. 1516–1530. ISSN: 0271-678X, 1559-7016. DOI: 10.1177/0271678X18776820. URL: http://journals.sagepub.com/doi/10.1177/0271678X18776820 (visited on 09/19/2022).

Tagliazucchi, Enzo et al. (2012). "Criticality in Large-Scale Brain fMRI Dynamics Unveiled by a Novel Point Process Analysis". In: *Frontiers in Physiology* 3. ISSN: 1664-042X. DOI: 10.3389/fphys.2012.00015. URL: http://journal.frontiersin.org/article/10.3389/fphys.2012.00015/abstract (visited on 04/03/2021).

Thompson, William H. and Peter Fransson (July 14, 2015). "The mean–variance relationship reveals two possible strategies for dynamic brain connectivity analysis in fMRI". In: *Frontiers in Human Neuroscience* 9. ISSN: 1662-5161. DOI: 10.3389/fnhum.2015.00398. URL: http://journal.frontiersin.org/Article/10.3389/fnhum.2015.00398/abstract (visited on 04/03/2021).

Tian, Ye et al. (Nov. 2020). "Topographic organization of the human subcortex unveiled with functional connectivity gradients". In: *Nature Neuroscience* 23.11, pp. 1421–1432. ISSN: 1097-6256, 1546-1726. DOI: 10.1038/s41593-020-00711-6. URL: https://www.nature.com/articles/s41593-020-00711-6 (visited on 08/28/2022).

Tibshirani, Robert (Jan. 1996). "Regression Shrinkage and Selection Via the Lasso". In: *Journal of the Royal Statistical Society: Series B (Methodological)* 58.1, pp. 267–288. ISSN: 00359246. DOI: 10.1111/j.2517-6161.1996.tb02080.x. URL: http://doi.wiley.com/10.1111/j.2517-6161.1996.tb02080.x (visited on 04/03/2021).

Titov, Dmitry et al. (Jan. 2017). "Metabolic connectivity for differential diagnosis of dementing disorders". In: *Journal of Cerebral Blood Flow & Metabolism* 37.1, pp. 252–262. ISSN: 0271-678X, 1559-7016. DOI: 10.1177/0271678X15622465. URL: http://journals.sagepub.com/doi/10.1177/0271678X15622465 (visited on 03/21/2021).

Tomasi, Dardo, Gene Jack Wang, and Nora D. Volkow (2013). "Energetic cost of brain functional connectivity". In: *Proceedings of the National Academy of Sciences of the United States of America* 110.33, pp. 13642–13647. DOI: 10.1073/pnas.1303346110.

Tomasi, Dardo G et al. (Dec. 2017). "Dynamic brain glucose metabolism identifies anti-correlated cortical-cerebellar networks at rest". In: *Journal of Cerebral Blood Flow & Metabolism* 37.12, pp. 3659–3670. ISSN: 0271-678X, 1559-7016. DOI: 10.1177/0271678X17708692. URL: http://journals.sagepub.com/doi/10.1177/0271678X17708692 (visited on 04/06/2021).

Tong, Yunjie et al. (Feb. 2017). "Perfusion information extracted from resting state functional magnetic resonance imaging". In: *Journal of Cerebral Blood Flow & Metabolism* 37.2, pp. 564–576. ISSN: 0271-678X, 1559-7016. DOI: 10.1177/0271678X16631755. URL: http://journals.sagepub.com/doi/10.1177/0271678X16631755 (visited on 05/02/2021).

Tonidandel, Scott and James M. LeBreton (Mar. 2011). "Relative Importance Analysis: A Useful Supplement to Regression Analysis". In: *Journal of Business and Psychology* 26.1, pp. 1–9. ISSN: 0889-3268, 1573-353X. DOI: 10.1007/s10869-010-9204-3. URL: http://link.springer.com/10.1007/s10869-010-9204-3 (visited on 05/01/2021).

Tonietto, Matteo et al. (Aug. 2015). "Modelling arterial input functions in positron emission tomography dynamic studies". In: *2015 37th Annual International Conference of the IEEE Engineering in Medicine and Biology Society (EMBC)*. 2015 37th Annual International Conference of the IEEE Engineering in Medicine and Biology Society (EMBC). Milan: IEEE, pp. 2247–2250. ISBN: 978-1-4244-9271-8. DOI: 10.1109/EMBC.2015.7318839. URL: http://ieeexplore.ieee.org/document/7318839/ (visited on 10/12/2021).

Tustison, N. et al. (2013). "The ANTs Longitudinal Cortical Thickness Pipeline". In: *SPIE Proceedings: Medical Imaging 2013: Biomedical Applications in Molecular, Structural, and Functional Imaging*. Ed. by John B. Weaver; and Robert C. Molthen.

Tustison, Nicholas J et al. (June 2010). "N4ITK: Improved N3 Bias Correction". In: *IEEE Transactions on Medical Imaging* 29.6, pp. 1310–1320. ISSN: 0278-0062, 1558-254X. DOI: 10.1109/TMI.2010.2046908. URL: http://ieeexplore.ieee.org/document/5445030/ (visited on 04/03/2021).

Ugurbil, Kamil (Oct. 5, 2016). "What is feasible with imaging human brain function and connectivity using functional magnetic resonance imaging". In:

Philosophical Transactions of the Royal Society B: Biological Sciences 371.1705, p. 20150361. ISSN: 0962-8436, 1471-2970. DOI: 10.1098/rstb.2015.0361. URL: https://royalsocietypublishing.org/doi/10.1098/rstb.2015.0361 (visited on 04/06/2021).

Ulrich, Xialing and Dmitriy A. Yablonskiy (Feb. 2016). "Separation of cellular and BOLD contributions to T2* signal relaxation". In: *Magnetic Resonance in Medicine* 75.2, pp. 606–615. ISSN: 0740-3194, 1522-2594. DOI: 10.1002/mrm.25610. URL: https://onlinelibrary.wiley.com/doi/10.1002/mrm.25610 (visited on 04/03/2021).

Vaishnavi, S. Neil et al. (Oct. 12, 2010). "Regional aerobic glycolysis in the human brain". In: *Proceedings of the National Academy of Sciences* 107.41, pp. 17757–17762. ISSN: 0027-8424, 1091-6490. DOI: 10.1073/pnas.1010459107. URL: http://www.pnas.org/lookup/doi/10.1073/pnas.1010459107 (visited on 04/03/2021).

Venkataraman, Ashwin V. et al. (Aug. 17, 2022). "Widespread cell stress and mitochondrial dysfunction occur in patients with early Alzheimer's disease". In: *Science Translational Medicine* 14.658, eabk1051. ISSN: 1946-6234, 1946-6242. DOI: 10.1126/scitranslmed.abk1051. URL: https://www.science.org/doi/10.1126/scitranslmed.abk1051 (visited on 08/25/2022).

Veronese, Mattia et al. (Dec. 2019). "Covariance statistics and network analysis of brain PET imaging studies". In: *Scientific Reports* 9.1, p. 2496. ISSN: 2045-2322. DOI: 10.1038/s41598-019-39005-8. URL: http://www.nature.com/articles/s41598-019-39005-8 (visited on 04/06/2021).

Villien, Marjorie et al. (Oct. 2014). "Dynamic functional imaging of brain glucose utilization using fPET-FDG". In: *NeuroImage* 100, pp. 192–199. ISSN: 10538119. DOI: 10.1016/j.neuroimage.2014.06.025. URL: https://linkinghub.elsevier.com/retrieve/pii/S1053811914005023 (visited on 04/06/2021).

Voigt, Katharina et al. (Apr. 19, 2022). "Metabolic and functional connectivity provide unique and complementary insights into cognition-connectome relationships". In: *Cerebral Cortex*, bhac150. ISSN: 1047-3211, 1460-2199. DOI: 10.1093/cercor/bhac150. URL: https://academic.oup.com/cercor/advance-article/doi/10.1093/cercor/bhac150/6570696 (visited on 08/15/2022).

Volpi, T, M De Francisci, et al. (2022). "The many faces of'metabolic connectivity': Comparing [18F] FDG kinetic model parameters vs. SUVR networks". In:

JOURNAL OF CEREBRAL BLOOD FLOW AND METABOLISM. Vol. 42. 1_ SUPPL. SAGE PUBLICATIONS INC 2455 TELLER RD, THOUSAND OAKS, CA 91320 USA, pp. 41–41.

Volpi, T, J Lee, et al. (2022). “The spatial organization of [18F] FDG inflow and phosphorylation and their association with resting-state fMRI measures”. In: *JOURNAL OF CEREBRAL BLOOD FLOW AND METABOLISM*. Vol. 42. 1_ SUPPL. SAGE PUBLICATIONS INC 2455 TELLER RD, THOUSAND OAKS, CA 91320 USA, pp. 42–43.

Volpi, T, E Silvestri, M Aiello, et al. (2022). “Investigating possible nonlinearities in the spatial association between [18F] FDG PET and resting-state fMRI variables”. In: *JOURNAL OF CEREBRAL BLOOD FLOW AND METABOLISM*. Vol. 42. 1_ SUPPL. SAGE PUBLICATIONS INC 2455 TELLER RD, THOUSAND OAKS, CA 91320 USA, pp. 204–204.

Volpi, T, E Silvestri, J Lee, et al. (2022). “The role of neurotransmitter systems in shaping glucose metabolism: Evidence from brain PET studies”. In: *JOURNAL OF CEREBRAL BLOOD FLOW AND METABOLISM*. Vol. 42. 1_ SUPPL. SAGE PUBLICATIONS INC 2455 TELLER RD, THOUSAND OAKS, CA 91320 USA, pp. 41–42.

Volpi, Tommaso, Marco Aiello, et al. (2021). “Anti-correlations between F-18-FDG PET and resting state dynamic functional connectivity: Insights into brain network variability”. In: *JOURNAL OF CEREBRAL BLOOD FLOW AND METABOLISM*. Vol. 41. 1_ SUPPL. SAGE PUBLICATIONS INC 2455 TELLER RD, THOUSAND OAKS, CA 91320 USA, pp. 199–200.

Volpi, Tommaso, John J. Lee, et al. (July 11, 2022). “Modeling venous plasma samples in \$[^{18}\mathrm{F}]\$ FDG PET studies: a nonlinear mixed-effects approach”. In: *2022 44th Annual International Conference of the IEEE Engineering in Medicine & Biology Society (EMBC)*. 2022 44th Annual International Conference of the IEEE Engineering in Medicine & Biology Society (EMBC). Glasgow, Scotland, United Kingdom: IEEE, pp. 4704–4707. ISBN: 978-1-72812-782-8. DOI: 10.1109/EMBC48229.2022.9871429. URL: https://ieeexplore.ieee.org/document/9871429/ (visited on 09/09/2022).

Volpi, Tommaso, Erica Silvestri, Marco Aiello, et al. (2021a). “A multiple regression modelling approach to investigate the coupling between [F-18] fluorodeoxyglucose positron emission tomography and resting-state functional MRI”. In: *JOURNAL OF CEREBRAL BLOOD FLOW AND METABOLISM*.

Vol. 41. 1_ SUPPL. SAGE PUBLICATIONS INC 2455 TELLER RD, THOUSAND OAKS, CA 91320 USA, pp. 89–90.

— (Aug. 4, 2021b). "The complexity of the relationship between spontaneous brain activity and glucose metabolism". In: DOI: 10.21203/rs.3.rs-728300/v1. URL: https://www.researchsquare.com/article/rs-728300/v1 (visited on 08/20/2021).

Volpi, Tommaso, Erica Silvestri, Maurizio Corbetta, et al. (Nov. 1, 2021). "Assessing different approaches to estimate single-subject metabolic connectivity from dynamic [^{18} F]fluorodeoxyglucose Positron Emission Tomography data". In: *2021 43rd Annual International Conference of the IEEE Engineering in Medicine & Biology Society (EMBC)*. 2021 43rd Annual International Conference of the IEEE Engineering in Medicine & Biology Society (EMBC). Mexico: IEEE, pp. 3259–3262. ISBN: 978-1-72811-179-7. DOI: 10.1109/EMBC46164.2021.9630441. URL: https://ieeexplore.ieee.org/document/9630441/ (visited on 01/06/2022).

Volpi, Tommaso, Erica Silvestri, Alexander Hammers, et al. (2021). "Individual-level molecular connectivity of GABA (A) receptors: assessing the similarity of [C-11] Ro15-4513 kinetics across brain regions". In: *JOURNAL OF CEREBRAL BLOOD FLOW AND METABOLISM*. Vol. 41. 1_ SUPPL. SAGE PUBLICATIONS INC 2455 TELLER RD, THOUSAND OAKS, CA 91320 USA, pp. 143–144.

Volpi, Tommaso, Giulia Vallini, et al. (2022). "Network hubs revealed by" metabolic connectivity" mapping from [18F] FDG kinetic parameters". In: *JOURNAL OF CEREBRAL BLOOD FLOW AND METABOLISM*. Vol. 42. 1_ SUPPL. SAGE PUBLICATIONS INC 2455 TELLER RD, THOUSAND OAKS, CA 91320 USA, pp. 289–290.

Vos de Wael, Reinder et al. (Dec. 2020). "BrainSpace: a toolbox for the analysis of macroscale gradients in neuroimaging and connectomics datasets". In: *Communications Biology* 3.1, p. 103. ISSN: 2399-3642. DOI: 10.1038/s42003-020-0794-7. URL: http://www.nature.com/articles/s42003-020-0794-7 (visited on 08/28/2022).

Wang, Hongzhi and Paul A. Yushkevich (2013). "Multi-atlas segmentation with joint label fusion and corrective learning—an open source implementation". In: *Frontiers in Neuroinformatics* 7. ISSN: 1662-5196. DOI: 10.3389/fninf.2013.00027. URL: http://journal.frontiersin.org/article/10.3389/fninf.2013.00027/abstract (visited on 04/03/2021).

Wang, Jingjuan et al. (Feb. 1, 2021). "The Relationship Among Glucose Metabolism, Cerebral Blood Flow, and Functional Activity: a Hybrid PET/fMRI Study". In: *Molecular Neurobiology*. ISSN: 0893-7648, 1559-1182. DOI: 10.1007/s12035-021-02305-0. URL: http://link.springer.com/10.1007/s12035-021-02305-0 (visited on 04/03/2021).

Ward, Joe H. (Mar. 1963). "Hierarchical Grouping to Optimize an Objective Function". In: *Journal of the American Statistical Association* 58.301, pp. 236–244. ISSN: 0162-1459, 1537-274X. DOI: 10.1080/01621459.1963.10500845. URL: http://www.tandfonline.com/doi/abs/10.1080/01621459.1963.10500845 (visited on 04/03/2021).

Watts, Duncan J. and Steven H. Strogatz (June 1998). "Collective dynamics of 'small-world' networks". In: *Nature* 393.6684, pp. 440–442. ISSN: 0028-0836, 1476-4687. DOI: 10.1038/30918. URL: http://www.nature.com/articles/30918 (visited on 04/03/2021).

Wehrl, Hans F. et al. (2013). "Simultaneous PET-MRI reveals brain function in activated and resting state on metabolic, hemodynamic and multiple temporal scales". In: *Nature Medicine* 19.9, pp. 1184–1189. ISSN: 10788956. DOI: 10.1038/nm.3290.

Wen, Jie et al. (Oct. 9, 2018). "Genetically defined cellular correlates of the baseline brain MRI signal". In: *Proceedings of the National Academy of Sciences* 115.41, E9727–E9736. ISSN: 0027-8424, 1091-6490. DOI: 10.1073/pnas.1808121115. URL: http://www.pnas.org/lookup/doi/10.1073/pnas.1808121115 (visited on 04/03/2021).

Wesolowski, Roman et al. (Mar. 2019). "Coupling between cerebral blood flow and cerebral blood volume: Contributions of different vascular compartments". In: *NMR in Biomedicine* 32.3, e4061. ISSN: 09523480. DOI: 10.1002/nbm.4061. URL: https://onlinelibrary.wiley.com/doi/10.1002/nbm.4061 (visited on 08/31/2022).

Wienhard, K. et al. (May 1991). "Estimation of Local Cerebral Glucose Utilization by Positron Emission Tomography: Comparison of [^{18} F]2-Fluoro-2-Deoxy-D-Glucose and [^{18} F]2-Fluoro-2-Deoxy-D-Mannose in Patients with Focal Brain Lesions". In: *Journal of Cerebral Blood Flow & Metabolism* 11.3, pp. 485–491. ISSN: 0271-678X, 1559-7016. DOI: 10.1038/jcbfm.1991.92. URL: http://journals.sagepub.com/doi/10.1038/jcbfm.1991.92 (visited on 04/06/2021).

Wijk, Bernadette C. M. van, Cornelis J. Stam, and Andreas Daffertshofer (2010). "Comparing brain networks of different size and connectivity density using graph theory." In: *PloS one* 5.10, e13701. DOI: 10.1371/journal.pone.0013701.

Wu, Guo-Rong, Nigel Colenbier, et al. (Dec. 2021). "rsHRF: A toolbox for resting-state HRF estimation and deconvolution". In: *NeuroImage* 244, p. 118591. ISSN: 10538119. DOI: 10.1016/j.neuroimage.2021.118591. URL: https://linkinghub.elsevier.com/retrieve/pii/S1053811921008648 (visited on 08/27/2022).

Wu, Guo-Rong, Wei Liao, et al. (Apr. 2013). "A blind deconvolution approach to recover effective connectivity brain networks from resting state fMRI data". In: *Medical Image Analysis* 17.3, pp. 365–374. ISSN: 13618415. DOI: 10.1016/j.media.2013.01.003. URL: https://linkinghub.elsevier.com/retrieve/pii/S1361841513000042 (visited on 04/03/2021).

Wu, Guo-Rong and Daniele Marinazzo (Aug. 20, 2015). *Retrieving the Hemodynamic Response Function in resting state fMRI: methodology and applications*. preprint. PeerJ PrePrints. DOI: 10.7287/peerj.preprints.1317v1. URL: https://peerj.com/preprints/1317v1 (visited on 04/03/2021).

— (May 13, 2016). "Sensitivity of the resting-state haemodynamic response function estimation to autonomic nervous system fluctuations". In: *Philosophical Transactions of the Royal Society A: Mathematical, Physical and Engineering Sciences* 374.2067, p. 20150190. ISSN: 1364-503X, 1471-2962. DOI: 10.1098/rsta.2015.0190. URL: https://royalsocietypublishing.org/doi/10.1098/rsta.2015.0190 (visited on 04/03/2021).

Wu, H (Feb. 2003). "Measurement of the Global Lumped Constant for 2-Deoxy-2-[18F]Fluoro-D-Glucose in Normal Human Brain Using [15O]Water and 2-Deoxy-2-[18F]Fluoro-D-Glucose Positron Emission Tomography Imaging A Method with Validation Based on Multiple Methodologies". In: *Molecular Imaging & Biology* 5.1, pp. 32–41. ISSN: 15361632. DOI: 10.1016/S1536-1632(02)00122-1. URL: https://linkinghub.elsevier.com/retrieve/pii/S1536163202001221 (visited on 04/06/2021).

Yakushev, Igor, Alexander Drzezga, and Christian Habeck (Dec. 2017). "Metabolic connectivity: methods and applications". In: *Current Opinion in Neurology* 30.6, pp. 677–685. ISSN: 1350-7540, 1473-6551. DOI: 10.1097/WCO.0000000000000494. URL: https://journals.lww.com/00019052-201712000-00018 (visited on 03/21/2021).

Yakushev, Igor, Isabelle Ripp, et al. (Mar. 2022). “Mapping covariance in brain FDG uptake to structural connectivity”. In: *European Journal of Nuclear Medicine and Molecular Imaging* 49.4, pp. 1288–1297. ISSN: 1619-7070, 1619-7089. DOI: 10.1007/s00259-021-05590-y. URL: https://link.springer.com/10.1007/s00259-021-05590-y (visited on 08/15/2022).

Yamaji, Shigeru et al. (Jan. 2000). “Evaluation of Standardized Uptake Value to Assess Cerebral Glucose Metabolism:” in: *Clinical Nuclear Medicine* 25.1, p. 11. ISSN: 0363-9762. DOI: 10.1097/00003072-200001000-00003. URL: http://journals.lww.com/00003072-200001000-00003 (visited on 08/15/2022).

Yan, Chao-Gan et al. (Oct. 2013). “Standardizing the intrinsic brain: Towards robust measurement of inter-individual variation in 1000 functional connectomes”. In: *NeuroImage* 80, pp. 246–262. ISSN: 10538119. DOI: 10.1016/j.neuroimage.2013.04.081. URL: https://linkinghub.elsevier.com/retrieve/pii/S105381191300428X (visited on 08/31/2022).

Yeh, Fang-Cheng et al. (2018). “Population-averaged atlas of the macroscale human structural connectome and its network topology”. In: *NeuroImage* 178, pp. 57–68. ISSN: 1053-8119. DOI: https://doi.org/10.1016/j.neuroimage.2018.05.027. URL: https://www.sciencedirect.com/science/article/pii/S1053811918304324.

Yeo, B. T. Thomas et al. (2011). “The organization of the human cerebral cortex estimated by intrinsic functional connectivity.” In: *Journal of neurophysiology* 106.3, pp. 1125–1165. DOI: 10.1152/jn.00338.2011.

Zang, Yufeng et al. (2004). “Regional homogeneity approach to fMRI data analysis”. In: *NeuroImage* 22.1, pp. 394–400. ISSN: 10538119. DOI: 10.1016/j.neuroimage.2003.12.030.

Zanotti-Fregonara, Paolo, Kewei Chen, et al. (Oct. 2011). “Image-Derived Input Function for Brain PET Studies: Many Challenges and Few Opportunities”. In: *Journal of Cerebral Blood Flow & Metabolism* 31.10, pp. 1986–1998. ISSN: 0271-678X, 1559-7016. DOI: 10.1038/jcbfm.2011.107. URL: http://journals.sagepub.com/doi/10.1038/jcbfm.2011.107 (visited on 10/12/2021).

Zanotti-Fregonara, Paolo, El Mostafa Fadaili, et al. (Nov. 2009). “Comparison of Eight Methods for the Estimation of the Image-Derived Input Function in Dynamic [^{18} F]-FDG PET Human Brain Studies”. In: *Journal of Cerebral Blood Flow & Metabolism* 29.11, pp. 1825–1835. ISSN: 0271-678X, 1559-7016.

DOI: 10.1038/jcbfm.2009.93. URL: http://journals.sagepub.com/doi/10.1038/jcbfm.2009.93 (visited on 10/12/2021).

Zhang, Xiaodi, Wen-Ju Pan, and Shella Dawn Keilholz (Feb. 2020). "The relationship between BOLD and neural activity arises from temporally sparse events". In: *NeuroImage* 207, p. 116390. ISSN: 10538119. DOI: 10.1016/j.neuroimage.2019.116390. URL: https://linkinghub.elsevier.com/retrieve/pii/S1053811919309814 (visited on 04/03/2021).

Zou, Qi-Hong et al. (July 2008). "An improved approach to detection of amplitude of low-frequency fluctuation (ALFF) for resting-state fMRI: Fractional ALFF". In: *Journal of Neuroscience Methods* 172.1, pp. 137–141. ISSN: 01650270. DOI: 10.1016/j.jneumeth.2008.04.012. URL: https://linkinghub.elsevier.com/retrieve/pii/S0165027008002458 (visited on 04/04/2021).

Zou, Hui and Trevor Hastie (Apr. 2005). "Regularization and variable selection via the elastic net". In: *Journal of the Royal Statistical Society: Series B (Statistical Methodology)* 67.2, pp. 301–320. ISSN: 1369-7412, 1467-9868. DOI: 10.1111/j.1467-9868.2005.00503.x. URL: http://doi.wiley.com/10.1111/j.1467-9868.2005.00503.x (visited on 04/03/2021).

List of Publications

Journals

- Palombit, A., Silvestri, E., Volpi, T., Aiello, M., Cecchin, D., Bertoldo A., Corbetta, M. Variability of regional glucose metabolism and the topology of functional networks in the human brain. Neuroimage 2022 May 4;257:119280. https://doi.org/10.1016/j.neuroimage.2022.119280.

Preprints

- Volpi, T., Silvestri E., Aiello M., Corbetta M., Bertoldo A., "The complexity of the relationship between spontaneous brain activity and glucose metabolism", 2021, https://doi.org/10.21203/rs.3.rs-728300/v1.

Conference Papers

- Volpi, T., Lee, J.J., Silvestri, E., Durbin, T., Corbetta, M., Goyal, M.S., Vlassenko, A.G., Bertoldo, A. Modeling venous plasma samples in [^{18}F]FDG PET studies: a nonlinear mixed-effects approach. IEEE EMBC 2022 (Oral Presentation, Student Paper Competition finalist). https://doi.org/10.1109/EMBC48229.2022.9871429.
- Volpi, T.*, Silvestri, E.*, Bettinelli, A., De Francisci, M., Jones, J., Corbetta, M., Cecchin, D., Bertoldo, A. Image-derived Input Function in brain [^{18}F]FDG PET studies: which alternatives to the carotid syphons? (*shared first author). IEEE EMBC 2022 (Oral Presentation). https://doi.org/10.1109/EMBC48229.2022.9871200.
- Volpi, T., Silvestri E., Corbetta M., Bertoldo A., "Assessing different approaches to estimate single-subject metabolic connectivity from dynamic [^{18}F]fluorodeoxyglucose Positron Emission Tomography data", IEEE EMBC 2021 (Oral Presentation). https://doi.org/10.1109/EMBC46164.2021.9630441.

Conference Abstracts

- Volpi, T., Lee, J.J., Vlassenko, A.G., Goyal, M.S., Bertoldo, A., Corbetta, M., The spatial organization of [^{18}F]FDG inflow and phosphorylation and their association with resting-state fMRI measures. Brain & Brain PET 2022 (Oral Presentation, Niels Lassen Award finalist). https://doi.org/10.1177/0271678X221096356.

- Volpi, T., De Francisci, M., Lee, J.J., Vlassenko, A.G., Goyal, M.S., Corbetta, M., Bertoldo, A., The many faces of 'metabolic connectivity': comparing [^{18}F]FDG kinetic model parameters vs. SUVR networks. Brain & Brain PET 2022 (Oral Presentation). https://doi.org/10.1177/0271678X221096356.

- Volpi, T., Silvestri, E., Lee, J.J., Vlassenko, A.G., Goyal, M.S., Corbetta, M., Bertoldo, A., The role of neurotransmitter systems in shaping glucose metabolism: evidence from brain PET studies. Brain & Brain PET 2022 (Oral Presentation). https://doi.org/10.1177/0271678X221096356.

- Volpi, T., Vallini, G., Lee, J.J., Goyal, M.S., Vlassenko, A.G., Corbetta, M., Bertoldo, A., Network hubs revealed by "metabolic connectivity" mapping from [^{18}F]FDG kinetic parameters. Brain & Brain PET 2022 (Flash Presentation and Poster). https://doi.org/10.1177/0271678X221099127.

- Volpi, T., Silvestri, E., Aiello, M., Corbetta, M., Bertoldo, A. Investigating possible nonlinearities in the spatial association between [^{18}F]FDG PET and resting-state fMRI variables. Brain & Brain PET 2022 (Poster Presentation). https://doi.org/10.1177/0271678X221096357.

- Volpi, T., Silvestri, E., Hammers, A., Bertoldo, A. Individual-level molecular connectivity of GABA$_A$ receptors: assessing the similarity of [^{11}C]Ro15-4513 kinetics across brain regions. NRM 2021 (Poster Presentation). https://doi.org/10.1177/0271678x211061050.

- Volpi, T., Silvestri, E., Aiello, M., Corbetta, M., Bertoldo, A. A multiple regression modelling approach to investigate the coupling between [^{18}F]fluorodeoxyglucose positron emission tomography and resting-state functional MRI. NRM 2021 (Poster Presentation). https://doi.org/10.1177/0271678x211061050.

- Narciso, L., Taha, A., Dassanayake, P., Volpi, T., Liu, L., Soddu, A., Anazodo, U., Bertoldo, A., St Lawrence, K. Development of a non-invasive PET/MRI method for quantifying cerebral glucose kinetics. NRM 2021 (Poster Presentation). https://doi.org/10.1177/0271678x211061050.

- Volpi, T., Aiello, M., Riedl, V., Corbetta, M., Bertoldo, A. Anti-correlations between ^{18}F-FDG PET and resting state dynamic functional connectivity: insights into brain network variability. NRM 2021 (Poster Presentation). https://doi.org/10.1177/0271678x211061050.